Structural Changes of Brain Areas Involved in Emotion and Memory Processing across Lifespan

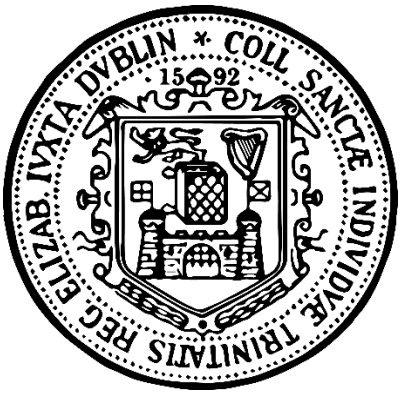

Francesca Sibilia

Thesis submitted to the University of Dublin, Trinity College
for the degree of

Doctor in Philosophy

2020

Supervisor

Prof. Arun L. W. Bokde

Declaration

I declare that this thesis has not been submitted as an exercise for a degree at this or any other university and it is entirely my own work.

I agree to deposit this thesis in the University's open access institutional repository or allow the library to do so on my behalf, subject to Irish Copyright Legislation and Trinity College Library conditions of use and acknowledgement.

Signed: 

Francesca Sibilia, February 2020

Summary

People are defined by their genes, familiar background and personal experiences, that can have either a negative or positive impact. Altogether, this represents and shapes their decisions, behaviours and relationships with others, but also their brain and body. In particular, external stimuli can have a big impact on the brain anatomy, resulting in specific behavioural and emotional responses. Cognitive abilities, such as memory, attention, emotional processing, are modulated by anatomical and functional connections between brain regions that process external stimuli from the environment and produce specific behavioural responses.

This thesis work aims to investigate the brain areas that are more structurally sensitive to physiological changes and environmental stimuli during two critical periods of time in life, such as adolescence and aging. In this thesis, three studies will be presented, exploring structural brain changes due to stress and brain aging with three different structural neuroimaging approaches. In Chapter 1, a general overview of the brain areas involved in emotion and memory processing is presented, along with a description of magnetic resonance imaging (MRI), which is the neuroimaging technique used in all the studies.

Chapter 2 illustrates the first study forming this thesis. Brain connectivity changes are investigated between two groups of adolescents with different levels of stress due to negative life events (Low vs High stress), by using both a graph theory and whole-brain connectivity approach. The High stress group showed a decrease of betweenness centrality measure in the somato-motor cortex, as well as an increase of degree centrality in the visual network and dorsal attention

network. The whole-brain connectivity showed an increase of connectivity strength between regions of the limbic and attentional networks. In Chapter 3, the effect of stress on the hippocampus subfields volume was investigated between the two groups of adolescents from the previous study. The relationship between and hippocampus and the personality trait of Neuroticism was also considered. A relationship between Neuroticism and volume changes was seen in more than one subfield in the left hemisphere of adolescents perceiving higher stress levels. The second part of the analysis explored longitudinal changes of the subfields volume across two time points representing two stages of adolescence. Negative results were found after statistical correction, showing no relationship between hippocampal volumes and stress over time. In Chapter 4, microstructural changes of the cingulum bundle were explored in normal aging, by dividing the whole tract into three branches. Tractography was run on each branch for both hemispheres, and diffusivity measures were extracted to investigate between-group differences. A bilateral reduced microstructural integrity was found in the subgenual (the most anterior) branch in older healthy people.

Overall, this thesis shows how brain areas involved in emotion and memory processing are those that are more affected and sensitive to changes during two critical stages of life, namely adolescence and aging. Structural alterations in these areas may lead to the development of psychiatric disorders, as well as to the acceleration of neurodegenerative processes. More knowledge about the impact that external factors have on the brain can help developing more effective therapeutic interventions.

Acknowledgments

This PhD work is as much a product of many hours of research as it is the product of the inspiration, guidance, support and help of many people without whom, this work would not be possible.

Firstly, I would like to thank Prof. Arun Bokde, for giving me the chance to work on more than one project, increasing my knowledge and passion for neuroimaging.

I would like to thank Dr. Brea Chouinard and Dr. Erik O'Hanlon for their professional support and guidance. Your expertise helped me in the steep learning curve of my PhD. To Coline, who had a crucial role in one of the projects and shared with me many days in coding.

Thanks to the Italian folks in TCIN: Dr. Leonardo Tozzi, Dr. Bernardo Nipoti and Dr. Luca Longo for sharing their professional knowledge on statistics and programming. To Camilla, Emanuela, Chiara, Valentina, and Emanuele - you made me feel closer to home while I was here, your emotional and professional support was never taken for granted. Each one of you gave me something in different ways that made me grow as person and scientist.

To so many other PhD fellows and people I met in the Lloyd during these four years I want to say thank you.

The biggest shout out goes to my two colleagues, Megan (the one and only 'number 1') and Therese. You ladies made my journey incredibly fun and special. I will bring with me all the laughs, tears, walks, nights out and dances we had together! You have become more than just colleagues, and I can't wait to see the amazing things life has in store for you. You shared the highs and lows of this experience till the very last end and gave me confidence in my abilities when I was losing it. Never doubt what amazing women and scientists you both are!

To the "Gruppo Crisi": Fra, Anna, Eugi, Fede, Lisa and Bea, and Mohamed. Thanks for being there always, professionally and personally. We get each other all the time, without too many words. To Fiore, whose mathematical mind saved me many times. I am so grateful for all the hours and Skype calls we had talking

about maths; you always pushed me to learn more. Thanks to Vincent Katongo for his unique way of encouraging, challenging and supporting me since I met him. You helped me so many times putting everything in the right prospective of life.

Special thanks to my friends in Dublin, especially Daniel, Ben, Tumieh, Kimberly and Immanuel. You guys were family when I felt far from mine. Your help, encouragement, and all the times you believed in me, even when I didn't, shaped me and made me grow. I will always be grateful for your friendship. You won't get rid of me that easily, I promise! And Dan, thanks for all the computer-related problems you helped me fix. You were a life saver in many occasions.

Thanks to my cousins and aunties, who have been always present, even if far, and for always believing in me. I valued every text and phone call more than you think. I am so proud of the type of relationship we have.

To my beautiful family – my parents, my sisters, my brother, my sister-in-law and my three nephews. To you all goes my biggest thank you! You are my backbone, my oasis in the desert, my refuge in the storm, my quiet place when there is so much noise. I'll never be grateful enough for each one of you. This work goes mainly to you.

And finally, thanks to Life – all my achievements, adventures and the people I met in these years are a treasure that I will protect and store in me. Because, no matter what I become or where I go, I know I will never be alone. And that says it all!

Acknowledgments for Study One and Study Two

The current analysis received support from the National Children's Hospital Foundation, Tallaght University Hospital, Ireland, under a grant to ALW Bokde. This work received support from the following sources: the European Union-funded FP6 Integrated Project IMAGEN (Reinforcement-related behaviour in normal brain function and psychopathology) (LSHM-CT- 2007-037286), the Horizon 2020 funded ERC Advanced Grant 'STRATIFY' (Brain network based stratification of reinforcement-related disorders) (695313), ERANID (Understanding the Interplay between Cultural, Biological and Subjective Factors in Drug Use Pathways) (PR-ST-0416-10004), BRIDGET (JPND: BRain Imaging, cognition Dementia and next generation GEnomics) (MR/N027558/1), Human Brain Project (HBP SGA 2, 785907), the FP7 project MATRICS (603016), the Medical Research Council Grant 'c-VEDA' (Consortium on Vulnerability to Externalizing Disorders and Addictions) (MR/N000390/1), the National Institute for Health Research (NIHR) Biomedical Research Centre at South London and Maudsley NHS Foundation Trust and King's College London, the Bundesministeriumfür Bildung und Forschung (BMBF grants 01GS08152; 01EV0711; Forschungsnetz AERIAL 01EE1406A, 01EE1406B), the Deutsche Forschungsgemeinschaft (DFG grants SM 80/7-2, SFB 940, TRR 265, NE 1383/14-1), the Medical Research Foundation and Medical Research Council (grants MR/R00465X/1 and MR/S020306/1), the National Institutes of Health (NIH) funded ENIGMA (grants 5U54EB020403-05 and 1R56AG058854-01). Further support was provided by grants from: – the ANR (ANR-12-SAMA-0004, AAPG2019 – GeBra), the Eranet Neuron (AF12-NEUR0008-01 – WM2NA; and ANR-18-NEUR00002-01 – ADORe), the Fondation de France (00081242), the

Fondation pour la Recherche Médicale (DPA20140629802), the Mission Interministérielle de Lutte-contre-les-Drogues-et-les-Conduites-Addictives (MILDECA), the Assistance-Publique-Hôpitaux-de-Paris and INSERM (interface grant), Paris Sud University IDEX 2012, the Fondation de l'Avenir (grant AP-RM-17-013), the Fédération pour la Recherche sur le Cerveau; the National Institutes of Health, Science Foundation Ireland (16/ERCD/3797), U.S.A. (Axon, Testosterone and Mental Health during Adolescence; RO1 MH085772-01A1), and by NIH Consortium grant U54 EB020403, supported by a cross-NIH alliance that funds Big Data to Knowledge Centres of Excellence.

Acknowledgment for Study Three

Thanks to Mr S. Josephs for his assistance in the acquisition of the MRI data, and IT Research (TCD) for providing access to computer resources.

Statement of work

This work of thesis has been possible thanks to the contribution of other people and researchers.

For Study One and Study Two, data acquisition and a first data quality step were done by scientists who are members of the IMAGEN Consortium, represented by eight different research centres and universities from four different European countries. My focus was on data analysis on T1-weighted structural images, which I pre-processed for my own analysis. Before the analysis, I performed an additional quality check on the MRI scans to confirm images with the best quality were used in the studies.

For study Three, both diffusion and structural data were acquired by scientists who were involved in the Neuroskill project before I joined the lab. My work was focused on image quality check, image pre-processing and tractography analysis on T1-weighted images for my own project, focusing on the segmentation of the cingulum branches.

Table of Contents

1. GENERAL INTRODUCTION **1**

1.1. Background 1

1.1.1. Brain Regions Involved in Stress and Memory 4

1.2. Magnetic Resonance Imaging (MRI) 9

1.2.1. MRI Physics 9

1.2.1.1. T1 and T2 Relaxation Time 11

1.2.2. Spin-Echo Sequence 14

1.2.2.1. Sequence SE with Short TE (<30ms) and Short TR (<600ms) 14

1.2.2.2. Sequence SE with Long TR (>1500ms) and Short-Intermediate TE (20-40ms) 14

1.2.2.3. Sequence SE with Long TR (>1500ms) and Long TE (>60ms) 14

1.2.3. Echo-Planar Imaging (EPI) 15

1.2.4. Fluid-Attenuated Inversion Recovery (FLAIR) 15

1.3. Thesis Objective 16

1.4. Research Methodology and Methods 18

2. BRAIN CONNECTIVITY CHANGES WITH STRESS IN ADOLESCENCE **19**

2.1. Adolescence 19

2.1.1. Brain Maturation in Adolescence 20

2.2. Stress and Cognition 22

2.2.1. Brain Structural Changes with Stress in Adolescence 26

2.3. Structural Connectivity 27

2.3.1. Graph Theory Measures 29

2.3.2. Brain Networks Parcellation 30

2.4. Manuscript – Structural Connectivity Alterations of the Cortex in Adolescents Due to Stressful Life Events 31

2.4.1. Introduction 32

2.4.2. Materials and Methods 35

2.4.2.1. Participants 35

2.4.2.2. Imaging 37

2.4.2.3. MRI Analysis 37

2.4.2.4. Statistical Analysis 42

2.4.3. Results 43

2.4.3.1. Results of Graph Theory Analysis 43

2.4.3.2. Whole-Brain Connectivity Results 48

2.4.4. Discussion 49

2.4.5. Conclusion 54

3. VOLUMETRIC CHANGES OF HIPPOCAMPUS SUBFIELDS DUE TO STRESS **56**

3.1. Introduction 56

3.1.1. Hippocampus Development in Adolescence 56

3.1.1.1 Psychiatric Disorders Caused by Stress 57

3.1.2. The Hippocampus and Its Subfields 62

3.1.2.1. Morphological Organization 62

3.1.2.2. Structural Changes with Stress-Related Disorders 65

3.1.2.3. Extraction of Subfields Volume with FreeSufer 6.0 66

3.1.3. Study Objective 68

3.2. Study Material and Methods 68

3.2.1. Study Population: IMAGEN Data Sub-Group 68

3.2.2. Longitudinal Pipeline on High-Computing System (TCHPC) 69

3.2.3. Data Post-Processing 72

3.2.4. Statistical Analysis 73

3.2.4.1. Cross-Sectional Analysis 73

3.2.4.2. Longitudinal Analysis 74

3.3. Results 76

3.3.1. Cross-Sectional Analysis 76

3.3.1.1. Between-Group Differences in Hippocampal Subfields 76

3.3.1.2. Correlation Between Neuroticism and Hippocampal Subfields 77

3.3.2. Longitudinal Analysis Results 79

3.4. Discussion 79

4. MICROSTRUCTURAL ALTERATION OF THE CINGULUM IN HEALTHY AGING 83

4.1. Brain and Aging 83

4.1.1. Age-Related Changes in Grey Matter 83

4.1.2. Age-Related Changes in White Matter 84

4.1.3. Age-Related Changes in Brain Connectivity 85

4.1.4. Age-Related Changes in Neurotransmission 86

4.2. Diffusion Imaging 87

4.2.1. Diffusion Tensor Imaging 90

4.2.2. Tractography 91

4.2.3. Constrained Spherical Deconvolution (CSD) 92

4.2.4. Atlas Based Tractography (ABT) approach 93

4.2.5. Diffusivity Measures 93

4.3. Manuscript – Aging-Related Microstructural Alterations Along the Length of the Cingulum Bundle 96

4.3.1. Introduction 96

4.3.2. Material and Methods 98

4.3.2.1. Participants 98

4.3.2.2. Neuropsychological Testing 99

4.3.2.3. MRI Scanning Protocol 101

4.3.2.4. DTI Pre-Processing 101

4.3.2.5. Tractography of the Cingulum 102

4.3.2.6. Definition of ROIs 102

4.3.2.7. Statistical Analysis 105

4.3.3. Results 106

4.3.3.1. Tractography Analysis 106

4.3.3.2. Within-Group Linear Correlation 108

4.3.4. Discussion 109

4.3.5. Conclusion 113

5. GENERAL DISCUSSION **115**

5.1. Review of Aims and Results 115

5.1.1. Overview of Findings from Chapter 2 115

5.1.2. Overview of Findings from Chapter 3 115

5.1.3. Overview of Findings from Chapter 4 116

5.2. Contribution of Findings to Prior Knowledge 117

5.2.1. Brain Connectivity Changes Related to Stress in Adolescence 117

5.2.2. Stress-Related Changes of Hippocampus Subfields in Adolescence 118

5.2.3. Microstructural Changes of the Cingulum Bundle in Healthy Aging 119

5.3. Overall Discussion 120

5.3.1. Limitations 126

5.3.1.1. Choice of Brain Parcellation in Connectivity Analysis 126

5.3.1.2. Restrictions in Longitudinal Analysis 127

5.3.1.3. Limitations in Running the Tractography in Native Space 128

5.5. Future Directions 129

5.6. Conclusion 130

REFERENCES **132**

APPENDIX A **165**

APPENDIX B **220**

APPENDIX C **225**

APPENDIX D **227**

Index of Figures

FIGURE 1.1:..... 5

FIGURE 1.2: 7

FIGURE 2.1: 23

FIGURE 2.2:..... 25

FIGURE 2.3: 40

FIGURE 2.4: 41

FIGURE 2.5: 44

FIGURE 2.6: 45

FIGURE 2.7: 47

FIGURE 2.8: 49

FIGURE 3.1: 64

FIGURE 3.2: 67

FIGURE 3.3: 78

FIGURE 4.1: 95

FIGURE 4.2: 104

FIGURE 4.3:. 105

FIGURE 4.4: 108

FIGURE 5.1: 118

List of tables

TABLE 1.1: 16

TABLE 2.1: 39

TABLE 2.2: 43

TABLE 3.1: 69

TABLE 3.2: 74

TABLE 3.3: 77

TABLE 4.1: 99

TABLE 4.2: 100

TABLE 4.3: 109

1. General Introduction

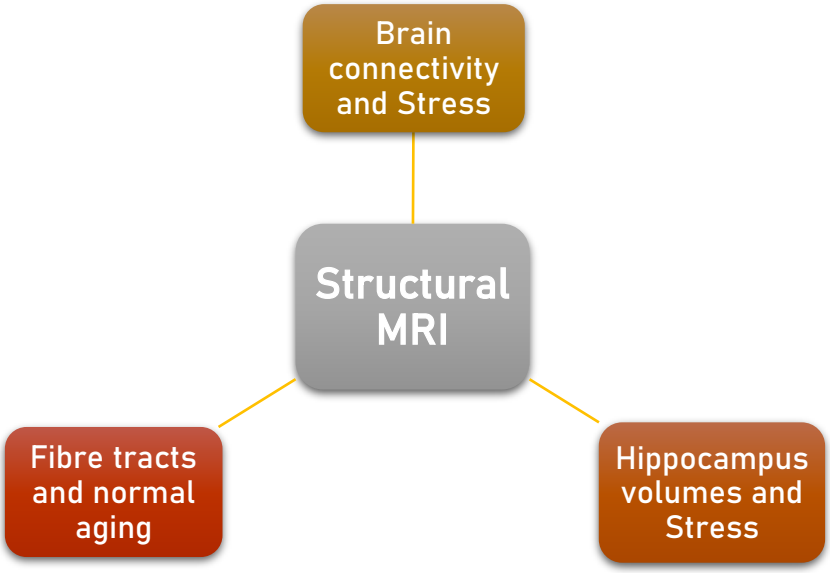

1.1. Background

People are defined by their genes, familiar background and personal events they experience, that can have either a negative or positive impact. Altogether, this represents and shapes not only their life externally, meaning their decisions, behaviours and relationships with others, but also internally, namely their brain and body. In particular, external stimuli can have a big impact on the brain anatomy and functioning, which then result in specific behavioural and emotional responses. Cognitive abilities, such as memory, attention and emotional processing, are possible through anatomical and functional connections between brain regions. For example, a group of regions form the so-called 'limbic system', described for the first time by Broca in 1878 as 'le gran lobe limbique', (from Latin limbus means border) (Pessoa and Hof 2015), referring to the curved rim which comprehends the cingulate and the parahippocampal gyri (Rajmohan and

Mohandas 2007). Almost a century later, Papez and Yakovlev (Yakovlev 1948, Papez 1995) attributed this system to emotional processing for the first time. The brain regions forming what today is known as the limbic system are the cingulate and parahippocampal gyri, the hippocampal formation (represented by the dentate gyrus, the subiculum complex and the hippocampus proper), the amygdala (responsible of the flight or fight mode response), the septal area and the hypothalamus, which altogether are responsible for the emotional and cognitive responses to external and internal stimuli, through memory and motivation (McLachlan 2009). Some of the regions belonging to the limbic system are also involved in memory processes (i.e. formation, consolidation, and retrieval) such as the hippocampus and parahippocampal gyrus. Therefore, the limbic system, together with other brain areas, is a key part in behavioural responses, and it influences how people interact with peers and the external world. Any type of external offense can alter the normal relationship between brain structures, leading to structural damages, which can trigger the development of neuropsychiatric disorders, such as mood disorders, schizophrenia, as well as accelerate neurodegenerative processes.

Neuroimaging is a powerful tool to investigate structural and functional changes of the brain, and useful to identify potential biomarkers in brain aging and diseases. In particular, structural imaging can identify, analyse and detect anatomical relationships between brain areas, based on investigating cortical thickness, structure volume changes and alterations in fibre microstructure. Looking at what happens inside the brain is useful to link the effect of external stimuli on specific brain regions that are responsible for behavioural and cognitive responses.

The brain is a plastic organ, and the extent of the brain damage is strictly associated to the time period during which an offense takes place. Literature on neurodevelopment shows there are specific time windows when the brain is more sensitive to external stimuli and have a bigger impact on either structural or functional organization. One key stage in someone's life is adolescence, which is a transitional stage during which the brain is still maturing, and some areas are less developed than others (Casey, Jones et al. 2008). For example, frontal regions (involved in reasoning) are not yet fully developed in adolescence, making adolescents more sensitive to life events in such a way that their brain is highly susceptible to morphological and microstructural alterations, which can rearrange information and emotional processing and culminate in atypical behavioural responses. Changes occurred during these years can be persistent and causing permanent structural alterations, that can increase the possibility of developing neuropsychiatric disorders in such a young age and continue in adulthood. Cognitive abilities, and eventual decline, are consequently influenced by the effect of life experiences.

Literature focused on investigating the effect of negative events on the brain shows changes in the volume of regions belonging to the limbic system, such as hippocampus, amygdala and anterior brain areas (McEwen 2012), and subcortical regions as the caudate and putamen (Soares, Marques et al. 2014). Soares investigated the effect that stress mood and aging have on both WM and GM volumes in an adult population. They found how WM volume changes were negatively correlated with age in the orbitofrontal cortex, superior frontal, inferior and middle temporal, parahippocampal, posterior cingulate. A significant interaction was found specifically between stress levels, aging and the frontal

brain areas, with behavioural stress and depressive symptoms affecting both structure and function of the prefrontal cortex in particular (Soares, Marques et al. 2014). Amygdala and hippocampal volumes have been found to be smaller in adults if the negative life event occurred in the early stages of life, confirming a relation between life events and age (Gerritsen, Kalpouzos et al. 2015) and, furthermore, pointing out childhood maltreatment is associated to brain alterations lasting throughout adulthood (Dannlowski, Stuhrmann et al. 2012). It is clear, then, the level of stress experienced in early life and during adolescence is crucial for brain development.

1.1.1. Brain Regions Involved in Stress and Memory

The brain regions involved in stress response and memory processing involve both GM structures and WM tracts, whose structure can be target of external offenses.

The fornix is mainly a projection tract connecting the hippocampus with the mammillary body, the anterior thalamic nuclei, and the hypothalamus. It also has a small commissural component known as the hippocampal commissure (Gupta, Sahni et al. 2016). Fibres arise from the hippocampus (subiculum and entorhinal cortex) of each side, run through the fimbria, and join beneath the splenium of the corpus callosum to form the body of the fornix (Catani, Dell'acqua et al. 2013). Most of the fibres within the body of the fornix run anteriorly beneath the body of the corpus callosum towards the anterior commissure. Above the interventricular foramen, the anterior body of the fornix divides into right and left columns. As each column approaches the anterior commissure, it diverges again into two components. One of these, the posterior columns of the fornix, curve ventrally in

front of the interventricular foramen of Monroe and posterior to the anterior commissure to enter the mammillary body (post-commissural fornix), adjacent areas of the hypothalamus, and anterior thalamic nucleus. The second component, the anterior columns of the fornix, enter the hypothalamus and project to the septal region and nucleus accumbens (Pascalau, Popa Stănilă et al. 2018) (Figure 1.1).

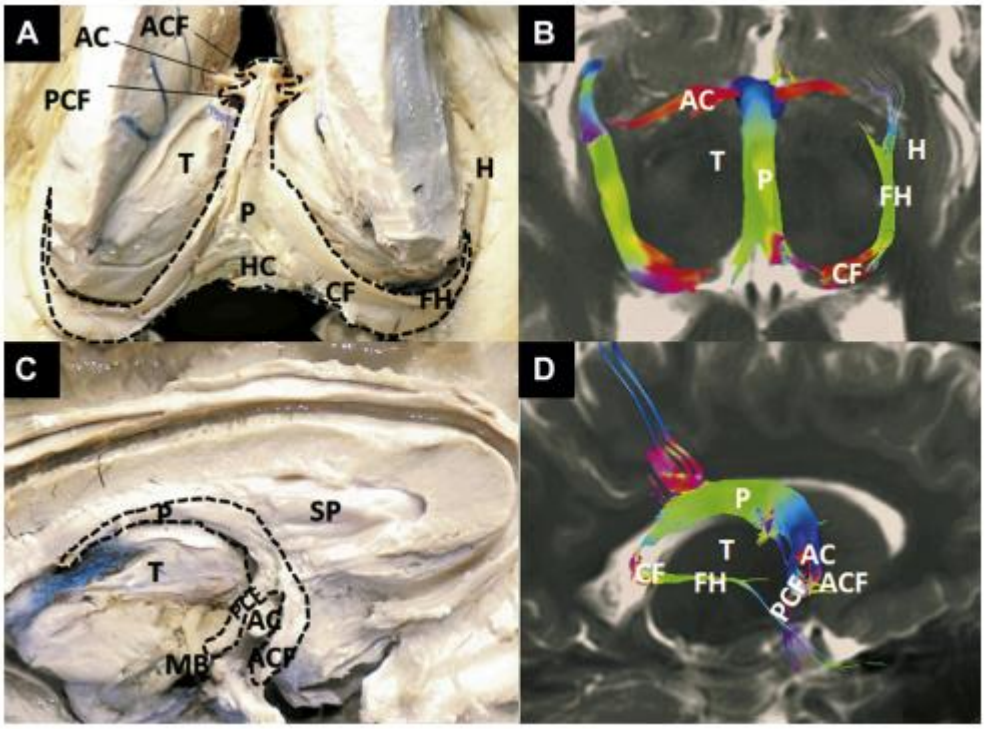

Figure 1.1: Dissection and tractography of the fornix (Pascalau et al., 2018)

The mammillo-thalamic tract originates from the mammillary bodies and after a very short course terminate in the anterior and dorsal nuclei of the thalamus (Pascalau, Popa Stănilă et al. 2018). A ventrally directed branch projects from the mammillary bodies to the tegmental nuclei (mammillo-tegmental tract). According to Nauta (1958), the mammillo-tegmental tract, together with other fibres of the medial forebrain bundle, forms an important circuit between medial

limbic structures of the midbrain and hypothalamus to relate visceral perception to emotion and behaviour (Nauta 1958).

The anterior thalamic nuclei are another important part involved in cognitive processes related to emotions and memory (Clark and Harvey 2016). They receive projections from the fornix and mammillo-thalamic tract and connect through the anterior thalamic projections to the orbitofrontal and anterior cingulate cortex. The anterior thalamic projections run in the anterior limb of the internal capsule (Pascalau, Popa Stănilă et al. 2018).

The cingulum bundle (CB) is a WM structure with a U-shape that runs from the anterior to the posterior part of the brain, just above the corpus callosum (Catani &Thiebaut de Schotten, 2008). Vogt conducted a study on the cingulum connectivity in monkeys, and he divided the cingulum in four regions: the anterior cingulate cortex (ACC), the medial cingulate cortex (MCC), the posterior cingulate cortex (PCC) and the retrosplenial cortex (RSC), shown in Figure 1.2. Each of these branches can be further sub-divided, as they present different connections to the other brain regions and reflect different cognitive functions at the same time (Vogt et al., 2009):

-ACC is defined as primary limbic cortex,

-aMCC is limbic premotor cortex,

-pMCC is limbic premotor orientation cortex,

-dPCC is defined as limbic association cortex and

-vPCC is limbic sensory assessment cortex.

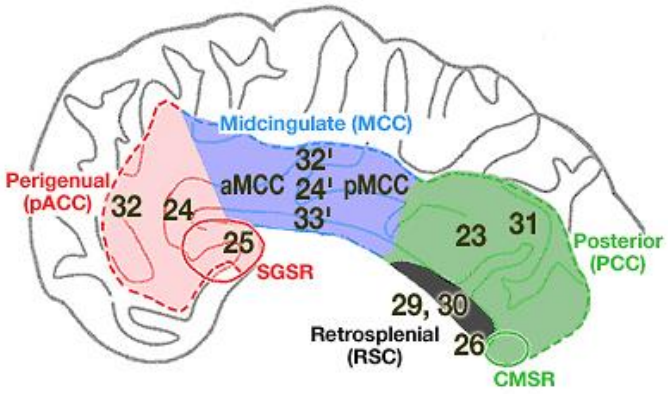

Figure 1.2: Location of each sub-region of the cingulum bundle in a flat map (Vogt, 2009)

In this division, four out of five subregions present connections to the limbic system. The limbic system includes the anterior cingulate gyrus, involved in emotional processing and error-monitoring (Whalen et al., 2006), the posterior cingulate gyrus, involved in the evaluation of risk and reward (McCoy and Platt, 2005), the isthmus of the cingulate gyrus, engaged in memory and pain processing (Nielsen et al., 2005), the parahippocampal cortex, implicated in memory, and the entorhinal cortex, involved in memory and spatial processing (Eustache et al., 2001). The grey matter subcomponents of the limbic cortex are structurally connected with each other via the cingulum.

The cingulum contains fibres of different lengths, the longest running from the amygdala, uncus, and parahippocampal gyrus to subgenual areas in the frontal lobe. From the medial temporal lobe, these fibres reach the occipital lobe and arch almost 180° around the splenium to continue anteriorly within the white matter of the cingulate gyrus (Bubb, Metzler-Baddeley et al. 2018). The dorsal and anterior fibres of the cingulum follow the shape of the superior aspect of the corpus callosum. After curving around the genu of the corpus callosum, the fibres

terminate in the subcallosal gyrus and the paraolfactory area. Shorter fibres that join and leave the cingulum along its length, connect adjacent areas of the medial frontal gyrus, paracentral lobule, precuneus, cuneus, cingulate, lingual, and fusiform gyri (Wu, Sun et al. 2016). The cingulum can be divided into an anterior-dorsal component, which constitutes most of the white matter of the cingulate gyrus, and a posterior-ventral component running within the parahippocampal gyrus, retrosplenial cingulate gyrus, and posterior precuneus. Preliminary data suggest that these subcomponents of the cingulum may have different anatomical features. For example, a higher fractional anisotropy has been found in the left anterior-dorsal segment of the cingulum compared to right, but reduced fractional anisotropy has been reported in the left posterior-ventral component compared to the right (Gong, Jiang et al. 2005).

The uncinate fasciculus connects the anterior part of the temporal lobe with the orbital part of the frontal cortex. The fibres of the uncinate fasciculus originate from the temporal pole, parahippocampal gyrus, and amygdala, then after changing their trajectory with a U shape, they enter the extreme capsule (Bhatia, Henderson et al. 2017). Between the insula and the putamen, the uncinate fasciculus runs inferior to the fronto-occipital fasciculus before entering the orbital region of the frontal lobe (Cellerini, Konze et al. 1997). Here, the uncinate splits into a ventrolateral branch, which terminates in the anterior insula and lateral orbitofrontal cortex, and an antero-medial branch that continues towards the cingulate gyrus and the frontal pole (Pascalau, Popa Stănilă et al. 2018). Whether the uncinate fasciculus is a lateralised bundle is still debated. An asymmetry of the volume and density of fibres has been reported in a human post-mortem neuro-histological study in which the uncinate fasciculus was found to be

asymmetric in 80% of subjects, containing on average 30% more fibres in the right hemisphere compared to the left (Highley, Walker et al. 2002). However, diffusion measurements have shown higher fractional anisotropy in the left uncinate compared to the right in children and adolescents (Eluvathingal, Hasan et al. 2007) but not in adults, suggesting how the brain is still maturing during adolescence.

1.2. Magnetic Resonance Imaging (MRI)

The three studies forming this work of thesis have been conducted by using three different modalities of structural imaging, all based on magnetic resonance imaging (MRI). The first MRI scan was done in New York in 1973 and since then it has been widely used to detect alterations in the human body. It is similar to computed tomography (CT), with the difference of no impact of x-ray on the body (Carr and Grey 2002).

1.2.1. MRI Physics

About 60% of the human body is made of water, while the brain contains about 73% of water (Whittall, MacKay et al. 1997). The atomic nucleus is formed by nucleons, differentiated in protons and neutrons, which have both a mass equal to 1, but different electric charge (protons have positive charge, whereas neutrons have charge equal to zero). Nuclei have a property of spin, which is associated to a small magnetic field. The magnetic fields of the particles creates a nuclear magnetic moment (NMM), equal to a spin value different from zero, that reflects the different number of nucleons (Khurshid and Hussain 1991). A value different from zero is the base of the interactions with an external magnetic field

applied, which makes the hydrogen atoms respond to its strength by absorbing its energy so that the atoms spin orient in the same direction as the magnetic field (Johnston, Liu et al. 1985). These interactions describe the principle of MRI. The NMM has properties of both intensity and direction. Without an applied magnetic field, the direction of the NMM is casual, whereas when a magnetic field is applied, the vector NMM tends to align itself to the direction of the vector magnetic field (defined B0). (Carr and Grey 2002). This whole process is called “precession”.

The frequency of precession around B0, is defined Larmor frequency (L), and it depends on two parameters: the strength of B0 and the type of nucleus of interest (Kiselev 2019). The latter determines the “gyromagnetic ratio”, indicated with the Greek letter *γ*. When an atom of H_2 spins, an electric current is also created, given the positive charge of the proton contained in the atom. When a proton spins, it generates both a magnetic moment and an angular moment; both are essential to generate MR signal. The speed of the precession defines the strength and intensity of the MR signal. This means, the frequency measurements can be used to distinguish MR signals at different positions in space, enabling the image reconstruction (Hansen and Kellman 2015). When a magnetic field B0 is applied without gradients the nuclei precess at the same frequency, whereas when a gradient is applied, nuclei respond at different speed, depending if they “precess” at a direction that is parallel or perpendicular to the magnetic field (Scott, Joy et al. 1995). Hydrogen nuclei respond to applied forces by moving their axes with a perpendicular direction to the one of the applied forces, creating a magnetic moment. The sum of all the magnetic moments is called “net magnetization” and it is generally zero in absence of a magnetic field,

but it increases proportionally to the strength of the magnetic field applied. The net magnetization can be thought as a vector with two components: a longitudinal component (that is either parallel or antiparallel to the magnetic field) and a transverse component (which is perpendicular to the magnetic field) (Scherzinger and Hendee 1985). To measure the intensity of the magnetic field, a perturbation in the equilibrium of the spins in a volume must be created. To change this equilibrium, radiofrequencies (RF) emit photons that create an excitation phase on protons. Usually, the net magnetization follows the Larmor frequency, and to excite protons, a series of electromagnetic energy must be given to the system for a certain period.

The event that energy pulses are given repeatedly to the net magnetization is defined “resonance” (Ai, Morelli et al. 2012). The electromagnetic pulses represent a second magnetic field given (B1), called also radiofrequency field (RF), lead to proton excitation, which usually lasts few seconds. The phase of excitation is followed by a phase of relaxation, where the particles return to the initial equilibrium state, after absorbing the energy of RF. The relaxation phase is a key event to detect MR signal (Martinez 2018). During the relaxation, the energy that is formed is released to the surrounding environment, and the perpendicular component to the B0 creates a RF signal.

1.2.1.1. T1 and T2 Relaxation Time

There are two types of relaxation, longitudinal and transverse relaxations, represented by the time constants, T1 and T2, respectively (Scherzinger and Hendee 1985). T1 is known as “spin-lattice relaxation”, whereby the “lattice” is the environment surrounding the nucleus. As longitudinal relaxation occurs,

energy is dissipated into the lattice. T1 is the time in milliseconds necessary to the net magnetization vector to recover 2/3 of its total projection, i.e. its thermal equilibrium following an RF pulse. T1 can be manipulated by varying the times between RF pulses, defined repetition time (TR) (Pykett, Rosen et al. 1983). Water and cerebrospinal fluid (CSF) have long T1 values (3000–5000 ms), and thus they appear dark on T1-weighted images, while fat has a short T1 value (260 ms) and appears bright on T1-weighted images. When a RF pulse is applied, nuclei align predominantly along the axis of the applied energy. The faster the proton realign, the brighter the MRI image is.

T2 relaxation time, or also called transverse relaxation, is the loss of net magnetization within the transverse plane due to loss of phase coherence of spins. In fact, when the spins are excited, they all precess at the same phase, but when they return to their initial state the different chemical components of nucleus lead to a diphase of spins. During this event, there is no exchange of energy between spins and environment, but the energy lost by a nucleus is absorbed by other nuclei near it, defined spin-spin relaxation (Scherzinger and Hendee 1985). The signal loss due to this event is called T2 decay. Generally, T2 is faster than T1 relaxation; usually the T2 signal is associated with two events. The first is the loss of “phase coherence”, indicated with T2 signal, and the second is the lack of homogeneity of the local magnetic field, indicated with T2*, which can be indicated as the effective T2 signal observed. T2* can be lower or equal to T2 (Chavhan, Babyn et al. 2009).

The signal MR is produced when the radiofrequency pulse is removed and the protons realign with the magnetic field, realising energy that is detected by the scanner during the relaxation process and converted into an image. The

sinusoidal shape detected by the system is modulated by the Free Induction Decay (FID), which contains information about the quantity of spins during the relaxation process (Scherzinger and Hendee 1985), that are the elements that define the MR signal. Multiple RF pulses are applied to obtain multiple FIDs, which are then averaged to improve the signal-to-noise ratio (SNR) (Uğurbil, Adriany et al. 2003); the signal averaged FID can be then resolved by a mathematical process known as Fourier transformation. The Spin echo (SE) signal, which is the refocusing of spin magnetisation by a pulse of resonant electromagnetic radiation, is influenced by two parameters which are the repetition time (TR) and the echo time (TE) (van Geuns, Wielopolski et al. 1999). The mathematical formula is the following:

$$S = kH \cdot \left(1 - e^{-TR/T1}\right) \cdot e^{-TE/T2}$$

where [H] is the spin (proton) density and K is a scaling factor. This equation shows how T1 effects are connected to TR and T2 effects are connected to TE, whereas [H] effects are always present. An increase of TR determines an increase of the signal, while an increase of TE determines a decrease of the signal. The repetition time (TR) and the echo time (TE) are used to control image contrast and defining the "weighting" of the MR image: a short TR and short TE give a T1-weighted image, whereas long TR and long TE give T2-weighted image. Based on the type of TE and TR, different acquisition sequences can be used and defined in MRI.

1.2.2. Spin-Echo Sequence

This type of sequences was born in 1950 and they are the most used sequences till today (Jung and Weigel 2013), thanks to the fact they can give information about the three types of brain tissue. There are three main families of SE: with short TR ad short TE, with long TR ad short TE, and with long TR ad long TE (Chavhan 2016).

1.2.2.1. Sequence SE with Short TE (<30 ms) and Short TR (<600 ms)

with these parameters the sequences SE produce images dependent by the T1 tissue, represented by hyper tensed tissues with short T1 and hypo tensed tissues with long T1. The highest intensities are found in the adipose tissues, while the CSF has the lowest intensities. A lower signal reflects more water content, like in case of inflammation, and high signal for fat. It measures spin-lattice relaxation.

1.2.2.2. Sequence SE with Long TR (>1500 ms) and Short-Intermediate TE (20-40 ms)

This second class includes images depending on the proton density (PD) of tissue to minimize T2, where the adipose tissues have higher level of hypertension than cerebro-spinal fluid (CSF).

1.2.2.3. Sequence SE with Long TR (>1500 ms) and Long TE (>60 ms)

These images depend on the T2 signal, measuring spin-spin relaxation. With this type of sequence, the images appearing brighter are those with the highest level of CSF. When different types of images need to be analysed (for example, T2 and PD), another sequence can be used which is the multi-echo sequence,

characterized by long TR and two or more echoes that have the same distance between them. Even if it is possible to have a high number of echoes per each image, the higher is the number of echoes per each image, the worse the signal-to-noise-ratio (SNR) becomes, leading to a lower image quality (Bitar, Leung et al. 2006). The most common solution is using multi-echo sequence with two asymmetric echoes, the first between the 20 and 40 ms and the second around the 100 ms, which in general produce all the information that are necessary for a diagnosis.

1.2.3. Echo-Planar Imaging (EPI)

Echo-planar imaging (EPI) is a very fast magnetic resonance imaging technique that is able to acquire a whole MR image in a fraction of second (DeLaPaz 1994). It is performed using a pulse sequence in which multiple echoes of different phase steps are acquired using rephasing gradients instead of repeated 180° radio frequency pulses following the 90°/180° in a spin echo sequence. In a single-shot echo planar sequence, the entire range of phase encoding steps (usually up to 128) are acquired in one TR. In multi-shot echo planar imaging, the range of phase steps is equally divided into several "shots" or TR periods (Edelman, Wielopolski et al. 1994). For example, an image with 256 phase steps could be divided into 4 shots of 64 steps each. The benefits of this type of sequence is reduced imaging time and reduced motion artefacts.

1.2.4. Fluid-Attenuated Inversion Recovery (FLAIR)

FLAIR is an imaging method that inverts time that leads to fluid suppression (there is a high signal in case of meningitis or multiple sclerosis) (Schreiner, Liu et al. 2014).

Table 1.1 summarizes the main terminology used to describe the physics of MRI, that are parameters influencing the image quality during data acquisition.

MRI terminology		
Abbreviation	**Name**	**Description**
T1	Spin-lattice relaxation	Time necessary to the net magnetization vector to recover 2/3 of its thermal equilibrium following an RF pulse.
T2	Spin-spin relaxation	Loss of net magnetization within the transverse plane due to loss of phase coherence of spins
T2*	T2 decay	Time indicating the decrease of signal strength after excitation.
TE	Echo Time	Time between the application of the radiofrequency excitation pulse and the peak of the signal
TR	Repetition Time	Time between radiofrequency pulses
FID	Free Induction Decay	Indicates the quantity of spins during the relaxation process. Mathematically represented by Fourier transformation.
EPI	Echo-planar Imaging	MRI technique able to acquire a whole MR image in a fraction of second
SNR	Signal-Noise Ratio	Measured by calculating the difference in signal intensity between the area of interest and the background
SE	Spin-echo	Refocusing of spin magnetisation by a pulse of resonant electromagnetic radiation, determined by TE and TR

Table 1.1: List of MRI-related terminology and definitions

1.3. Thesis Objective

Literature shows the limbic system is a target for environmental factors that can potentially alter its normal structural composition. For example, the hippocampus, important for memory processing, is rich in glucocorticoids receptors that are strictly associated to the level of cortisol in the brain. This can affect the circuits related to memory and emotion processing. This thesis work aims to investigate what are the human brain areas that are more structurally sensitive to physiological changes and environmental stimuli during two critical periods of time in life, such as adolescence and aging. In this thesis, three studies will be presented, exploring structural brain changes due to stress and brain aging with

three different structural neuroimaging approaches. Questions like: “How do cortical connections change in adolescents when they are exposed to stressful experiences?”, “How are brain areas related to emotions affected with stress over time?”, and “What effect does healthy aging have on the microstructure of brain tracts involved in memory and emotions?” are the objective of this thesis. The first study focuses on the effect of stressful events on brain connectivity in the cortex of the adolescent brain, divided into 17 networks; brain connectivity was measured both with graph theory measures and connectivity strength between edges.

In the second study, volumetric changes of the hippocampus subfields are investigated, both cross-sectionally and longitudinally. The cross-sectional analysis focused on potential changes between two groups experiencing two different levels of stress in middle adolescence, while the longitudinal analysis sought to investigate changes within each stress group (defined at baseline) across two stages of adolescence (i.e. middle and late adolescence).

Finally, the third study looked at microstructural changes in the cingulum with normal aging, that was divided into three branches, namely subgenual, retrospenial and parahippocampal branches. To carry out such analysis, diffusivity measures were statistically compared between young and old healthy people. All the three studies focus on key stages of a “journey” that starts at a young age in adolescence, and goes on till old age, exploring changes of the limbic brain areas along the “way”. In fact, an increase of cortisol release as consequence to negative life events is toxic for limbic structures, contributing to structural maturation and acceleration of cognitive decline.

1.4. Research Methodology and Methods

For all the three studies forming this work, secondary data have been used. In the first study, brain connectivity changes have been investigated in a big population of adolescents that experienced negative events. The impact of stress was considered by analysing whole-brain connectivity and graph theory measures alterations in the cortex between two groups with different levels of stress perceived, i.e. Low vs. High stress. Such alterations were represented by decrease/increase of connectivity strength between brain areas, as well as by decrease/increase of measures indicating network properties of segregation, integration and centrality. Brain networks were obtained by applying an ROI-atlas to MRI grey matter segmentations. The second study can be considered as an extension of the first one, since it is focused on investigating the longitudinal changes of the hippocampus subfields volume in a sub-group of the adolescent population. This was done by extracting subfields volumes in Freesurfer 6.0 at three time points and see how they change overtime within each group based on the stress level at baseline. Finally, microstructural changes of the cingulum bundle were investigated with diffusion tensor imaging (DTI), comparing young healthy adults to an older healthy population. The cingulum is a fibre tract that embraces the corpus callosum, connecting anterior regions with the posterior part of the brain. The bundle was divided into three branches and diffusivity measures were extracted for each branch in both hemispheres. Diffusivity measures were considered both on a tract-average level and along the length of the tract.

2. Brain Connectivity Changes with Stress in Adolescence

2.1. Adolescence

Adolescence is a transitional period where humans experience physical, psychological and emotional changes. Researchers define adolescence as a window of time that usually starts with puberty and ends when youth reach the age of 19, or, as in some studies, in young adulthood (at 24 year old) (Sawyer, Afifi et al. 2012). Even though the age range is not universally defined, there are some key events that represent the end of adolescence, such as getting an independent job or becoming parent (Pringle, Mills et al. 2016). The hormonal shift happening in these years influences also the brain maturation of adolescents, which is key for their cognitive and behavioural responses. In fact, when puberty starts, the cognitive abilities increase drastically, represented for example by shorter reaction time, improved working memory, setting rules for adaptive behaviours (Ernst and Mueller 2008). The World health organization (WHO) divided adolescence into three stages: the first two stages are early (10-14 years old) and late (15-19 years old) adolescence, whereas the third one is defined young adulthood (20-24 years old). During early adolescence, physical change starts with the growth of body hair and the development of sexual body parts, whereas, cognitively speaking, adolescents are better in thinking in an abstract way and more focused on the present (“here and now”), rather than the future. In late adolescence, physical growth slows down for girls, but it continues for boys, having reached, in both sexes, almost 95% of the adult growth. Cognitively, at this stage, adolescents start thinking more about the future, are

fully self-absorbed and are more prone to set goals. At this stage the frontal areas of the brain develop, and such development can be influenced by the events experienced during these years. Finally, during young adulthood adolescents are fully physically mature, and cognitively they are projected more into the future, planning their life (Sawyer, Afifi et al. 2012).

2.1.1. Brain Maturation in Adolescence

In adolescence, brain maturation is represented by changes in both grey and white matter. Global grey matter volume has seen being negatively correlated with the pubertal stage, gonadal hormone and testosterone levels, whereas white matter density increases with age (Vijayakumar, Op de Macks et al. 2018).

During childhood and early adolescence an increase of axonal and synapses production takes place, followed by neural pruning in areas involved in attention, emotional response and memory, such as the nucleus accumbens, the prefrontal cortex and amygdala (Casey, Jones et al. 2010). Changes seem to progress from posterior to anterior dorsal regions, such that parietal grey matter loss is seen mostly from childhood to adolescence, while frontal grey matter decreases mostly from adolescence to adulthood (Ernst and Mueller 2008). The peculiar behavioural features of adolescence are influenced by an increase use of the limbic structures associated to emotions, and reduced use of cognitive inhibitory structures such as the ventrolateral prefrontal cortex. This may lead to unbalanced employment and development of emotion-related circuits over reasoning and reward-related systems; in terms of brain areas development, incorrect growth of amygdala, nucleus accumbens, and prefrontal regions involved in these circuits may occur (Casey, Jones et al. 2008). For example, the

enhancement in the nucleus accumbens activity may be associated to the increase of impulsivity and risk-taking behaviours observed in adolescents (Ernst, Nelson et al. 2005). Cognitively speaking, neurodevelopmental studies found an enhanced activity of regions involved in working memory, such as the temporo-parietal junction and frontal areas.

Literature showed different changes in the brain development based on sex (Peper, Schnack et al. 2009, Berenbaum, Beltz et al. 2015, Gur and Gur 2016, Kaczkurkin, Raznahan et al. 2019). A relationship between the level of sex-specific hormones is seen in adolescence, in particular a positive association between testosterone levels and global grey matter density was found in males, while females showed a negative association between oestradiol levels and grey matter density (Peper, Schnack et al. 2009). Gur and Gur described in their review the structural changes of the brain during puberty, highlighting sex differences in both GM and WM (Gur and Gur 2016), in a cohort of adolescents from Philadelphia. Regarding GM, females showed an increase of hippocampal volume, while changes in WM were represented by higher fractional anisotropy (FA) in the splenium of the corpus callosum. On the other hand, males presented a higher FA in the frontal part of the brain, confirmed by a recent study (Kaczkurkin, Raznahan et al. 2019). Furthermore, gender-based connectivity differences were seen, with males engaging more intra-hemisphere networks, whereas, in females, the wiring of brain connections tend to be more inter-hemispheric. Specifically, in cortical connections, another study (Ingalhalikar, Smith et al. 2014) suggested that males engage more brain networks involved in perception and coordinated action, while females engage brain regions involved more in analytical and intuitive processes.

2.2. Stress and Cognition

The term “stress” was used for the first time by Hans Selye in 1936 and it is defined as a threat to the physical or psychological integrity of an individual. Determinants can be defined stressful when a situation is novel, unpredictable, threatening to the ego or leading to a decrease of sense of control, as defined by the psychologist John Mason in 1960s. When a situation is perceived as stressful, two systems are activated, releasing hormones to cope with the stress effect on the body (McEwen 2012). The first one to activate is the sympathetic-adrenal-medullary system, which releases catecholamine (epinephrine and norepinephrine – as known as adrenalin and noradrenalin) by the adrenal glands. The second system is the hypothalamic-pituitary-adrenal (HPA) axis, which releases glucocorticoids (GCs, that are steroid hormones) (Rudolph, Troop-Gordon et al. 2018). To respond to the stressor effect (the situation or the factor causing stress), neurons in the hypothalamus are activated, which release a hormone called corticotropin releasing hormone (CRH), secreting a polypeptide hormone called adrenocorticotropin (ACTH) from the pituitary gland. The ACTH receptors on the adrenal glands release then the GCs. This top-down control of stress hormone release is counter-balanced by a negative feedback process carried out by the GCs through receptors at the pituitary, hypothalamic and the hippocampus levels. A graphical description of how the HPA axis works is shown in Figure 2.1. In humans, GCs concentration is the highest in the morning, while the lowest levels are in the late afternoon (Kuhlman, Geiss et al. 2018). According to the American Psychological Association (APA), three types of stress can be defined: *acute stress*, *episodic acute stress* and *chronic stress*. They can be present as single, or even combined, having more or less severe effects on the

body and brain (Peters, McEwen et al. 2017). Positive response to stress is characterized by the return of the physiological homeostasis, without inducing deep structural brain changes, whereas repeated and negatively perceived episodes are those that can cause permanent alterations at physiological and psychological levels (Bucci, Marques et al. 2016).

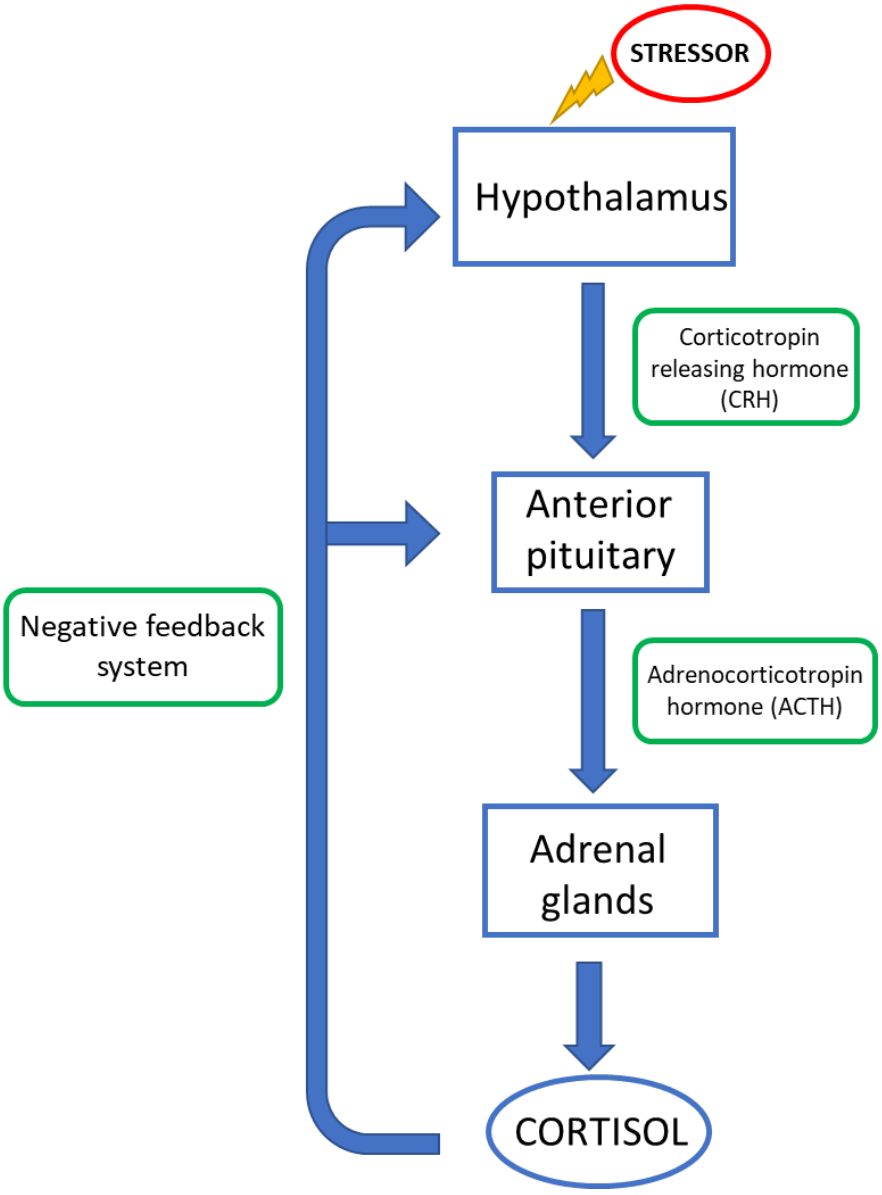

Figure 2.1: Graphical representation of the HPA axis

The presence of stress hormone receptors in the hippocampus, amygdala and prefrontal cortex is key for cognitive processes such as learning and memory.

The prefrontal cortex is involved in reasoning, planning, selective attention, working memory and decision making (Rolls 2015), but more importantly, the PFC is responsible to decide which information will be considered and which one will be inhibited during the performance of goal-directed behaviours (such as selective attention). The amygdala is involved in assessing the emotional significance of events, and it processes emotions of anger, aggression and fear (Scherf, Smyth et al. 2013). The hippocampal formation, divided into subfields, is involved in learning and memory; it is engaged both in the formation and retrieval of episodic memories (Tamnes, Walhovd et al. 2014). These three structures are involved in evaluating a situation and selecting an appropriate response (operated by the PFC) considering the emotional content of the situation (attributed to the amygdala) and past experiences (associated to hippocampal formation) (Vogel and Schwabe 2016).

The process of acute stress response in the brain involves the anterior cingulate cortex (ACC) that determines the level of uncertainty of future events, whereas the amygdala responses to external or internal threats by its flight or fight response. These two structures form a descendant pathway to the brainstem nuclei, reaching the locus coeruleus (LC), which is activated by an increase of vigilant state, and the hypothalamic nuclei, that are key component of the HPA axis (Peters, McEwen et al. 2017).

This suggests stress-related hormones can influence learning and memory processes, having an impact on these three areas. Elevated GCs levels during the encoding phase can result in impaired retention performance, but when emotional stimuli are used the opposite is true, encoding and consolidating the emotional component (Vogel and Schwabe 2016). The mechanism leading to

that sees the secretion of norepinephrine by the locus coeruleus and the GCs by the adrenal gland, resulting in an increased activation of adrenergic receptors throughout the brain. This modulates the hippocampal activity involved in the consolidation of emotionally component of events. The stress-related response to negative events is highly influenced also by personality traits; one study showed that more extrovert adolescents release lower levels of cortisol, whereas a linear association was found between the level of neuroticism and cortisol released (Evans, Stam et al. 2016).

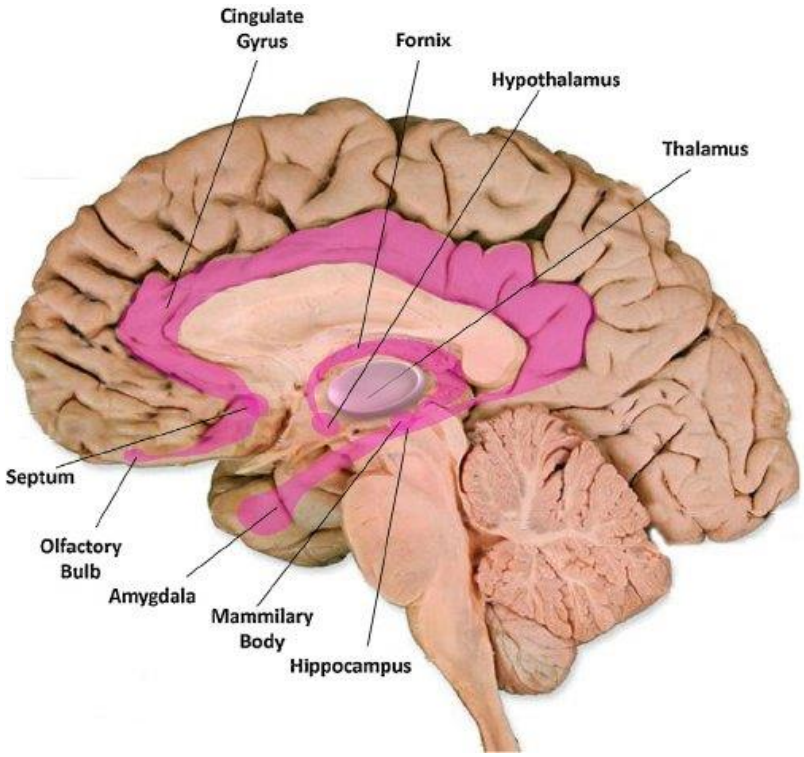

Figure 2.2: Brain regions that are part of the limbic system and are target of structural changes in stressful situations (Adjamian et al., 2014)

2.2.1. Brain Structural Changes with Stress in Adolescence

Stress-related effect on the brain has been investigated for many years. Literature shows how the structural alterations in the brain determine emotional and cognitive responses, depending on the level and the type of stress experienced (Lupien, McEwen et al. 2009). Adolescence is a transitional stage, and the amount of novel stimuli, both physically, socially and emotionally can affect the teenager's brain, and cause permanent changes lasting throughout adulthood (Andersen and Teicher 2008) both at structural and functional levels (Blakemore and Choudhury 2006, Ernst and Mueller 2008, Casey, Jones et al. 2010). As said before, the hippocampus, the amygdala and the prefrontal cortex are among the structures that are mainly targeted by stress. The hippocampus presents a high number of glucocorticoids receptors interacting with the cortisol released during the stress response, and hippocampus volume reduction has been found in adolescents experiencing stressful events, especially in the cornu ammonis (CA) 3 and 4 and dentate gyrus (Eiland and Romeo 2013) as well as reductions of neurons and dendritic branches are seen in case of chronic stress. At a cognitive level, this was shown to affect memories formation and retrieval and spatial navigation (Yaribeygi, Panahi et al. 2017). Regarding amygdala alterations, repeated stressful events have been associated to increased volumes (Bucci, Marques et al. 2016), dendritic hypertrophy in the basolateral nucleus (Eiland and Romeo 2013), higher concentration of CRH, and abnormal connectivity in networks involving the amygdala, altogether affecting the neural circuitry responsible for the emotional response (Chen and Baram 2016). Finally, in the prefrontal cortex, which is the last to develop, a higher level of atrophy, reduction of synapsis and dendrites has been found caused by repeated stressful

events (Bucci, Marques et al. 2016) (Eiland and Romeo 2013). A study investigating the relationship between perceived stress and brain networks connectivity involved in emotional responses showed how the connectivity between amygdala and the ventromedial PFC associated to perceived stress changes with age (Wu, Geng et al. 2018). They found that, while in adolescence there was a positive correlation between the level of perceived stress (PSS) and amygdala-ventromedial prefrontal connectivity, young adults showed a negative relationship between PSS and the connectivity of the amygdala–vmPFC circuit. This suggests the brain circuits can undergo reorganization during neurodevelopment and, therefore, are more sensitive to the effect external factors.

2.3. Structural Connectivity

Structural connectivity describes anatomical connections between two regions, generally measured with diffusion imaging, which reconstructs anatomical connections in form of fibre tracts (Sporns, Tononi et al. 2002). Structural MRI measures not only the variations in the volume or surface of brain areas that are considered, but it allows the inference of structural connectivity. Correlations in thickness, volume, morphological composition similarity between two brain areas across people were shown to be associated with the presence of structural connections (fibres) between two areas (Tijms, Series et al. 2012).

Structural connectivity can be calculated by using different approaches. An example is using DTI from T1-weigthed images. Diffusion anisotropy is associated to the brain white matter, with a maximum that coincides with the spatial orientation of nerve fibres within each voxel (Assaf and Pasternak 2008).

The signal generated by diffusion imaging can give information about the direction of the fibre tracts within each voxel of the brain. The spatial resolution of the signal is limited by the voxel size, which can influence the output tract, or the correlation coefficients associated to that voxel. Diffusivity measures are calculated to indicate the microstructural composition of WM fibres, and correlation matrices can be calculated based on the anatomical connection between two brain areas (Whitford, Kubicki et al. 2011). The second way is an ROI-analysis, where correlation matrices are built based on the linear correlation coefficients between two brain regions, after they have been parcelled based on a template, where each parcellation has its own coordinates. Thanks to the use of coordinates for each parcel, it is possible to obtain spatial information about the connections between regions of the cortex (Tijms, Series et al. 2012).

Many studies have focused on structural connectivity alterations with diseases, which can be measured by investigating graph theory and connectivity changes (Whitford, Kubicki et al. 2011, Tijms, Moller et al. 2013, Bourque, Spechler et al. 2017, Rimkus, Schoonheim et al. 2019), or changes in connectomes as pattern classifiers for diseases prediction (Shao, Myers et al. 2012). Structural connectivity can be used also in a multimodal neuroimaging approach to study the relation between structural and functional connectivity. In fact, dynamic processes shape the topology of a network and, in turn, the topology of the network influences the dynamic of the system. This is an example of the so-called “adaptive co-evolutionary networks” (Gross and Blasius 2008), that emphasizes how structural and functional connectivity influence each other. Understanding the relationship between the two types of connectivity can give a clearer picture of what happens in the brain with diseases.

2.3.1. Graph Theory Measures

Graph theory is a mathematical approach (Sporns 2013) that defines the brain as a network, made of nodes (i.e. regions of interest) and edges (structural or functional connections between brain regions) (van den Heuvel and Sporns 2013). Graphs can be distinguished in directed or undirected, where the directed graphs have edges connected to vertices in a specific direction (Bullmore and Sporns 2009). Connectivity correlation coefficients are estimated between all possible node pairs, building a connectivity matrix (also called adjacency matrix). For weighted graphs, edges are indicated by weights, which represent the connectivity strength between the two nodes that the edge connects. A threshold is then applied to binarize the weighted correlation matrix, such that if the value is higher than the threshold, the correlation coefficient will be equal to 1, whereas if the value is lower than the threshold then it will be 0, distinguishing the correlation matrices in either weighted or binary. The binary adjacency matrix is then used to compute graph theory metrics (Tijms, Series et al. 2012). Furthermore, graph theory describes network properties such as *segregation*, *integration*, *centrality* and *density* (Bullmore and Sporns 2009). Segregation allows information flow and processing within highly connected groups of brain regions, defined clusters, while integration refers to the global transmission of information across brain regions (Sporns 2013). Together they allow information to flow rapidly at a low wiring cost, defining the network economy. When networks are characterized by higher cluster coefficient and characteristic path length approximately the same of random networks, it says they have a property of small-worldness, which was observed by Watts and Strogatz for the first time

(Watts and Strogatz 1998). The graph theory measures considered in this thesis work have been described in the manuscript below.

2.3.2. Brain Networks Parcellation

Brain networks analysis is broadly carried out by an ROI-based approach. Usually a template or atlas is chosen, which divides the brain in a certain number of ROIs, or parcels. Each parcel is represented by a number of voxels and associated to different networks and functions (Arslan, Ktena et al. 2018). An advantage of using atlases for this type of analysis is that it considers the geometry of the brain, so that it is possible to investigate changes in connectivity strength with neuropsychiatric disorders or neurodegenerative diseases for each brain network. The choice of the atlas depends mainly on the research question. Parcellations can be built on cytoarchitectural organization of the brain, on the morphological similarity of the brain areas or on resting-state fMRI signals (Tzourio-Mazoyer, Landeau et al. 2002, Desikan, Segonne et al. 2006, Destrieux, Fischl et al. 2010). They can include only the cortex, as for example Yeo et al (2011), while other atlases include also sub-cortical structures. Usually a non-linear registration is performed on MRI images to co-register them to the atlas stereotaxic space, and then correlation matrices are extracted.

In this thesis work, brain connectivity changes in the cortex of adolescents were investigated in relation to different levels of perceived stress. The main research interest was to understand the impact of high stress levels on the brain networks properties when compared to adolescents who had none or minor exposure to stress, i.e. exploring how the severity of stressful events affects the brain structure in adolescents. The analysis results are reported in a manuscript which

has been submitted to a scientific journal. Below the entire manuscript can be found. Further material can be found in the Appendix A of this thesis.

2.4. Manuscript – Structural Connectivity Alterations of the Cortex in Adolescents Due to Stressful Life Events

Abstract

Adolescence is a crucial period for physical and psychological development. As literature shows, negative life events (NLEs) experienced during this transitional stage can lead to stress and contribute to the onset of psychiatric disorders. The objective of this study is to investigate the relationship between NLEs and structural brain connectivity alterations, investigating changes in both graph theory measures and whole-brain connectivity. A sample of adolescents from the IMAGEN Consortium data was divided into two groups, Low and High Stress. Brain networks were extracted from individual grey matter segmentations, computing linear correlation matrices based on the morphological similarity between brain regions. The number and the parcellation of the brain areas were defined using an atlas-based region of interest approach. Between-group statistical comparisons were conducted on both global and local graph theory measures, and whole-brain connectivity was calculated with network-based statistics (NBS) method. No between-group differences were seen in the global graph theory measures. Results showed how sparsity was a key factor in structural connectivity changes, especially in the local graph theory measures. In the High stress group, centrality measures changed in the left somatomotor network (a decrease of betweenness centrality was seen at sparsity 5%, p_{corr}=0.0042), in the bilateral central visual network (increase of degree at sparsity

10%, p_{corr}=0.048) and in the left dorsal attention network (increase of degree at sparsity 30%, p_{corr}= 0.042). The whole connectome analysis with NBS showed changes in the dorsal attention (as seen in the graph theory measures), limbic and salience networks, represented by an increase of connectivity in the High Stress group between both inter- and intra-hemispherical edges. This study suggests that stress doesn't alter structural connectivity globally, but it leads to local changes in the group who perceived higher levels of stress.

2.4.1. Introduction

Adolescence is defined as the transitional period between childhood and adulthood, beginning with the onset of puberty until the attainment of sexual maturity and neurobehavioral characteristics associated with the adulthood, reflecting changes physically, emotionally and physiologically (Holmbeck 2002). The maturation of the brain is a key event during adolescence, when both grey matter (GM) and white matter (WM) change due to neural pruning and myelination, influenced by the activity of sex hormones that leads to the re-organization of perceptual, motivational, affective, and cognitive systems (Juraska and Markham 2004, Scherf, Smyth et al. 2013).

Giedd and colleagues described how GM and WM brain compartments in the various lobes develop from childhood through adolescence (Giedd, Blumenthal et al. 1999). White matter tends to increase linearly with age (Giedd and Rapoport 2010, Giorgio, Watkins et al. 2010, Ladouceur, Peper et al. 2012), with limbic tracts developing earlier than association tracts (Khundrakpam, Lewis et al. 2016). Grey matter development, on the other hand, follows an inverted U shape, reaching its peak during adolescence. The age peak differs based on sex and

brain area: the frontal and parietal lobes reach the peak sooner in females than males, while the temporal lobe reaches its peak at the same age in both sexes (Gogtay, Giedd et al. 2004).

Amid all these changes, stressful experiences can alter the normal brain development. The term “stress” was coined by Hans Selye in 1936 to indicate “the non-specific response of the body to any demand for change” (Seyle, 1936), whereas the specific factor triggering such changes is defined “stressor”. The effect of stressors alters the glucocorticoids secretion, leading to hyper-activation (or in some cases hypo-activation) of the hypothalamic-pituitary-adrenal (HPA) axis, that is responsible of behavioural responses (Lupien, McEwen et al. 2009), and that affects the normal development of specific brain areas involved in emotion regulation, decision making and reward systems (McEwen 2011). Alterations in the normal functioning of the HPA axis can influence the efficiency of information flow between brain regions, reflecting changes in brain connectivity (Eiland and Romeo 2013).

Brain networks, usually referred as “connectome”, can be used as potential biomarkers to study alterations in brain connectivity such as due to stress and brain disorders in adolescence (Khundrakpam, Lewis et al. 2016). A common approach to quantify such changes is graph theory, which is a branch of mathematics (Sporns 2013) that describes the brain as a network, made of “nodes” (i.e. brain regions) and “edges” (connections between nodes) (Bullmore and Sporns 2009, van den Heuvel and Sporns 2013).

Graph theory metrics can be applied to either structural (MRI, DTI) or functional (fMRI) imaging data. A study describing the change of such metrics during

development showed that, in adolescence, there was a decrease in the efficiency of information flow from one region to another (Khundrakpam, Reid et al. 2013) compared to childhood. Another study reported changes in the centrality of specific nodes following past maltreatment stress (Teicher, Anderson et al. 2014): the main alterations were seen especially in the salience network (SN) and default-mode network (DMN). Two studies that used functional connectivity reported alterations in the clustering property of brain regions and in the path length between nodes in adolescents (13-14 years old) suffering of post-traumatic stress disorder (PTSD)(Suo, Lei et al. 2015, Xu, Chen et al. 2018). Zalesky and colleagues reported that adolescents with PTSD showed loss of connections in dorsolateral prefrontal cortex, middle temporal gyrus, bilateral thalamus and middle occipital gyrus (Zalesky, Cocchi et al. 2012). Another study comparing PTSD and healthy teenagers showed a hypoconnectivity within the default-mode network (DMN), specifically between posterior cingulate and occipital cortex. Additionally to that, they found a decreased connectivity between the DMN and both the salient (SN) and the central executive network (CEN) (Viard, Mutlu et al. 2019) compared to healthy teenagers.

The objective of this study is to further elucidate the relationship between stress and brain connectivity changes during adolescence. Our hypothesis is that the structural networks in the high stress group will be altered from the low stress group. This is the first study exploring stress-related changes in structural connectivity in a large sample of healthy adolescents, where the stress level has been measured based on the number of negative life events. Results of this study will contribute to increase our knowledge on how stress may alter healthy brain maturation process.

2.4.2. Materials and Methods

2.4.2.1. Participants

Participants are from the IMAGEN study (Schumann, Loth et al. 2010), a longitudinal study on the brain development and behaviour of adolescents, with data being collected from eight different centres across Europe (in Germany, UK, France and Ireland). The IMAGEN cohort has more than 2,200 adolescents who underwent a series of behavioural, neuropsychological assessments, genetic screening and neuroimaging. Parents gave informed written consent and adolescents gave written assent to the study procedure prior to inclusion. All procedures were approved by each local institutional ethics committee. Further descriptions of the study design, sample, and recruitment procedure, including data storage and safety can be found elsewhere (Schumann, Loth et al. 2010). The population analysed in this study is a subgroup of the IMAGEN study at baseline (N=487, age mean=14.45 ± 0.55), who were the participants at the higher and lower distribution ends of the stress measure, who passed the MRI quality check and had all the covariates included in this analysis.

To assess the level of stress in each participant, we used the Life Event Questionnaire (LEQ) (Newcomb et al., 1981) - a 39 item questionnaire – where each question asked about a specific event. The scoring scale had a range from -2 (very negative) to +2 (very positive), with the scoring indicating how the respondent rated the event. Events were classified into clusters: Family/Parents Accident/illness, Sexuality, Deviance, Relocation, Distress and Autonomy. The questions chosen from the LEQ are listed in Appendix A (Figure A3), based on a previous published paper (Galinowski et al., 2015) on resilience, that is defined

as the capacity to cope with NLEs. That is the reason why the same events indicated in Galinowski's paper were selected for this study, and to have a uniform distribution of events across clusters. The number of NLEs was calculated adding up every time a participant experienced a negative event; the score was calculated adding up events which were scored either -2 or -1. Both the total score and the total number of NLEs were calculated.

Furthermore, we also considered the pubertal change in adolescents, using the Pubertal Developmental Scale (PDS) (Petersen, Crockett et al. 1988). This is a self-report measure of physical development for youth under the age of 16. There are male and female versions of the PDS, where boys are asked whether growth has begun on body hair, facial hair, voice change, skin change, and growth spurt. The same questions are asked to girls about body hair, skin change, breast development, and growth spurt. Responses are based on 4-point scales (1 = no development and 4 = completed development). For girls, there is an additional yes-no question about the onset of menarche. For both genders, ratings are then averaged to create an overall score for physical maturation. Socio-economic status (SES) was also considered. It is based on the level of income, occupation, and education in the household, obtained from the parental European school Survey Project on Alcohol and other Drugs (ESPAD).

Included in our statistical models were age, sex, centre, PDS and SES as covariates. PDS scores were standardized, using z-transformation.

As the main objective of the study was to explore how the severity of stress level affects brain connectivity, the population was divided into two groups (N=487, Low Stress=360 and High Stress=127), taking into account the highest and

lowest stress levels perceived in both groups. The number of NLEs and the cumulative negative score were used as cut-off value to divide participants into Low and High stress groups. A cut-off of five NLE was chosen to define significant exposure to stress, corresponding to the level of stress experienced by 15% of young adults followed since childhood (Caspi et al. 2003). Adolescents who experienced from none to 5 NLEs and the total score was from -5 to 0 were categorized as Low Stress group, while those who had 6 or more NLEs and total score from -20 to -11 were defined as High Stress group. Both groups were gender balanced (Low Stress: male=182, female=178; High Stress: male=55, female=72).

2.4.2.2. Imaging

Details of the magnetic resonance imaging (MRI) acquisition protocols and quality checks have been described elsewhere (Schumann et al., 2010). MRI scans were acquired at the eight IMAGEN sites, using 3T MRI systems made by different manufacturers. High-resolution anatomical magnetic resonance images were acquired using a 3D T1-weighted gradient echo sequence based on the ADNI protocol (http://www.loni.ucla.edu/ADNI/Cores/in-dex.shtml), which allowed comparable data to be acquired from all sites despite these scanner differences.

2.4.2.3. MRI Analysis

2.4.2.3.1. Pre-processing and Segmentation

Images were pre-processed in SPM8, and segmented into grey matter (GM), white matter (WM) and cerebro-spinal fluid (CSF).

2.4.2.3.2. Extraction of Brain Networks

Brain networks were extracted using a method previously published (Tijms, Series et al. 2012). At each voxel within the GM compartment, a cubic region of interest (ROI) was centred at each voxel, composed of 3x3x3 voxels (6x6x6 mm^3). Morphological similarity between all cube pairs (regions of interest) was calculated based on linear correlation (Tijms, Moller et al. 2013), and each cube was rotated relative to the other one to find the maximum linear correlation between two ROIs. The cubes maintained the structure of the cortex unaltered (calculations were performed in native space), and so geometrical information was part of the morphological similarity between nodes (Tijms, Moller et al. 2013).

2.4.2.3.3. Matrix Resizing

The above voxel-based analysis was then parcellated into 400 ROIs and organised into 17 networks using an atlas by (Schaefer, Kong et al. 2017) that was applied to each participant's MRI image in native space. Table 2.1 describes the ROIs belonging to each network.

Networks	Name network	ROIs
1	Visual Central	Striate, extrastriate
2	Visual peripheral	Striate, extrastriate
3	SomatomotorA	Central sulcus, secondary somatosensory
4	SomatomotorB	Auditory cortex, central sulcus
5	Dorsal Attention A	Temporal Occipital, parietal occipital, superior parietal lobule
6	Dorsal Attention B	Post-cingulate, frontal eye field, precuneus
7	Salience Ventral Attention A	Par opercularis, insular cortex, medial parietal and frontal
8	Salience Ventral Attention B	Lateral, ventral, medio-parietal, orbital frontal cortex
9	Limbic	Orbito-frontal
10	Limbic	Temporal pole
11	Control A	Temporal, inferior parietal sulcus, dorsal and lateral prefrontal cortex, cingulate
12	Control B	Inferior parietal lateral, dorsal, ventro-lateral prefrontal and medio-parietal frontal
13	Control C	Posterior cingulum, precuneus
14	Default A	Dorsal and medio-dorsal prefrontal, posterior cingulate
15	Default B	Temporal, inferior parietal, ventral and dorsal prefrontal
16	Default C	Inferior parietal, retrosplenial, parahippocampal
17	Temporo-parietal	Temporal cortex

Table 2.1: Regions of interest (ROIs) that comprise the 17 networks in Schaefer template. Additional details of the network are included in the supplementary data

The atlas was non-linearly registered to each participant's MRI using DARTEL (in SPM8) (Ashburner and Friston 2000). Thus, the linear correlation coefficient between each pair of voxels was allocated to the respective 400 ROIs in the atlas, and then all the linear correlation values between ROIs were averaged, obtaining a matrix of 400x400 for all subjects – this process was called matrix resizing. To create a symmetric matrix, the transpose of the upper triangle of the matrix was calculated. A graphical representation of how the correlation matrices were resized is included in the Appendix A (Figure A5).

2.4.2.3.4. Thresholding Levels

Then Fisher's r-to-z transformation was applied to the linear correlation matrices. Seven different sparsity levels (from 0.05 to 0.35 with increments of 0.05) were

chosen to investigate whether different thresholds altered the statistical comparisons between groups. Sparsity is defined as connectivity density in brain networks, i.e. it indicates the percentage of existing connections compared to the maximum number of possible connections in the network (Sporns 2013). For example, with a sparsity level of 0.2, only the highest 20% of all the connections (linear correlation values) was retained and used to calculate the graph measures. Finally, all the correlation matrices were binarized to create unweighted and undirected networks (see Figure 2.3).

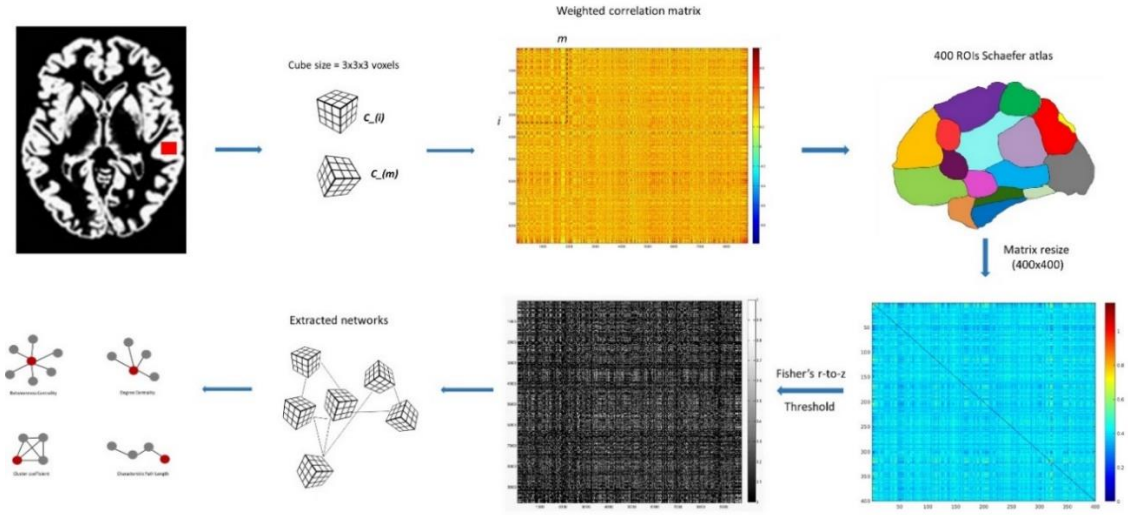

Figure 2.3: Graphical representation of the method used to calculate brain networks and extract graph theory measures. Correlation matrices are built by calculating the morphological similarity between two cubes. Connectivity matrices are resized based on an atlas

To identify changes in brain networks due to stress, graph theory measures were quantified using the Brain Connectivity Toolbox (Rubinov and Sporns 2010). The global graph theory measures calculated were mean cluster coefficient (CP), mean degree centrality (DC), characteristic path length (LP), small-worldness

and global efficiency. The local graph theory measures were nodal betweenness centrality (BC), nodal degree and nodal clustering coefficient. Cluster coefficient (CP) describes the number of connections among a node's topological neighbours (Sporns 2013), whereas characteristic path length (LP) indicates the global average of the shortest paths in the network (Rubinov and Sporns 2010) and it is linked to global efficiency, that is the average of the inverse of all the distances across the nodes (Stam and Reijneveld 2007). Node centrality is measured by degree and betweenness centrality. Degree centrality is defined as the number of edges for each node (Bullmore and Sporns 2009, Rubinov and Sporns 2010) while BC measures centrality at a local level, indicating the fraction of all shortest paths in the network that pass through a given node (Rubinov and Sporns 2010); nodes with high BC or degree are often defined network hubs (van den Heuvel and Sporns 2013). When networks have high cluster coefficient and short path length they present a property of small-worldness, which influences the network wiring cost (Watts and Strogatz 1998) (see Figure 2.4 for a graphical representation of graph theory measures. Further images are found in Appendix A).

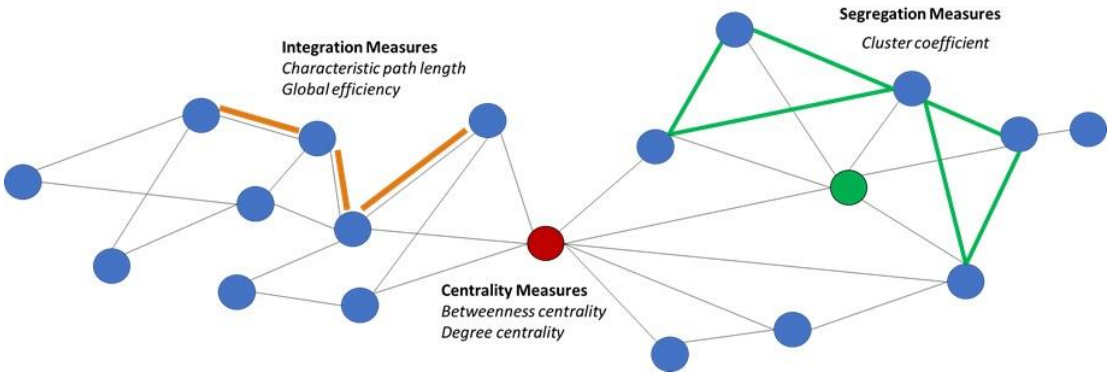

Figure 2.4: Graphical representation of graph theory measures. Integration, segregation and centrality are network properties that help to describe and define brain connectivity

2.4.2.4. Statistical Analysis

To investigate between-group statistical differences (using SPSS v.24, IBM Inc, USA) on global graph theory measures, ANCOVA models were used on the mean cluster coefficient, mean degree, path length, global efficiency and small-worldness, with age, sex, centre, PDS and SES as covariates; sex and centre were dummy coded in the model.

At a local level, only network hubs were inspected, running two-tailed t–tests on nodal betweenness centrality, degree centrality and cluster coefficient. In this study, ROIs which had BC and DC values at 2 SD above the mean were identified as network hubs. For the CP all the 400 ROIs were considered, since differences in overall distributions between the groups were of interest. Statistical tests were corrected for multiple comparisons using false discovery rate (FDR), based on the Benjamini and Hochberg procedure (Benjamini & Hochberg, 1995).

Graph theory measures describe between-group changes related to the node properties, but our interest was also in investigating the effect of stress on the edge connectivity strength between two nodes (such strength is indicated graphically by different thickness levels of the edges). To do so, we used Network-based Statistics (NBS) (Zalesky, Fornito et al. 2010), a toolbox based on a nonparametric statistical method to correct for multiple comparisons. In this study between-group differences at a single connection level were analysed, controlling for false discovery rate (i.e. number of false positive connections among all positive connections), based on 100,000 permutations, $\alpha = 0.05$ and a two-sided t-test between groups. Any edge showing a p-values lower than the α value was considered statistically significant.

2.4.3. Results

Table 2.2 summarizes the demographic information of the two groups. Chi-square tests showed no statistically significant differences between groups in age, sex, or PDS scores. Data were also checked for the influence of the different centres in which the MRI scans were acquired, showing no statistically differences between groups ($\chi^2 = 0.104$).

N=487	Low Stress		High Stress		P-value
Group size	360		127		
Gender	Female	178 (49.4%)	Female	72 (56.7%)	p= 0.160
	Male	182 (50.6%)	Male	55 (43.3%)	
Age	14.44 ± 0.56		14.47 ± 0.547		p= 0.527
Nr of NLE	2.71 ± 1.22		8.96 ± 1.41		P< 0.001
LEQ scores	-3.36 ± 1.419		-14.18± 2.389		P< 0.001
PDS	15.89 ± 2.830		16.68 ± 2.439		p=0.99
SES	6.76 ± 3.215		8.5 ± 3.172		p= 0.00001

Table 2.2: Demographic information of the sub-sample considered in this study

2.4.3.1. Results of Graph Theory Analysis

There were no statistically significant between-group differences in the global graph theory measures. Figure 2.5 shows how BC, DC, CP and LP change as a function of sparsity level. The lack of between-group differences in the global network measures reflects how stress due to negative life events does not alter the global structural connectivity in the adolescent brain, i.e. the brain's properties as a network - that each graph theory measure describes - remain intact even after stressful experiences.

Figure 2.5: Graph theory measures at different sparsity levels. The x axis represents the sparsity levels, while the y axis represents graph theory measures values. LS=Low Stress (green), HS=High Stress (red)

Regarding local network measures, in supplementary table 1 to 28 the top 50 nodes are detailed, as quantified using DC or BC, at each sparsity level. Figure 2.6 shows the node rank in the two groups at sparsity 10% based on DC. A statistically significant increase of DC was found in two hubs of the High Stress group: the left (xyz coord: [-14 -84 -13]) and right (xyz coord: [18 -86 -11]) extrastriate areas of the central visual network at sparsity 10% (t= -2.736, p_{corr}=0.048 and t= -2.951, p_{corr}= 0.048 respectively), while an increase in the posterior cingulate hub was seen in the left dorsal attention network (xyz coord: [-42 -37 46]) at sparsity level of 30% (t= -2.993, p_{corr}= 0.042).

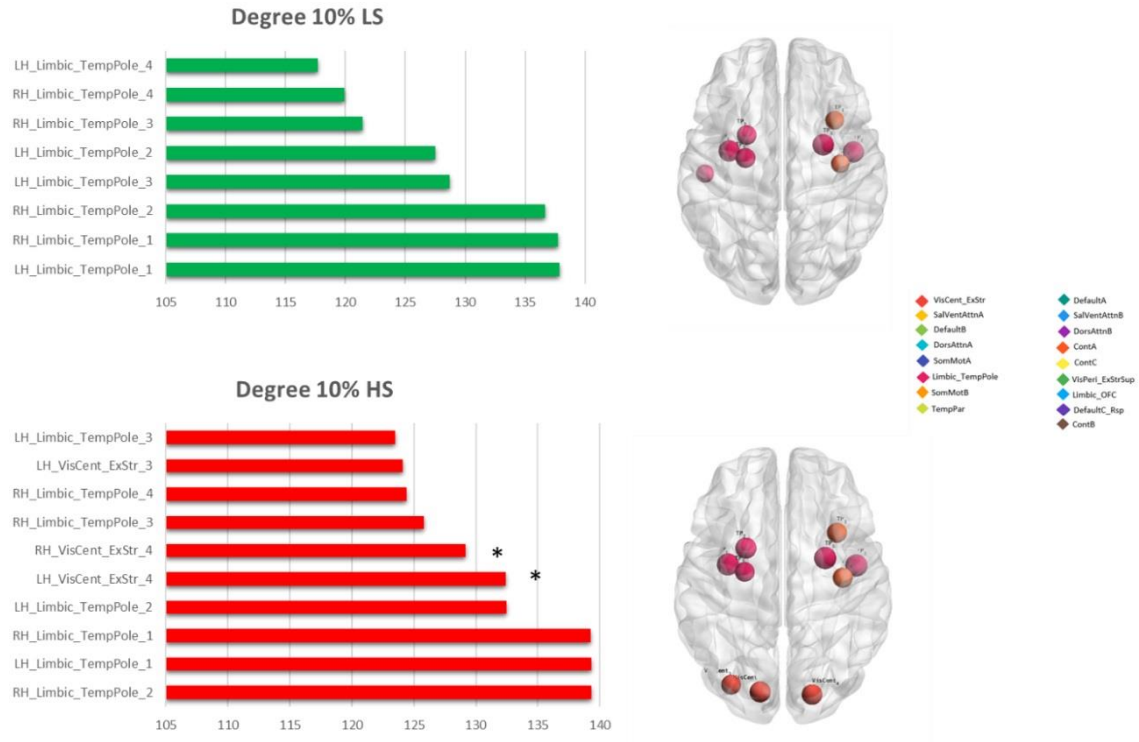

Figure 2.6: Hubs rank changes between Low stress (green) and High stress (red) groups based on degree centrality at sparsity of 10%

No between-group statistically significant differences were detected in the other sparsity levels. At all sparsity levels, the top 50 nodes as quantified by DC for each group are detailed in supplementary tables 1-14. Although not statistically significant, the nodes which were identified as hubs based on degree centrality all belong to the limbic network in the temporal pole, dorsal attention network and central executive and salience networks across sparsity levels.

At a sparsity level of 5%, there is a statistically significant difference in BC between the high and low stress groups at the left somatomotor cortex (xyz coord: [-10 -41 72]) in the High stress group (t= 3.674, p_{corr}=0.0042). Figure 2.7 also illustrates the locations of the highest nodes at this sparsity level. No other statistically significant differences between BC hubs were detected at other

sparsity levels. The node values of the BC at each sparsity level for each group are detailed in supplemental table 15-28.

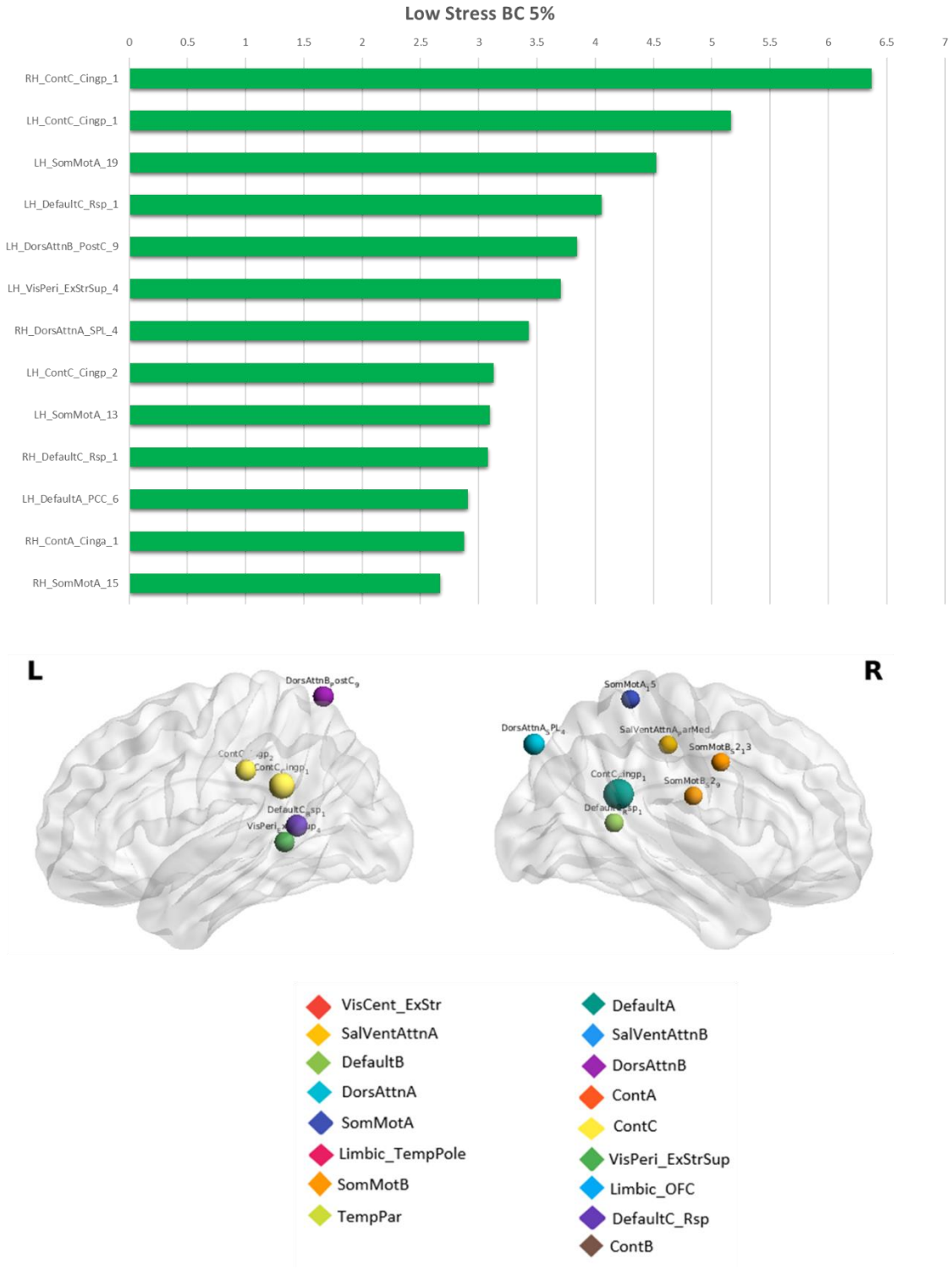

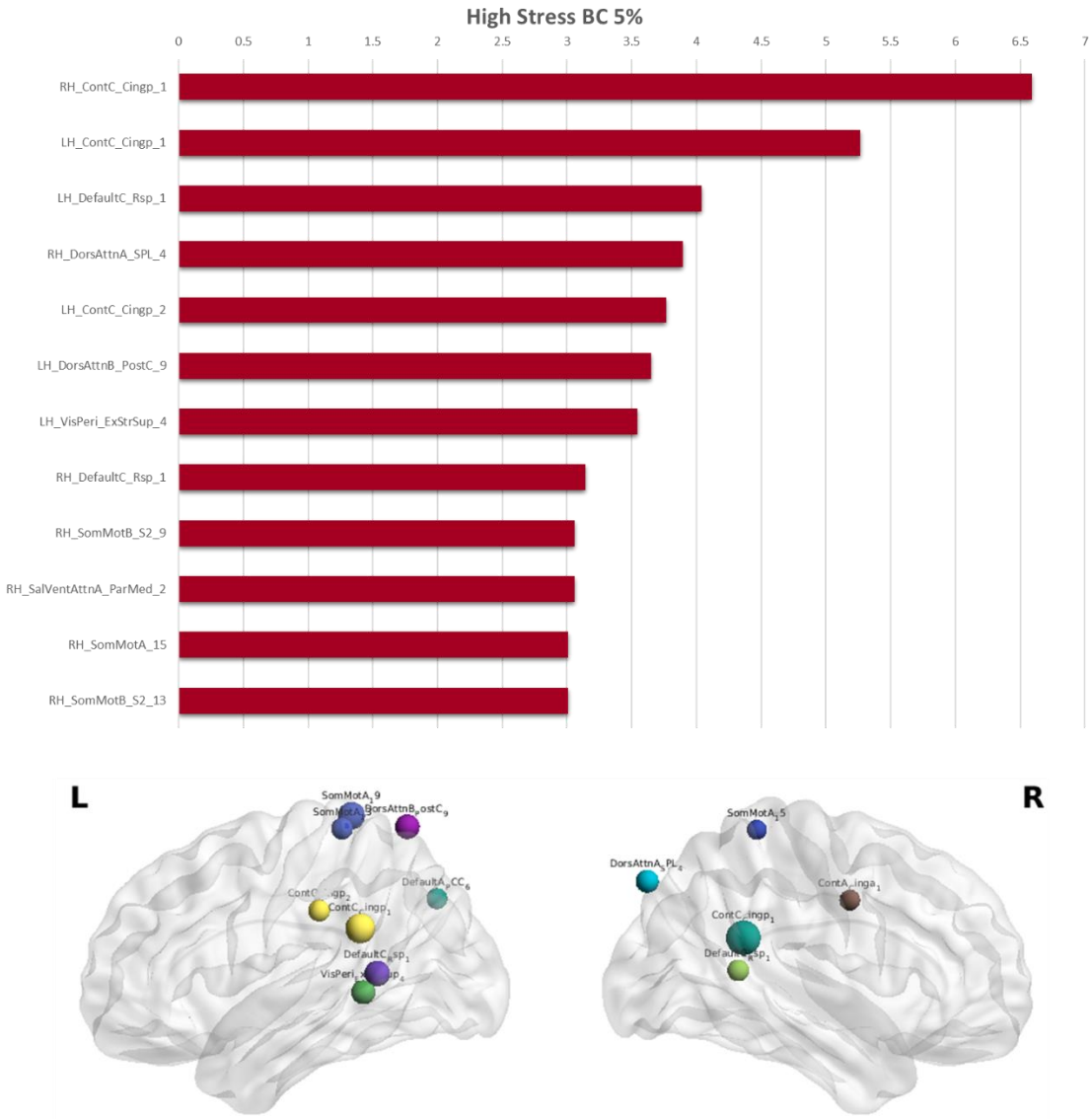

Figure 2.7: Hubs rank in both groups based on betweenness centrality (BC) at sparsity=0.05. The size of the node is proportional to betweenness value and colour of node indicates to which network it belongs to. A star indicated the region with a statistically significant between-group difference (FDR corrected)

Examining nodal CP, where all 400 nodes were considered, no p-value survived FDR correction, except for the network at sparsity 35%, where an increase was seen in one of the nodes belonging to the orbital frontal cortex (p_{corr}= 0.04) of the

High stress group. No statistically significant between-group differences were seen at the other sparsity levels.

2.4.3.2. Whole-Brain Connectivity Results

There were statistically significant increases of edge connectivity strength in the high stress group compared to the low stress group as shown in Figure 2.8. Specifically, two statistically significant increases were seen: an inter-hemispheric edge connecting a node in the orbito-frontal cortex (xyz coord = [-11 21 -4]) to a node in the right superior parietal lobule (xyz coord= [25 -85 34]), belonging respectively to the limbic network and dorsal-attention network (t-value= 3.83, p<0.0001). The second edge connected the posterior cingulate cortex node of the left dorsal attention network (xyz coord= [-42 -37 46]) to the pars opercularis node of the left salience network (xyz coord= [-53 -49 30]), t-test = 4.39, p<0.00001. There were no statistically significant increases in connectivity detected in the low stress group compared to the high stress group.

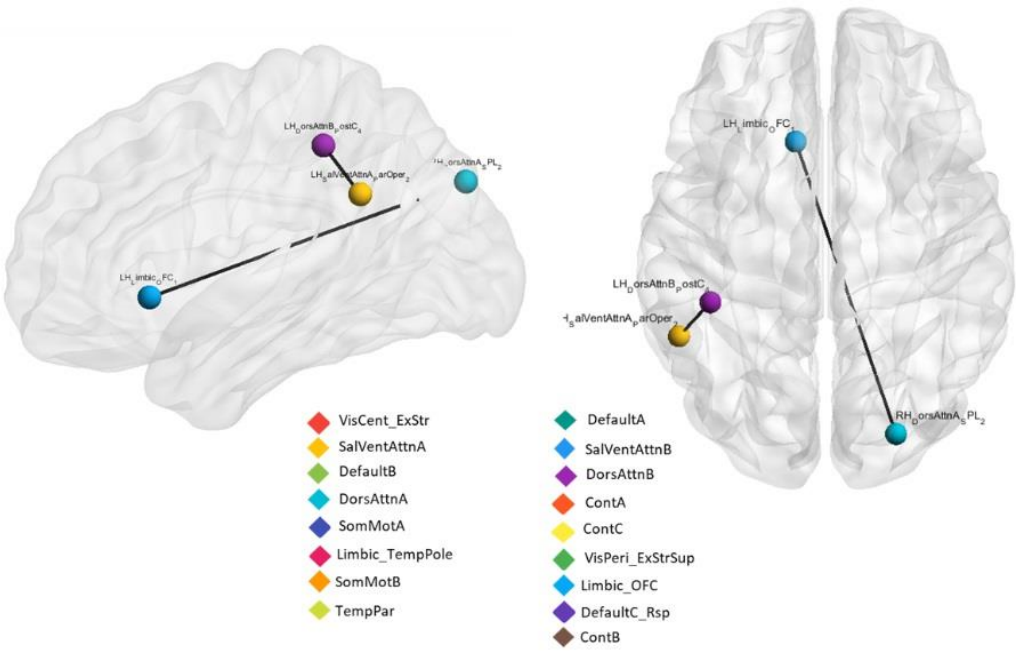

Figure 2.8: Single edges showing significant increase of connectivity in High stress group compared to Low stress group

2.4.4. Discussion

This study investigated stress-related changes of structural connectivity in the cerebral cortex of the adolescent brain. Graph theory measures were calculated across a range of sparsity levels, reflecting different connectivity densities. Overall, there were no changes in structural network measures (mean DC, mean CP, LP, global efficiency and small-worldness) between Low and High Stress groups. Another study using our same methodological approach found no differences in any global or local graph theory measures between adolescents (13-18 years old) suffering with major depressive disorder (MDD) and healthy control (HC) (Sacchet, Ho et al. 2016), consistent with our findings. The lack of statistically significant results in the global measures suggest that stress does not lead to global structural connectivity changes in the brain. Ho and colleagues reviewed studies on MDD connectivity changes in adolescents, finding no differences in the global measures (Ho, Dennis et al. 2018).

Regarding the global connectivity differences between the groups, changes analysed at an individual connection level with NBS were seen in two edges, showing an increase of connectivity in the High stress group. The first edge connected the orbital frontal cortex (OFC) of the left limbic network to the superior parietal lobule (SPL) of the right dorsal attention network (DAN). The second edge connected the pars opercularis of the left ventral attention network (VAN) to the posterior cingulate cortex of the left DAN. These results confirm previous studies on connectivity, showing the SPL is involved in top-down attention, and

attentional guidance of saccades (Asscheman, Thakkar et al. 2015), and it was found to be structurally altered in PTSD (Tan, Zhang et al. 2013), where volume reductions were seen (Yuii, Suzuki et al. 2007). Results of a previous study on structural brain changes in children who suffered early stress found a structural alterations in the OFC and parietal lobe in children victim of physical abuse, which was also correlated with social and learning difficulties (Hanson, Chung et al. 2010).

The pars opercularis node belongs to the cingulo-opercular network (CON), and it is involved in vigilance and alertness for working memory (Sadaghiani and D'Esposito 2015). Kolsnar and colleagues defined the cingulo-opercularis as a key network node for the neurodevelopment in adolescent. They showed that centrality measures in cingulo-opercular, cerebellar and frontoparietal areas were highly associated with better task and working memory performances (Kolskar, Alnaes et al. 2018). The pars opercularis cortical thickness was also shown to be inversely associated with the level of cortisol released as consequence of stress (Frodl and O'Keane 2013). Another study showed how the cingulo-opercular network had increased functioning in people suffering of general anxiety disorders (GAD), PTSD and social anxiety episodes (Sylvester, Corbetta et al. 2012). A review on the development of human functional network suggested from early to mid-adolescence, anterior regions (including the anterior cingulate cortex for example) reorganize connectivity from fronto-parietal to cingulo-opercular salience networks. Where the fronto-parietal and the cingulo-opercular compartments represent a single graph component in younger children (7-9 years old), they break into two separate compartments at age 10-15 years

old (Power, Fair et al. 2010), shown by investigating connectivity in task-related ROIs with fMRI.

The cingulate cortex was found to be altered in the default-mode network. For example, Soares and colleagues investigated the effect of stress on resting-state fMRI networks in a young adult population after a stressful situation. In particular, they reported an increase of connectivity in the posterior cingulate cortex and the precuneus (pCUN) of the group with higher levels of stress, along with anterior brain areas, such as medial prefrontal cortex and mOFC (Soares, Sampaio et al. 2013), some of which are nodes of the DMN. Another study showed a hyperactivity of the DMN after the exposure to social stressors (Clemens, Wagels et al. 2017), with an increase in regions focused on visual motion processing and alertness. The increase of alertness state seen in the high stress group could explain the increase of degree centrality in the visual central network we found in our population. Such increase, in fact, reflects a higher number of edges connecting the visual central extrastriate node to other brain regions in both hemispheres. Also Soares' findings (Soares, Sampaio et al. 2013) seems to reinforce such findings where he showed an increase of connectivity in the visual network of the high stress group, specifically at the level of the calcarine cortex. The other region where we found an increase of degree was the posterior cingulate node of the dorsal attention network. It is known that the posterior cingulate is part of the DMN, but a previous study showed dorsal PCC to be functionally correlated to other networks, such as attentional, somatomotor and executive control networks (Leech, Braga et al. 2012). In particular, functionally connectivity between the PCC and amygdalae has been shown to increase with

social stressful events, associated with an increased connectivity between the amygdalae and the orbito-frontal cortex (Veer, Oei et al. 2011).

Other studies on rsfMRI networks and stress found a decrease of degree centrality in the visual cortex of PTSD adolescent population (Yin, Jin et al. 2012, Suo, Lei et al. 2015) associated with alterations in autobiographical and declarative memory in PTSD patients. Other nodes that came up as hubs in more than one sparsity levels belonged to the limbic, central executive and attentional networks, and even they were not statistically significant, previous studies confirmed such result (Power, Fair et al. 2010, Sacchet, Ho et al. 2016).

A decrease of nodal BC in the High stress group in the left somatomotor network was found, suggesting a link between the high stress group and the brain morphological alterations in that area. Previous studies observed earliest GM loss in primary sensory-motor cortex (Paus 2005) during adolescence, starting around puberty and spreading rostrally over the frontal cortex and caudally over the parietal and finally to temporal cortex. In typical development, GM loss occurs firstly in primary sensorimotor areas and later in association areas (Gogtay, Giedd et al. 2004) at different stages across the lifespan (Ernst and Mueller 2008). Alterations in this area can be sign of potential neuro-disorders. For example, a previous study defined the somatomotor centrality measures as one of the strongest predictors to identify connectivity alterations between typical developing children and patients with ADHD (dos Santos Siqueira, Biazoli Junior et al. 2014).

Results from previous studies on brain connectivity have not been consistent. This may be due to methodological approaches such as network segmentation,

neuroimaging modality (structural vs. functional) and methods for calculating connectivity. For example, Suo and colleagues reported a decrease in global efficiency and path length in PTSD group when they extracted the connectivity from DTI data (Suo, Lei et al. 2017), but they didn't find the same effects with rsfMRI data (Suo, Lei et al. 2015). In both cases no small-worldness changes were detected between groups.

In the results of this study, some of the between-group differences were seen in some sparsity levels but not others, indicating a lack of consistency across sparsity levels. Changes in sparsity level lead to different number of nodes included as a part of the network, thus the network would be altered, and it may lead to changes in defining which nodes may be hubs and in their relative connectivity to the neighbouring nodes. The choice of calculating connectivity metrics at different sparsity levels is linked to the definition of sparsity itself. In fact, when the network density increases, more edges are included. This influences the definition of hubs, and therefore, the computation of the metrics, especially at the local level (i.e. nodal degree and betweenness centrality, cluster coefficient) (Tsai SY, 2018), improving the reliability of network metrics. A few studies investigated how the brain connectivity measures were influenced by the choice of different sparsity levels, measured by the intra-class correlation coefficient (ICC) on both structural (DTI) (Dennis, Jahanshad et al. 2012, Yuan, Henje Blom et al. 2019) and resting-state functional connectivity (Wang, Zuo et al. 2011). As one of the main interests in this study was to explore the level of consistency and reliability of the graph measures with the variation of the edge number within networks, the range of different thresholds was a key factor in our analysis. For example, Dennis and colleagues found that LP and global efficiency

were very unstable until sparsity level of 0.25. Cluster coefficient had some dips within the sparsity range of 30-35%, whereas small-worldness presented many fluctuations, with peaks and dips. The least stable measures were found at the lowest sparsity levels, maybe due to the different nodes retained for the calculation of graph theory metrics (Dennis et al., 2012). Path length and global efficiency were less reliable than CP also because longer connections are trimmed before the shorter ones. Results on rsfMRI confirmed CP to have low reliability, whereas among the graph theory measures, nodal degree centrality showed high reliability (Wang, Zuo et al. 2011). Furthermore, they showed how the most reliable connections were in the frontal cortex, suggesting that the reliability is influenced also by the brain networks. Overall, literature indicates a tight relationship between the calculation of graph theory measures and the sparsity level. The methodological approach used in this study to extract brain networks from grey matter segmentation provides insight into the relationship between stress and brain connectivity, since it keeps the geometric and spatial information of the cortex. (Rimkus, Schoonheim et al. 2019).

2.4.5. Conclusion

The present study investigated changes of single-subject grey matter networks in adolescents who experienced negative life events. Overall, results showed group differences at a local level, whereas no differences were observed in the global graph theory measures. It is the first time that stress-related changes in brain connectivity were studied on such a large population of adolescents, giving a picture of what happens to the brain structural connectivity when healthy adolescents experience stressful events. Previously, only few studies were published on stress and brain networks from DTI and rsfMRI, and graph theory

measures, mostly in clinical populations. The findings of this study can provide insight of how stress contributes to alter the brain structure in adolescents, and which role plays in the development of neuropsychiatric conditions, such as major depressive disorder, anxiety disorders, emotional dysfunctions and PTSD. Knowing the key regions that are target of dysfunctions and disconnections during stressful events can help understanding better the adolescent emotional and behavioural disorders and developing effective interventions.

3. Volumetric Changes of Hippocampus Subfields Due to Stress

3.1. Introduction

3.1.1. Hippocampus Development in Adolescence

During adolescence, the brain structures involved in memory and emotions that includes the hippocampus, amygdala, nucleus accumbens (NAc), prefrontal, frontal cortices and the hypothalamus, undergo prominent reorganization. Neuroimaging studies investigated how the hippocampal subfields change in a heterogeneous way during neurodevelopment from childhood to adolescence (Krogsrud, Tamnes et al. 2014, Tamnes, Bos et al. 2018, Lynch, Shi et al. 2019). In particular, an hemispheric-specific increase of hippocampus volume was found until 13-15 years, with the right hippocampal volume being bigger than the left side (Krogsrud, Tamnes et al. 2014), and gender-specific differences before 13 years old. Regarding hippocampal subfields, they showed nonlinear trajectories with volume increases in the subiculum, molecular layer, fimbria and CA1 until early adolescence, whereas granular cellular layer of the dentate gyrus (GC-DG), para- and pre-subiculum, and CA2/3/4 showed linear volume decreases (Keresztes, Bender et al. 2017, Tamnes, Bos et al. 2018). Specific to adolescence, age-related increases were found in the right CA3, DG and CA1 (Lee, Ekstrom et al. 2014), but not in the left side.

Gender differences were found also when the hippocampus shape was considered , with females having larger surface expansion than males, especially in the superior posterior lateral surface of the left hippocampus (Lynch, Shi et al.

2019). Such gender differences can be explained with differences in testosterone levels, which influence prefrontal-hippocampal development in childhood and adolescence, representing an important factor for cognitive and mnemonic processes (Nguyen, Lew et al. 2017). It was found memory abilities increase with age (Riley, Chen et al. 2018), even though specific memory processes can be related to the hippocampus in different ways. For example, memories recall and retention have been associated to an increase of volume in the cornua ammonus, whereas a decrease of CA4 was associated to verbal learning (Tamnes, Walhovd et al. 2014). Another study investigated gender-specific interactions between brain networks critical for memory in early and late adolescence by calculating effective connectivity (Riley, Chen et al. 2018). They found younger boys had a higher number of connections between posterior visual areas and multi-sensorial regions in the parietal and frontal lobes, with fewer connections to the limbic system. Older boys showed the opposite trend, having more anterior connections between association and frontal multi-modal areas, such as the OFC. Younger girls showed connections similar to the older boys, where the limbic and sensory regions were connected more homogenously. Finally, older girls had connections widely spread, and this was the only group showing efferent connections from the hippocampus to not limbic regions.

3.1.1.1 Psychiatric Disorders Caused by Stress

Stress has been described as a potential factor that triggers alteration in the brain during adolescence, disrupting the physiological balance in structure, function and chemical components of brain areas involved in behavioural response and emotional processing (Andersen and Teicher 2008, Eiland and Romeo 2013, Bucci, Marques et al. 2016). In these years, according to Stanley Hall,

adolescents develop three specific key behaviours: mood disruptions, conflicts with parents and risk-seeking behaviours (Arnett 1999), reinforcing the idea of how the environment surrounding individuals at that age is key for their psychological and behavioural development. He defined this stage as the “storm and stress” view. This storm of events makes adolescence the period of time where individuals are more sensitive to stress and emotional perturbations, increasing the risk of developing psychiatric disorders, such as anxiety problems, post-traumatic stress disorders (PTSD) and depressive symptoms (Casey, Jones et al. 2010).

Structural alterations caused by stress have been identified with smaller volume of the hippocampus in adolescents suffering of MDD; at the functional level young people affected by depressive disorders presented a higher activity of the amygdala when experiencing negative life events, while there was a reduced activation of the amygdala with positive life events (Redlich, Opel et al. 2018). Another multi-modal study including VBM and resting-state functional connectivity (RSFC) compared changes in both brain structures volume and connectivity in an adult population suffering of MDD and bipolar disorder (BD), compared to healthy people. They found alterations in frontal-limbic networks, specifically showed decreased grey matter volume (GMV) in the left anterior cingulate cortex, right hippocampus compared with the healthy controls. A decrease of resting-state connectivity was found that both the MDD and BD groups between the ACC and the left orbitofrontal cortex in both people with depressive and mood symptoms, compared to healthy people (Chen, Wang et al. 2018).

Another study investigated the relationship between genetic predisposition to experience stress and changes in stress-related brain areas in school-age children (Pagliaccio, Luby et al. 2015). They showed increasing genetic risk predicted alterations in connectivity between amygdala and the caudate, as well as with the postcentral gyrus. Furthermore, a higher number of stressful life events predicted weakened connectivity between the amygdala and ACC, the inferior and middle frontal gyri, caudate, and parahippocampal gyrus in those children with more adverse environmental conditions. Finally, changes in amygdala connectivity predicted the likelihood of developing anxiety and decreased emotion regulation skills longitudinally (Pagliaccio, Luby et al. 2015).

Another study looked at the intra and inter-connectivity of the default-mode network with the salience and central executive networks, in an adolescent population suffering of post-traumatic stress disorder (PTSD) (Viard, Mutlu et al. 2019). Analyses revealed decreased within-DMN connectivity (between PCC and occipital cortex) in patients compared to controls. Furthermore, within-DMN connectivity (between PCC and hippocampus) was found to have a negative relationship with anxiety and depressive symptoms (Viard, Mutlu et al. 2019). These results were strengthened by another study that found smaller volume in some of the hippocampus subfields, namely CA2/3 and DG in adolescents with PTSD (Postel, Viard et al. 2019).

In neurodevelopment, structures related in mnemonic and affective reactivity processes, such as the amygdala, hippocampus and striatum, mature earlier than frontal areas (including the ventromedial and dorsolateral PFC) that monitor and regulate the subcortical limbic functions. Anatomically, the volume of the amygdala starts to stabilize around late adolescence, whereas the ventromedial

prefrontal cortical thickness keeps changing throughout adolescence until young adulthood (Wu, Geng et al. 2018). This influences the connectivity between limbic structures and ventromedial prefrontal cortex (vmPFC), and the relationship with perceived stress in adolescents and young adults, supporting the idea that connectivity between emotion-related structures and prefrontal areas tends to be changing during brain development (Wu, Geng et al. 2018) (Kaiser, Clegg et al. 2018).

When an individual is exposed to stress, the amygdala sends signals to the hypothalamus about physiological perturbations, which activate an endocrinal cascade through the hypothalamic pituitary adrenocortical (HPA) axis, increasing the levels of circulating cortisol. When cortisol binds to the glucocorticoid receptors, there is an increment of corticotropin releasing hormone production in the amygdala, leading to greater HPA axis activity (Rudolph, Troop-Gordon et al. 2018). When exposed to severe threat-related stress or chronic stress, the continuous increase of cortisol can affect hippocampal mechanisms regulating the activity of the HPA axis, while boosting amygdala activity and making the brain more sensitive to the action of new stressors (Kuhlman, Geiss et al. 2018). The continuous activation of the HPA axis due to stressful experiences affects the chemical balance in the body and the neurotransmitter systems in the brain. Dopaminergic system alterations were found in children and adolescents exposed to early maltreatments, causing lower ventral tegmental area (VTA) connectivity with the right hippocampus in trauma-exposed children relative to the control group (Marusak, Hatfield et al. 2017).

A study investigating the relation between anxiety, depressive symptoms, impulsivity and brain regions structural changes in adolescents reported that

reductions in cortical thickness were seen in ventromedial PFC and medial OFC, as well as smaller GMV in the hippocampus bilaterally (Merz, He et al. 2018). Such reductions were associated with higher depressive symptoms, while higher impulsivity was associated with reduced thickness in frontal regions, for example pars orbitalis and frontal pole. They did not find any statistically significant relation with anxiety.

Adolescent stress-related symptoms are related to both social and cognitive factors. Examples of social factors are social exclusion or the perception of judgment from others. Examples of cognitive factors are negative life events, which trigger cognitive vulnerability or negative self-representation (Jankowski, Batres et al. 2018). Both these factors increase the chances to develop psychiatric disorders during adolescence, and brain regions involved in peer victimization, intra- and interpersonal stress undergo structural changes as the brain is highly plastic over those years. These areas are amygdala, parahippocampal gyrus and subgenual anterior cingulate, which result in increased reactivity if investigated with functional MRI (Silk, Siegle et al. 2014). Such offenses to key areas of the brain involved in self-processing and emotional responses contribute to disruption of neural networks that can be lasting also in adulthood. In fact, studies conducted with fMRI investigated the reactivity of specific areas of the limbic and frontal regions in adults, and they found a hyperactivity of the anterior insula, anterior cingulate and amygdala, along with a reduced activity of the prefrontal cortex linked to negative stimuli (Hamilton, Etkin et al. 2012). Such pattern has been found to be common in depressed adolescents, where atypical activity of the anterior insula has been associated to altered connectivity in the limbic network (Ho, Yang et al. 2014).

3.1.2. The Hippocampus and Its Subfields

3.1.2.1. Morphological Organization

The hippocampus is a part of the limbic system that is involved in memory processing and navigation, autobiographical and episodic memory, as well as relational representations. This structure is situated in the temporal lobe bilaterally and its name derives from its share that reminds the sea-horse (Schultz and Engelhardt 2014). It is usually divided into three (or four) parts: the head, body and tail. Some papers include also the parahippocampal gyrus, which, is situated just under the hippocampus, and it is formed by the anterior and posterior halves. This last part is involved in memories retrieval related to emotions.

The hippocampus is formed by subfields, which in turn are formed by different types or amount of fibres. The subfields of the hippocampus are the cornua ammonis 1,2,3,4 (CA1-CA4) (that is defined the" hippocampus proper"), the dentate gyrus (DG), the subicular complex and the entorhinal cortex. The most external layer of the hippocampus is the alveus, formed by myelinated axons. The CA1-CA4 are formed by stratum oriens, stratum pyramidale, stratum radiatum and stratum lacunosum-moleculare, located before the hippocampal sulcus (Li and Pleasure 2014). The stratum pyramidale is formed by pyramidal cells, that are principal excitatory neurons of the hippocampus formation, while the stratum radiatum is formed by Schaeffer fibres, dendrites that belong to the memory formation and emotional network (Booker and Vida 2018). The subicular complex is formed by three main parts: the parasubiculum (which is formed by grid cells, that are neurons responsive to movements), the presubiculum, that is

part of the spatial and memory systems, and the subiculum, which is the main output of the hippocampus formation. Finally, the parahippocampal gyrus is part of a circuit that sees the entorhinal cortex transmitting its signal from the parahippocampal cortex to the dentate gyrus via the perforant way (made of granule cell fibres) (Jones 1993).

The different subfields of the hippocampus are involved in two circuits: the perforant (called also monosynaptic) and the trisynaptic circuits. In the monosynaptic circuitry, the entorhinal cortex and the CA1 play a role in the bigger trisynaptic circuitry, which has the function of producing and retrieving declarative memories (Yeckel and Berger 1990). The trisynaptic circuitry involves the three types of cells that form the HC subfields, and it develops later than the performant one. In this circuitry the information received by the entorhinal cortex from the neocortex travel to the subiculum and the dentate gyrus, to finish then in the parahippocampal gyrus (Figure 3.1). Gomez showed how the information flow from these regions to the CA1 and CA3, where the critical learning phase happens, i.e. new information are stored (Gómez and Edgin 2016). The new information flow to the subiculum through the fornix; from the subiculum it goes finally to the nucleus accumbens, amygdala and prefrontal cortex.

The hippocampus represents a highly heterogeneous morphology of its subfields that are differently associated with age and gender. For example, age was negatively associated with the volume of combined CA1-2, whereas the entorhinal cortex, CA3 and DG, showed first a negative correlation with age during mid-childhood which was then attenuated in adulthood, around 50 year old (Daugherty, Bender et al. 2016). Regarding sex differences, no difference in the hippocampus morphology was found between males and females before

puberty, whereas larger hippocampi in both hemispheres at the level of the CA1 subfield were found in females after puberty (Satterthwaite, Vandekar et al. 2014). Morphological changes of the hippocampus subfields showed a temporal influence in their developmental trajectory, associated mainly to internal cortical myelination (Vos de Wael, Lariviere et al. 2018). For example, the dentate gyrus and the subiculum develop slowly over time, while CA develops more rapidly, due probably to different functional specializations (Cembrowski, Phillips et al. 2018, Dimsdale-Zucker, Ritchey et al. 2018). For example, multivariate pattern similarity analysis showed how CA1 subfield was associated to objects that had a different episodic context, while CA2-3 and DG were engaged more in differentiating between objects from the same episodic context (Dimsdale-Zucker, Ritchey et al. 2018).

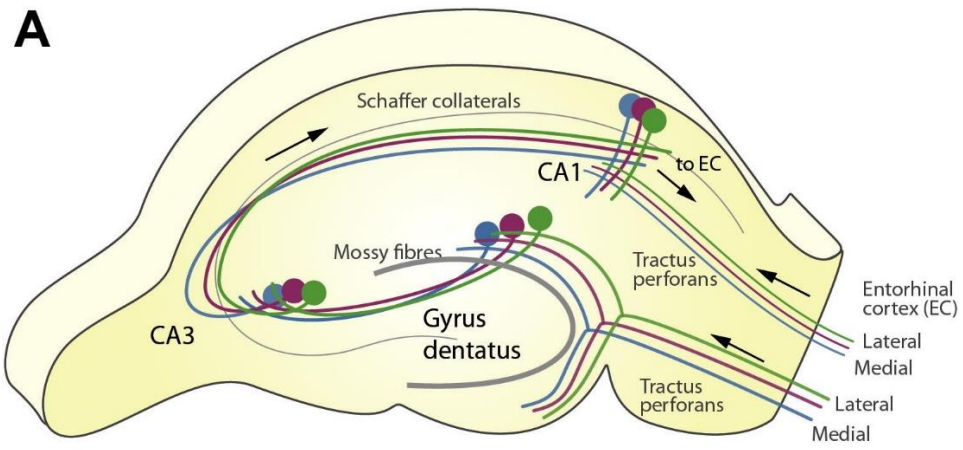

Figure 3.1: Anatomy of the hippocampus including the trisynaptic pathway as the principal neural circuit involved in the processing of information (Bartsch et al., 2015)

3.1.2.2. Structural Changes with Stress-Related Disorders

Animal studies suggest that stress primarily acts to suppress neurogenesis of dentate gyrus granule neurons, and to cause remodelling of dendrites in the CA3 (McEwen 2002). Reduced neurogenesis and consequent increases of neural loss lead the way to morphological changes in the brain structure, such as hippocampal atrophy, which contributes to cognitive impairment. A large part of these changes with stress has similar characteristics to those observed in neurodegeneration. This suggests that gene expression patterns might be shared between stress and neurodegeneration, as well as chronic stress or acute stress may be risk factors for earlier neurodegeneration.

Hippocampus subfields are subjects to structural changes when adolescents experience childhood traumatic events. Literature showed how the anxiety and mood disorders related to negative experiences are associated to reduction of the hippocampal volume, especially in the left hemisphere (Teicher, Anderson et al. 2012, Chalavi, Vissia et al. 2015). The gravity of the hippocampal volume loss is associated to the severity of the childhood traumatic event, and the subfields more affected were shown to be the left CA2/3/4, DG, fimbria and subiculum, both in people without history of neuropsychiatric disorders (Teicher, Anderson et al. 2012), and in patients suffering with PTSD (Chalavi, Vissia et al. 2015), the latter presenting decreased volumes of CA2-3 and DG regions in both hemispheres when compared to controls (Postel, Viard et al. 2019). Female adolescents suffering of anorexia nervosa, associated to symptoms of depression, showed a decrease in GM volumes in most of the hippocampus subfields (Myrvang, Vangberg et al. 2018). Children and adolescents suffering of mood disorders, such as bipolar disorder (BD), showed a decrease In the right

CA1, CA4, subiculum, the GCL, ML and the hippocampal tail (Tannous, Amaral-Silva et al. 2018).

Maltreatment in childhood has been demonstrated to have a negative impact on limbic system structures when comparing with maltreated youth with PTSD, youth without PTSD and healthy controls (Morey, Haswell et al. 2016). Youth without PTSD had larger volumes in the left amygdala and right hippocampus when compared with maltreated youth with PTSD and non-maltreated control youth. Another study investigated the longitudinal effects of maltreatment on hippocampal sub-region volumes in young people from early to late adolescence, and the association between psychopathological component and the severity of the hippocampal alterations (Whittle, Simmons et al. 2017). Childhood maltreatment was linked to changes in the development of hippocampal sub-regions in adolescents, particularly in the left subiculum and CA4-DG subfields. Furthermore, gender-based analyses showed a stronger effect in males compared to females. Other components related to adolescent lifestyle, such as socio-economic status (SES) and internal factors, for example perceived stress, were also found to be crucial for the healthy development of hippocampus subfields (Piccolo and Noble 2018, Yu, Daugherty et al. 2018).

3.1.2.3. Extraction of Subfields Volume with FreeSurfer 6.0

The hippocampal subfield segmentation tool implemented in Freesurfer 6.0 has been hugely used in the last few years to investigate between-group differences in the hippocampus volume. This method is based on an atlas built ex vivo from MRI data with a resolution of 0.13 mm isotropically (Iglesias, Augustinack et al. 2015). This resolution has led to define the hippocampus subfields in a more

accurate way than the previous version (V5.3), including structures that were missing, such as the molecular layer and the sub-division of the HC in head, body and tail. If compared to other two atlases known in the literature, the in-vivo atlas in Freesurfer 5.3 (Van Leemput, Bakkour et al. 2009) and the ex-vivo "UPenn" atlas (Yushkevich, Avants et al. 2009), the atlas implemented in Freesurfer 6.0 has a higher number of subfields defined (15 vs 5 in the UPenn atlas) at ultra-high resolution that can be only obtained ex vivo, determining more precise borders for each subfield. To build the new atlas, post-mortem brains were collected and scanned in a 7T Siemens scanner with a 0.1 mm isotropic resolution, (100 µm). When the subfields are more difficult to define, previously contrast images were used (Iglesias, Augustinack et al. 2015). The subfields obtained with this new segmentation algorithm are the alveus, the para- and presubiculum, the subiculum, the cornu ammonis from 1 to 4, the granule cell layer of dentate gyrus (GC-DG), the hippocampus-amygdala-transition-area (HATA), then fimbria, the molecular layer (ML), the hippocampal fissure, and the hippocampus tail (Figure 3.2).

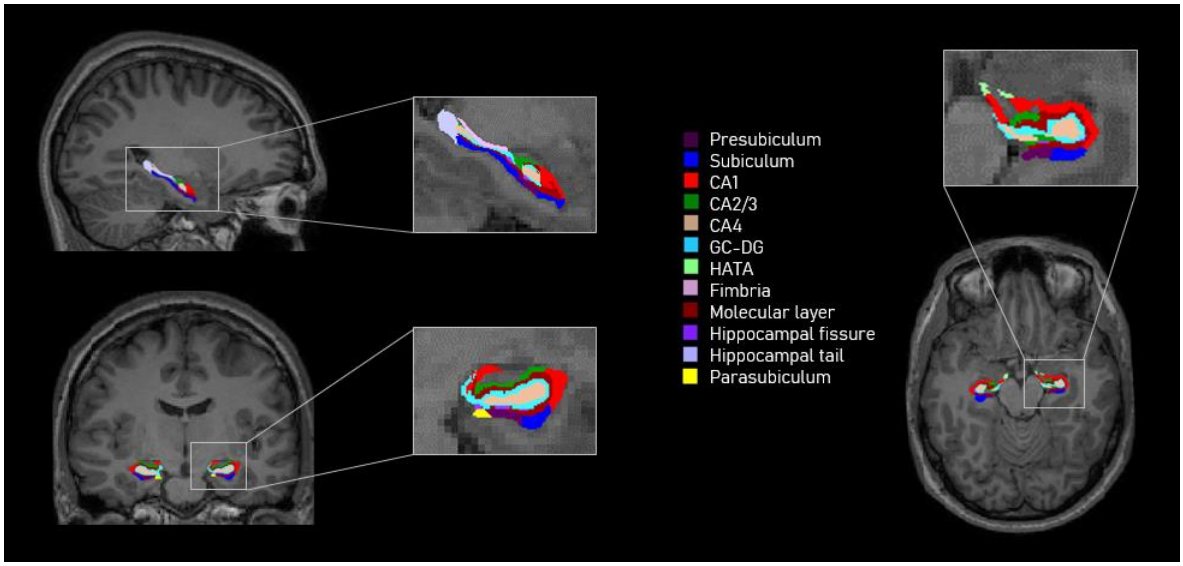

Figure 3.2: Segmentation of hippocampus subfields in FreeSurfer 6.0

Compared to the previous version of FreeSurfer (5.3), this newer version has a better resolution to distinguish the HC sub-regions, because it is based on defining the subfields by using an atlas (~0.1mm isotropic) ex-vivo MRI data, which gives a better visualization of anatomical boundaries. Additionally, pyramidal layer thickness and intensity were used to divide the subfields; that is more accurate than geometrical criteria (Iglesias et al., 2015). Finally, this new version has an additional feature to divide the HC in head, body and tail (using the developmental version of FS 6.0).

3.1.3. Study Objective

The objective of this study is to investigate the effect stress has on the hippocampus subfields volume changes. This was done both cross-sectionally at baseline, and longitudinally, investigating if hippocampus volume changes between two stages of adolescence are determined and correlated with the level of stress experienced throughout adolescence.

3.2. Study Material and Methods

3.2.1. Study Population: IMAGEN Data Sub-Group

In this study, a sub-group of 329 participants from IMAGEN was considered and hippocampus subfield volumes were extracted at three time points. The sample size was obtained by considering the initial population in the previous study, keeping only those participants who had MRI scans acquired at three time points. This was done for both groups. Demographic information of the group of this study are found in Table 3.1.

N=329	Baseline		
	Low	High	p-value
n	207	122	
Age (yrs)	14.5 ± .459	14.41 ± .474	p=0.096
Gender	F= 114 (55.1%)	F= 73 (59.8%)	p=0.3996
	M= 93 (44.9%)	M= 49 (40.2%)	
LEQ (NLE score)	4.33 ± 2.071	10.59 ± 2.795	p<0.001
LEQ (nr NLE)	3.17 ± 1.395	7.36 ± 1.385	p<0.001
PDS (raw)	16.28 ± 2.744	16.54 ± 2.45	p=0.365
SES (raw)	6.29 ± 3.245	7.54 ± 3.123	p<0.001

Table 3.1: Demographic information of participants of the first time point. For age, total number of negative events, total score of NLE, PDS and SES values are reported showing the mean and SD in both groups

3.2.2. Longitudinal Pipeline on High-Computing System (TCHPC)

To define longitudinal changes in the hippocampus (HC) subfields volumes, FreeSurfer offers a pipeline that is based on creating a subject-specific unbiased atlas obtained by averaging the T1 images across all the time points considered, as discussed above (Iglesias, Augustinack et al. 2015). In the technical language, the unbiased template is called '-base', and it is used to process each time point longitudinally. The template that is created is based on the median of the volume of all the time points, and each one of them is then registered to the unbiased template (in the specific language, they are co-registers cross-sectionally). After the longitudinal process, each time point filename has the suffix '-long'. The output of the longitudinal pipeline allows the statistical comparison of volume and surface differences across groups.

In this analysis, the hippocampus subfields were extracted by using the developmental version of FreeSurfer. The advantages of this version (v6-dev-20180918) are less RAM memory requirement, the calculation of the amygdala nuclei, and the sub-division of the hippocampus in body head and tail (Iglesias et al., 2015). The use of longitudinal approach with FreeSurfer increases the robustness of the segmentation and the sensitivity in extracting sub-region volumes, and higher number of time-points whose MRI are considered help having a clearer idea of the neurodevelopmental changes in the hippocampus structural organization.

The HC volumes were extracted by using a pipeline, including all the steps necessary for the longitudinal pipeline:

1) cross-sectional 'recon-all' for each time point, and segmentation of the hippocampus cross-sectionally. Recon-all is the standard pre-processing step implemented in FreeSurfer, that runs all the cortical reconstruction process (Fischl 2012)
2) creation of the unbiased averaged template (base), which is the result of the average image of all the time points (Reuter and Fischl 2011), using the stable version of FreeSurfer (v6.0)
3) longitudinal recon-all and the segmentation of the hippocampus per each time point cross-sectionally. The developmental version calculates also the amygdala nuclei (which is subdivided into lateral, basal, accessory basal, central, medial, cortical and paralaminar nuclei, and cortico-amygdaloid transition and anterior amygdala areas), the brainstem and the sub-thalamic nuclei (Iglesias, Augustinack et al. 2015).

FreeSurfer was loaded on the high computing system available in Trinity College (https://www.tchpc.tcd.ie/resources/clusters/kelvin), as that would improve considerably the computational time. Part of the data set was run with single batch scripts for each time point, since /fresh was developed thereafter when part of the subjects had already been processed. The subjects were distributed into folders, with each folder containing 33 subjects with three time-points each. That helped in managing computational processes. The cross-sectional part was taking ~10 hours for each time point, while the creation of the base and the longitudinal recon-all took about ~18-20 hours per subjects. The computing time is strictly related to the pre-processing parameters, as well as the type of structural data used in the study.

The rest of the subjects was analysed by using the same pipeline, which was automated thanks to the collaboration of a computer scientist and few other scientists working in the Neuroscience department. This pipeline is available on GitHub (https://github.com/smcgrat/fresh/blob/master/fresh), and that took about 3 days of computing per subject. There were few technical problems during this step, either represented by missing output files, or lack of enough memory on the cluster. This was fixed repeating the segmentations for those scans that didn't work and requesting more disk space when necessary.

The output files have three suffices:

1) "HBT" to indicate the HC divided into head body and tail
2) "FS60" it mimics the segmentation of the stable version FS 6.0 (without the head and body)
3) "CA" to indicate the molecular layer is included in the nearest neighbour, and GC-ML-DG are included in cornu ammonis 4 (CA4)

3.2.3. Data Post-Processing

The next step was to extract the volume values for each subfield longitudinally, and this was done by using a script containing the bash function provided by the FreeSurfer webpage[1]:

```
quantifyHAsubregions.sh hippoSf <T1>-<analysisID>
<output_file> <OPTIONAL_SUBJECTS_DIR>
```

and

```
quantifyHAsubregions.sh amygNuc <T1>-<analysisID>
<output_file> <OPTIONAL_SUBJECTS_DIR>.
```

The first argument indicates the structure whose volume to extract, the second is the type of analysis done (in this study it is a longitudinal analysis, so 'T1.long' is used), the output file is the filename chosen (in .txt format), and finally the optional subject directory specifies the directory where the output data are stored. This script extracts and complies all the subfields volumes for each participant in one single spreadsheet, which was used for the statistical analysis. An additional column was added in the spreadsheet to indicate the estimated total intracranial volume (eTIV) at each time point that is part of FreeSurfer output. The eTIV resulted to be the same for all the three time points, as it is based on the average image calculated as base template.

To extract the subfields volume values at single time points, the function asegstats2table implemented on FreeSurfer was used. It works in the same way as 'quantifyHAsubregions.sh', but it can be used cross-sectionally or for single subjects, and it extract the volume values per each hemisphere.

[1] https://surfer.nmr.mgh.harvard.edu/fswiki/HippocampalSubfieldsAndNucleiOfAmygdala

3.2.4. Statistical Analysis

All the subfield values extracted from FreeSurfer were compiled in a spreadsheet. The data were inspected, checking for normality and potential outliers for each subfield. In case extreme outliers (values bigger than 3*inter-quartiles) were found, the single values were removed. Some subfields presented outliers more consistently than others across participants, for example fimbria and subiculum, but most of the population volumes fell into the 95% CI. The two groups were gender-matched (chi-square $\chi 2 = 0.4$). The statistical analysis was divided into two parts. The first analysis explored between-group differences of each HC subfield at baseline (Low vs High stress). The second analysis investigated the relationship over time between the level of stress experienced across the first two time points and the potential changes in the hippocampus subfields.

3.2.4.1. Cross-Sectional Analysis

All the participants chosen for this study were considered for the analysis (n=329). ANCOVAs were ran in SPSS (IBM, v24.0). Each subfield was considered as a dependent variable, and the effect of stress level as group factor. Covariates of interest were gender, age, PDS and SES (these last two were first standardized) and centre (after being dummy coded). Within-group Pearson's linear correlation was run between each hippocampus subfield and the standardized score of Neuroticism from the Neo-Five Factor Inventory (McCrae and John 1992), to investigate if the relationship between the level of Neuroticism and the volume of the hippocampus subfields is affected by the severity of stress experienced. Neuroticism is a personality trait related to emotional stability and response to adverse situation. In fact, when people present high level of

Neuroticism, their response to stressors influences the interpretation of ordinary situations as threatening and more difficult. Each item is scored on 5 levels of Likert-type scale (from 'strongly disagree' to 'strongly agree').

3.2.4.2. Longitudinal Analysis

In the longitudinal analysis, five participants (two in the Low stress and three in the High stress) were removed as their LEQ scores at time point 2 were missing. Demographic information of both time points is shown in Table 3.2.

N=323	Baseline		Follow-up 2	
	Low	High	Low	High
n	205	118	205	118
Age (years)	14.5 ± .46	14.41 ± .480	19.04 ± .871	18.90 ± .778
Gender	F= 113	F= 72	F= 113	F= 72
	M= 92	M= 46	M= 92	M= 46
NLEs score (LEQ)	4.31 ± 2.065	10.64 ± 2.772	7.35 ± 3.274	15.59 ± 4.303
Nr NLEs (LEQ)	3.16 ± 1.396	7.40 ± 1.391	6.009 ± 2.483	11.47 ± 2.806

Table 3.2: Demographic information of participants belonging to the baseline and Follow-up 2. For each time point, information is reported for each sub-group (Low and High stress). For age, total number of negative events, total score of NLE, values are reported

For the longitudinal analysis, R and the package 'lme4' were chosen to run a linear mixed model (LME) with a maximum likelihood (ML) method. Data were organized in spreadsheets with the 'long' format, indicating the three time points as a "repeated" measure for each subject. The LME model was chosen because it deals with missing values and it does not assume independence between time points and variables. In this analysis, the stress level based on baseline was

considered as a grouping criterion. The aim was to explore if, starting from the level of stress at baseline, the increase of total stress score at the second time point affected the volume of hippocampus subfields over time..

The question of interest was to explore within-group longitudinal changes of the hippocampus subfields in adolescents with stress over time. The time different between the first two time points was of approximately 5 years. In the linear mixed model, an outcome is predicted from fixed components, random components, and error. Estimates are the fixed-effect parameters that describe the population mean behaviour at each level of the fixed factor. Random effects define the subject-specific intercepts in the model, explaining a specific effect for the "random" sample considered. The random intercept accounts for the non-independence of measures from the same participant. Maximum likelihood (ML) estimation methods with Satterthwaite approximations were used to compute degrees of freedom employed on each general linear mixed model (Luke 2017). The interaction between increase of the total stress scores and time points was used as fixed factor, and random intercept was chosen as random factor. Age, gender, centre and estimated intracranial volume were used as nuisance covariates. Age, LEQ, eTIV were scaled before putting them in the model. Outliers were removed by inspecting each dependent variable and taking out the values that were higher than three times the inter-quartile.

The longitudinal analysis was run only on the hippocampus subfields that were shown to be more affected by traumatic and stressful experiences or in major depressive disorder during adolescence (Teicher, Anderson et al. 2012, Huang, Coupland et al. 2013, Tannous, Amaral-Silva et al. 2018, Malhi, Das et al. 2019, Postel, Viard et al. 2019). The subfields chosen were hippocampal tail and body,

subiculum (divided into head and body), CA1/3/4 (divided into head and body) granular and molecular layer of the dentate gyrus (GC-ML-DG) (divided into head and body) and the whole hippocampus. Since the hippocampus shows that structural maturation could be different across the two hemispheres (Zach, Vales et al. 2016, Guadalupe, Mathias et al. 2017), the subfields for both left and right side were analysed.

3.3. Results

3.3.1. Cross-Sectional Analysis

3.3.1.1. Between-Group Differences in Hippocampal Subfields

The results from the ANCOVAs showed a stress effect on the left fimbria (p= 0.009 unc), the right granule cell and molecular layer of the dentate gyrus (ML-DG) head (p= 0.047, unc) as well as in the right head of cornu ammonis (CA)3 (p=0.042, unc), represented by a decrease of the volumes in the High stress group (Table 3.3). P-values were corrected for multiple comparisons by using the function ‘p-adjust (method=fdr)’ in RStudio (Version 1.1.423). None of the results obtained survived correction (all $p_{corr} > 0.05$).

l_Hippocampal_tail	.967	r_Hippocampal_tail	.677
l_subiculum_body	.713	r_subiculum_body	.449
l_CA1_body	.338	r_CA1_body	.802
l_subiculum_head	.229	r_subiculum_head	.878
l_hippocampal_fissure	.909	r_hippocampal_fissure	.068
l_presubiculum_head	.423	r_presubiculum_head	.697
l_CA1_head	.057	rCA1_head	.401
l_presubiculum_body	.985	r_presubiculum_body	.338
l_parasubiculum	.556	r_parasubiculum	.768
l_molecular_layer_HP_head	.131	r_molecular_layer_HPhead	.458
l_molecular_layer_HP_body	.443	r_molecular_layer_HP_body	.911
l_GC_ML_DG_head	.062	rGC_ML_DG_head	.047*
l_CA3_body	.776	rCA3_body	.882
l_GC_ML_DG_body	.416	rGC_ML_DG_body	.959
l_CA4_head	.096	rCA4_head	.058
l_CA4_body	.534	rCA4_body	.847
l_fimbria	.009*	r_fimbria	.147
l_CA3_head	.266	rCA3_head	.042*
l_HATA	.289	rHATA	.278
l_Whole_hippocampal_body	.835	r_Whole_hippocampal_body	.645
l_Whole_hippocampal_head	.107	r_Whole_hippocampal_head	.293
l_Whole_hippocampus	.319	r_Whole_hippocampus	.386

Table 3.3: Uncorrected p-values of between-group differences in hippocampus subfields at baseline

3.3.1.2. Correlation Between Neuroticism and Hippocampal Subfields

Within-group linear correlations showed a negative relationship between Neuroticism and hippocampal subfields, mostly in the left hemisphere of the High stress group. Higher levels of Neuroticism were associated with decreased volume of the head of the left subiculum (r = -.264), the head of the cornu ammonis 1 (r= -.270), the molecular layer of the head of the hippocampus (r = -.241), the fimbria (r= -.238) and the head of the whole hippocampus (r=-.245). All correlation coefficients were FDR corrected for multiple comparisons at the level of each hemisphere, showing a corrected p-value < 0.05 (p= .0396). In Figure 3.3 correlation graphs between two hippocampus subfields (i.e. subiculum and hippocampal head) and Neuroticism are shown. Correlation plots between Neuroticism and the other subfields can be found in Appendix B.

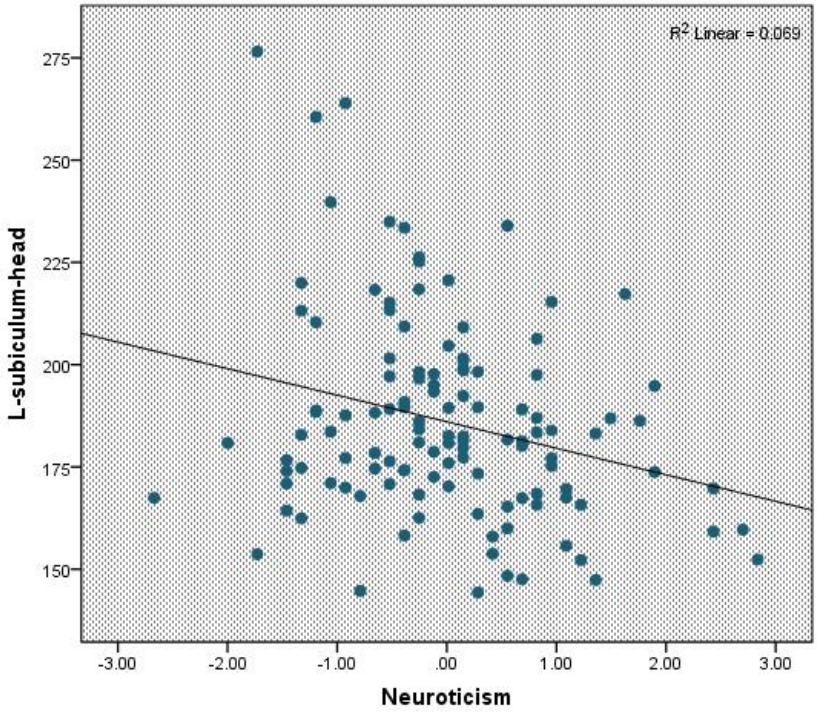

a)

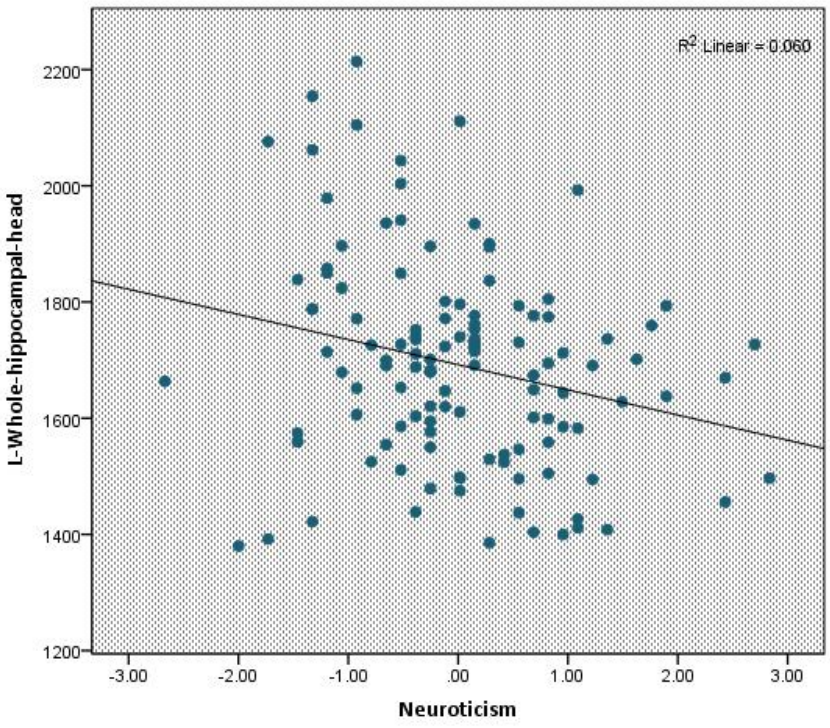

b)

Figure 3.3: Negative relationship between Neuroticism and a) the left subiculum and b) the whole hippocampal head in High stress group

3.3.2. Longitudinal Analysis Results

In the High stress group, uncorrected p-values showed that stress was a predictor of decrease in the volume of the left granular molecular layer of the dentate gyrus body (p= 0.02, unc), body of cornu ammonis 4 (p=0.042, unc), as well as an increase of the subiculum body (p=0.045, unc). None of the observed effects survived correction for multiple comparisons. The right hemisphere did not show such effect. In the Low stress group, the right hemisphere show stress was associated to a decrease the subiculum volume over time (p= 0.0412, unc), and an increasing of the volume in the hippocampal tail (p=0.037, unc), but even in this case the effect disappeared when correcting for FDR. Uncorrected p-values are shown in Appendix B - Table 2.

3.4. Discussion

The aim of this of this study was to investigate changes in the volumetric changes in the hippocampal structures with the effect of stress. The first part of the statistical analysis was focused on potential between-group volumetric alterations of the hippocampus subfields in adolescents divided according to their level of stress perceived in life (Low vs High). Furthermore, association between changes in volume and the level of neuroticism was also part of the analysis. Results showed no between-group differences in any of the subfields after correcting for multiple comparisons. A negative correlation was found between scores of Neuroticism and the head of the left subiculum, the cornu ammonis 1 (CA1), fimbria, the molecular layer (ML) of the hippocampus head, and the head of the whole hippocampus.

The second part of the analysis was exploring the effect of stress over time on the hippocampus subfields known to be affected by stress-related disorders and depressive symptoms in participants who were defined as part of Low or High stress group at baseline. To carry out the longitudinal part, the hippocampus subfields were obtained by using an automated segmentation method implemented in FreeSurfer (v6.0), which created a within-subject template based on the number of time points considered. The level of stress was defined by looking at the total score of the LEQ across baseline and the second time point. Even if there were subfields alterations associated to the level of stress across time in both hemispheres, such effect disappeared after correction for multiple comparison.

Most of the studies on hippocampus subfields changes showed volumetric alterations in adolescents who experienced childhood maltreatment and trauma (Carrion and Wong 2012, Teicher, Anderson et al. 2012, Kuhlman, Geiss et al. 2018), as well as suffering of PTSD and major depressive disorder (Bremner, Narayan et al. 2000, Gerritsen, van Velzen et al. 2015, Chen, Sun et al. 2018, Postel, Viard et al. 2019). Results in this study may reflect the type of population considered. In fact, the participants of this research did not suffer of any mood or emotion-related disorder. They were healthy adolescents who experienced negative life events, but that did not report any cognitive or psychiatric disorder at the time they were screened. The subfields shown in this study to be affected with stress before correcting for multiple comparisons are the same found to be structurally altered in mood disorders (Cao, Passos et al. 2017), anxiety (Chen, Chen et al. 2018), major depressive disorder (Roddy, Farrell et al. 2019) and PTSD (Postel, Viard et al. 2019). This could represent a factor explaining the lack

of significant changes in the hippocampal subfields, as well as that the perception of stress is not an aggravating factor triggering atrophic processes, but that a more severe, or persistent overtime, emotional offense causes alterations in the volume of structures related to emotions and behavioural responses in adolescents.

Findings show a significant negative relationship between the volume of the hippocampal subfields and the level of neuroticism in adolescents who perceived higher levels of stress at baseline. This result is the opposite of what was found in another study (Gray, Owens et al. 2018), where no association between neuroticism and morphological changes in the hippocampus and amygdala were seen. Neuroticism is the tendency of worrying and being anxious that leads to unbalanced emotional behaviours in relation to life events (Tzschoppe, Nees et al. 2014), representing a potential cause of the development of chronic mood disorders. Neuroticism has been associated to influence fear response, anticipation of aversive stimuli and emotional regulations (Servaas, van der Velde et al. 2013), which are cognitive processes that are particularly enhanced during adolescence.

Literature on changes of volume in the hippocampus subfields is not homogeneous in the results. This is mainly due to the choice of the subfield's segmentation, the number of subfields chosen, and the statistical model performed. In this study, a linear mixed model was used to account for the longitudinal data, and for the variance across participants due to factors, such as the different centre were the scans were obtained, which can influence, at least partly, the segmentation of the hippocampal structures. The choice of the number of time points to create the within-subject template is another factor to consider

when results are interpreted. In this study, three time points were used to improve the definition of the subfields, but the cognitive measures for the last time point were consistently missing, due to the fact data acquisition is currently still going on. That led to run the statistical analysis only on the first two time points, which was a limitation for this study, since that did not make possible to explore the effect of stress across all the three stages of adolescence.

Future directions will include gathering the missing information and replicate the same statistical model. In this explorative analysis, results did not show any association of the hippocampal subfields across two stages of adolescence by considering the score of stressful events. An alternative approach could be considering other cognitive measures to define stress levels, or different grouping criteria for the participants. First, further analyses will investigate how the participants' level of stress changes across time, i.e. some of the adolescents being categorized as Low stress at baseline could have scored a higher level of stress at the second time point, hence would be defined as High stress, and the groups size would change. Another interesting approach to answer the question of what happens in the hippocampus sub-structures when adolescents experience traumatic events could be not only look more broadly at the stress component, but also taking into account the development of depressive symptoms in adolescents and how they are related to alterations in the sub-cortical structures related to emotional processing. In fact, the tool in FreeSurfer used in this study performed also the segmentation of the amygdala nuclei, the thalamic nuclei and the brain stem, which are all part of limbic circuitry and responsible for the emotional and mood responses.

4. Microstructural Alteration of the Cingulum in Healthy Aging

4.1. Brain and Aging

In normal aging, structural and functional changes of the brain reflect cognitive decline in older people (Lockhart and DeCarli 2014). Several studies focused on age-related changes in the brain, comparing grey and white matter differences between young and old adults (DeCarli, Massaro et al. 2005, Sugiura 2016, Bajaj, Alkozei et al. 2017, Cole and Franke 2017), that help understanding what happens in the brain structure over time, and which are the brain areas more affected during this period of life. Such knowledge is important to identify the relationship between anatomical changes and cognitive decline (Fan, Fang et al. 2019) and to help individuals at risk of developing neurodegenerative diseases (Lockhart and DeCarli 2014).

4.1.1. Age-Related Changes in Grey Matter

A key study on age-related volumetric changes (DeCarli, Massaro et al. 2005) considered more than 2000 MRI of people from 34 to 97 years old, and showed that the most affected brain areas with aging were in the frontal lobe, with a decrease of volume of 12%, followed by the temporal lobe, with a decrease of 9%. Other studies focusing on regional changes found grey matter atrophy in the hippocampus, parahippocampal gyrus, amygdala and insula, that are involved in the limbic system. Additional regions structurally affected with aging were temporal gyrus, precuneus, cingulate gyrus, orbital and superior medial frontal

lobe, fusiform gyrus, inferior and middle occipital gyrus, bilateral putamen, pallidum, thalamus in both hemispheres (Li, Wang et al. 2016) and the cerebellum cortex (Lockhart and DeCarli 2014). In particular, hippocampus head and body were found to be among those regions used to discriminate old people who will develop mild cognitive impairment (MCI) from people who will not, along with the entorhinal cortex, all located in the medial temporal lobe (Martin, Smith et al. 2010).

Another study investigating longitudinal WM and GM changes across lifespan showed an accelerated GM atrophy in the lateral, medial frontal and anterior cingulate cortex, during two specific age ranges, that are between 20 and 40 years of age, and after 60 years of age (Pfefferbaum, Rohlfing et al. 2013). Hippocampus volume decreases were also found with aging, especially in people older than 60 years old, when the level of atrophy was accelerated and correlated with the cognitive impairment.

4.1.2. Age-Related Changes in White Matter

White matter increases until 40 years old of age (Lockhart and DeCarli 2014), and then it starts decreasing approximately after 50 years of age (Gunning-Dixon, Brickman et al. 2009). Alterations in the microstructural integrity of WM tracts are usually investigated with diffusion imaging (DWI), by detecting differences in the diffusivity measures, which describe myelination processes and axonal “health” (Gunbey, Ercan et al. 2014). Diffusivity measures are described later in this chapter. Studies showed WM age-related changes in tracts involved in both emotional processing and memory retrieval, namely the genu of the corpus callosum (Smith 2012), the cingulum, the fornix, the superior and inferior

longitudinal fasciculus, fronto-occipital fasciculus and uncinate fasciculus. Such changes are represented by decreases of FA and increase of mean (MD) and radial diffusivity (RD) (Stadlbauer, Salomonowitz et al. 2008, Gunbey, Ercan et al. 2014, Lockhart and DeCarli 2014, Bajaj, Alkozei et al. 2017), that can indicate axonal damage or myelination alterations due to aging processes (Aung, Mar et al. 2013). Other studies confirmed a negative relationship between age and FA of the left hippocampus and fornix (Stadlbauer, Salomonowitz et al. 2008, Gunbey, Ercan et al. 2014, Christiansen, Aggleton et al. 2016), and an increase of MD in the left hippocampus (Gunbey, Ercan et al. 2014).

4.1.3. Age-Related Changes in Brain Connectivity

Studies showed aging has an impact on brain networks. Alterations in the limbic-diencephalic network, formed by the medial temporal lobe, the posterior cingulate, the anterior thalamus and mammillary bodies, were associated to early AD-related symptoms and memory impairment (Acosta-Cabronero and Nestor 2014). The thalamus has been found to be connected to many cortical areas involved in limbic system, and it has a critical role in the fronto-limbic circuitry as bridge between tracts connecting parts of the limbic system. In the normal memory functioning, the mammillo-thalamic tracts (MTT) are connected to the amygdala and hippocampus through the fornix (Kamali, Yousem et al. 2015), and such interaction is pivotal for emotional memory processes.

Throughout adulthood, not all the networks change in the same way with age. One study where the brain was divided into several networks (network 1: visual network, network 2: somatomotor network, network 3: dorsal attention network, network 4: ventral attention network, network 5: limbic network, network 6: fronto-

parietal network and network 7: default mode network) investigated associations between each network and age (Bajaj, Alkozei et al. 2017). Results showed age was negatively correlated to the cortical thickness of all the networks considered, except for the limbic network, suggesting the limbic network might resist structural alterations with aging. Such findings might be explained by the increased level of resilience seen in older people (Sampedro-Piquero, Alvarez-Suarez et al. 2018), reflected by the way they respond to negative situations (Mather 2012).

4.1.4. Age-Related Changes in Neurotransmission

Dopamine (DA) is a neurotransmitter involved in reward, motivation and in the so-called “positive stress”. The dopaminergic innervation starts from the ventral tegmental area (VTA) and substantia nigra, and it reaches the amygdala, the hippocampus, and prefrontal areas. In the hippocampus (where the dopaminergic neurons are mostly found), the dopamine arrives in the CA1-subiculum subfields (Barili, De Carolis et al. 1998), where regulates and modulates learning and memory processes. For example, the hippocampus controls, in an excitatory/inhibitory effect, the neural activity of the nucleus accumbens and VTA through the prefrontal cortex, regulating functions as spatial working memory (Thurm, Schuck et al. 2016). Alterations of these circuits are thought to cause neurodegenerative and neuropsychiatric disease, such as Parkinson’s disease or schizophrenia, which present imbalances of dopaminergic neurotransmission. Dopaminergic neurons and transporters decrease in density during aging, leading to a decline in executive functions in elderly people, not only related to motor skills, but also episodic memory, visual skills and attention levels (Bäckman and Farde 2001). Literature shows that

during normal aging the number of dopamine receptors decreases in the striatum, frontal and temporal regions, hippocampus and thalamus of about 4-10% per year after 20 years of age (Rollo 2009). There is also a genetic relationship between dopaminergic system efficiency and cognitive abilities, that is more evident in late than early life, suggesting a strong influence of genetics in the dopamine-related decline (Morcom, Bullmore et al. 2010).

4.2. Diffusion Imaging

Diffusion imaging is a neuroimaging technique that measures the movement of water particles in biological tissues and in vivo. Particles usually have an isotropy diffusion, meaning they are free to move in whichever direction they flow. This type of diffusivity is represented by a spherical shape (Assaf and Pasternak 2008). In the axons, nevertheless, there are myelin sheaths that limit the free diffusion of the water molecules, so that in the axons there is a preferred direction. This type of diffusivity is defined anisotropic, and the diffusion of water molecules reaches a shape of ellipsoid, i.e. stretched out circle. The ellipsoid itself has a principal long axis and then two more small axes that describe its width and depth. All three of these are perpendicular to each other and cross at the centre point of the ellipsoid. The axes are called *eigenvectors* and the measures of their length are defined *eigenvalues*. In each voxel the preferred direction of the water molecules is estimated, and a change of diffusion direction can indicate a microstructural damage in that specific voxel (Aung, Mar et al. 2013).

The diffusion of water in the biological tissues refers to the microstructural compositions of neurons; a water molecule has a flow of 60 μm in 1 second. The water diffusion in the axons is influenced by several factors, such as temperature,

membrane permeability, cellular dimensions, anisotropy level, chemical composition of the tissue (Bammer 2003). MRI is the only imaging technique that can give information about the water flow in a non-invasive way and in-vivo. Changes in this diffusion helps understanding possible alterations in the microstructural composition of white matter, which indicate an axonal damage or neurodegeneration (Le Bihan, Mangin et al. 2001). The molecules of water in the tissues are in constant movement and moving towards dis-homogeneous magnetic fields (generated by the resonance gradients) obtain a phase or direction change, which is responsible of the attenuation of the signal. That's why we can obtain images where the contrast is determined by the diffusion coefficient of the water.

The acquisition of diffusion images is based on the EPI, rapid sequences that produce images with high matrix in few seconds (Taylor, Alhamud et al. 2016). Usually in EPI acquisition the matrix size is reduced and it is 64x64, instead of the full matrix 128x128 (Assaf and Pasternak 2008).The first gradient causes a small distortion of the main magnetic field (B0), so that the frequencies of hydrogen nuclei are diphasic. The impulse of 180° has the effect of rotating the vector representing each spin of 180°, so that the next gradient brings the spins back to the phase. This happens for the nuclei H that are bound to macromolecules; for this type of nuclei that are not moving along a direction of the gradient, the effect of the second impulse dephasing nullifies the one created by the first one and there is no signal attenuation. If the nuclei move in a casual way (isotropic diffusion), every nuclear spin undergoes a magnetic field that has different intensity during the second pulse. This results in a different intensity of the signal, where the areas with high diffusion are less bright than areas with low

diffusion, i.e. the intensity of the signal is inverse proportional to the molecule movement (Le Bihan, Mangin et al. 2001).

The signal depends on the proton movement but also on the gradient of the magnetic field, defined b-value, which can be defined as the diffusion sensitizing factor. Since the diffusion coefficient can be affected and influenced by other physiological noise (such as breathing, or capillary perfusion) the parameter that is measured in diffusion imaging is called Apparent Diffusion Coefficient (ADC), which is measured in mm^2/sec. The diffusion in the axons is constrained by the myelin sheaths that form axons. The longer is the time of diffusion, the bigger is the distance that the water molecules can achieve, meaning that they have higher chance of meeting a barrier during their diffusion which can underestimate the calculation of ADC (Bammer 2003). Therefore, to get a higher sensitivity of the sequence to the diffusion, the b-value should be increased allowing a better image quality and estimation of the ADC. The ideal b-value is the one which can separate healthy tissue from a damaged one, and it is usually higher than 800 mm^2/sec. The higher the value of ADC is, the less bright the images appear (McKinnon, Jensen et al. 2017).

In a homogenous medium the diffusion is usually casual, defined isotropic; in a biological tissue, the diffusion is constrained by cellular and extra-cellular structures. In the brain, the grey matter presents an isotropic diffusion, whereas in the white matter the diffusion is related to the different orientation of the myelin pathways, that determine the diffusion direction. The myelin sheaths represent barriers that cause water molecule to diffuse along a preferred direction along the main axis of diffusion, making the diffusion anisotropic (Assaf and Pasternak 2008). The movement of the water molecules is facilitated when they diffuse

parallel to the main axis of the axons, while it is constrained when the water molecule move perpendicularly to the main axis (Le Bihan, Mangin et al. 2001).

4.2.1. Diffusion Tensor Imaging

Diffusion tensor imaging (DTI) is a specific approach of DWI, used to graphically represent WM fibre shape, geometry and pathways of the brain. It is also used to describe anatomical connections between two different regions of the brain. Different gradients of magnetic fields are applied to calculate the direction in each voxel, and at least 6 different gradients are needed to get a DTI image, and then an algorithm calculates the main direction in that voxel. A colour-map of the tract is generated, and different diffusion directions are indicated with different colours: red (left-right), green (anterior-posterior) and blue (inferior-superior). The diffusivity measures are extracted to measure the integrity of the fibres and the diffusivity properties (Shaikh, Kumar et al. 2018).

Diffusion tensor is a mathematical model that allows the estimation of the direction and intensity of the local diffusion in non-isotropic structures, and it is determined mainly by the water diffusion in the tissue. The tensor is based on using multiple gradients, along six different axes, which maximises the effect of anisotropy (Basser and Jones 2002). This model allows reaching values close to the mission of the absolute diffusion and allows evaluating the changes of the tissue microstructures between different subjects. In the image acquisition with the tensor model, the brain regions with isotropic diffusion look dark, while the areas with anisotropic diffusion are brighter. The ellipsoid shape and orientation are determined by three eigenvalues, $\lambda 1$, $\lambda 2$, and $\lambda 3$, and three eigenvectors, v1, v2 and v3, reflecting the magnitude and directions of the three major planes of

the diffusion ellipsoid. With DTI, the tensor is calculated at each pixel location, creating a map of diffusion that shows the magnitude and the main direction of the process (Shaikh, Kumar et al. 2018).

4.2.2. Tractography

Tractography is a method generates 3D representations of white matter tracts (Ciccarelli et al., 2008). The diffusion tensor gives two important pieces of information in each imaging voxel, which are the magnitude of diffusion anisotropy and the orientation of the maximum diffusion. Tractography algorithms use this information to track the whole white matter pathway by inferring the continuity of fibre paths from voxel to voxel (Mori et al., 2002), that is, the direction of maximum diffusion in a voxel is followed into an adjacent voxel. If the angle between the two directions is less than a predetermined angle, then the two voxels are connected, and the process is repeated to proceed the pathway (streamline) through the white matter in the brain image. However, if the angle between maximum diffusion directions is greater than the chosen threshold, the streamline is terminated at that point (Shaikh, Kumar et al. 2018). Tractography uses this information about orientation to reconstruct pathways through the eigenvector field. This is usually achieved by linking eigenvectors that have similar orientation such that the angle between them is less than a given threshold (Basser and Jones 2002). There is, then, the ‘anisotropy threshold’ that ensures the streamlines advances only if the anisotropy in each voxel is higher than a pre-determined threshold (Ciccarelli et al., 2008).

4.2.3. Constrained Spherical Deconvolution (CSD)

One big DTI limitation is that, even if it is growing as technique in the field, it is partially incomplete assuming of a single Gaussian diffusing component in each voxel. A single tensor cannot, in fact, capture the complex orientation structure present in heterogeneous tissue, for example in regions where white matter fibre bundles cross (Tournier et al., 2004). To solve this DTI limitation, an alternative method is constrained spherical deconvolution (CSD). CSD is based on high-angular resolution diffusion imaging (HARDI) and it is good in reconstructing the fibre orientation distribution (FOD) functions with remarkable reduced noise sensitivity (Tournier et al., 2007). Fibres orientation presents a coloured map: red (right/left), blue (superior/inferior) and green (anterior/posterior). Usually DTI studies have a b-value between 500 and 1200sec/mm^2, while CSD approach demands a higher b-value. The downside of choosing a higher b-value is the higher chance of obtaining a larger signal-to-noise ratio (SNR) (Burdette et al., 2001), which makes images “noisier”. The CSD method has significant advantages over a DTI-based approach, primarily a more accurate segmentation of tracts and the reconstruction of the original fibre orientation. An advantage of CSD is also there is no need to make any *a priori* assumption about the fibre populations, as required in the DTI-model (Tournier et al., 2004). The DTI model can create artefacts when there are more than two different fibre populations in the same voxel, whereas the CSD approach reconstructs the fibre orientation with more than two fibre populations and solves for the intravoxel fibre orientation (Jeurissen et al., 2011). Finally, one of the CSD approach assumptions is that the response function seen for a certain fibre population orientation is constant throughout the brain. This may change in WM structures where there are different

diffusion characteristics, for example in fibre populations with different myelination levels or axonal densities. In these cases, the response function would change the anisotropy of a small percentage, but the results would be still reliable and the fibres orientation would be still preserved (Tournier et al., 2004).

4.2.4. Atlas Based Tractography (ABT) approach

In this study, an atlas-based tractography was the method used to compute the white matter tracts between the two groups. This is a technique useful to calculate the same tract across participants, but a disadvantage of such method is represented by alignment errors between subjects belonging to different groups, or between healthy and diseased brains. Additionally, the inter-subject variability can also produce misleading results in the application to patients (Preti et al., 2012). ABT is a tool included in ExploreDTI, that adjusts ROIs drawn for a template (that can be a subject picked randomly or the averaged structural image of all the scans) to all the subjects' images. The template must match at least partially with the shape of the brain, and in case of patients' brain, it is important to consider the structural alterations that their brains may have.

4.2.5. Diffusivity Measures

In diffusion imaging, it is possible to quantify the diffusion by extracting diffusivity measures related to the water particles movement. These are the fractional anisotropy (FA), the mean diffusivity (MD), the radial and axial diffusivity (RD and AD) (Thomas, Sadeghi et al. 2018). All these values are based on the eigenvalues, which represent the magnitude of the diffusion process (see Figure 4.1).

The FA measures the level of anisotropy of the water molecule in each voxel, the MD is the average of all the diffusivity directions along the axon, the RD describes the diffusivity perpendicularly to the main axis of the axon, whereas AD is the diffusivity parallel to the main axis. The sum of radial and axial diffusivities represents the mean diffusivity, which is known also as the apparent diffusion coefficient (ADC) (Bammer 2003). The FA formula is:

$$FA = \sqrt{\frac{1}{2}} \frac{\sqrt{(\lambda 1 - \lambda 2)^2 + (\lambda 2 - \lambda 3)^2 + (\lambda 3 - \lambda 1)^2}}{\sqrt{\lambda_1^2 + \lambda_2^2 + \lambda_3^2}}$$

The eigenvalues in the formula are tightly linked to the eigenvectors of the ellipsoid, with the major axes and two minors. FA indicates the direction selectivity and it is higher in more organized white matter regions. Indeed, it has been demonstrated that the higher is FA, the healthier is the WM tract measured (Greicius et al., 2009). The FA range goes from 0 (isotropic diffusion) and 1 (anisotropic diffusion). FA decreases due to the loss of coherence in the main preferred diffusion direction, which can occur in brain injury, neurodegeneration and neurological trauma. Studies showed vastly how fractional anisotropy decreases in normal aging, neuropsychiatric disorders and neurodegenerative diseases (Catheline, Periot et al. 2010, Teipel, Walter et al. 2014, Daianu, Mendez et al. 2016, Sibilia, Kehoe et al. 2017). Such decrease reflects the loss of anisotropy in the damaged connections, i.e. loss of diffusion coherence.

MD is calculated by the mean of the three eigenvalues and corresponds to the molecular diffusion rate, reflecting the average magnitude of molecular displacement by diffusion. The higher is MD, the more isotropic is the diffusion (Assaf and Pasternak 2008); it is generally low in healthy tracts, starting to

increase during neurodegeneration. White matter changes may precede grey matter atrophy in some regions of the cortex, such as loss of tracts connecting frontal regions to the temporal lobe, through the cingulum which contains fibres of different length and connections to all the lobes (Catani et al., 2008). The mathematical formulas of the diffusivity measures are represented by the eigenvectors:

$$Axial\ Diffusivity\ (AD)\ =\ \lambda 1$$

$$Radial\ Diffusivity\ (RD)\ =\ \frac{\lambda 1 + \lambda 2}{2}$$

$$Mean\ Diffussivity\ (MD)\ =\ \frac{\lambda 1 + \lambda 2 + \lambda 3}{3}$$

Changes in the axonal diameters or density may also influence RD, which represents the average of the two shorter eigenvectors and increases in WM with demyelination (Westin et al., 2002). On the other hand, AD has been reported to increase with brain maturation, representing the longest eigenvector.

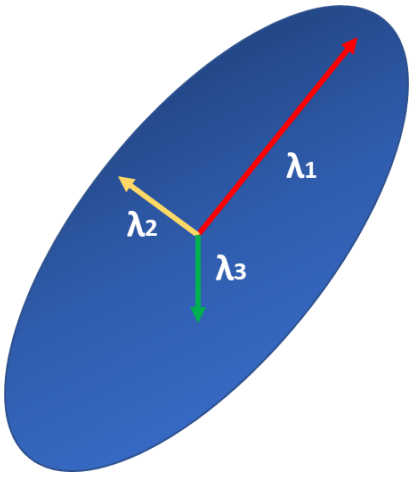

Figure 4.1: Eigenvectors that diffusivity measures AD, RD and MD are based on

The results of this study have been published on a scientific journal (Sibilia, Kehoe et al. 2017), reference: Sibilia, F., Kehoe, E. G., Farrell, D., Kerskens, C., O'Neill, D., McNulty, J. P., Mullins, P., Bokde, A. L. W. (2017). Aging-Related Microstructural Alterations Along the Length of the Cingulum Bundle. Brain Connect, 7(6), 366-372. doi:10.1089/brain.2017.0493. The entire manuscript is part of this thesis and it can be found below.

Further results that are not present in the attached manuscript can be found in Appendix C.

4.3. Manuscript – Aging-Related Microstructural Alterations Along the Length of the Cingulum Bundle

4.3.1. Introduction

During the lifespan, the brain is subject to aging-related changes in volume, metabolism and cognition. White matter (WM) volume changes with an inverted U shape in relation to aging , increasing until age 40s (Peters 2006), followed by a plateau phase till age 60s, and start declining in older ages. Myelin sheaths deterioration leads to neural loss, decrease of fibre number and reduction of WM volume (Gunbey, Ercan et al. 2014), causing alterations in brain connections which underlie cognitive abilities.

The cingulum bundle (CB) is one of the most prominent fibre bundles in the brain, going from the anterior to the posterior part of the brain (Jones, Christiansen et al. 2013). It has short and long associative fibres populations, which connect different brain areas, including frontal, parietal and temporal regions (Catheline,

Periot et al. 2010); functionally, it is involved in attention, memory, problem solving, visual and spatial abilities, as well as in regulating heart rate and blood pressure (Gunbey, Ercan et al. 2014).

Previous studies have measured the changes in the CB integrity during aging, analysing the average value of the entire tract, not focusing on changes along the tract length (Sullivan and Pfefferbaum 2006, Jang, Kwon et al. 2016). Sullivan and Pfefferbaum (2006) proposed WM tracts integrity started decreasing in frontal circuits, describing an anteroposterior gradient, similar to the pattern of cognitive declines found in aging. Jang's study results (2016) supported this hypothesis; the authors divided the cingulum into five parts and observed a WM integrity decrease first in the anterior fibre branches.

Literature about WM changes during normal aging is not homogeneous, but a few studies reported no significant differences along the cingulum with healthy aging (Stadlbauer, Salomonowitz et al. 2008, Gunbey, Ercan et al. 2014). Stadlbauer et al. (2008) did not find any significant age-related modifications in the cingulum, either in the diffusivity parameters or in the number of fibres per voxel. Furthermore, Gunbey and colleagues (2014) subdivided the fornix, the cingulum and the parahippocampal gyrus, finding no FA changes in older healthy adults compared to younger people.

The studies mentioned above used a DTI-based approach, which presents limitations in brain areas with complex WM frameworks. In the present study, a constrained spherical deconvolution (CSD)-approach tractography (Jeurissen, Leemans et al. 2011) was chosen, as it allows a more accurate reconstruction of

fibre pathways and gives a higher sensitivity in identifying microstructural anomalies (Reijmer, Leemans et al. 2012).

The main hypothesis of this study was that aging lead to decreased structural integrity of the cingulum compared to healthy young group. The cingulum was divided in three segments, based on a ROI-based methodological approach (Jones, Christiansen et al. 2013). The methodological novelty of this study was the along-tract analysis for each branch of the cingulum to locate the structural changes with aging, as well as segmenting each individual branch.

4.3.2. Material and Methods

4.3.2.1. Participants

35 healthy young adults (22.3 ± 2.7 years) and 33 healthy older people (69.5 ± 3.5 years) were recruited through online advertisement. Demographic information is presented in Table 4.1. Each participant went through neuropsychological tests and an MRI scan. The study had approval from the Research Ethics Committee of the Adelaide and Meath Hospital, incorporating the National Children's Hospital, and St. James Hospital. All participants gave written informed consent before taking part in the study.

Group		Young	Old	p-value
Gender	**M**	16	17	p=0.638
	F	19	16	
Age		22.3 ± 2.7	69.5 ± 3.5	p<0.001
NART		117.27±4.7	114.5 ± 7.8	p=0.09
Education (n. of yrs)		17.1 ± 2	13.8 ± 3.7	p<0.001
MMSE		n/a	28.8 ± 0.9	

Table 4.1: Demographic characteristics of participants

4.3.2.2. Neuropsychological Testing

The neuropsychological tests that participants underwent were the Beck's Depression Inventory II (BDI-II) (Beck et al, 1996) and the NART (National Adult Reading Test, Nelson et al., 1982); the older group of participants underwent the CERAD (Consortium to Establish a Registry for Alzheimer's Disease (Morris, Mohs et al. 1988) and the MMSE (Mini Mental State Examination (Folstein, Folstein et al. 1975), in order to exclude any possible cognitive impairment. The scores in each sub-test of the CERAD were within 1.5 standard deviation of the age-corrected norms, and the scores in the BDI were below 14, as participants did not show any significant depressive symptoms (scores from 0 to 13 indicate minimal depression).

Both groups performed the CANTAB (Cambridge Neuropsychological Test Automated Battery (Sahakian, Morris et al. 1988)), a computerized group of cognitive tests. Three different tests from the CANTAB were included: (a)

learning of abstract images (immediate recognition and delayed recognition tests), (b) paired associate learning (PAL), and (c) spatial working memory (SWM). The learning task used was the Pattern Recognition Memory (PRM), which is a test of visual pattern recognition memory in a 2-choice forced discrimination paradigm. The PAL assesses episodic memory and new learning; it has twenty-one outcome measures, covering the errors made by the participant, the number of trials required to locate the pattern(s) correctly, memory scores and stages completed. Lastly, the spatial working memory task had different levels of difficulty. These tests were chosen above others because, among all the CANTAB tests, these were specifically used to diagnose mild cognitive impairment (MCI); in fact, part of the Neuroskill dataset was represented by MCI patients, not considered in this study. The scores were normalized accounting for age and gender of the participant and included in the analysis (Table 4.2 includes group results): PRM initial standardized, PRM delay standardized, PAL Total Error Standard, PAL Total Error 6 Standardized (with errors recorded when there are 6 different patterns), SWM between-errors standardized and SWM Strategy Standardized.

CANTAB / GROUP	PRM initial standard	PRM-delayed standard	PAL total errors standard	PAL t.e. 6 shapes standard	SWM between errors standard	SWM strategy standard
Young	0.99± 0.58	-0.3 ± 1.4	0.05± 1.13	0.03 ± 1.0	-0.02 ± 0.9	0.3 ± 1.2
Old	0.7 ± 0.9	-1.5 ± 1.3	0.04± 1.15	0.1 ± 0.9	0.21 ± 0.8	-0.07 ± 0.9
p-value	p=0.208	p<0.001	p=0.963	p=0.753	p=0.275	p=0.126

Table 4.2: Standardized results from CANTAB test battery

4.3.2.3. MRI Scanning Protocol

Scanning was performed on a 3.0 Tesla Philips Achieva system (Best, The Netherlands) equipped with an eight-channel head coil. The diffusion weighted imaging (DWI) sequence was a whole-brain high angular resolution diffusion imaging (HARDI) acquired with a TR = 14,556 ms and TE = 81 ms. A parallel sensitivity encoding (SENSE) approach (Pruessmann, Weiger et al. 1999) with a reduction factor of 2 was used during the DWI acquisition. Single-shot spin echo-planar imaging (EPI) was used to acquire the DWI data with following parameters: matrix 112 x 112, isotropic voxel of 2 x 2 x 2 mm^3 and 60 slices, with 2 mm thickness, and no gap between the slices. Diffusion gradients were applied in 61 isotropically distributed orientations with b = 2000 s/mm^2, and four images with b = 0 s/mm^2 were acquired.

4.3.2.4. DTI Pre-Processing

The raw data were par/rec format that were converted to NIFTI format (using Chris Rorden's "dcm2nii" tool, and then read into ExploreDTI v4.8.4 (Leemans and Jeurissen, 2009), the software used for the preprocessing and analysis. Data quality control was assessed by checking for motion artifacts and image orientation; DWI images color maps and gradient components were also checked. Correction for head motion, eddy current (EC) and EPI distortion was performed thereafter. The data were corrected for distortions and head motion using an affine transformation to the non-diffusion-weighted images (Leemans and Jones 2009). For EPI susceptibility correction the T1-weighted anatomical image was co-registered to the diffusion image.

4.3.2.5. Tractography of the Cingulum

The cingulum segmentation was based on CSD-based (Jeurissen, Leemans et al. 2011) method. This approach has been chosen over a DTI-based one because it takes into account complex white matter orientation (Reijmer, Leemans et al. 2012). After the pre-processing, a CSD-whole brain tractography was performed. Each trajectory was followed until the direction of the pathway changed with an angle of more than 60°, that considers the shape of the fiber pathway. In this study, the cingulum was divided in three segments, namely subgenual, retrosplenial and parahippocampal branches, in both hemispheres. The segmentation of each tract was performed following an established method (Jones, Christiansen et al. 2013), with a modification in segmenting the parahippocampal subdivision, developed in our lab. Regions of interest (ROIs) were drawn on the subjects' native space to define each segment in the most accurate way. To get the fibers branches from each participant, an atlas-based tractography (ABT) approach was performed, based on the idea of drawing ROIs on a template and applying them on other participants' images after co-registration (Lebel, Walker et al. 2008). Two templates were picked to account for the anatomical variability in the two groups and to get an improved segmentation of the cingulum. It should be emphasized that the location of the ROIs was not different relative to the anatomical landmarks used to place them (described below).

4.3.2.6. Definition of ROIs

Figure 4.2 illustrates the location of the ROIs to segment the three branches of the cingulum (Jones, Christiansen et al. 2013). The first AND ROI of the

subgenual section was drawn five slices anterior the back of the curve of the genu and the second AND ROI was placed on the third/fourth coronal slice caudal to the most anterior part of the genu. A NOT gate was added on the same slice of the first AND gate. The retrosplenial branch was defined placing the first AND ROI five slices posterior the front of splenium, while the second AND gate was determined by finding the most ventral plane of splenium and identifying the horizontal section, that was three or four slices above the base of splenium (Jones, Christiansen et al. 2013). The parahippocampal branch was segmented by drawing the first AND gate in the same location as the second AND ROI in the retrosplenial tract; the second AND ROI was placed in the posterior part of the hippocampus. The first NOT gate was positioned above the body of the corpus callosum (Jones, Christiansen et al. 2013). A second NOT gate was placed 17 slices (~25 mm) posterior to the first one, to isolate the tract better. After performing ABT, output tracts from ExploreDTI were finally defined using additional NOT gates where necessary (see Figure 4.3).

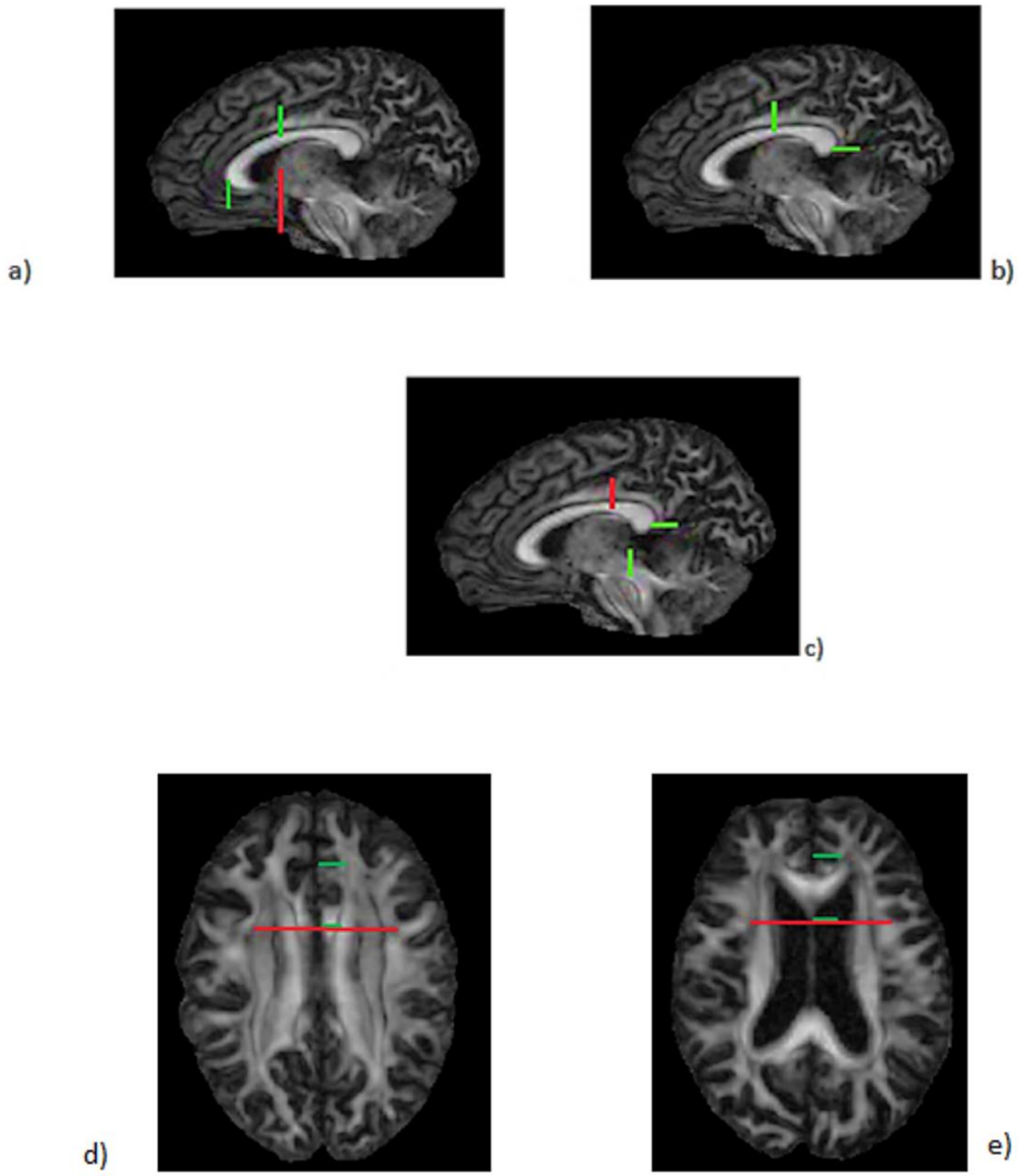

Figure 4.2: Definition of each cingulum segment: a) subgenual, b) retrosplenial and c) parahippocampal branches, sagittal view. Figures d) and e) show the location of ROIs on d) a young subject and e) an old healthy subject. The ventricular enlargement made impossible to use the same template for both groups in the ABT approach

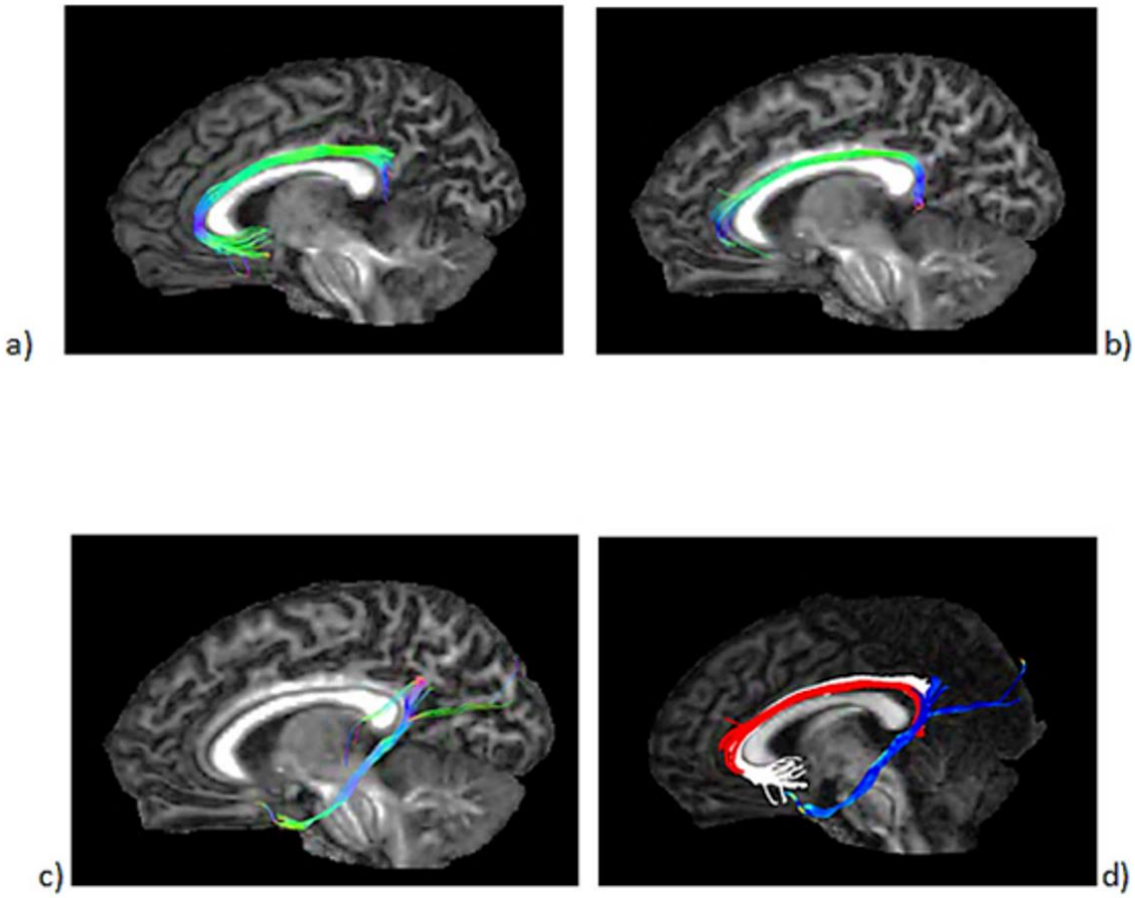

Figure 4.3: Output of the three different branches of the cingulum after ABT tractography. a) subgenual, b) retrosplenial and c) parahippocampal segment. d) the three segments with different colors (subgenual = white; retrosplenial = red; parahippocampal = blue).

4.3.2.7. Statistical Analysis

Data statistical analysis was performed using SPSS (SPSS Software 22, IBM). The variables were the DTI indexes, namely FA, MD, axial and radial diffusivity (AD and RD). The FA and diffusivity measures were analyzed by an along-tract analysis, which makes possible to determine WM structural variation along each point of the cingulum. It is an approach developed by Colby and colleagues (Colby, Soderberg et al. 2012), detecting within-tract heterogeneities. The right and the left hemisphere were considered separately. The three fiber bundles

were sampled within ExploreDTI, to have the same number of points spread along the length in each participant. The number of points was calculated dividing the average -across subjects- of the tract length and the voxel size (Colby, Soderberg et al. 2012). The left subgenual was divided in 54 points, the left retrosplenial presented 51 points and the left parahippocampal was split in 35 points. In the right hemisphere, the subgenual part was divided into 53 points, the retrosplenial in 49 points and the parahippocampal branch in 37 points. Each fibre bundle (i.e. set of trajectories) was reduced to a single “averaged” pathway and the DTI-based measures (FA, MD, RD, AD) were extracted and analysed in a repeated-measures ANOVA model. The p-value chosen was p=0.0028, which is a global p<0.05 after Bonferroni correction for multiple comparisons (Nichols and Hayasaka 2003), that is divided by the three diffusivity directions, the number of branches and the number of hemispheres considered. False discovery rate (FDR) correction was used in the along-tract analysis to correct for multiple comparisons following the Benjamini and Hochberg FDR procedure (Benjamini and Hochberg, 1995) (http://imaging.mrc-cbu.cam.ac.uk/statswiki/FAQ/FDR). Independent t-tests were used to localize the points that resulted statistically significant after the repeated-measures ANOVA.

Furthermore, an intra-group linear correlation between the DTI parameters and the CANTAB tests was also carried out for each of the three branches.

4.3.3. Results

4.3.3.1. Tractography Analysis

A between-group (healthy young and older) effect was observed in the subgenual part of cingulum in the left hemisphere. Results show a statistically significant

decrease in FA (p=0.0013, FDR corrected) and AD (p=0.0024, FDR corrected) in the rostral part of the subgenual branch, as well as a statistically significant increase of RD (p=0.0011, FDR corrected) in the caudal part of the subgenual branch of the healthy older people (Figure 4.4).

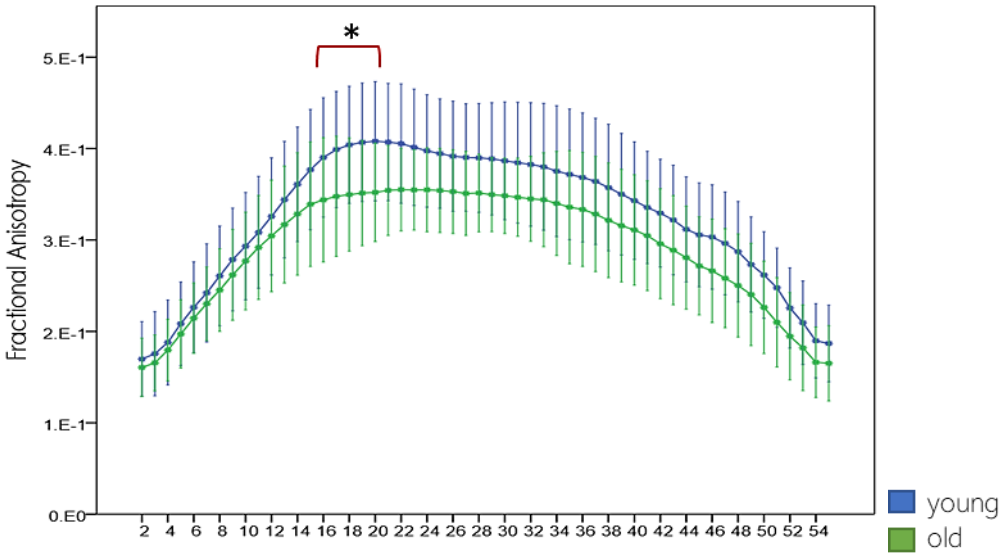

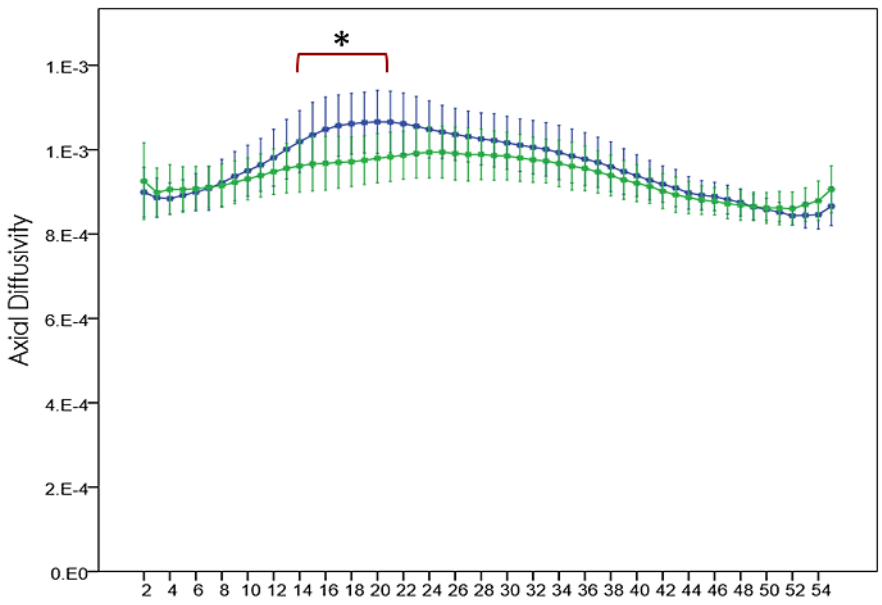

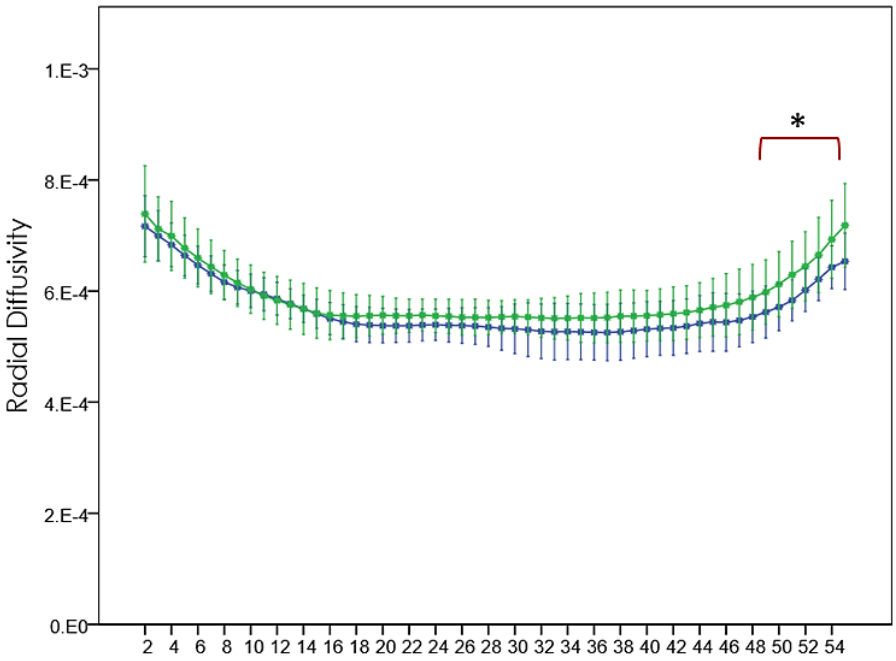

Figure 4.4: Along-tract analysis in the left hemisphere of the subgenual branch between young healthy people (blue line) and older healthy people (green line). The data represent the mean of DTI-measures for each point along the tract +/- 1

4.3.3.2. Within-Group Linear Correlation

A within-group linear correlation was conducted between each of the DTI measures and the scores of each test of the CANTAB, both with averaged diffusivity and along-tract diffusivity measures. There were no statistically significant linear correlations detected between any averaged measures and cognitive tests, while the results of the linear correlation with the along-tract measure showed linear correlation in the right hemisphere, but did not survive the FDR correction.

Cingulum segment	Hemisphere	Diffusivity measures			
		FA	MD	AD	RD
Subgenual	Left	0.006↓	ns	0.014↓	0.002↑
	Right	ns	ns	ns	ns
Retrosplenial	Left	ns	ns	ns	ns
	Right	ns	ns	ns	ns
Parahippocampal	Left	ns	ns	ns	ns
	Right	ns	ns	ns	ns

Table 4.3: Between-group effect in the repeated-measures ANOVA before FDR correction

4.3.4. Discussion

The current study advanced our knowledge about aging-related changes by employing a CSD-approach to segment the cingulum branches; it analysed the fibre integrity measures along the tract length. Previous studies revealed that tract-average diffusivity measures change in the older participants represented by a decrease in FA and AD and an increase in MD and RD compared to a healthy young group (Sullivan and Pfefferbaum 2006, Catheline, Periot et al. 2010, Jang, Kwon et al. 2016). We performed a group comparison approach to determine whether there were changes in diffusivity measures during aging, but our analysis didn't include the measurement of the change magnitude; this could be a step to consider in a further analysis.

Our findings were consistent with the hypothesized anterior-posterior gradient pattern in WM demyelination with aging (Sullivan and Pfefferbaum 2006, Madden, Bennett et al. 2012), and consistent with other WM studies using a DTI-

based approach (Head, Buckner et al. 2004, Pfefferbaum, Adalsteinsson et al. 2005). We found a high similarity with the results of Catheline et al (Catheline, Periot et al. 2010). They found a decrease in the FA of the left subgenual between healthy young and older adults, while there was no significant difference in the other branches. Differently from Catheline et al., we measured changes not only in FA, but also in the other diffusivity measures, finding a decrease in AD and increase in RD of the left hemisphere.

The subgenual branch showed a decrease of FA and AD in the rostral part of the branch, and an increase of RD in the posterior end. Before the FDR correction, diffusivity measures changes were seen in the same points of the branch for FA, AD and RD, but after the correction, RD increased only in the posterior end of the branch. The relation between cognitive changes and the cingulum points showing significant differences is still unknown, even though a previous study (Abdul-Rahman, Qiu et al. 2011) on diffusion measures changes in schizophrenia patients found an increase of RD in the same points, suggesting a demyelination process and disrupt of connectivity. Bennett and colleagues (Bennett et al., 2010) explained such variation of DTI measures (FA/AD decrease and RD increase) to be associated with an underlying lesion-induced axonal loss and gliosis, found already in the internal capsule, the superior corona radiate and the frontal forceps, but it is the first time that is detected in the subgenual cingulum.

The subgenual branch is involved in selective attention, emotional conflict and perceptual processing (Jang, Kwon et al. 2016). Madden and colleagues (Madden, Bennett et al. 2012) reviewed DTI studies of the WM integrity, considering the relation between DTI measures, neurobiological changes and decline of cognitive performances in WM structures of older people, including the

cingulum. They pointed out that sensory and motor functions (defined fluid cognitive abilities), that are associated with the anterior cingulate, tend to decline with aging, reflecting changes in the integrity of the WM tracts, while the crystallized abilities (referred to expertise and knowledge) remain quite stable.

Older people are able to compensate for a decrease in the WM density and networks efficiency occurring in aging, as explained by Park and Reuter-Lorenz. They described studies on functional neuroimaging and aging show how old people can perform the same task as younger people, despite their neural decline. This is possible when, in older people, both hemispheres are activated in cognitive tasks that require only one hemisphere in younger people (Park and Reuter-Lorenz 2009).

Our study supports the idea that aging-related changes are not homogenous across the length of the subgenual branch; this study gives more specific insights on the exact locations of the changes along the bundle, previously demonstrated only in clinical populations (Abdul-Rahman, Qiu et al. 2011). In the older group, significant differences were seen in the rostral part of the branch for AD and FA, specifically at the point of the major curve of the segment, corresponding to the rostral part of Brodmann area 32. A study about the parcellation of the cingulate cortex (Beckmann, Johansen-Berg et al. 2009) suggested the locations of the differences found in the subgenual branch correspond to the area where the subgenual cingulum is connected to the orbitofrontal and medial prefrontal cortex, confirmed by resting-state functional connectivity studies (Cao, Luo et al. 2014). RD showed statistically significant changes only in the caudal part, where the fibres exit the cingulum bundle and reach the precuneus, as seen in primates (Heilbronner and Haber 2014).

The observed discrepancies between studies may be due to methodological differences in anatomical definitions of the cingulum regions, as well as to different b-values. DTI studies usually have a b-value between 500 and 1200 s/mm^2, whereas our study had a b-value of 2000 s/mm^2. The images with a higher b-value appear “noisier” when compared with images with a lower b-value, given by a larger signal-to-noise ratio (SNR) (Burdette, Durden et al. 2001). The choice of a higher b-value is because we wanted to utilize a CSD-type approach to segment the cingulum (Jeurissen, Leemans et al. 2011). The CSD approach has significant advantages over a DTI-based approach, primarily a more accurate segmentation of the CB, and the reconstruction of the original fibre orientation, without any a priori assumption about the number of fibre populations, as required in the DTI-model (Tournier, Calamante et al. 2004). The CB is one of the biggest fibre bundles in the brain, presenting several fibre populations along its length; the DTI-model can create artefacts when there are more than two different fibre populations in the same voxel, whereas the CSD-approach reconstructs the fibre orientation with more than two fibre population and solve for the intra-voxel fibre orientation (Jeurissen, Leemans et al. 2011). Finally, one of the CSD-approach assumptions is that the response function seen for a certain fibre population orientation is constant throughout the brain. This may change in WM structures where there are different diffusion characteristics, for example in fibres with different myelination levels or axonal densities. In these cases, the response function would change the anisotropy of a small percentage, but the results would be still reliable and the fibre orientation would be still preserved (Tournier, Calamante et al. 2004).

In our study variability in regional anatomy influenced the choice of the templates required to obtain robust tracts. The atlas-based approach was chosen over the manual segmentation to minimize the differences in ROIs size and location that could arise with manual drawing (Pievani, Agosta et al. 2010). A first attempt was made using one template for both groups, but the lateral ventricles atrophy due to aging led to inaccuracies in the segmentation of the tracts, because the ROIs were located incorrectly relative to the enlarged ventricles (Figure 1; d) and e)). Thus, the large anatomical changes due to aging necessitated the use of two templates to correctly place the ROIs, one template with small lateral ventricles and another template with enlarged lateral ventricles typically seen in older populations.

Within-group linear correlations were performed between CANTAB scores and each branch of the cingulum, to test if there was a linear association between memory performance and the fibre microstructure. We did not detect any statistically significant association between memory performance and cingulum integrity in either group.

4.3.5. Conclusion

In the present study, the three branches of the cingulum were investigated using constrained spherical deconvolution that allowed for detailed analysis along the cingulum. The findings of this study add to our knowledge about the brain during aging, and it helps in further elucidating the changes in aging-related disorders.

Author Disclosure Statement

This study was part funded by the EU European Regional Development Fund 2007- 2013 (Project 087 - Neuroskill) awarded to ALWB, PM, JM. FS was supported by a PhD Studentship awarded by Trinity College Dublin. No competing financial interests exist.

5. General Discussion

5.1. Review of Aims and Results

5.1.1. Overview of Findings from Chapter 2

The first study looked at brain connectivity changes in an adolescent population divided into two groups, based on the stress level perceived in their life. In the analysis both whole-brain connectivity approach and graph theory measures of centrality, segregation and integration were considered. Findings showed an increase of connectivity strength in the high stress group between the orbito-frontal cortex and the superior parietal lobule, belonging to the limbic and the dorsal attentional networks, as well as between the posterior cingulate and the pars opercularis, belonging to the attentional network and salience network respectively. In the graph theory analysis, performed over a range of different sparsity levels, the high stress group showed a decrease of betweenness centrality in the somatomotor cortex, and an increase of degree centrality in the visual network and in the dorsal attentional network. Results on the graph theory measures indicated sparsity level (i.e. the network density) was an important factor influencing the computation of such metrics.

5.1.2. Overview of Findings from Chapter 3

The second study could be considered as an extension of the first one. The study aimed to answer two questions: the first was to investigate whether volumetric changes in the hippocampus subfields were related to stress. The second question was to explore if the stress level defined at the first time point might be associated to longitudinal changes of the hippocampus subfields across two time

points, when participants were in the late adolescence stage (18-20 years of age). The subfields segmentation was performed using the developmental version of FreeSurfer 6.0, having the advantage to divide the hippocampus into head, body and tail. Results of the first analysis showed decreases in the left fimbria and right cornu ammonis 3 and granular layer of the dentate gyrus, even though such effects disappeared after correction for multiple comparisons. In the High stress group, the level of neuroticism was found to be negatively associated with the volumes of some subfields of the left hemisphere, namely the subiculum, the head of cornu ammonis 1, the molecular layer, the whole head of the hippocampus and the fimbria. Such association was lateralized, as no relationship was found in the right hemisphere. Results of the longitudinal analysis were negative, indicating stress at baseline was not a significant predictor of hippocampal subfields changes over time.

5.1.3. Overview of Findings from Chapter 4

The aim of the third study was to investigate age-related microstructural changes of the cingulum bundle in healthy aging. The analysis was carried out by using deterministic tractography with a constrained spherical deconvolution (CSD) approach, that is more innovative than the classical DTI method. The cingulum bundle was divided manually into three branches by using a ROI-based method, and diffusivity measures were extracted at both tract-averaged level and along the length of each tract for the two hemispheres. Results showed a decrease in fractional anisotropy and axial diffusivity, as well as an increase of radial diffusivity in the left subgenual branch of the older group. Averaged-tract results showed decreases in the left FA and AD, as well as an increase in the left RD. In the right hemisphere there was an increase in mean diffusivity.

5.2. Contribution of Findings to Prior Knowledge

5.2.1. Brain Connectivity Changes Related to Stress in Adolescence

The results of this study showed adolescents who experienced higher levels of stress in their life had altered connectivity in areas involved in emotional and mnemonic processes, influencing cognitive processes and behavioural responses (Sachser, Kaiser et al. 2013). The connections found to be altered with stress were part of networks involved in the integration of sensory, emotional, and cognitive information, such as the salience network, sharing those areas with limbic circuits (Bolsinger, Seifritz et al. 2018). Findings of this study were confirmed by previous research on the relationship between attentional deficits and frontal brain areas, such as the orbital cortex in children (Park, Leonard et al. 2018), and an increase in connectivity between prefrontal cortex and posterior cingulate, putamen and caudate (Fan, Pestke et al. 2015) with acute stressful events.

Even though literature about alteration in graph theory measures in adolescents is not vast, the results found in this study are confirmed by previous published studies. These studies found decreased nodal centralities in areas belonging to the sensorial cortex (Xu, Chen et al. 2018), as well as an increase of nodal centrality in the visual areas and regions belonging to the salience network (Suo, Lei et al. 2015, Ho, Dennis et al. 2018) in adolescents suffering of PTSD. Authors suggested stress could hamper the correct interactions between network modules, causing structural disruptions and re-organization of brain networks and enhancing the chance to develop neuropsychiatric disorders. Another study that used the same parcellation showed reductions of local betweenness

centrality in the somatomotor cortex of adolescents suffering of major depressive disorders (MDD), whereas global graph metrics changes were not seen in any of these studies. This suggested it would take a more severe emotional insult, persistent in time, to have network organizational alterations at a global level (Ho, Dennis et al. 2018).

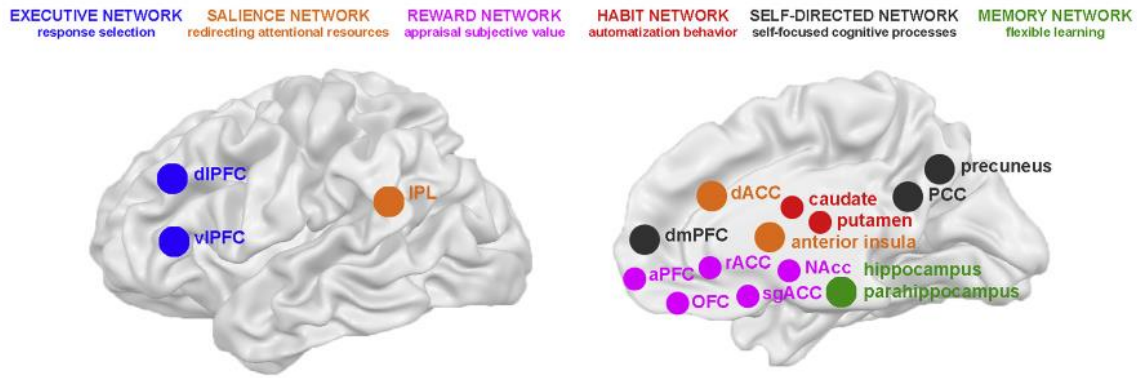

Figure 5.1: Representation of the brain regions forming the main large-scale networks (Zilverstand et al., 2018)

5.2.2. Stress-Related Changes of Hippocampus Subfields in Adolescence

Adolescents who experienced different stress levels (low vs. high) in their life did not show significant changes in the hippocampus subfields volume, but higher levels of Neuroticism were related to decrease in volume of the left subiculum, CA1, and hippocampus head in the High stress group. The tendency of experiencing that feeling of discomfort and internal pressure were all consequences of perceiving stress due to a specific situation. Some studies confirmed such association (Montag, Reuter et al. 2013), whereas others showed no relationship between the level of neuroticism and hippocampal volume changes in young adults (Gray, Owens et al. 2018), suggesting further

investigation on Neuroticism being an effect rather than a cause of alterations in hippocampal subfields volume.

A previous published study explored the longitudinal changes of hippocampal volumes on an adult population (from 25 till 60 years old) divided into high and low stress group using FreeSurfer 5.3 (the previous version than the one used in this thesis). They debated whether a smaller hippocampus represented a consequence of stress (especially chronic stress), or rather could be a factor increasing vulnerability in developing stress-related disorders. They found consistent reduced hippocampal volume across the time points, coming to the conclusion a volume decrease could enhance the possibility of developing stress-related disorders rather than a consequence (Lindgren, Bergdahl et al. 2016). Translating the same study design on the adolescent brain was of crucial importance, as the brain is still maturing in those years, and any offence could lead to permanent structural alterations. Not only this, but using a multi-centre population, as well as the up-to-date version of FreeSurfer, added value and novelty to the existing literature on this topic.

5.2.3. Microstructural Changes of the Cingulum Bundle in Healthy Aging

The microstructural changes seen in this study confirmed results found previously (Sala, Agosta et al. 2012), where analysis on the cingulum showed that decreases of fractional anisotropy and increase of mean diffusivity were associated with aging. In particular, what was observed in this study was an age-related decrease of myelination coherence in the subgenual cingulum, which corresponds to the most anterior part. Previous studies that divided the cingulum bundle in five parts confirmed such results, finding a similar trend in diffusivity

measures changes in the anterior cingulum and anterior superior cingulum (Jang, Kwon et al. 2016). The novelty of this study findings was the extraction of diffusivity measures along the length of each tract, which contributed to pinpointing the right location as to where changes happened. The subgenual branch microstructure was found to change at the level of the curve embracing the genu of the corpus callosum, reflected by a decrease of FA and AD, as well as an increase of RD at the posterior end of the same branch. This might suggest a decrease of myelination, or axonal damage, occurring in specific parts along the tract as people's brain age. Finally, the lack of association between microstructural alterations and cognitive performance seen in this study might indicate the cingulum resistance to cognitive decline with aging (Zahr, Rohlfing et al. 2009), and the old people tendency of using compensation mechanisms to carry out cognitive tasks.

5.3. Overall Discussion

This thesis work aimed to contribute to the existing literature on the changes of the limbic system in crucial time periods across lifespan by using structural neuroimaging. Findings of the three studies highlighted a common factor, that is how both aging processes and traumatic experiences affected brain areas and structures belonging to the limbic system. The limbic system is formed by specific cortical and sub-cortical structures and connections involved in the emotional responses to life situations (Bove et al., 2016). Both stress in adolescence and aging were found to affect the structural morphology of this system, reflected in altered behavioural responses and cognitive decline. The limbic system development is not homogeneous across lifespan (Schneider et al., 2007): sub-

cortical structures mature earlier compared to the frontal areas, that are responsible for the “rational” response to life events. This is why adolescents tend to have a higher level of impulsivity, risk taking behaviours and tendency to develop depressive symptoms as response to stressful situations (Merz, He et al. 2018). In fact, impulsivity was found to be associated to reduced cortical thickness in frontal regions, such as the pars orbitalis and superior frontal gyrus, whereas reduced hippocampal volumes were associated to higher number of depressive symptoms. The high level of plasticity of the brain during adolescence makes the limbic system one of the easiest targets for the development of neuropsychiatric disorders. In their multimodal study, Chen and colleagues combined structural (voxel-based morphometry) and functional connectivity (FC) to investigate changes in the brain structures and connectivity attributed to the limbic system (Chen, Wang et al. 2018). A decrease of grey matter was seen in the left anterior cingulate cortex (ACC) and right hippocampus of patients compared to healthy controls, along with a decrease of connectivity between the left ACC and the left orbitofrontal cortex (OFC).

The limbic circuits and the correct functioning of the HPA axis influence each other in situation of chronic and acute stress (Jankord and Herman 2008). The reactivity of the HPA axis is, in fact, associated to the pituitary gland volume (PGV) development in mid and late adolescence (Ganella, Allen et al. 2015); a higher number of childhood stressful experiences can lead to an accelerated PGV growth especially in young girls, suggesting a gender-based difference in stress response. The underlying mechanisms responsible for the correct emotional responses to stress might be affected by the continual activation of the HPA and the prolonged release of cortisol. This could cause a substantial

anatomical reorganization of stress-related circuits (Jankord and Herman 2008), and lead to the premature development of mood-related disorders, reflecting an accelerated maturation of brain circuits in the limbic system.

Stress and the development of depressive symptoms were also shown to influence the relation between the HPA axis activation and motivation in adolescents (Rudolph, Troop-Gordon et al. 2018). A higher level of motivation and engagement was associated to reduced functioning of the HPA, whereas the opposite was also seen. Internalization and externalization of depressive symptoms were also associated to the activation of the HPA axis (Kuhlman, Geiss et al. 2018), representing risk factors for the development of psychiatric disorders in adolescents.

One study investigated the influence that depressive symptoms developed by stressful events had on maturation coupling (another term to indicate cortical development during adolescence) (Vijayakumar, Allen et al. 2017), especially in the amygdala across time. Cognitive and neuroimaging data were acquired at three time points, and maturation coupling was negatively associated to the number of depressive symptoms, especially in the right amygdala and the prefrontal cortex over time. Another longitudinal study investigated the changes in cortical thickness, surface area and volume in limbic areas, such as hippocampus and amygdala (Bos, Peters et al. 2018) in adolescents divided into two groups based on the number of depressive symptoms (Low depression and High depression). Over time, adolescents with higher number of depressive symptoms showed a more severe reduction of cortical thickness in the frontal lobe, specifically in precentral, paracentral and lateral orbitofrontal areas.

Throughout adulthood and in aging, literature showed that reduced amount of serotonin, a neurotransmitter involved in improving mood and social behaviour, appetite and memory (Berger, Gray et al. 2009), could lead old people to be more sensitive to negative emotions (Meltzer, Smith et al. 1998). In general, studies on the relation between emotional perception and aging affirmed older people have the ability of being more stable emotionally (Lim, Zipursky et al. 1990), showing no relationship between limbic networks and age, whereas all the other networks were found to decrease in connectivity coherence over time (Bajaj, Alkozei et al. 2017). Nevertheless, when an event or emotion was perceived as negative, older people tended to lose this stability (Kaszniak and Menchola 2012), showing volumetric and connectivity reductions in brain areas belonging to the limbic system (Mather 2012, Gunbey, Ercan et al. 2014). Aging was associated with reduction in the hippocampal volume (Lim, Zipursky et al. 1990), as well as with structural alterations in the frontal regions involved in emotional processing, such as ACC and ventromedial PFC (Mather 2012). One study investigating fibre tracts microstructure of the limbic system showed a negative correlation between age and the FA of left hippocampus, bilateral parahippocampal gyrus, and fornix. The ADC values of right amygdala and left cingulum interestingly also showed a negative relationship with age (Gunbey, Ercan et al. 2014), confirming a decrease of the anisotropy level in older adults.

Negative life events and stress may, therefore, affect emotional balance in two critical periods of life, such as adolescence and aging. The level of cortisol produced as response to adverse situations is regulated by the amount of glucocorticoid receptors (GRs) in the body, that have the highest concentration in adolescence and older adulthood (Lupien, McEwen et al. 2009), increasing the

sensitivity of limbic structures to external events. Furthermore, the high level of brain plasticity in those years may lead to structural changes which could be permanent and last throughout adulthood, influencing the way people age (Bajaj, Alkozei et al. 2017). This can contribute to increase the risk of developing psychiatric disorders in adulthood, and to affect brain aging processes, accelerating cognitive decline (Mather 2012).

A large part of this thesis work was related to data analysis, including learning new software and statistical models in each project. Methodological approaches and study design were thought carefully to answer the research questions of interest. This brought to spend a considerable amount of time in self-learning neuroimaging methods and coding languages to carry out statistical analyses. In the first study, besides understanding the graph theory terminology and concepts never used before, a huge amount of work went in data cleaning and sorting all the demographic information and cognitive scores used in the analysis. Further challenges were found in the computational part to extract networks from GM segmentations and adjusting it to the data, as additional steps were required before using the program. Finally, the whole graph theory analysis was based on Matlab scripts which were developed in the lab, calculated at more than one sparsity level, which also protracted the computational times. In the second study, the biggest challenge was to segment the hippocampus subfields longitudinally, as it extended the computational times considerably. For some participants, the segmentation did not run successfully after few attempts, and this also delayed the extraction of the volume values and the final statistical analysis. The use of TCHPC and the development of a program within it to run the segmentation required also time in understanding how to perform this step in

the most efficient and time-saving way. Lastly, in the third project, the segmentation of the parahippocampal tract developed in the lab was the step that required more time. Vast search in previous published literature on the hippocampus anatomy and parahippocampal WM tract was done to determine the best location to draw the second ROI. Finally, as the tractography was run in native space, time was required to inspect tractography output subject by subject. In some cases, the ROIs set drawn on the template was not fitting the different brain shape of specific subjects, and this led to draw individual ROIs to run tractography successfully.

This PhD work was carried out by using secondary data for all the three projects. In the first two studies, data were obtained from the IMAGEN Consortium, whereas in the third study data were part of the Neuroskill project. Working with secondary data had some strengths, but also many downsides. Having data already acquired made possible to focus on data analysis mainly, which gave enough time to learn more about methodological approaches and software. Also, some steps, for example a first data quality check, were already performed by other people of the IMAGEN Consortium, which saved time in excluding bad quality MRI images. All the demographic information and scores for neuropsychological tests were already organized and sorted in spreadsheets for each participant. Regarding the downsides, working with secondary data did not give the opportunity to acquire data. This could represent a big limitation in the study methodology, as data collection was not designed with the specific question in mind. The type of images acquired, or the cognitive tests used might, therefore, not always represent the optimum data to answer the research question. A lot of time was spent in learning all these steps performed by other

people, therefore communication among all the parts involved in the project was crucial to have a clear idea of all the data available for the study. On a more general level, another step that represented a downside was organizing all the data, i.e. excluding participants with missing data across all the demographic information and cognitive tests scores, since it required a lot of data cleaning before the actual data analysis could be performed. Finally, especially in the first study, the Matlab-based program chosen for the extraction of networks from GM segmentations required the understanding of the logic behind the software and the technical knowledge of the programming language used.

5.3.1. Limitations

5.3.1.1. Choice of Brain Parcellation in Connectivity Analysis

The investigation of brain connectivity changes in adolescents who experienced stress was performed by using an ROI-based atlas. The template chosen in this study was the 17 networks and four hundred parcellations of Yeo. While the sub-division in 400 parcellations gave a better understanding of where potential structural connectivity changes might occur, one potential disadvantage was that parcellations included only the cortex, and none of the sub-cortical structures. This represented a limitation in understanding what happens in the brain connectivity with stress, without considering networks and connections including limbic structures, such as amygdala, basal ganglia and thalamic nuclei. A potential solution could be incorporating an additional atlas including these missing brain structures. Furthermore, this atlas was built based on resting-state functional connectivity, which could be a factor influencing the results in a study on structural connectivity. In relation to the cognitive component, only a sub-

group of questions from the LEQ was chosen, which could determine a different sub-division of the population.

5.3.1.2. Restrictions in Longitudinal Analysis

In this study, the hippocampal subfields were calculated based on three time points, and volumes were extracted for all the time points. Unfortunately, it was not possible to investigate longitudinal changes at the third time point as most of the cognitive and demographic information were missing. This was due to the fact the data used for this analysis are part of a research project still on, and information still needed to be gathered and made available. Data being collected across different European countries has been a factor that delayed such process. Another limitation of this study was that some participants MRI scans did not run successfully across the three time points, as FreeSurfer was not able to extract volume values in all the participants. Some of them, in fact, had only one time-point run successfully, other two time points, which led to the choice of removing those participants for the longitudinal analysis. Hemispherical differences were also seen when volumes were extracted. In fact, for some participants, the volume information was obtained only for one hemisphere. Even in this case, participants were excluded from the analysis. The results of this analysis were explorative, and the criteria used to define the two groups could influence the outcome. In fact, in this study, the total score of LEQ was used as a metric to measure stress, but a further analysis could be done by considering the number of events rather than the score. Another factor to consider was the number of subfields and the way they were analysed longitudinally. The methodological approach to investigate longitudinal changes only on the subfields associated to stress that were most cited in literature, and summing the volumes when the

subfields were divided into head and body, was made to reduce the number of variables to put in the statistical model, which could affect the final results.

Another significant limitation for this second study was that the stress levels measured at the second timepoint have not been included in the statistical analysis. Stress-related differences in the subfields volume were explored considering the grouping criteria at baseline. This was the very first question to answer to understand the potential effect of two different levels of stress (i.e. Low and High stress) on the hippocampal subfields. After answering this question, the next step would have been to consider the stress level at follow-up 2 as grouping criteria for the longitudinal analysis. Unfortunately, this was not possible for lack of time; therefore, investigating how the change of stress level between baseline and follow-up 2 might affect the analysis on the hippocampal subfields could represent one of the next steps in this study.

5.3.1.3. Limitations in Running the Tractography in Native Space

Each branch of the cingulum bundle was manually segmented by using both AND and NOT gates. Tracts were obtained with an atlas-based tractography approach that was performed on brains in native space. Further inspection and string removal were necessary after the ABT. This method was generally faster but has a few limitations: it was strictly related to the structure of the participant brain, and results needed to be checked to make sure the tractography worked correctly, since there could be sporadic fibres not belonging to the tract of interest. This happened for approximately 1/3 of the population, as some brains had a very different shape compared to the template chosen. In those cases, ROIs were drawn manually on those specific subjects and then tractography was run on

single participant's scan. This step was performed visually, and fibres were removed manually. The level of precision during this stage could then be a pivotal factor influencing the calculation of the diffusivity measures.

5.5. Future Directions

The data used for the first two studies have the potential of giving much more information needed in relation to the development of psychiatric diseases in adolescents and young adults. In this work, only the cognitive component of stress was considered, but several other factors might lead to disruption in the neural circuits of adolescents. Replicating the same analysis carried out in this work with other cognitive measures will give a better understanding of the plasticity and the effect that every single event has on the brain. Considering, for example, the development of depressive symptoms and how it affects brain connectivity and sub-cortical structures represents the next step that could explain how stressful events start a process of structural alterations in the brain, and trigger the development of mood-related and psychiatric diseases at a young age. In IMAGEN, the Development and well-being assessment (DAWBA) is used to define depressive symptomatology in youths, where different scores represent a different probability to develop depressive symptoms (with a score of 0, the percentage is <0.1%, with scores between 1 and 3, the percentage is less or equal to 50%, with scores equal to 4 and 5, the percentage is higher than 50%). Not only this, but also how the genetic component and the type of lifestyle adolescents have may account for the aggravation of brain damage in structure and function (Biddle and Asare 2011, Xia and Yao 2015, Sallis, Evans et al. 2017). A more gender-specific analysis can also be performed. It is known from literature that boys and girls experience and process life events in different ways,

internalizing feeling in different ways and externalizing them with different behavioural responses. It would be interesting then to see if such change in behaviours is related to different brain regions affected. The next analysis will focus on the effect of depressive symptoms developed across the next two time points and explore the relationship they have with potential structural atrophy and alterations in organization and properties of brain networks.

Future research on stress and MRI is crucial to understand that what happens in the first years of life can have a lifetime impact on people. More longitudinal studies will be of great help in monitoring the brain alterations due to stress on different levels. To do so, a multi-modal approach could be used, considering more than one aspect of the brain, i.e. not only changes in its structure, but also in functionality, chemical and hormonal balance. Nowadays, big data have been using in helping answering brain-related questions, combining different disciplines, such as neuroimaging, artificial intelligence, data miming and machine learning algorithms, to diagnose and predict the development of psychiatric disorders on populations.

5.6. Conclusion

This thesis work showed how structural imaging can be of great help and guidance to investigate anatomical changes in the brain at different stages of life. The three studies forming this work illustrate that in crucial life stages as adolescence and aging, the brain is particularly sensitive at the level of the limbic structures. The microstructural changes of the anterior part of the cingulum, the changes in brain connectivity at the level of limbic and salience networks, and finally the relationship between hippocampal subfields and level of stress and

neuroticism, suggest how the limbic system represents a main target throughout life. The structural changes seen in adolescents experiencing high levels of stress are found to be part of same brain circuits that are affected in healthy older people. Such areas are part of limbic circuits and they suggest an underlying accelerated maturation of emotional circuits in the adolescent brain as an adaptation mechanism to stress.

It is important to understand the association between the anatomical brain connections between regions involved in the limbic system, to be able then to explore the associations between these connections and the behavioural and emotional responses to external stimuli. Increasing knowledge on how people's brain is structurally impacted by negative experiences can lead to develop more efficient therapeutic approaches to treat psychiatric disorders and diseases related to different stages of life.

References

Abdul-Rahman, M. F., A. Qiu and K. Sim (2011). "Regionally specific white matter disruptions of fornix and cingulum in schizophrenia." PLoS One **6**(4): e18652.

Acosta-Cabronero, J. and P. J. Nestor (2014). "Diffusion tensor imaging in Alzheimer's disease: insights into the limbic-diencephalic network and methodological considerations." Frontiers in aging neuroscience **6**: 266-266.

Adjamian P, Hall DA, Palmer AR, Allan TW, Langers DR. (2014). "Neuroanatomical abnormalities in chronic tinnitus in the human brain. Neuroscience and Biobehavioral Reviews." Sep;45:119-133.

Ai, T., J. N. Morelli, X. Hu, D. Hao, F. L. Goerner, B. Ager and V. M. Runge (2012). "A historical overview of magnetic resonance imaging, focusing on technological innovations." Invest Radiol **47**(12): 725-741.

Andersen, S. L. and M. H. Teicher (2008). "Stress, sensitive periods and maturational events in adolescent depression." Trends Neurosci **31**(4): 183-191.

Arnett, J. J. (1999). "Adolescent storm and stress, reconsidered." Am Psychol **54**(5): 317-326.

Arslan, S., S. I. Ktena, A. Makropoulos, E. C. Robinson, D. Rueckert and S. Parisot (2018). "Human brain mapping: A systematic comparison of parcellation methods for the human cerebral cortex." Neuroimage **170**: 5-30.

Ashburner, J. and K. J. Friston (2000). "Voxel-based morphometry--the methods." Neuroimage **11**(6 Pt 1): 805-821.

Assaf, Y. and O. Pasternak (2008). "Diffusion tensor imaging (DTI)-based white matter mapping in brain research: a review." J Mol Neurosci **34**(1): 51-61.

Asscheman, S. J., K. N. Thakkar and S. F. Neggers (2015). "Changes in Effective Connectivity of the Superior Parietal Lobe during Inhibition and Redirection of Eye Movements." J Exp Neurosci **9**(Suppl 1): 27-40.

Aung, W. Y., S. Mar and T. L. Benzinger (2013). "Diffusion tensor MRI as a biomarker in axonal and myelin damage." Imaging in medicine **5**(5): 427-440.

Bäckman, L. and L. Farde (2001). "Dopamine and cognitive functioning: brain imaging findings in Huntington's disease and normal aging." Scandinavian journal of psychology **42**(3): 287-296.

Bajaj, S., A. Alkozei, N. S. Dailey and W. D. S. Killgore (2017). "Brain Aging: Uncovering Cortical Characteristics of Healthy Aging in Young Adults." Frontiers in aging neuroscience **9**: 412-412.

Bajaj, S., A. Alkozei, N. S. Dailey and W. D. S. Killgore (2017). "Brain Aging: Uncovering Cortical Characteristics of Healthy Aging in Young Adults." Front Aging Neurosci **9**: 412.

Bammer, R. (2003). "Basic principles of diffusion-weighted imaging." European journal of radiology **45**(3): 169-184.

Barili, P., G. De Carolis, D. Zaccheo and F. Amenta (1998). "Sensitivity to ageing of the limbic dopaminergic system: a review." Mech Ageing Dev **106**(1-2): 57-92.

Bartsch T, Wulff P. (2015). "The hippocampus in aging and disease: From plasticity to vulnerability." Neuroscience 309:1-16.

Basser, P. J. and D. K. Jones (2002). "Diffusion-tensor MRI: theory, experimental design and data analysis - a technical review." NMR Biomed **15**(7-8): 456-467.

Beck, A. T., Steer, R. A., & Brown, G. K. (1996). "The Beck Depression Inventory (2nd ed.)." San Antonio: The Psychological Corporation.

Beckmann, M., H. Johansen-Berg and M. F. Rushworth (2009). "Connectivity-based parcellation of human cingulate cortex and its relation to functional specialization." J Neurosci **29**(4): 1175-1190.

Benjamini, Y. Hochberg, Y. (1995). "Controlling the false discovery rate: a practical and powerful approach to multiple testing." Journal of the Royal Statistical Society, Series B. **57**(1): 289–300.

Bennett, I. J., Madden, D. J., Vaidya, C. J., Howard, D. V., & Howard, J. H., Jr (2010). "Age-related differences in multiple measures of white matter integrity: A diffusion tensor imaging study of healthy aging." Human brain mapping **31**(3), 378–390.

Berenbaum, S. A., A. M. Beltz and R. Corley (2015). "The importance of puberty for adolescent development: conceptualization and measurement." Advances in child development and behavior **48**: 53-92.

Berger, M., J. A. Gray and B. L. Roth (2009). "The expanded biology of serotonin." Annual review of medicine **60**: 355-366.

Bhatia, K., L. Henderson, M. Yim, E. Hsu and R. Dhaliwal (2017). "Diffusion Tensor Imaging Investigation of Uncinate Fasciculus Anatomy in Healthy Controls: Description of a Subgenual Stem." Neuropsychobiology **75**(3): 132-140.

Biddle, S. J. H. and M. Asare (2011). "Physical activity and mental health in children and adolescents: a review of reviews." British journal of sports medicine **45**(11): 886-895.

Bitar, R., G. Leung, R. Perng, S. Tadros, A. R. Moody, J. Sarrazin, C. McGregor, M. Christakis, S. Symons, A. Nelson and T. P. Roberts (2006). "MR pulse sequences: what every radiologist wants to know but is afraid to ask." Radiographics : a review publication of the Radiological Society of North America, Inc **26**(2): 513-537.

Blakemore, S. J. and S. Choudhury (2006). "Development of the adolescent brain: implications for executive function and social cognition." J Child Psychol Psychiatry **47**(3-4): 296-312.

Bolsinger, J., E. Seifritz, B. Kleim and A. Manoliu (2018). "Neuroimaging Correlates of Resilience to Traumatic Events-A Comprehensive Review." Frontiers in psychiatry **9**: 693-693.

Booker, S. A. and I. Vida (2018). "Morphological diversity and connectivity of hippocampal interneurons." Cell and tissue research **373**(3): 619-641.

Bos, M. G. N., S. Peters, F. C. van de Kamp, E. A. Crone and C. K. Tamnes (2018). "Emerging depression in adolescence coincides with accelerated frontal cortical thinning." J Child Psychol Psychiatry **59**(9): 994-1002.

Bourque, J., P. A. Spechler, S. Potvin, R. Whelan, T. Banaschewski, A. L. W. Bokde, U. Bromberg, C. Buchel, E. B. Quinlan, S. Desrivieres, H. Flor, V. Frouin,

P. Gowland, A. Heinz, B. Ittermann, J. L. Martinot, M. L. Paillere-Martinot, S. C. McEwen, F. Nees, D. P. Orfanos, T. Paus, L. Poustka, M. N. Smolka, N. C. Vetter, H. Walter, G. Schumann, H. Garavan and P. J. Conrod (2017). "Functional Neuroimaging Predictors of Self-Reported Psychotic Symptoms in Adolescents." Am J Psychiatry **174**(6): 566-575.

Bove D, Bove RM, Caccavale S, Bravaccio C, Marino M, La Montagna M. (2016). "Adolescence, imperceptible boundary between normality and pathology: a literature review." Minerva Pediatr. **68**(2):148-151.

Bremner, J. D., M. Narayan, E. R. Anderson, L. H. Staib, H. L. Miller and D. S. Charney (2000). "Hippocampal volume reduction in major depression." Am J Psychiatry **157**(1): 115-118.

Bubb, E. J., C. Metzler-Baddeley and J. P. Aggleton (2018). "The cingulum bundle: Anatomy, function, and dysfunction." Neurosci Biobehav Rev **92**: 104-127.

Bucci, M., S. S. Marques, D. Oh and N. B. Harris (2016). "Toxic Stress in Children and Adolescents." Advances in pediatrics **63**(1): 403-428.

Bullmore, E. and O. Sporns (2009). "Complex brain networks: graph theoretical analysis of structural and functional systems." Nat Rev Neurosci **10**(3): 186-198.

Burdette, J. H., D. D. Durden, A. D. Elster and Y. F. Yen (2001). "High b-value diffusion-weighted MRI of normal brain." J Comput Assist Tomogr **25**(4): 515-519.

Burt, K. B., R. Whelan, P. J. Conrod, T. Banaschewski, G. J. Barker, A. L. Bokde, U. Bromberg, C. Buchel, M. Fauth-Buhler, H. Flor, A. Galinowski, J. Gallinat, P. Gowland, A. Heinz, B. Ittermann, K. Mann, F. Nees, D. Papadopoulos-Orfanos, T. Paus, Z. Pausova, L. Poustka, M. Rietschel, T. W. Robbins, M. N. Smolka, A. Strohle, G. Schumann and H. Garavan (2016). "Structural brain correlates of adolescent resilience." J Child Psychol Psychiatry **57**(11): 1287-1296.

Cao, B., I. C. Passos, B. Mwangi, H. Amaral-Silva, J. Tannous, M. J. Wu, G. B. Zunta-Soares and J. C. Soares (2017). "Hippocampal subfield volumes in mood disorders." Mol Psychiatry **22**(9): 1352-1358.

Cao, W., C. Luo, B. Zhu, D. Zhang, L. Dong, J. Gong, D. Gong, H. He, S. Tu, W. Yin, J. Li, H. Chen and D. Yao (2014). "Resting-state functional connectivity in anterior cingulate cortex in normal aging." Front Aging Neurosci **6**: 280.

Carr, M. W. and M. L. Grey (2002). "Magnetic resonance imaging." The American journal of nursing **102**(12): 26-33.

Carrion, V. G. and S. S. Wong (2012). "Can traumatic stress alter the brain? Understanding the implications of early trauma on brain development and learning." J Adolesc Health **51**(2 Suppl): S23-28.

Casey, B. J., R. M. Jones and T. A. Hare (2008). "The adolescent brain." Ann N Y Acad Sci **1124**: 111-126.

Casey, B. J., R. M. Jones, L. Levita, V. Libby, S. S. Pattwell, E. J. Ruberry, F. Soliman and L. H. Somerville (2010). "The storm and stress of adolescence: insights from human imaging and mouse genetics." Dev Psychobiol **52**(3): 225-235.

Caspi, A., Sugden, K., Moffitt, T. E., Taylor, A., Craig, I. W., Harrington, H., McClay, J., Mill, J., Martin, J., Braithwaite, A., Poulton, R.(2003). "Influence of life stress on depression: moderation by a polymorphism in the 5-HTT gene". Science **301**: 386-389.

Catani M, Thiebaut de Schotten M. (2008). "A diffusion tensor imaging tractography atlas for virtual in vivo dissections." Cortex **44**(8):1105-1132.

Catani, M., F. Dell'acqua and M. Thiebaut de Schotten (2013). "A revised limbic system model for memory, emotion and behaviour." Neuroscience and biobehavioral reviews **37**(8): 1724-1737.

Catheline, G., O. Periot, M. Amirault, M. Braun, J. F. Dartigues, S. Auriacombe and M. Allard (2010). "Distinctive alterations of the cingulum bundle during aging and Alzheimer's disease." Neurobiol Aging **31**(9): 1582-1592.

Cellerini, M., A. Konze, G. Caracchini, M. Santoni and G. Dal Pozzo (1997). "Magnetic resonance imaging of cerebral associative white matter bundles employing fast-scan techniques." Acta anatomica **158**(3): 215-221.

Cembrowski, M. S., M. G. Phillips, S. F. DiLisio, B. C. Shields, J. Winnubst, J. Chandrashekar, E. Bas and N. Spruston (2018). "Dissociable Structural and Functional Hippocampal Outputs via Distinct Subiculum Cell Classes." Cell **173**(5): 1280-1292.e1218.

Chalavi, S., E. M. Vissia, M. E. Giesen, E. R. Nijenhuis, N. Draijer, J. H. Cole, P. Dazzan, C. M. Pariante, S. K. Madsen, P. Rajagopalan, P. M. Thompson, A. W. Toga, D. J. Veltman and A. A. Reinders (2015). "Abnormal hippocampal morphology in dissociative identity disorder and post-traumatic stress disorder correlates with childhood trauma and dissociative symptoms." Hum Brain Mapp **36**(5): 1692-1704.

Chavhan, G. B. (2016). "Appropriate selection of MRI sequences for common scenarios in clinical practice." Pediatr Radiol **46**(6): 740-747.

Chavhan, G. B., P. S. Babyn, B. Thomas, M. M. Shroff and E. M. Haacke (2009). "Principles, techniques, and applications of T2*-based MR imaging and its special applications." Radiographics **29**(5): 1433-1449.

Chen, L., Y. Wang, C. Niu, S. Zhong, H. Hu, P. Chen, S. Zhang, G. Chen, F. Deng, S. Lai, J. Wang, L. Huang and R. Huang (2018). "Common and distinct abnormal frontal-limbic system structural and functional patterns in patients with major depression and bipolar disorder." Neuroimage Clin **20**: 42-50.

Chen, L. W., D. Sun, S. L. Davis, C. C. Haswell, E. L. Dennis, C. A. Swanson, C. D. Whelan, B. Gutman, N. Jahanshad, J. E. Iglesias, P. Thompson, H. R. Wagner, P. Saemann, K. S. LaBar and R. A. Morey (2018). "Smaller hippocampal CA1 subfield volume in posttraumatic stress disorder." Depress Anxiety **35**(11): 1018-1029.

Chen, Y. and T. Z. Baram (2016). "Toward Understanding How Early-Life Stress Reprograms Cognitive and Emotional Brain Networks." Neuropsychopharmacology : official publication of the American College of Neuropsychopharmacology **41**(1): 197-206.

Chen, Z., X. Chen, M. Liu, L. Ma and S. Yu (2018). "Lower hippocampal subfields volume in relation to anxiety in medication-overuse headache." Molecular pain **14**: 1744806918761257-1744806918761257.

Christiansen, K., J. P. Aggleton, G. D. Parker, M. J. O'Sullivan, S. D. Vann and C. Metzler-Baddeley (2016). "The status of the precommissural and postcommissural fornix in normal ageing and mild cognitive impairment: An MRI tractography study." Neuroimage **130**: 35-47.

Ciccarelli, O., Catani, M., Johansen-Berg, H., Clark, C., Thompson, A. (2008). " Diffusion-based tractography in neurological disorders: concepts, applications, and future developments" Lancet Neurol **7**: 715–27.

Clark, B. J. and R. E. Harvey (2016). "Do the anterior and lateral thalamic nuclei make distinct contributions to spatial representation and memory?" Neurobiology of learning and memory **133**: 69-78.

Clemens, B., L. Wagels, M. Bauchmuller, R. Bergs, U. Habel and N. Kohn (2017). "Alerted default mode: functional connectivity changes in the aftermath of social stress." Sci Rep **7**: 40180.

Colby, J. B., L. Soderberg, C. Lebel, I. D. Dinov, P. M. Thompson and E. R. Sowell (2012). "Along-tract statistics allow for enhanced tractography analysis." Neuroimage **59**(4): 3227-3242.

Cole, J. H. and K. Franke (2017). "Predicting Age Using Neuroimaging: Innovative Brain Ageing Biomarkers." Trends in neurosciences **40**(12): 681-690.

Daianu, M., M. F. Mendez, V. G. Baboyan, Y. Jin, R. J. Melrose, E. E. Jimenez and P. M. Thompson (2016). "An advanced white matter tract analysis in frontotemporal dementia and early-onset Alzheimer's disease." Brain Imaging Behav **10**(4): 1038-1053.

Dannlowski, U., A. Stuhrmann, V. Beutelmann, P. Zwanzger, T. Lenzen, D. Grotegerd, K. Domschke, C. Hohoff, P. Ohrmann, J. Bauer, C. Lindner, C. Postert, C. Konrad, V. Arolt, W. Heindel, T. Suslow and H. Kugel (2012). "Limbic scars: long-term consequences of childhood maltreatment revealed by functional and structural magnetic resonance imaging." Biological psychiatry **71**(4): 286-293.

Daugherty, A. M., A. R. Bender, N. Raz and N. Ofen (2016). "Age differences in hippocampal subfield volumes from childhood to late adulthood." Hippocampus **26**(2): 220-228.

DeCarli, C., J. Massaro, D. Harvey, J. Hald, M. Tullberg, R. Au, A. Beiser, R. D'Agostino and P. A. Wolf (2005). "Measures of brain morphology and infarction in the framingham heart study: establishing what is normal." Neurobiology of aging **26**(4): 491-510.

DeLaPaz, R. L. (1994). "Echo-planar imaging." Radiographics **14**(5): 1045-1058.

Dennis, E. L., N. Jahanshad, A. W. Toga, K. L. McMahon, G. I. de Zubicaray, N. G. Martin, M. J. Wright and P. M. Thompson (2012). "Test-retest reliability of graph theory measures of structural brain connectivity." Med Image Comput Comput Assist Interv **15**(Pt 3): 305-312.

Desikan, R. S., F. Segonne, B. Fischl, B. T. Quinn, B. C. Dickerson, D. Blacker, R. L. Buckner, A. M. Dale, R. P. Maguire, B. T. Hyman, M. S. Albert and R. J. Killiany (2006). "An automated labeling system for subdividing the human cerebral cortex on MRI scans into gyral based regions of interest." Neuroimage **31**(3): 968-980.

Destrieux, C., B. Fischl, A. Dale and E. Halgren (2010). "Automatic parcellation of human cortical gyri and sulci using standard anatomical nomenclature." Neuroimage **53**(1): 1-15.

Dimsdale-Zucker, H. R., M. Ritchey, A. D. Ekstrom, A. P. Yonelinas and C. Ranganath (2018). "CA1 and CA3 differentially support spontaneous retrieval of episodic contexts within human hippocampal subfields." Nat Commun **9**(1): 294.

dos Santos Siqueira, A., C. E. Biazoli Junior, W. E. Comfort, L. A. Rohde and J. R. Sato (2014). "Abnormal functional resting-state networks in ADHD: graph theory and pattern recognition analysis of fMRI data." Biomed Res Int **2014**: 380531.

Edelman, R. R., P. Wielopolski and F. Schmitt (1994). "Echo-planar MR imaging." Radiology **192**(3): 600-612.

Eiland, L. and R. D. Romeo (2013). "Stress and the developing adolescent brain." Neuroscience **249**: 162-171.

Eluvathingal, T. J., K. M. Hasan, L. Kramer, J. M. Fletcher and L. Ewing-Cobbs (2007). "Quantitative diffusion tensor tractography of association and projection fibers in normally developing children and adolescents." Cerebral cortex (New York, N.Y. : 1991) **17**(12): 2760-2768.

Ernst, M. and S. C. Mueller (2008). "The adolescent brain: insights from functional neuroimaging research." Dev Neurobiol **68**(6): 729-743.

Ernst, M., E. E. Nelson, S. Jazbec, E. B. McClure, C. S. Monk, E. Leibenluft, J. Blair and D. S. Pine (2005). "Amygdala and nucleus accumbens in responses to receipt and omission of gains in adults and adolescents." Neuroimage **25**(4): 1279-1291.

Evans, B. E., J. Stam, A. C. Huizink, A. M. Willemen, P. M. Westenberg, S. Branje, W. Meeus, H. M. Koot and P. A. C. van Lier (2016). "Neuroticism and extraversion in relation to physiological stress reactivity during adolescence." Biol Psychol **117**: 67-79.

Fan, Y., K. Pestke, M. Feeser, S. Aust, J. C. Pruessner, H. Böker, M. Bajbouj and S. Grimm (2015). "Amygdala-Hippocampal Connectivity Changes During Acute Psychosocial Stress: Joint Effect of Early Life Stress and Oxytocin." Neuropsychopharmacology : official publication of the American College of Neuropsychopharmacology **40**(12): 2736-2744.

Fan, Y. T., Y. W. Fang, Y. P. Chen, E. D. Leshikar, C. P. Lin, O. J. L. Tzeng, H. W. Huang and C. M. Huang (2019). "Aging, cognition, and the brain: effects of age-related variation in white matter integrity on neuropsychological function." Aging Ment Health **23**(7): 831-839.

Fischl, B. (2012). "FreeSurfer." NeuroImage **62**(2): 774-781.

Folstein, M. F., S. E. Folstein and P. R. McHugh (1975). ""Mini-mental state". A practical method for grading the cognitive state of patients for the clinician." J Psychiatr Res **12**(3): 189-198.

Frodl, T. and V. O'Keane (2013). "How does the brain deal with cumulative stress? A review with focus on developmental stress, HPA axis function and hippocampal structure in humans." Neurobiol Dis **52**: 24-37.

Galinowski, A., R. Miranda, H. Lemaitre, M. L. Paillere Martinot, E. Artiges, H. Vulser, R. Goodman, J. Penttila, M. Struve, A. Barbot, T. Fadai, L. Poustka, P. Conrod, T. Banaschewski, G. J. Barker, A. Bokde, U. Bromberg, C. Buchel, H. Flor, J. Gallinat, H. Garavan, A. Heinz, B. Ittermann, V. Kappel, C. Lawrence, E. Loth, K. Mann, F. Nees, T. Paus, Z. Pausova, J. B. Poline, M. Rietschel, T. W. Robbins, M. Smolka, G. Schumann and J. L. Martinot (2015). "Resilience and corpus callosum microstructure in adolescence." Psychol Med **45**(11): 2285-2294.

Ganella, D. E., N. B. Allen, J. G. Simmons, O. Schwartz, J. H. Kim, L. Sheeber and S. Whittle (2015). "Early life stress alters pituitary growth during adolescence-a longitudinal study." Psychoneuroendocrinology **53**: 185-194.

Gerritsen, L., G. Kalpouzos, E. Westman, A. Simmons, L. O. Wahlund, L. Bäckman, L. Fratiglioni and H. X. Wang (2015). "The influence of negative life events on hippocampal and amygdala volumes in old age: a life-course perspective." Psychological medicine **45**(6): 1219-1228.

Gerritsen, L., L. van Velzen, L. Schmaal, Y. van der Graaf, N. van der Wee, M. J. van Tol, B. Penninx and M. Geerlings (2015). "Childhood maltreatment modifies the relationship of depression with hippocampal volume." Psychol Med **45**(16): 3517-3526.

Giedd, J. N., J. Blumenthal, N. O. Jeffries, F. X. Castellanos, H. Liu, A. Zijdenbos, T. Paus, A. C. Evans and J. L. Rapoport (1999). "Brain development during childhood and adolescence: a longitudinal MRI study." Nat Neurosci **2**(10): 861-863.

Giedd, J. N. and J. L. Rapoport (2010). "Structural MRI of pediatric brain development: what have we learned and where are we going?" Neuron **67**(5): 728-734.

Giorgio, A., K. E. Watkins, M. Chadwick, S. James, L. Winmill, G. Douaud, N. De Stefano, P. M. Matthews, S. M. Smith, H. Johansen-Berg and A. C. James

(2010). "Longitudinal changes in grey and white matter during adolescence." Neuroimage **49**(1): 94-103.

Gogtay, N., J. N. Giedd, L. Lusk, K. M. Hayashi, D. Greenstein, A. C. Vaituzis, T. F. Nugent, 3rd, D. H. Herman, L. S. Clasen, A. W. Toga, J. L. Rapoport and P. M. Thompson (2004). "Dynamic mapping of human cortical development during childhood through early adulthood." Proc Natl Acad Sci U S A **101**(21): 8174-8179.

Gómez, R. L. and J. O. Edgin (2016). "The extended trajectory of hippocampal development: Implications for early memory development and disorder." Developmental cognitive neuroscience **18**: 57-69.

Gong, G., T. Jiang, C. Zhu, Y. Zang, Y. He, S. Xie and J. Xiao (2005). "Side and handedness effects on the cingulum from diffusion tensor imaging." Neuroreport **16**(15): 1701-1705.

Gray, J. C., M. M. Owens, C. S. Hyatt and J. D. Miller (2018). "No evidence for morphometric associations of the amygdala and hippocampus with the five-factor model personality traits in relatively healthy young adults." PloS one **13**(9): e0204011-e0204011.

Greicius M.D., Supekar K., Menon V., Dougherty R.F. (2009) "Resting-state functional connectivity reflects structural connectivity in the default mode network." Cereb. Cortex **19**:72–78.

Gross, T. and B. Blasius (2008). "Adaptive coevolutionary networks: a review." J R Soc Interface **5**(20): 259-271.

Guadalupe, T., S. R. Mathias, T. G. M. vanErp, C. D. Whelan, M. P. Zwiers, Y. Abe, L. Abramovic, I. Agartz, O. A. Andreassen, A. Arias-Vásquez, B. S. Aribisala, N. J. Armstrong, V. Arolt, E. Artiges, R. Ayesa-Arriola, V. G. Baboyan, T. Banaschewski, G. Barker, M. E. Bastin, B. T. Baune, J. Blangero, A. L. W. Bokde, P. S. W. Boedhoe, A. Bose, S. Brem, H. Brodaty, U. Bromberg, S. Brooks, C. Büchel, J. Buitelaar, V. D. Calhoun, D. M. Cannon, A. Cattrell, Y. Cheng, P. J. Conrod, A. Conzelmann, A. Corvin, B. Crespo-Facorro, F. Crivello, U. Dannlowski, G. I. de Zubicaray, S. M. C. de Zwarte, I. J. Deary, S. Desrivières, N. T. Doan, G. Donohoe, E. S. Dørum, S. Ehrlich, T. Espeseth, G. Fernández,

H. Flor, J.-P. Fouche, V. Frouin, M. Fukunaga, J. Gallinat, H. Garavan, M. Gill, A. G. Suarez, P. Gowland, H. J. Grabe, D. Grotegerd, O. Gruber, S. Hagenaars, R. Hashimoto, T. U. Hauser, A. Heinz, D. P. Hibar, P. J. Hoekstra, M. Hoogman, F. M. Howells, H. Hu, H. E. Hulshoff Pol, C. Huyser, B. Ittermann, N. Jahanshad, E. G. Jönsson, S. Jurk, R. S. Kahn, S. Kelly, B. Kraemer, H. Kugel, J. S. Kwon, H. Lemaitre, K.-P. Lesch, C. Lochner, M. Luciano, A. F. Marquand, N. G. Martin, I. Martínez-Zalacaín, J.-L. Martinot, D. Mataix-Cols, K. Mather, C. McDonald, K. L. McMahon, S. E. Medland, J. M. Menchón, D. W. Morris, O. Mothersill, S. M. Maniega, B. Mwangi, T. Nakamae, T. Nakao, J. C. Narayanaswaamy, F. Nees, J. E. Nordvik, A. M. H. Onnink, N. Opel, R. Ophoff, M.-L. Paillère Martinot, D. Papadopoulos Orfanos, P. Pauli, T. Paus, L. Poustka, J. Y. Reddy, M. E. Renteria, R. Roiz-Santiáñez, A. Roos, N. A. Royle, P. Sachdev, P. Sánchez-Juan, L. Schmaal, G. Schumann, E. Shumskaya, M. N. Smolka, J. C. Soares, C. Soriano-Mas, D. J. Stein, L. T. Strike, R. Toro, J. A. Turner, N. Tzourio-Mazoyer, A. Uhlmann, M. V. Hernández, O. A. van den Heuvel, D. van der Meer, N. E. M. van Haren, D. J. Veltman, G. Venkatasubramanian, N. C. Vetter, D. Vuletic, S. Walitza, H. Walter, E. Walton, Z. Wang, J. Wardlaw, W. Wen, L. T. Westlye, R. Whelan, K. Wittfeld, T. Wolfers, M. J. Wright, J. Xu, X. Xu, J.-Y. Yun, J. Zhao, B. Franke, P. M. Thompson, D. C. Glahn, B. Mazoyer, S. E. Fisher and C. Francks (2017). "Human subcortical brain asymmetries in 15,847 people worldwide reveal effects of age and sex." Brain imaging and behavior **11**(5): 1497-1514.

Gunbey, H. P., K. Ercan, A. S. Findikoglu, H. T. Bulut, M. Karaoglanoglu and H. Arslan (2014). "The limbic degradation of aging brain: a quantitative analysis with diffusion tensor imaging." ScientificWorldJournal **2014**: 196513.

Gunbey, H. P., K. Ercan, A. S. Fındıkoglu, H. T. Bulut, M. Karaoglanoglu and H. Arslan (2014). "The limbic degradation of aging brain: a quantitative analysis with diffusion tensor imaging." TheScientificWorldJournal **2014**: 196513-196513.

Gunning-Dixon, F. M., A. M. Brickman, J. C. Cheng and G. S. Alexopoulos (2009). "Aging of cerebral white matter: a review of MRI findings." International journal of geriatric psychiatry **24**(2): 109-117.

Gupta, T., D. Sahni, R. S. Tubbs and S. K. Gupta (2016). "Flattened sheet-like fornix forming a "Cobra Hood" deformity: A previously unreported variant of fornix

anatomy and its implication for surgical approaches to the third ventricle." Neurology India **64**(5): 943-946.

Gur, R. E. and R. C. Gur (2016). "Sex differences in brain and behavior in adolescence: Findings from the Philadelphia Neurodevelopmental Cohort." Neurosci Biobehav Rev **70**: 159-170.

Hamilton, J. P., A. Etkin, D. J. Furman, M. G. Lemus, R. F. Johnson and I. H. Gotlib (2012). "Functional neuroimaging of major depressive disorder: a meta-analysis and new integration of base line activation and neural response data." Am J Psychiatry **169**(7): 693-703.

Hansen, M. S. and P. Kellman (2015). "Image reconstruction: an overview for clinicians." J Magn Reson Imaging **41**(3): 573-585.

Hanson, J. L., M. K. Chung, B. B. Avants, E. A. Shirtcliff, J. C. Gee, R. J. Davidson and S. D. Pollak (2010). "Early stress is associated with alterations in the orbitofrontal cortex: a tensor-based morphometry investigation of brain structure and behavioral risk." J Neurosci **30**(22): 7466-7472.

Head, D., R. L. Buckner, J. S. Shimony, L. E. Williams, E. Akbudak, T. E. Conturo, M. McAvoy, J. C. Morris and A. Z. Snyder (2004). "Differential vulnerability of anterior white matter in nondemented aging with minimal acceleration in dementia of the Alzheimer type: evidence from diffusion tensor imaging." Cereb Cortex **14**(4): 410-423.

Heilbronner, S. R. and S. N. Haber (2014). "Frontal cortical and subcortical projections provide a basis for segmenting the cingulum bundle: implications for neuroimaging and psychiatric disorders." J Neurosci **34**(30): 10041-10054.

Highley, J. R., M. A. Walker, M. M. Esiri, T. J. Crow and P. J. Harrison (2002). "Asymmetry of the uncinate fasciculus: a post-mortem study of normal subjects and patients with schizophrenia." Cerebral cortex (New York, N.Y. : 1991) **12**(11): 1218-1224.

Ho, T. C., E. L. Dennis, P. M. Thompson and I. H. Gotlib (2018). "Network-based approaches to examining stress in the adolescent brain." Neurobiol Stress **8**: 147-157.

Ho, T. C., G. Yang, J. Wu, P. Cassey, S. D. Brown, N. Hoang, M. Chan, C. G. Connolly, E. Henje-Blom, L. G. Duncan, M. A. Chesney, M. P. Paulus, J. E. Max, R. Patel, A. N. Simmons and T. T. Yang (2014). "Functional connectivity of negative emotional processing in adolescent depression." J Affect Disord **155**: 65-74.

Holmbeck, G. N. (2002). "A developmental perspective on adolescent health and illness: an introduction to the special issues." J Pediatr Psychol **27**(5): 409-416.

Huang, Y., N. J. Coupland, R. M. Lebel, R. Carter, P. Seres, A. H. Wilman and N. V. Malykhin (2013). "Structural changes in hippocampal subfields in major depressive disorder: a high-field magnetic resonance imaging study." Biol Psychiatry **74**(1): 62-68.

Iglesias, J. E., J. C. Augustinack, K. Nguyen, C. M. Player, A. Player, M. Wright, N. Roy, M. P. Frosch, A. C. McKee, L. L. Wald, B. Fischl and K. Van Leemput (2015). "A computational atlas of the hippocampal formation using ex vivo, ultra-high resolution MRI: Application to adaptive segmentation of in vivo MRI." Neuroimage **115**: 117-137.

Ingalhalikar, M., A. Smith, D. Parker, T. D. Satterthwaite, M. A. Elliott, K. Ruparel, H. Hakonarson, R. E. Gur, R. C. Gur and R. Verma (2014). "Sex differences in the structural connectome of the human brain." Proc Natl Acad Sci U S A **111**(2): 823-828.

Jang, S. H., Y. H. Kwon, M. Y. Lee, J. R. Kim and J. P. Seo (2016). "Aging of the cingulum in the human brain: Preliminary study of a diffusion tensor imaging study." Neurosci Lett **610**: 213-217.

Jankord, R. and J. P. Herman (2008). "Limbic regulation of hypothalamo-pituitary-adrenocortical function during acute and chronic stress." Annals of the New York Academy of Sciences **1148**: 64-73.

Jankowski, K. F., J. Batres, H. Scott, G. Smyda, J. H. Pfeifer and K. Quevedo (2018). "Feeling left out: depressed adolescents may atypically recruit emotional salience and regulation networks during social exclusion." Soc Cogn Affect Neurosci **13**(8): 863-876.

Jeurissen, B., A. Leemans, D. K. Jones, J. D. Tournier and J. Sijbers (2011). "Probabilistic fiber tracking using the residual bootstrap with constrained spherical deconvolution." Hum Brain Mapp **32**(3): 461-479.

Johnston, D. L., P. Liu, G. L. Wismer, B. R. Rosen, D. D. Stark, P. F. New, R. D. Okada and T. J. Brady (1985). "Magnetic resonance imaging: present and future applications." Canadian Medical Association journal **132**(7): 765-777.

Jones, D. K., K. F. Christiansen, R. J. Chapman and J. P. Aggleton (2013). "Distinct subdivisions of the cingulum bundle revealed by diffusion MRI fibre tracking: implications for neuropsychological investigations." Neuropsychologia **51**(1): 67-78.

Jones, R. S. (1993). "Entorhinal-hippocampal connections: a speculative view of their function." Trends in neurosciences **16**(2): 58-64.

Jung, B. A. and M. Weigel (2013). "Spin echo magnetic resonance imaging." Journal of magnetic resonance imaging : JMRI **37**(4): 805-817.

Juraska, J. M. and J. A. Markham (2004). "The cellular basis for volume changes in the rat cortex during puberty: white and gray matter." Ann N Y Acad Sci **1021**: 431-435.

Kaczkurkin, A. N., A. Raznahan and T. D. Satterthwaite (2019). "Sex differences in the developing brain: insights from multimodal neuroimaging." Neuropsychopharmacology : official publication of the American College of Neuropsychopharmacology **44**(1): 71-85.

Kaiser, R. H., R. Clegg, F. Goer, P. Pechtel, M. Beltzer, G. Vitaliano, D. P. Olson, M. H. Teicher and D. A. Pizzagalli (2018). "Childhood stress, grown-up brain networks: corticolimbic correlates of threat-related early life stress and adult stress response." Psychol Med **48**(7): 1157-1166.

Kamali, A., D. M. Yousem, D. D. Lin, H. I. Sair, S. P. Jasti, Z. Keser, R. F. Riascos and K. M. Hasan (2015). "Mapping the trajectory of the stria terminalis of the human limbic system using high spatial resolution diffusion tensor tractography." Neurosci Lett **608**: 45-50.

Kaszniak, A. W. and M. Menchola (2012). "Behavioral neuroscience of emotion in aging." Current topics in behavioral neurosciences **10**: 51-66.

Keresztes, A., A. R. Bender, N. C. Bodammer, U. Lindenberger, Y. L. Shing and M. Werkle-Bergner (2017). "Hippocampal maturity promotes memory distinctiveness in childhood and adolescence." Proc Natl Acad Sci U S A **114**(34): 9212-9217.

Khundrakpam, B. S., J. D. Lewis, L. Zhao, F. Chouinard-Decorte and A. C. Evans (2016). "Brain connectivity in normally developing children and adolescents." Neuroimage **134**: 192-203.

Khundrakpam, B. S., A. Reid, J. Brauer, F. Carbonell, J. Lewis, S. Ameis, S. Karama, J. Lee, Z. Chen, S. Das and A. C. Evans (2013). "Developmental changes in organization of structural brain networks." Cereb Cortex **23**(9): 2072-2085.

Khurshid, S. J. and A. M. Hussain (1991). "Nuclear magnetic resonance imaging (MRI)." J Pak Med Assoc **41**(10): 259-264.

Kiselev, V. G. (2019). "Larmor frequency in heterogeneous media." J Magn Reson **299**: 168-175.

Kolskar, K. K., D. Alnaes, T. Kaufmann, G. Richard, A. M. Sanders, K. M. Ulrichsen, T. Moberget, O. A. Andreassen, J. E. Nordvik and L. T. Westlye (2018). "Key Brain Network Nodes Show Differential Cognitive Relevance and Developmental Trajectories during Childhood and Adolescence." eNeuro **5**(4).

Krogsrud, S. K., C. K. Tamnes, A. M. Fjell, I. Amlien, H. Grydeland, U. Sulutvedt, P. Due-Tonnessen, A. Bjornerud, A. E. Solsnes, A. K. Haberg, J. Skrane and K. B. Walhovd (2014). "Development of hippocampal subfield volumes from 4 to 22 years." Hum Brain Mapp **35**(11): 5646-5657.

Kuhlman, K. R., E. G. Geiss, I. Vargas and N. Lopez-Duran (2018). "HPA-Axis Activation as a Key Moderator of Childhood Trauma Exposure and Adolescent Mental Health." J Abnorm Child Psychol **46**(1): 149-157.

Ladouceur, C. D., J. S. Peper, E. A. Crone and R. E. Dahl (2012). "White matter development in adolescence: the influence of puberty and implications for affective disorders." Dev Cogn Neurosci **2**(1): 36-54.

Le Bihan, D., J. F. Mangin, C. Poupon, C. A. Clark, S. Pappata, N. Molko and H. Chabriat (2001). "Diffusion tensor imaging: concepts and applications." J Magn Reson Imaging **13**(4): 534-546.

Lebel, C., L. Walker, A. Leemans, L. Phillips and C. Beaulieu (2008). "Microstructural maturation of the human brain from childhood to adulthood." Neuroimage **40**(3): 1044-1055.

Lee, J. K., A. D. Ekstrom and S. Ghetti (2014). "Volume of hippocampal subfields and episodic memory in childhood and adolescence." Neuroimage **94**: 162-171.

Leech, R., R. Braga and D. J. Sharp (2012). "Echoes of the brain within the posterior cingulate cortex." J Neurosci **32**(1): 215-222.

Leemans A, Jeurissen B, Sijbers J, and Jones DK. "ExploreDTI: a graphical toolbox for processing, analyzing, and visualizing diffusion MR data." In: 17th Annual Meeting of Intl Soc Mag Reson Med, p. 3537, Hawaii, USA, 2009

Leemans, A. and D. K. Jones (2009). "The B-matrix must be rotated when correcting for subject motion in DTI data." Magn Reson Med **61**(6): 1336-1349.

Li, G. and S. J. Pleasure (2014). "The development of hippocampal cellular assemblies." Wiley interdisciplinary reviews. Developmental biology **3**(2): 165-177.

Li, X., H. Wang, Y. Tian, S. Zhou, X. Li, K. Wang and Y. Yu (2016). "Impaired White Matter Connections of the Limbic System Networks Associated with Impaired Emotional Memory in Alzheimer's Disease." Front Aging Neurosci **8**: 250.

Lim, K. O., R. B. Zipursky, G. M. Murphy, Jr. and A. Pfefferbaum (1990). "In vivo quantification of the limbic system using MRI: effects of normal aging." Psychiatry research **35**(1): 15-26.

Lin, C.-S., C.-Y. Wu, S.-Y. Wu and H.-H. Lin (2018). "Brain activations associated with fearful experience show common and distinct patterns between younger and

older adults in the hippocampus and the amygdala." Scientific reports **8**(1): 5137-5137.

Lindgren, L., J. Bergdahl and L. Nyberg (2016). "Longitudinal Evidence for Smaller Hippocampus Volume as a Vulnerability Factor for Perceived Stress." Cerebral cortex (New York, N.Y. : 1991) **26**(8): 3527-3533.

Lockhart, S. N. and C. DeCarli (2014). "Structural imaging measures of brain aging." Neuropsychology review **24**(3): 271-289.

Luke, S. G. (2017). "Evaluating significance in linear mixed-effects models in R." Behavior research methods **49**(4): 1494-1502.

Lupien, S. J., B. S. McEwen, M. R. Gunnar and C. Heim (2009). "Effects of stress throughout the lifespan on the brain, behaviour and cognition." Nat Rev Neurosci **10**(6): 434-445.

Lynch, K. M., Y. Shi, A. W. Toga and K. A. Clark (2019). "Hippocampal Shape Maturation in Childhood and Adolescence." Cereb Cortex **29**(9): 3651-3665.

Madden, D. J., I. J. Bennett, A. Burzynska, G. G. Potter, N. K. Chen and A. W. Song (2012). "Diffusion tensor imaging of cerebral white matter integrity in cognitive aging." Biochim Biophys Acta **1822**(3): 386-400.

Malhi, G. S., P. Das, T. Outhred, L. Irwin, D. Gessler, Z. Bwabi, R. Bryant and Z. Mannie (2019). "The effects of childhood trauma on adolescent hippocampal subfields." Aust N Z J Psychiatry: 4867418824021.

Martin, S. B., C. D. Smith, H. R. Collins, F. A. Schmitt and B. T. Gold (2010). "Evidence that volume of anterior medial temporal lobe is reduced in seniors destined for mild cognitive impairment." Neurobiology of aging **31**(7): 1099-1106.

Martinez, G. V. (2018). "Introduction to MRI Physics." Methods Mol Biol **1718**: 3-19.

Marusak, H. A., J. R. B. Hatfield, M. E. Thomason and C. A. Rabinak (2017). "Reduced Ventral Tegmental Area-Hippocampal Connectivity in Children and Adolescents Exposed to Early Threat." Biol Psychiatry Cogn Neurosci Neuroimaging **2**(2): 130-137.

Mather, M. (2012). "The emotion paradox in the aging brain." Annals of the New York Academy of Sciences **1251**(1): 33-49.

McCrae, R. R. and O. P. John (1992). "An introduction to the five-factor model and its applications." J Pers **60**(2): 175-215.

McEwen, B. S. (2002). "Sex, stress and the hippocampus: allostasis, allostatic load and the aging process." Neurobiol Aging **23**(5): 921-939.

McEwen, B. S. (2011). "Effects of stress on the developing brain." Cerebrum **2011**: 14.

McEwen, B. S. (2012). "Brain on stress: how the social environment gets under the skin." Proc Natl Acad Sci U S A **109 Suppl 2**: 17180-17185.

McKinnon, E. T., J. H. Jensen, G. R. Glenn and J. A. Helpern (2017). "Dependence on b-value of the direction-averaged diffusion-weighted imaging signal in brain." Magn Reson Imaging **36**: 121-127.

McLachlan, R. S. (2009). "A brief review of the anatomy and physiology of the limbic system." Can J Neurol Sci **36 Suppl 2**: S84-87.

Meltzer, C. C., G. Smith, S. T. DeKosky, B. G. Pollock, C. A. Mathis, R. Y. Moore, D. J. Kupfer and C. F. Reynolds, 3rd (1998). "Serotonin in aging, late-life depression, and Alzheimer's disease: the emerging role of functional imaging." Neuropsychopharmacology : official publication of the American College of Neuropsychopharmacology **18**(6): 407-430.

Merz, E. C., X. He and K. G. Noble (2018). "Anxiety, depression, impulsivity, and brain structure in children and adolescents." Neuroimage Clin **20**: 243-251.

Minuzzi, L., S. K. Syan, M. Smith, A. Hall, G. B. Hall and B. N. Frey (2018). "Structural and functional changes in the somatosensory cortex in euthymic females with bipolar disorder." Aust N Z J Psychiatry **52**(11): 1075-1083.

Montag, C., M. Reuter, M. Jurkiewicz, S. Markett and J. Panksepp (2013). "Imaging the structure of the human anxious brain: a review of findings from neuroscientific personality psychology." Reviews in the neurosciences **24**(2): 167-190.

Morcom, A. M., E. T. Bullmore, F. A. Huppert, B. Lennox, A. Praseedom, H. Linnington and P. C. Fletcher (2010). "Memory encoding and dopamine in the aging brain: a psychopharmacological neuroimaging study." Cereb Cortex **20**(3): 743-757.

Morey, R. A., C. C. Haswell, S. R. Hooper and M. D. De Bellis (2016). "Amygdala, Hippocampus, and Ventral Medial Prefrontal Cortex Volumes Differ in Maltreated Youth with and without Chronic Posttraumatic Stress Disorder." Neuropsychopharmacology **41**(3): 791-801.

Mori S, Kaufmann W. E., Davatzikos C., et al., (2002). “Imaging Cortical Association Tracts in the Human Brain Using Diffusion-Tensor-Based Axonal Tracking,” Magnetic Resonance in Medicine, **47**(2), pp. 215-223.

Morris, J. C., R. C. Mohs, H. Rogers, G. Fillenbaum and A. Heyman (1988). "Consortium to establish a registry for Alzheimer's disease (CERAD) clinical and neuropsychological assessment of Alzheimer's disease." Psychopharmacol Bull **24**(4): 641-652.

Myrvang, A. D., T. R. Vangberg, K. Stedal, O. Ro, T. Endestad, J. H. Rosenvinge and P. M. Aslaksen (2018). "Hippocampal subfields in adolescent anorexia nervosa." Psychiatry Res Neuroimaging **282**: 24-30.

Nauta, W. J. (1958). "Hippocampal projections and related neural pathways to the midbrain in the cat." Brain : a journal of neurology **81**(3): 319-340.

Nelson, H.E. (1982). "National Adult Reading Test. Windsor", UK:NFER-Nelson.

Newcomb, M., Huba, C., & Bentler, P. (1981). "A multidimensional assessment of stressful life events among adolescents: Derivation and correlates." Journal of Health and Social Behavior **22**, 400-414.

Nguyen, T. V., J. Lew, M. D. Albaugh, K. N. Botteron, J. J. Hudziak, V. S. Fonov, D. L. Collins, S. Ducharme and J. T. McCracken (2017). "Sex-specific associations of testosterone with prefrontal-hippocampal development and executive function." Psychoneuroendocrinology **76**: 206-217.

Nichols, T. and S. Hayasaka (2003). "Controlling the familywise error rate in functional neuroimaging: a comparative review." Stat Methods Med Res **12**(5): 419-446.

Pagliaccio, D., J. L. Luby, R. Bogdan, A. Agrawal, M. S. Gaffrey, A. C. Belden, K. N. Botteron, M. P. Harms and D. M. Barch (2015). "Amygdala functional connectivity, HPA axis genetic variation, and life stress in children and relations to anxiety and emotion regulation." J Abnorm Psychol **124**(4): 817-833.

Papez, J. W. (1995). "A proposed mechanism of emotion. 1937." J Neuropsychiatry Clin Neurosci **7**(1): 103-112.

Park, A. T., J. A. Leonard, P. Saxler, A. B. Cyr, J. D. E. Gabrieli and A. P. Mackey (2018). "Amygdala-medial prefrontal connectivity relates to stress and mental health in early childhood." Soc Cogn Affect Neurosci.

Park, D. C. and P. Reuter-Lorenz (2009). "The adaptive brain: aging and neurocognitive scaffolding." Annu Rev Psychol **60**: 173-196.

Pascalau, R., R. Popa Stănilă, S. Sfrângeu and B. Szabo (2018). "Anatomy of the Limbic White Matter Tracts as Revealed by Fiber Dissection and Tractography." World neurosurgery **113**: e672-e689.

Paus, T. (2005). "Mapping brain maturation and cognitive development during adolescence." Trends Cogn Sci **9**(2): 60-68.

Peper, J. S., H. G. Schnack, R. M. Brouwer, G. C. Van Baal, E. Pjetri, E. Szekely, M. van Leeuwen, S. M. van den Berg, D. L. Collins, A. C. Evans, D. I. Boomsma, R. S. Kahn and H. E. Hulshoff Pol (2009). "Heritability of regional and global brain structure at the onset of puberty: a magnetic resonance imaging study in 9-year-old twin pairs." Hum Brain Mapp **30**(7): 2184-2196.

Pessoa, L. and P. R. Hof (2015). "From Paul Broca's great limbic lobe to the limbic system." J Comp Neurol **523**(17): 2495-2500.

Peters, A., B. S. McEwen and K. Friston (2017). "Uncertainty and stress: Why it causes diseases and how it is mastered by the brain." Prog Neurobiol **156**: 164-188.

Peters, R. (2006). "Ageing and the brain." Postgrad Med J **82**(964): 84-88.

Petersen, A. C., L. Crockett, M. Richards and A. Boxer (1988). "A self-report measure of pubertal status: Reliability, validity, and initial norms." J Youth Adolesc **17**(2): 117-133.

Pfefferbaum, A., E. Adalsteinsson and E. V. Sullivan (2005). "Frontal circuitry degradation marks healthy adult aging: Evidence from diffusion tensor imaging." Neuroimage **26**(3): 891-899.

Pfefferbaum, A., T. Rohlfing, M. J. Rosenbloom, W. Chu, I. M. Colrain and E. V. Sullivan (2013). "Variation in longitudinal trajectories of regional brain volumes of healthy men and women (ages 10 to 85 years) measured with atlas-based parcellation of MRI." NeuroImage **65**: 176-193.

Piccolo, L. R. and K. G. Noble (2018). "Perceived stress is associated with smaller hippocampal volume in adolescence." Psychophysiology **55**(5): e13025.

Pievani, M., F. Agosta, E. Pagani, E. Canu, S. Sala, M. Absinta, C. Geroldi, R. Ganzola, G. B. Frisoni and M. Filippi (2010). "Assessment of white matter tract damage in mild cognitive impairment and Alzheimer's disease." Hum Brain Mapp **31**(12): 1862-1875.

Postel, C., A. Viard, C. Andre, F. Guenole, R. de Flores, J. M. Baleyte, P. Gerardin, F. Eustache, J. Dayan and B. Guillery-Girard (2019). "Hippocampal subfields alterations in adolescents with post-traumatic stress disorder." Hum Brain Mapp **40**(4): 1244-1252.

Power, J. D., D. A. Fair, B. L. Schlaggar and S. E. Petersen (2010). "The development of human functional brain networks." Neuron **67**(5): 735-748.

Preti M.G., Baglio F., Laganà M.M., Griffanti, L., Nemni, R., Clerici, M., Bozzali, M., Baselli, G.(2012). "Assessing corpus callosum changes in Alzheimer's disease: comparison between tract-based spatial statistics and atlas-based tractography." PLoS One **7**(4):e35856.

Pringle, J., K. Mills, J. McAteer, R. Jepson, E. Hogg, N. Anand and S. J. Blakemore (2016). "A systematic review of adolescent physiological development and its relationship with health-related behaviour: a protocol." Syst Rev **5**: 3.

Pruessmann, K. P., M. Weiger, M. B. Scheidegger and P. Boesiger (1999). "SENSE: sensitivity encoding for fast MRI." Magn Reson Med **42**(5): 952-962.

Pykett, I. L., B. R. Rosen, F. S. Buonanno and T. J. Brady (1983). "Measurement of spin-lattice relaxation times in nuclear magnetic resonance imaging." Physics in medicine and biology **28**(6): 723-729.

Rajmohan, V. and E. Mohandas (2007). "The limbic system." Indian J Psychiatry **49**(2): 132-139.

Redlich, R., N. Opel, C. Burger, K. Dohm, D. Grotegerd, K. Forster, D. Zaremba, S. Meinert, J. Repple, V. Enneking, E. Leehr, J. Bohnlein, L. Winters, N. Frobose, S. Thrun, J. Emtmann, W. Heindel, H. Kugel, V. Arolt, G. Romer, C. Postert and U. Dannlowski (2018). "The Limbic System in Youth Depression: Brain Structural and Functional Alterations in Adolescent In-patients with Severe Depression." Neuropsychopharmacology **43**(3): 546-554.

Reijmer, Y. D., A. Leemans, S. M. Heringa, I. Wielaard, B. Jeurissen, H. L. Koek and G. J. Biessels (2012). "Improved sensitivity to cerebral white matter abnormalities in Alzheimer's disease with spherical deconvolution based tractography." PLoS One **7**(8): e44074.

Reuter, M. and B. Fischl (2011). "Avoiding asymmetry-induced bias in longitudinal image processing." NeuroImage **57**(1): 19-21.

Riley, J. D., E. E. Chen, J. Winsell, E. P. Davis, L. M. Glynn, T. Z. Baram, C. A. Sandman, S. L. Small and A. Solodkin (2018). "Network specialization during adolescence: Hippocampal effective connectivity in boys and girls." Neuroimage **175**: 402-412.

Rimkus, C. M., M. M. Schoonheim, M. D. Steenwijk, H. Vrenken, A. J. Eijlers, J. Killestein, M. P. Wattjes, C. C. Leite, F. Barkhof and B. M. Tijms (2019). "Gray matter networks and cognitive impairment in multiple sclerosis." Mult Scler **25**(3): 382-391.

Roddy, D. W., C. Farrell, K. Doolin, E. Roman, L. Tozzi, T. Frodl, V. O'Keane and E. O'Hanlon (2019). "The Hippocampus in Depression: More Than the Sum of Its

Parts? Advanced Hippocampal Substructure Segmentation in Depression." Biological psychiatry **85**(6): 487-497.

Rollo, C. D. (2009). "Dopamine and aging: intersecting facets." Neurochemical research **34**(4): 601-629.

Rolls, E. T. (2015). "Limbic systems for emotion and for memory, but no single limbic system." Cortex **62**: 119-157.

Rubinov, M. and O. Sporns (2010). "Complex network measures of brain connectivity: uses and interpretations." Neuroimage **52**(3): 1059-1069.

Rudolph, K. D., W. Troop-Gordon, H. H. Modi and D. A. Granger (2018). "An exploratory analysis of the joint contribution of HPA axis activation and motivation to early adolescent depressive symptoms." Dev Psychobiol **60**(3): 303-316.

Sacchet, M. D., T. C. Ho, C. G. Connolly, O. Tymofiyeva, K. Z. Lewinn, L. K. Han, E. H. Blom, S. F. Tapert, J. E. Max, G. K. Frank, M. P. Paulus, A. N. Simmons, I. H. Gotlib and T. T. Yang (2016). "Large-Scale Hypoconnectivity Between Resting-State Functional Networks in Unmedicated Adolescent Major Depressive Disorder." Neuropsychopharmacology **41**(12): 2951-2960.

Sachser, N., S. Kaiser and M. B. Hennessy (2013). "Behavioural profiles are shaped by social experience: when, how and why." Philosophical transactions of the Royal Society of London. Series B, Biological sciences **368**(1618): 20120344-20120344.

Sadaghiani, S. and M. D'Esposito (2015). "Functional Characterization of the Cingulo-Opercular Network in the Maintenance of Tonic Alertness." Cereb Cortex **25**(9): 2763-2773.

Sahakian, B. J., R. G. Morris, J. L. Evenden, A. Heald, R. Levy, M. Philpot and T. W. Robbins (1988). "A comparative study of visuospatial memory and learning in Alzheimer-type dementia and Parkinson's disease." Brain **111 (Pt 3)**: 695-718.

Sala, S., F. Agosta, E. Pagani, M. Copetti, G. Comi and M. Filippi (2012). "Microstructural changes and atrophy in brain white matter tracts with aging." Neurobiology of aging **33**(3): 488-498.e482.

Sallis, H., J. Evans, R. Wootton, E. Krapohl, A. J. Oldehinkel, G. Davey Smith and L. Paternoster (2017). "Genetics of depressive symptoms in adolescence." BMC psychiatry **17**(1): 321-321.

Sampedro-Piquero, P., P. Alvarez-Suarez and A. Begega (2018). "Coping with Stress During Aging: The Importance of a Resilient Brain." Current neuropharmacology **16**(3): 284-296.

Satterthwaite, T. D., S. Vandekar, D. H. Wolf, K. Ruparel, D. R. Roalf, C. Jackson, M. A. Elliott, W. B. Bilker, M. E. Calkins, K. Prabhakaran, C. Davatzikos, H. Hakonarson, R. E. Gur and R. C. Gur (2014). "Sex differences in the effect of puberty on hippocampal morphology." J Am Acad Child Adolesc Psychiatry **53**(3): 341-350.e341.

Sawyer, S. M., R. A. Afifi, L. H. Bearinger, S. J. Blakemore, B. Dick, A. C. Ezeh and G. C. Patton (2012). "Adolescence: a foundation for future health." Lancet **379**(9826): 1630-1640.

Schaefer, A., R. Kong, E. M. Gordon, T. O. Laumann, X. N. Zuo, A. J. Holmes, S. B. Eickhoff and B. T. T. Yeo (2017). "Local-Global Parcellation of the Human Cerebral Cortex from Intrinsic Functional Connectivity MRI." Cereb Cortex: 1-20.

Scherf, K. S., J. M. Smyth and M. R. Delgado (2013). "The amygdala: an agent of change in adolescent neural networks." Horm Behav **64**(2): 298-313.

Scherzinger, A. L. and W. R. Hendee (1985). "Basic principles of magnetic resonance imaging--an update." The Western journal of medicine **143**(6): 782-792.

Schneider JF, Vergesslich K (2007). "Maturation of the limbic system revealed by MR FLAIR imaging. Pediatr Radiol **37**(4):351-355.

Schreiner, S. J., X. Liu, A. F. Gietl, M. Wyss, S. C. Steininger, E. Gruber, V. Treyer, I. B. Meier, A. M. Kalin, S. E. Leh, A. Buck, R. M. Nitsch, K. P. Pruessmann, C. Hock and P. G. Unschuld (2014). "Regional Fluid-Attenuated Inversion Recovery (FLAIR) at 7 Tesla correlates with amyloid beta in hippocampus and brainstem of cognitively normal elderly subjects." Front Aging Neurosci **6**: 240.

Schultz, C. and M. Engelhardt (2014). "Anatomy of the hippocampal formation." Frontiers of neurology and neuroscience **34**: 6-17.

Schumann, G., E. Loth, T. Banaschewski, A. Barbot, G. Barker, C. Buchel, P. J. Conrod, J. W. Dalley, H. Flor, J. Gallinat, H. Garavan, A. Heinz, B. Itterman, M. Lathrop, C. Mallik, K. Mann, J. L. Martinot, T. Paus, J. B. Poline, T. W. Robbins, M. Rietschel, L. Reed, M. Smolka, R. Spanagel, C. Speiser, D. N. Stephens, A. Strohle and M. Struve (2010). "The IMAGEN study: reinforcement-related behaviour in normal brain function and psychopathology." Mol Psychiatry **15**(12): 1128-1139.

Scott, G. C., M. G. Joy, R. L. Armstrong and R. M. Henkelman (1995). "Electromagnetic considerations for RF current density imaging [MRI technique]." IEEE Trans Med Imaging **14**(3): 515-524.

Servaas, M. N., J. van der Velde, S. G. Costafreda, P. Horton, J. Ormel, H. Riese and A. Aleman (2013). "Neuroticism and the brain: a quantitative meta-analysis of neuroimaging studies investigating emotion processing." Neuroscience and biobehavioral reviews **37**(8): 1518-1529.

Shaikh, S., A. Kumar and A. Bansal (2018). "Diffusion tensor imaging: An overview." Neurology India **66**(6): 1603-1611.

Shao, J., N. Myers, Q. Yang, J. Feng, C. Plant, C. Bohm, H. Forstl, A. Kurz, C. Zimmer, C. Meng, V. Riedl, A. Wohlschlager and C. Sorg (2012). "Prediction of Alzheimer's disease using individual structural connectivity networks." Neurobiol Aging **33**(12): 2756-2765.

Sibilia, F., E. G. Kehoe, D. Farrell, C. Kerskens, D. O'Neill, J. P. McNulty, P. Mullins and A. L. W. Bokde (2017). "Aging-Related Microstructural Alterations Along the Length of the Cingulum Bundle." Brain Connect **7**(6): 366-372.

Silk, J. S., G. J. Siegle, K. H. Lee, E. E. Nelson, L. R. Stroud and R. E. Dahl (2014). "Increased neural response to peer rejection associated with adolescent depression and pubertal development." Soc Cogn Affect Neurosci **9**(11): 1798-1807.

Smith, C. D. (2012). "Structural imaging in early pre-states of dementia." Biochimica et biophysica acta **1822**(3): 317-324.

Soares, J. M., P. Marques, R. Magalhaes, N. C. Santos and N. Sousa (2014). "Brain structure across the lifespan: the influence of stress and mood." Front Aging Neurosci **6**: 330.

Soares, J. M., A. Sampaio, L. M. Ferreira, N. C. Santos, P. Marques, F. Marques, J. A. Palha, J. J. Cerqueira and N. Sousa (2013). "Stress Impact on Resting State Brain Networks." PLoS One **8**(6): e66500.

Sporns, O. (2013). "Structure and function of complex brain networks." Dialogues Clin Neurosci **15**(3): 247-262.

Sporns, O., G. Tononi and G. M. Edelman (2002). "Theoretical neuroanatomy and the connectivity of the cerebral cortex." Behav Brain Res **135**(1-2): 69-74.

Stadlbauer, A., E. Salomonowitz, G. Strunk, T. Hammen and O. Ganslandt (2008). "Quantitative diffusion tensor fiber tracking of age-related changes in the limbic system." Eur Radiol **18**(1): 130-137.

Stam, C. J. and J. C. Reijneveld (2007). "Graph theoretical analysis of complex networks in the brain." Nonlinear Biomed Phys **1**(1): 3.

Sugiura, M. (2016). "Functional neuroimaging of normal aging: Declining brain, adapting brain." Ageing research reviews **30**: 61-72.

Sullivan, E. V. and A. Pfefferbaum (2006). "Diffusion tensor imaging and aging." Neurosci Biobehav Rev **30**(6): 749-761.

Suo, X., D. Lei, F. Chen, M. Wu, L. Li, L. Sun, X. Wei, H. Zhu, L. Li, G. J. Kemp and Q. Gong (2017). "Anatomic Insights into Disrupted Small-World Networks in Pediatric Posttraumatic Stress Disorder." Radiology **282**(3): 826-834.

Suo, X., D. Lei, K. Li, F. Chen, F. Li, L. Li, X. Huang, S. Lui, L. Li, G. J. Kemp and Q. Gong (2015). "Disrupted brain network topology in pediatric posttraumatic stress disorder: A resting-state fMRI study." Hum Brain Mapp **36**(9): 3677-3686.

Sylvester, C. M., M. Corbetta, M. E. Raichle, T. L. Rodebaugh, B. L. Schlaggar, Y. I. Sheline, C. F. Zorumski and E. J. Lenze (2012). "Functional network dysfunction in anxiety and anxiety disorders." Trends Neurosci **35**(9): 527-535.

Tamnes, C. K., M. G. N. Bos, F. C. van de Kamp, S. Peters and E. A. Crone (2018). "Longitudinal development of hippocampal subregions from childhood to adulthood." Dev Cogn Neurosci **30**: 212-222.

Tamnes, C. K., K. B. Walhovd, A. Engvig, H. Grydeland, S. K. Krogsrud, Y. Ostby, D. Holland, A. M. Dale and A. M. Fjell (2014). "Regional hippocampal volumes and development predict learning and memory." Dev Neurosci **36**(3-4): 161-174.

Tan, L., L. Zhang, R. Qi, G. Lu, L. Li, J. Liu and W. Li (2013). "Brain structure in post-traumatic stress disorder: A voxel-based morphometry analysis." Neural Regen Res **8**(26): 2405-2414.

Tannous, J., H. Amaral-Silva, B. Cao, M.-J. Wu, G. B. Zunta-Soares, I. Kazimi, C. Zeni, B. Mwangi and J. C. Soares (2018). "Hippocampal subfield volumes in children and adolescents with mood disorders." Journal of psychiatric research **101**: 57-62.

Tannous, J., H. Amaral-Silva, B. Cao, M. J. Wu, G. B. Zunta-Soares, I. Kazimi, C. Zeni, B. Mwangi and J. C. Soares (2018). "Hippocampal subfield volumes in children and adolescents with mood disorders." J Psychiatr Res **101**: 57-62.

Taylor, P. A., A. Alhamud, A. van der Kouwe, M. G. Saleh, B. Laughton and E. Meintjes (2016). "Assessing the performance of different DTI motion correction strategies in the presence of EPI distortion correction." Hum Brain Mapp **37**(12): 4405-4424.

Teicher, M. H., C. M. Anderson, K. Ohashi and A. Polcari (2014). "Childhood maltreatment: altered network centrality of cingulate, precuneus, temporal pole and insula." Biol Psychiatry **76**(4): 297-305.

Teicher, M. H., C. M. Anderson and A. Polcari (2012). "Childhood maltreatment is associated with reduced volume in the hippocampal subfields CA3, dentate gyrus, and subiculum." Proc Natl Acad Sci U S A **109**(9): E563-572.

Teipel, S. J., M. Walter, Y. Likitjaroen, P. Schonknecht and O. Gruber (2014). "Diffusion tensor imaging in Alzheimer's disease and affective disorders." Eur Arch Psychiatry Clin Neurosci **264**(6): 467-483.

Thomas, C., N. Sadeghi, A. Nayak, A. Trefler, J. Sarlls, C. I. Baker and C. Pierpaoli (2018). "Impact of time-of-day on diffusivity measures of brain tissue derived from diffusion tensor imaging." Neuroimage **173**: 25-34.

Thurm, F., N. W. Schuck, M. Fauser, C. F. Doeller, Y. Stankevich, R. Evens, O. Riedel, A. Storch, U. Lueken and S. C. Li (2016). "Dopamine modulation of spatial navigation memory in Parkinson's disease." Neurobiol Aging **38**: 93-103.

Tijms, B. M., C. Moller, H. Vrenken, A. M. Wink, W. de Haan, W. M. van der Flier, C. J. Stam, P. Scheltens and F. Barkhof (2013). "Single-subject grey matter graphs in Alzheimer's disease." PLoS One **8**(3): e58921.

Tijms, B. M., P. Series, D. J. Willshaw and S. M. Lawrie (2012). "Similarity-based extraction of individual networks from gray matter MRI scans." Cereb Cortex **22**(7): 1530-1541.

Tournier, J. D., F. Calamante, D. G. Gadian and A. Connelly (2004). "Direct estimation of the fiber orientation density function from diffusion-weighted MRI data using spherical deconvolution." Neuroimage **23**(3): 1176-1185.

Tournier, J. D., Calamante, F., Connelly, A. (2007). " Robust determination of the fibre orientation distribution in diffusion MRI: non-negativity constrained super-resolved spherical deconvolution". Neuroimage **35**(4):1459-1472.

Tsai S.Y. (2018). "Reproducibility of structural brain connectivity and network metrics using probabilistic diffusion tractography." Sci Rep **8**(1): 11562.

Tyborowska, A., I. Volman, H. C. M. Niermann, J. L. Pouwels, S. Smeekens, A. H. N. Cillessen, I. Toni and K. Roelofs (2018). "Early-life and pubertal stress differentially modulate grey matter development in human adolescents." Sci Rep **8**(1): 9201.

Tzourio-Mazoyer, N., B. Landeau, D. Papathanassiou, F. Crivello, O. Etard, N. Delcroix, B. Mazoyer and M. Joliot (2002). "Automated anatomical labeling of

activations in SPM using a macroscopic anatomical parcellation of the MNI MRI single-subject brain." Neuroimage **15**(1): 273-289.

Tzschoppe, J., F. Nees, T. Banaschewski, G. J. Barker, C. Büchel, P. J. Conrod, H. Garavan, A. Heinz, E. Loth, K. Mann, J.-L. Martinot, M. N. Smolka, J. Gallinat, A. Ströhle, M. Struve, M. Rietschel, G. Schumann, H. Flor and I. consortium (2014). "Aversive learning in adolescents: modulation by amygdala-prefrontal and amygdala-hippocampal connectivity and neuroticism." Neuropsychopharmacology : official publication of the American College of Neuropsychopharmacology **39**(4): 875-884.

Uğurbil, K., G. Adriany, P. Andersen, W. Chen, M. Garwood, R. Gruetter, P.-G. Henry, S.-G. Kim, H. Lieu, I. Tkac, T. Vaughan, P.-F. Van De Moortele, E. Yacoub and X.-H. Zhu (2003). "Ultrahigh field magnetic resonance imaging and spectroscopy." Magnetic resonance imaging **21**(10): 1263-1281.

van den Heuvel, M. P. and O. Sporns (2013). "Network hubs in the human brain." Trends Cogn Sci **17**(12): 683-696.

van Geuns, R. J., P. A. Wielopolski, H. G. de Bruin, B. J. Rensing, P. M. van Ooijen, M. Hulshoff, M. Oudkerk and P. J. de Feyter (1999). "Basic principles of magnetic resonance imaging." Prog Cardiovasc Dis **42**(2): 149-156.

Van Leemput, K., A. Bakkour, T. Benner, G. Wiggins, L. L. Wald, J. Augustinack, B. C. Dickerson, P. Golland and B. Fischl (2009). "Automated segmentation of hippocampal subfields from ultra-high resolution in vivo MRI." Hippocampus **19**(6): 549-557.

Veer, I. M., N. Y. Oei, P. Spinhoven, M. A. van Buchem, B. M. Elzinga and S. A. Rombouts (2011). "Beyond acute social stress: increased functional connectivity between amygdala and cortical midline structures." Neuroimage **57**(4): 1534-1541.

Viard, A., J. Mutlu, S. Chanraud, F. Guenole, P. J. Egler, P. Gerardin, J. M. Baleyte, J. Dayan, F. Eustache and B. Guillery-Girard (2019). "Altered default mode network connectivity in adolescents with post-traumatic stress disorder." Neuroimage Clin **22**: 101731.

Vijayakumar, N., N. B. Allen, M. Dennison, M. L. Byrne, J. G. Simmons and S. Whittle (2017). "Cortico-amygdalar maturational coupling is associated with depressive symptom trajectories during adolescence." Neuroimage **156**: 403-411.

Vijayakumar, N., Z. Op de Macks, E. A. Shirtcliff and J. H. Pfeifer (2018). "Puberty and the human brain: Insights into adolescent development." Neurosci Biobehav Rev **92**: 417-436.

Vogel, S. and L. Schwabe (2016). "Learning and memory under stress: implications for the classroom." NPJ science of learning **1**: 16011-16011.

Vogt B.A. "Cingulate neurobiology and disease." Oxford: Oxford UniversityPress; 2009.

Vos de Wael, R., S. Lariviere, B. Caldairou, S. J. Hong, D. S. Margulies, E. Jefferies, A. Bernasconi, J. Smallwood, N. Bernasconi and B. C. Bernhardt (2018). "Anatomical and microstructural determinants of hippocampal subfield functional connectome embedding." Proc Natl Acad Sci U S A **115**(40): 10154-10159.

Wang, J. H., X. N. Zuo, S. Gohel, M. P. Milham, B. B. Biswal and Y. He (2011). "Graph theoretical analysis of functional brain networks: test-retest evaluation on short- and long-term resting-state functional MRI data." PLoS One **6**(7): e21976.

Watts, D. J. and S. H. Strogatz (1998). "Collective dynamics of 'small-world' networks." Nature **393**(6684): 440-442.

Westin C.F., Maier S.E. Mamata H., et al., (2002). “Processing and Visualization for Diffusion Tensor MRI,” Medical Image Analysis **6**(2), pp. 93-108.

Whitford, T. J., M. Kubicki and M. E. Shenton (2011). "Diffusion tensor imaging, structural connectivity, and schizophrenia." Schizophrenia research and treatment 2011: 709523-709523.

Whittall, K. P., A. L. MacKay, D. A. Graeb, R. A. Nugent, D. K. Li and D. W. Paty (1997). "In vivo measurement of T2 distributions and water contents in normal human brain." Magnetic resonance in medicine **37**(1): 34-43.

Whittle, S., J. G. Simmons, S. Hendriksma, N. Vijayakumar, M. L. Byrne, M. Dennison and N. B. Allen (2017). "Childhood maltreatment, psychopathology, and the development of hippocampal subregions during adolescence." Brain Behav **7**(2): e00607.

Wu, J., X. Geng, R. Shao, N. M. L. Wong, J. Tao, L. Chen, C. C. H. Chan and T. M. C. Lee (2018). "Neurodevelopmental changes in the relationship between stress perception and prefrontal-amygdala functional circuitry." Neuroimage Clin **20**: 267-274.

Wu, Y., D. Sun, Y. Wang, Y. Wang and S. Ou (2016). "Segmentation of the Cingulum Bundle in the Human Brain: A New Perspective Based on DSI Tractography and Fiber Dissection Study." Frontiers in neuroanatomy **10**: 84-84.

Xia, L. and S. Yao (2015). "The Involvement of Genes in Adolescent Depression: A Systematic Review." Frontiers in behavioral neuroscience **9**: 329-329.

Xu, J., F. Chen, D. Lei, W. Zhan, X. Sun, X. Suo, Z. Peng, T. Wang, J. Zhang and Q. Gong (2018). "Disrupted Functional Network Topology in Children and Adolescents With Post-traumatic Stress Disorder." Front Neurosci **12**: 709.

Yakovlev, P. I. (1948). "Motility, behavior and the brain; stereodynamic organization and neural coordinates of behavior." J Nerv Ment Dis **107**(4): 313-335.

Yaribeygi, H., Y. Panahi, H. Sahraei, T. P. Johnston and A. Sahebkar (2017). "The impact of stress on body function: A review." Excli j **16**: 1057-1072.

Yeckel, M. F. and T. W. Berger (1990). "Feedforward excitation of the hippocampus by afferents from the entorhinal cortex: redefinition of the role of the trisynaptic pathway." Proceedings of the National Academy of Sciences of the United States of America **87**(15): 5832-5836.

Yin, Y., C. Jin, L. T. Eyler, H. Jin, X. Hu, L. Duan, H. Zheng, B. Feng, X. Huang, B. Shan, Q. Gong and L. Li (2012). "Altered regional homogeneity in post-traumatic stress disorder: a resting-state functional magnetic resonance imaging study." Neurosci Bull **28**(5): 541-549.

Yu, Q., A. M. Daugherty, D. M. Anderson, M. Nishimura, D. Brush, A. Hardwick, W. Lacey, S. Raz and N. Ofen (2018). "Socioeconomic status and hippocampal volume in children and young adults." Dev Sci **21**(3): e12561.

Yuan, J. P., E. Henje Blom, T. Flynn, Y. Chen, T. C. Ho, C. G. Connolly, R. A. Dumont Walter, T. T. Yang, D. Xu and O. Tymofiyeva (2019). "Test-Retest Reliability of Graph Theoretic Metrics in Adolescent Brains." Brain Connect **9**(2): 144-154.

Yuii, K., M. Suzuki and M. Kurachi (2007). "Stress sensitization in schizophrenia." Ann N Y Acad Sci **1113**: 276-290.

Yushkevich, P. A., B. B. Avants, J. Pluta, S. Das, D. Minkoff, D. Mechanic-Hamilton, S. Glynn, S. Pickup, W. Liu, J. C. Gee, M. Grossman and J. A. Detre (2009). "A high-resolution computational atlas of the human hippocampus from postmortem magnetic resonance imaging at 9.4 T." Neuroimage **44**(2): 385-398.

Zach, P., K. Vales, A. Stuchlik, P. Cermakova, J. Mrzilkova, A. Koutela and M. Kutova (2016). "Effect of stress on structural brain asymmetry." Neuro endocrinology letters **37**(4): 253-264.

Zahr, N. M., T. Rohlfing, A. Pfefferbaum and E. V. Sullivan (2009). "Problem solving, working memory, and motor correlates of association and commissural fiber bundles in normal aging: a quantitative fiber tracking study." NeuroImage **44**(3): 1050-1062.

Zalesky, A., L. Cocchi, A. Fornito, M. M. Murray and E. Bullmore (2012). "Connectivity differences in brain networks." Neuroimage **60**(2): 1055-1062.

Zalesky, A., A. Fornito and E. T. Bullmore (2010). "Network-based statistic: identifying differences in brain networks." Neuroimage **53**(4): 1197-1207.

Zilverstand, A., Huang, A. S., Alia-Klein, N., & Goldstein, R. Z. (2018). "Neuroimaging Impaired Response Inhibition and Salience Attribution in Human Drug Addiction: A Systematic Review." Neuron, **98**(5), 886–903.

Appendix A

Supplementary material of the manuscript entitled: "STRUCTURAL CONNECTIVITY ALTERATIONS OF THE CORTEX IN ADOLESCENTS DUE TO STRESSFUL LIFE EVENTS" by Sibilia et al.

1. Supplementary introduction

Graph theory is a mathematical approach to further understand brain connectivity (Sporns 2013), that defines the brain as a network, made of "nodes" (i.e. regions of interest, or also called vertices) and "edges" (structural or functional connections between brain regions) (van den Heuvel and Sporns 2013). Graphs can be distinguished in directed or undirected, where the directed graphs have edges connected to vertices in a specific direction (Bullmore and Sporns 2009). Connectivity correlation coefficients are estimated between all possible node pairs, building a connectivity matrix (or sometimes called also adjacency matrix); a threshold is then applied to binarize the weighted correlation matrix, such that an edge is present if its value is higher than the threshold (taking on a value of 1; if its value is lower than the threshold, then it is 0). The binary adjacency matrix is used to compute graph metrics (Tijms, Series et al. 2012). For weighted graphs, edges are indicated by weights, which represent the connectivity strength between two nodes considered. Metrics used in graph analysis can provide information about brain networks at both a "global" level (considering the whole brain) and "local" level (describing the properties at the level of each node) in a given network (Ho, Dennis et al. 2018).

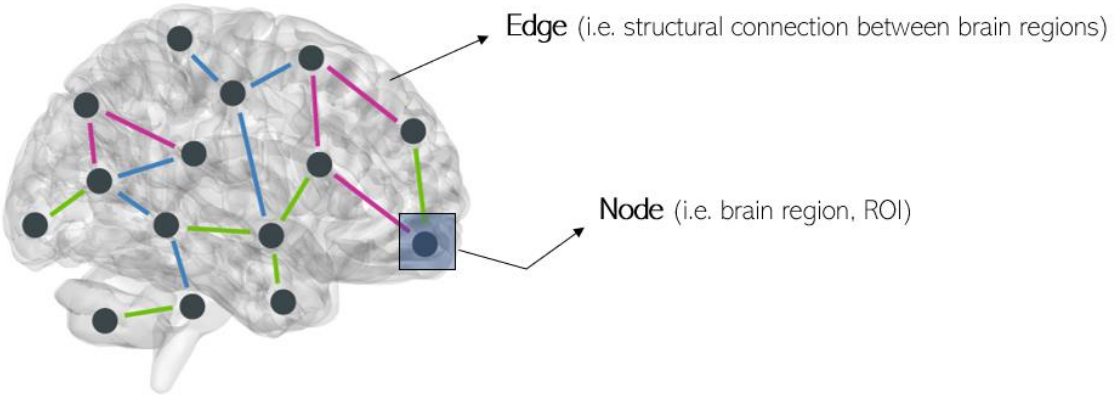

Graph theory measures describe the network properties of segregation, integration, centrality and density (Bullmore and Sporns 2009) (Figure A1). Segregation allows information flow and processing within highly connected groups of brain regions, called clusters; integration refers to the global transmission of information across brain regions (Sporns 2013). Segregation and integration are two important properties in brain networks, allowing information to flow rapidly at a low wiring cost. Cluster coefficient (CP) is a measure of functional segregation in the brain, which is the ability of some brain areas to cluster because of structural or functional connections; it calculates the number of connections among a node's topological neighbours (Sporns 2013), also defined as the number of closed triangles that a node's neighbours form. A brain region (node) is defined neighbour of node *i* when it is connected to node *i* by and edge (Stam and Reijneveld 2007). Cluster coefficient can be measured at a local level, indicating the tendency of each node to form clusters with its neighbours, and at a global level, calculating the mean cluster coefficient. High CP means high resilience of the network against random alterations.

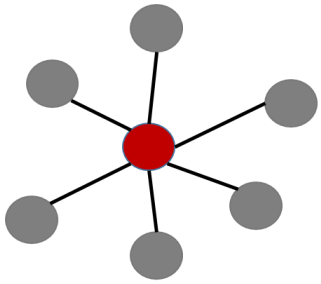

Betweenness Centrality

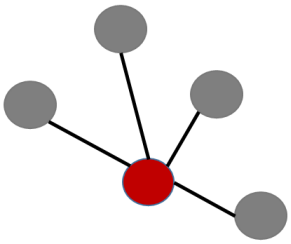

Degree Centrality

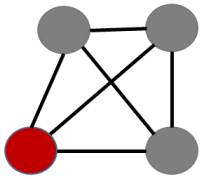

Cluster coefficient

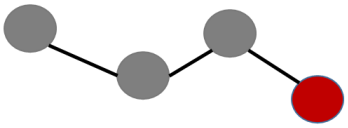

Characteristic Path Length

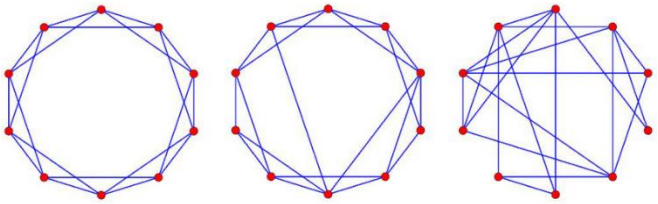

Figure A1: Graphical representation of graph theory metrics considered in this study. Betweenness and degree are measures of node centrality, cluster coefficient described segregation properties and characteristic path length represents the integration property of brain networks. The last image represents the organization of the brain as graph, defined "small-worldness", which influences the network economy.

2. Supplementary Methods

MRI Quality check

Images were checked and classified as: A (best image quality), B (intermediate image quality) or C (bad image quality). The Consortium provided material with information on the parameters used to determine image quality:

1) Ring (R1 at R4): Global motion
2) Blink (BL1 or BL2): eyes motion
3) Noise (N1 or N2): antenna's quality, sequence parameters
4) Small field of view (1 or 2): sequence parameters, operator dependant
5) Artefacts: sequence parameters (noise on one slice), operator dependant (metal object)
6) Others: anatomical anomalies (cyst, large ventricles)

Images were classified as "A" (best image quality) if they satisfied the following criteria:

a) R0
b) BL0
c) N0 or N1
d) Small field of view 1
e) BL at the bottom

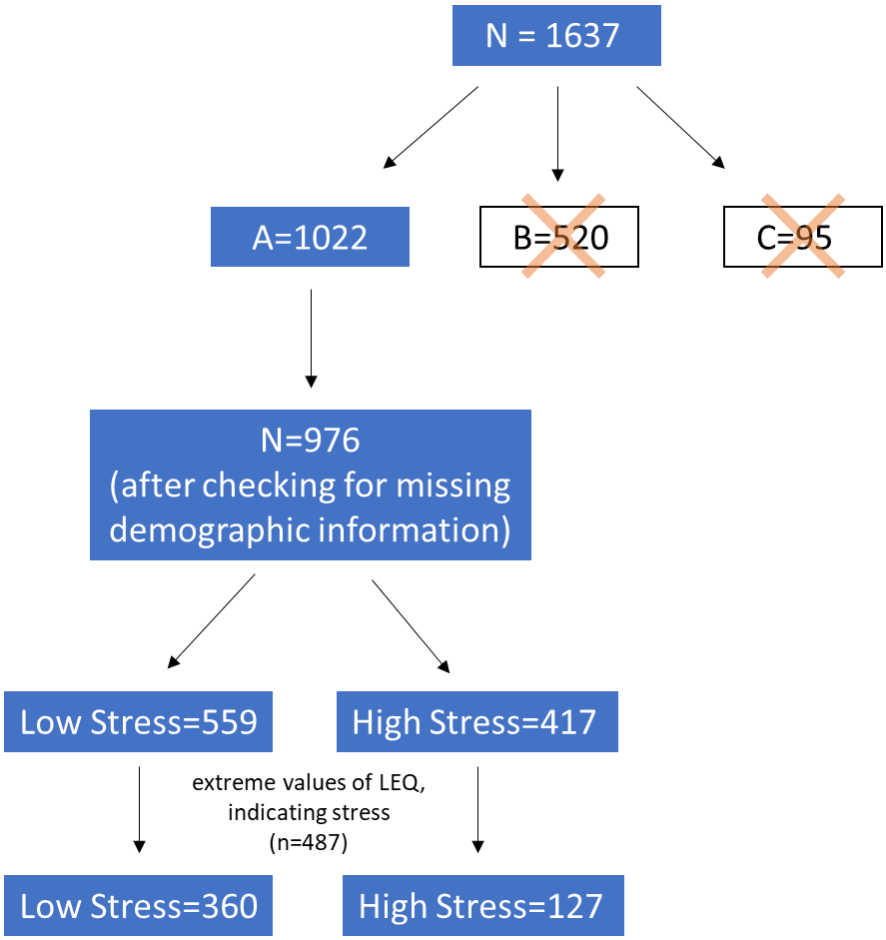

Figure A2: Diagram describing the steps to obtain the population size used in this study, including image quality check and missing demographic information

Figure A3 represents the list of negative life events we considered in our study. Life Event Questionnaire is a 39-question test, where each question represents a specific life event, which can be classified as negative, neutral or positive. Participants were asked to indicate if such event ever happened in their lifetime, if it happened in the last year of their life, and to rate the perceived desirability of each event on a numerical scale from -2 to +2 (-2= 'very unhappy' and +2= 'very happy'). The number of questions are from a previous study (Galinowski, Miranda et al. 2015) plus two more, i.e. "changed school" and "got poor grades at school", because we decided these two events representing a potential cause of stress.

item	Negative Life Events
1	Parents divorced
2	Family accident or illness
4	Got in trouble with the law
8	Death in family
9	Face broke out with pimples
11	Started seeing a therapist
14	Got or made pregnant
19	Got in trouble at school
20	Got or gave sexually transmitted disease
22	Family had money problems
24	Parents argued or fought
25	Ran away from home
30	Broke up with boy/girlfriend
31	Family moved
34	Parent remarried
35	Had a gay experience
36	Gained a lot of weight
37	Serious accident or illness
39	Parent abused alcohol

Figure A3: list of negative life events used in this study Galinowski et al., 2015), plus two additional questions.

2.1. Atlas-based ROI approach

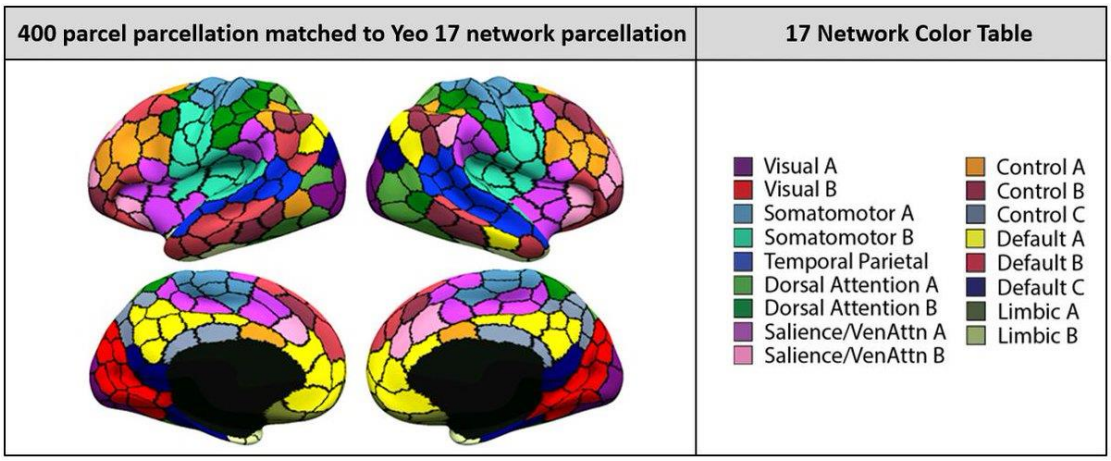

Figure A4: Representation of the 400 parcel and 17 network parcellation used in this study to carry out an ROI-based analysis (Yeo et al., 2011).

To get the coordinates, we calculated the centroids for each parcel/ROI. To do so, we used the command: **`3dcalc -prefix output.nii -a input -expr 'within(a,nROI, nROI)'`** in AFNI to extract each ROI from the brain parcellation singularly; afterwards, we used a command in FSL to calculate the coordinates of the centroid: **fslstats –t *output.nii* –C.**

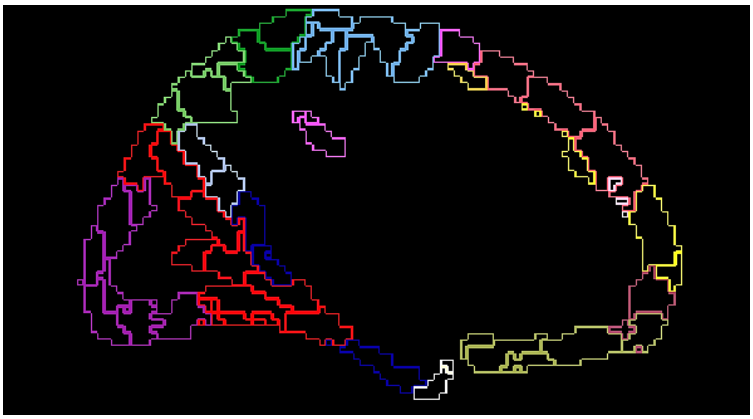

Figure A5: Sagittal view of the single parcels that form the 17 networks. Different colors identify the networks according to the lookup table indicated by Schaefer et al., 2018. The list of all the ROI order is available here: https://github.com/ThomasYeoLab/CBIG/blob/master/stable_projects/brain_parcellation/Schaefer2018_LocalGlobal/Parcellations/MNI/Schaefer2018_400Parcels_17Networks_order.txt.

2.2. Resize of the correlation matrices

Figure A6 describes the steps we did to reshape the correlation matrices for each individual in matrices of size 400x400 nodes (i.e. the number of parcels in Schaefer template). As shown in the image below, we took all the elements (i.e. indices) of the rows belonging to the ROI ***a***, and all the elements of the columns belonging to the ROI ***b***. We then calculated the average across all the two ROIs values, and we stored the new value in position (***a,b***) of the reshaped matrix.

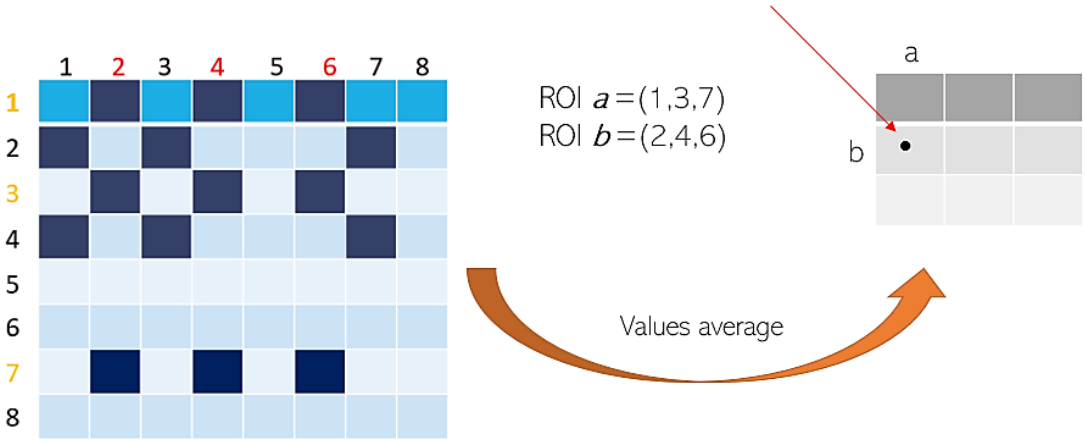

Figure A6: Graphical representation of the correlation matrices reshape steps.

3. Supplementary Results

3.1. Results of graph theory comparisons between the two groups with extreme stress values (N=487) at each sparsity level

		sp5	sp10	sp15	sp20	sp25	sp30	sp35
DC	LS	[39.995 40.004]	[79.990 80.002]	[119.989 120.003]	[159.994 160.008]	[199.996 200.01]	[239.992 240.007]	[279.987 280.001]
	HS	[39.988 40.005]	[79.983 80.004]	[119.980 120.004]	[159.988 160.012]	[200.004 200.029]	[239.997 240.021]	[279.992 280.015]
CP	LS	[.621 .626]	[.694 .698]	[.718 .721]	[.737 .740]	[.761 .764]	[.794 .795]	[.834 .835]
	HS	[.614 .623]	[.695 .701]	[.718 .724]	[.736 .741]	[.761 .765]	[.793 .796]	[.833 .834]
LP	LS	[2.207 2.219]	[1.926 1.931]	[1.750 1.754]	[1.614 1.617]	[1.497 1.501]	[1.391 1.395]	[1.288 1.292]
	HS	[2.202 2.222]	[1.924 1.934]	[1.748 1.754]	[1.612 1.618]	[1.496 1.503]	[1.390 1.397]	[1.287 1.295]
GE	LS	[.509 .511]	[.582 .584]	[.643 .645]	[.699 .700]	[.752 .754]	[.803 .805]	[.854 .856]
	HS	[.509 .512]	[.582 .584]	[.643 .645]	[.698 .701]	[.751 .754]	[.802 .805]	[.852 .857]
SW	LS	[11.665 11.793]	[6.575 6.614]	[4.901 4.921]	[4.016 4.027]	[3.495 3.502]	[3.183 3.191]	[3.008 3.019]
	HS	[11.540 11.758]	[6.576 6.642]	[4.905 4.940]	4.015 4.034]	[3.492 3.505]	[3.178 3.191]	[2.999 3.019]

Figure A7: 95% confident intervals (CI) values of global graph theory measure, which showed no significant differences between groups. Abbreviations: sp=sparsity, LS=Low Stress, HS=High Stress, DC= Degree Centrality, CP= Cluster Coefficient, LP=Path Length, GE=Global Efficiency, SW=Small Worldness.

4. Supplementary discussion

It has been shown that grey matter volume changes related to negative life events in adolescence are linked to the time of when such events happen, as well as the type of event they experience: Tyborowska and colleagues (2018) divided the event type into two groups, that is personal events (related to adolescents' relationship with parents and themselves) and social ones (related to their relationships with peers) (Tyborowska, Volman et al. 2018). Researchers found that adolescents between 14 and 17 years old had lower GMV due to NLE, and that such reductions depended on the nature of the negative life experience: more personal early-life stressful events were associated with larger reductions in GMV over anterior prefrontal cortex, amygdala and insula; whereas ongoing stress from the adolescents' interactions with their peers was related to smaller reductions over the orbitofrontal lobe and anterior cingulate cortex, which are involved in emotional processing and reward system. Researchers suggest that early-life stress accelerates pubertal development, whereas a difficult social life disturbs brain maturation with potential mental health implications. Another study taking into account our same psychological test to measure the stress level in adolescents, divided the events in three groups, i.e. event related to family, to personal distress and accident, measuring the correlation between functional connectivity in limbic regions, finding correlation between the type of events and the neural response, specifically for the 'distress' sub-scale of stressful events

(Burt, Whelan et al. 2016). This highlights the fact that the choice of NLEs grouping can affect connectivity analysis. In our study, we divided the two groups based on the total number of events each teenager experienced in their lifetime. It would be worthy looking at the same type of analysis with a different event grouping approach.

Supplementary information

Distribution of nodes based on degree centrality for all the sparsity levels (from 5% to 35%) in both groups

DC value (raw)	DC value (*z*)	ROI
109.1	4.738245748	LH_Limbic_TempPole_1
106.0833333	4.531392096	RH_Limbic_TempPole_2
105.825	4.513678109	RH_Limbic_TempPole_1
90.95277778	3.493885796	LH_Limbic_TempPole_2
88.64722222	3.335793226	LH_Limbic_TempPole_3
83.65833333	2.993703762	RH_Limbic_TempPole_3
81.93333333	2.875420044	RH_Limbic_TempPole_4
80.975	2.809706867	LH_Limbic_TempPole_4
78.96388889	2.671804432	LH_VisCent_ExStr_4
74.80277778	2.386475914	LH_VisCent_ExStr_3
74.08055556	2.336952941	LH_VisPeri_ExStrSup_4
72.01944444	2.195621993	LH_DefaultC_Rsp_1
71.83333333	2.182860303	RH_VisCent_ExStr_4
69.86944444	2.048195909	RH_VisCent_ExStr_2
69.675	2.034862801	RH_DefaultC_Rsp_1
69.54166667	2.025720098	RH_ContC_Cingp_1
69.24444444	2.00533949	RH_DefaultB_AntTemp_1
66.31388889	1.8043905	LH_VisCent_ExStr_5
66.21666667	1.797723946	RH_VisCent_ExStr_5
65.96111111	1.780200432	RH_DefaultC_PHC_1
65.32777778	1.736772594	RH_VisPeri_ExStrSup_2
65.275	1.733153607	LH_VisCent_ExStr_1
64.79166667	1.700011309	LH_DefaultC_PHC_1
64.3	1.666297593	LH_SomMotA_19
63.65833333	1.622298335	LH_DorsAttnB_PostC_9
63.61111111	1.619060294	RH_VisCent_ExStr_6

62.69722222	1.556394685	RH_DefaultB_Temp_2
61.51111111	1.475062725	LH_ContC_Cingp_1
61.46111111	1.471634211	RH_DorsAttnA_SPL_4
61.26388889	1.45811063	RH_Limbic_TempPole_5
61.16111111	1.45106313	LH_Limbic_TempPole_5
60.73611111	1.421920764	LH_DefaultB_Temp_1
60.31944444	1.393349818	RH_TempPar_3
60.15555556	1.382111912	LH_DefaultC_Rsp_2
59.74722222	1.354112385	LH_VisPeri_ExStrSup_5
59.22777778	1.318493939	LH_DefaultB_PFCv_2
58.43611111	1.26420914	LH_DefaultB_Temp_2
58.30555556	1.255256911	LH_DefaultC_PHC_3
58.03611111	1.236781032	RH_Limbic_TempPole_6
57.91944444	1.228781167	LH_SalVentAttnB_PFCv_1
57.68333333	1.212590964	LH_Limbic_TempPole_6
57.45277778	1.196781707	LH_ContC_Cingp_2
57.33888889	1.188972315	RH_VisPeri_ExStrSup_5
57.31944444	1.187639004	RH_DorsAttnA_TempOcc_1
57.13888889	1.175258261	RH_SomMotB_S2_9
56.83611111	1.154496706	LH_VisPeri_ExStrSup_2
56.77222222	1.150115828	RH_SomMotA_15
56.23333333	1.11316407	LH_SomMotA_6
55.91111111	1.091069205	LH_DorsAttnA_TempOcc_1
55.75833333	1.080593192	RH_DefaultB_Temp_1

Table A1: Distribution of nodes based on degree centrality at sparsity level 5% in Low Stress group. The first column contains the DC values, 2nd column are the DC values standardized to Z values, and 3rd column the name of the ROI.

DC value (raw)	DC value (*z*)	ROI
109.7322835	4.496596748	LH_Limbic_TempPole_1
107.4015748	4.346310611	RH_Limbic_TempPole_2
107.2362205	4.335648419	RH_Limbic_TempPole_1
94.58267717	3.51973686	LH_Limbic_TempPole_2
90.15748031	3.23439629	LH_VisCent_ExStr_4
86.8503937	3.021152447	RH_VisCent_ExStr_4
85.4488189	2.930777676	RH_Limbic_TempPole_3
84.56692913	2.873912651	LH_Limbic_TempPole_3
84.35433071	2.860204119	RH_Limbic_TempPole_4
83.88188976	2.829740712	LH_VisCent_ExStr_3
81.76377953	2.693163109	LH_Limbic_TempPole_4
76.17322835	2.33267947	LH_VisCent_ExStr_5
74.13385827	2.201179101	RH_ContC_Cingp_1
72.64566929	2.105219371	LH_VisPeri_ExStrSup_4
72.22047244	2.077802306	LH_VisCent_ExStr_1
71.47244094	2.02956858	LH_DefaultC_Rsp_1

70.54330709	1.969657214	LH_DefaultB_Temp_1
70.01574803	1.935639744	RH_VisCent_ExStr_6
68.17322835	1.816832461	RH_DefaultB_AntTemp_1
68.08661417	1.811247503	RH_SomMotB_S2_9
67.70866142	1.786876778	RH_VisCent_ExStr_5
66.66929134	1.719857285	RH_Limbic_TempPole_5
66.33070866	1.698025177	RH_DefaultC_Rsp_1
66.09448819	1.682793474	LH_DorsAttnB_PostC_9
66.01574803	1.67771624	LH_DefaultC_PHC_1
65.91338583	1.671115835	RH_VisCent_ExStr_2
64.23622047	1.562970743	RH_DefaultC_PHC_1
62.8503937	1.473611419	LH_ContC_Cingp_1
62.49606299	1.450763864	LH_DefaultB_PFCv_2
62.00787402	1.419285011	RH_VisPeri_ExStrSup_2
61.97637795	1.417254118	RH_Limbic_OFC_3
61.23622047	1.369528115	RH_DorsAttnA_SPL_4
61.15748031	1.364450881	RH_Limbic_TempPole_6
60.87401575	1.346172837	RH_SomMotA_15
60.68503937	1.333987475	LH_VisCent_ExStr_7
60.38582677	1.314693984	LH_Limbic_OFC_1
60.16535433	1.300477728	LH_ContC_Cingp_2
60.16535433	1.300477728	RH_SalVentAttnA_ParMed_2
59.49606299	1.257321236	RH_SomMotB_S2_5
58.91338583	1.219749702	LH_SomMotA_6
57.83464567	1.150191591	RH_SomMotA_20
57.70866142	1.142068016	LH_Limbic_TempPole_6
57.7007874	1.141560293	RH_DefaultB_PFCv_1
57.54330709	1.131405824	LH_DefaultB_Temp_2
57.22834646	1.111096887	LH_SomMotA_19
56.62992126	1.072509906	LH_VisPeri_ExStrSup_5
56.21259843	1.045600564	LH_DorsAttnA_TempOcc_1
55.75590551	1.016152605	LH_Limbic_TempPole_5
55.44094488	0.995843667	LH_DefaultC_Rsp_2
55.41732283	0.994320497	RH_Limbic_OFC_5

Table A2: Distribution of nodes based on degree centrality at sparsity level 5% in High Stress group. The first column contains the DC values, 2nd column are the DC values standardized to Z values, and 3rd column the name of the ROI.

DC value (raw)	DC value (*z*)	ROI
137.85	3.877297334	LH_Limbic_TempPole_1
137.7527778	3.870781598	RH_Limbic_TempPole_1
136.65	3.796874541	RH_Limbic_TempPole_2
128.6972222	3.263887374	LH_Limbic_TempPole_3

127.4972222	3.183464582	LH_Limbic_TempPole_2
121.4138889	2.775765701	RH_Limbic_TempPole_3
119.8888889	2.673561735	RH_Limbic_TempPole_4
117.6833333	2.525747621	LH_Limbic_TempPole_4
115.8527778	2.403065629	LH_VisCent_ExStr_3
115.6638889	2.390406486	LH_VisCent_ExStr_4
115.1222222	2.35410453	LH_VisPeri_ExStrSup_4
111.5888889	2.117304085	RH_DefaultC_Rsp_1
110.3111111	2.031668704	RH_VisCent_ExStr_4
110.2611111	2.028317754	LH_DefaultC_Rsp_1
109.6222222	1.985500063	RH_VisCent_ExStr_2
109.4611111	1.974702559	LH_DorsAttnB_PostC_9
108.0805556	1.882179114	LH_SomMotA_19
107.5888889	1.849228109	RH_DefaultB_AntTemp_1
107.1277778	1.818324906	RH_DefaultC_PHC_1
106.5638889	1.78053364	RH_ContC_Cingp_1
105.4944444	1.708860549	RH_VisCent_ExStr_5
104.7833333	1.661202598	RH_SalVentAttnA_ParMed_8
104.2888889	1.628065428	RH_DorsAttnA_SPL_4
103.6805556	1.58729554	LH_DefaultC_PHC_1
103.3972222	1.568306825	RH_VisPeri_ExStrSup_2
103.2944444	1.561418762	LH_VisCent_ExStr_5
102.8055556	1.528653921	RH_DefaultB_Temp_2
102.7805556	1.526978446	LH_VisCent_ExStr_1
102.6555556	1.518601071	RH_VisCent_ExStr_6
102.6277778	1.516739433	LH_SomMotA_6
101.925	1.469639973	LH_SomMotA_5
101.7055556	1.454933027	LH_VisPeri_ExStrSup_5
101.6472222	1.451023586	LH_SomMotA_13
101.0638889	1.411929173	LH_DefaultC_Rsp_2
100.45	1.370786957	RH_SomMotA_15
99.89722222	1.333740346	RH_VisPeri_ExStrSup_5
99.60277778	1.314006976	LH_DefaultB_Temp_1
99.58888889	1.313076156	RH_TempPar_3
99.19722222	1.28682705	LH_ContC_Cingp_2
99.10277778	1.280497479	LH_SalVentAttnB_PFCv_1
99.01666667	1.274726399	LH_DefaultB_PFCv_2
98.74722222	1.256668503	RH_ContA_Cinga_1
98.725	1.255179192	LH_Limbic_TempPole_5
98.50277778	1.240286082	RH_Limbic_TempPole_5
98.42777778	1.235259658	RH_SomMotB_S2_9
98.33333333	1.228930086	RH_SalVentAttnA_ParMed_2
98.21111111	1.220738876	RH_SalVentAttnA_ParMed_5
97.88055556	1.198585375	LH_ContA_Cinga_1
97.50555556	1.173453252	RH_DorsAttnA_TempOcc_1
96.60833333	1.113322321	RH_Limbic_TempPole_6

Table A3: Distribution of nodes based on degree centrality at sparsity level 10% in Low Stress

group. The first column contains the DC values, 2nd column are the DC values standardized to *Z* values, and 3rd column the name of the ROI.

DC value (raw)	DC value (*z*)	ROI
139.3307087	3.607009761	RH_Limbic_TempPole_2
139.2913386	3.604616536	LH_Limbic_TempPole_1
139.2755906	3.603659246	RH_Limbic_TempPole_1
132.4645669	3.189631221	LH_Limbic_TempPole_2
132.4015748	3.18580206	LH_VisCent_ExStr_4
129.1968504	2.990993498	RH_VisCent_ExStr_4
125.8110236	2.785176098	RH_Limbic_TempPole_3
124.4330709	2.701413203	RH_Limbic_TempPole_4
124.0866142	2.680352817	LH_VisCent_ExStr_3
123.480315	2.643497144	LH_Limbic_TempPole_3
119.1496063	2.38024233	LH_Limbic_TempPole_4
116.8346457	2.239520666	LH_VisCent_ExStr_5
115.3385827	2.148578094	RH_ContC_Cingp_1
114.9448819	2.124645838	LH_VisPeri_ExStrSup_4
113.2440945	2.021258493	LH_VisCent_ExStr_1
113.1181102	2.013600171	LH_DorsAttnB_PostC_9
112.0708661	1.949940371	RH_SomMotB_S2_9
110.5669291	1.858519154	LH_DefaultC_Rsp_1
109.8267717	1.813526513	LH_DefaultB_Temp_1
108.503937	1.733114133	RH_VisCent_ExStr_6
107.8661417	1.694343879	RH_SalVentAttnA_ParMed_2
107.6141732	1.679027235	RH_SomMotA_15
107.4173228	1.667061107	RH_DefaultB_AntTemp_1
106.5354331	1.613452854	RH_VisCent_ExStr_2
105.7322835	1.564631053	RH_VisCent_ExStr_5
105.3858268	1.543570668	RH_SomMotA_20
105.3464567	1.541177442	RH_Limbic_TempPole_5
105.2598425	1.535912346	LH_ContC_Cingp_2
105.2283465	1.533997765	LH_DefaultC_PHC_1
104.3543307	1.480868157	LH_SomMotA_6
103.3385827	1.419122937	RH_DorsAttnA_SPL_4
102.9606299	1.396147972	LH_SomMotA_19
102.3307087	1.357856363	RH_DefaultC_Rsp_1
102.3228346	1.357377718	RH_DefaultC_PHC_1
102.1653543	1.347804815	LH_DefaultB_PFCv_2
101.4724409	1.305684045	RH_SomMotA_14
101.0314961	1.278879919	RH_VisPeri_ExStrSup_2
100.6771654	1.257340888	RH_ContA_IPS_3
100.5984252	1.252554437	LH_ContC_Cingp_1
100.5511811	1.249682567	RH_SomMotA_16
100.519685	1.247767986	LH_DorsAttnA_SPL_5
100.503937	1.246810696	LH_Limbic_OFC_1

100.3779528	1.239152374	LH_VisCent_ExStr_7
100.0629921	1.220006569	RH_Limbic_OFC_3
98.72440945	1.1386369	RH_SomMotB_S2_5
98.59055118	1.130499933	RH_SomMotA_8
98.54330709	1.127628062	LH_DefaultC_Rsp_2
97.83464567	1.084550002	LH_VisPeri_ExStrSup_5
97.81102362	1.083114066	RH_Limbic_TempPole_6
97.77165354	1.080720841	LH_TempPar_2

Table A4: Distribution of nodes based on degree centrality at sparsity level 10% in High Stress group. The first column contains the DC values, 2nd column are the DC values standardized to Z values, and 3rd column the name of the ROI.

DC value (raw)	DC value (*z*)	ROI
160.1916667	3.269268984	RH_Limbic_TempPole_1
159.5055556	3.21346505	LH_Limbic_TempPole_3
158.2138889	3.10840906	RH_Limbic_TempPole_2
157.4277778	3.044471758	LH_Limbic_TempPole_1
155.8972222	2.919986058	LH_Limbic_TempPole_2
151.7944444	2.586292085	RH_Limbic_TempPole_3
150.6527778	2.493436146	RH_Limbic_TempPole_4
150.3222222	2.46655085	LH_VisCent_ExStr_3
147.7027778	2.25350182	LH_VisPeri_ExStrSup_4
147.4861111	2.235879525	LH_Limbic_TempPole_4
147.1388889	2.207638668	RH_SalVentAttnA_ParMed_8
146.6277778	2.166068125	LH_DorsAttnB_PostC_9
146.025	2.117041997	LH_VisCent_ExStr_4
145.075	2.03977501	RH_DefaultC_Rsp_1
144.7305556	2.01176008	LH_SomMotA_19
144.2527778	1.97290066	RH_VisCent_ExStr_2
142.7805556	1.853159424	LH_SomMotA_6
142.0611111	1.794644367	LH_SomMotA_5
141.9194444	1.783122097	RH_VisCent_ExStr_4
141.6694444	1.76278868	RH_DefaultC_PHC_1
141.4416667	1.744262677	LH_DefaultC_Rsp_1
141.2888889	1.7318367	RH_DefaultB_AntTemp_1
141.1472222	1.72031443	LH_SomMotA_13
139.1277778	1.556065602	RH_SomMotA_15
139.1	1.553806334	RH_VisCent_ExStr_5
138.7833333	1.528050672	RH_DorsAttnA_SPL_4
138.2444444	1.484220861	RH_SalVentAttnA_ParMed_5
138.0916667	1.471794883	RH_SalVentAttnA_ParMed_2

137.8694444	1.453720735	RH_VisPeri_ExStrSup_5
137.2388889	1.402435337	RH_DefaultB_Temp_2
137.2305556	1.401757557	RH_SomMotA_8
137.125	1.393172336	LH_DorsAttnB_FEF_3
137.0555556	1.387524165	LH_DefaultC_PHC_1
137.0194444	1.384587115	LH_ContA_Cinga_1
136.9527778	1.379164871	RH_SomMotA_14
136.9305556	1.377357456	LH_VisPeri_ExStrSup_5
136.7777778	1.364931479	RH_VisCent_ExStr_6
136.1472222	1.313646081	LH_DefaultC_Rsp_2
136.0138889	1.302801592	RH_VisPeri_ExStrSup_2
135.7527778	1.281564467	LH_VisCent_ExStr_5
135.6277778	1.271397758	RH_ContC_Cingp_1
135.4916667	1.260327342	LH_SomMotA_7
135.3833333	1.251516195	LH_VisCent_ExStr_1
135.3416667	1.248127292	RH_ContA_Cinga_1
135.0694444	1.225986459	RH_SomMotA_20
134.9555556	1.216723458	RH_SomMotA_17
134.9555556	1.216723458	RH_DorsAttnA_TempOcc_1
134.8555556	1.208590091	LH_SalVentAttnB_PFCv_1
134.7805556	1.202490066	LH_DorsAttnB_PostC_2
134.4555556	1.176056623	LH_ContC_Cingp_2

Table A5: Distribution of nodes based on degree centrality at sparsity level 15% in Low Stress group. The first column contains the DC values, 2nd column are the DC values standardized to *Z* values, and 3rd column the name of the ROI.

DC value (raw)	DC value (*z*)	ROI
164.6141732	3.166168988	LH_VisCent_ExStr_4
162.3622047	3.006380963	RH_Limbic_TempPole_1
161.2834646	2.929839147	RH_Limbic_TempPole_2
160.8031496	2.895758484	RH_VisCent_ExStr_4
160.2519685	2.856649527	LH_Limbic_TempPole_2
159.6850394	2.816423171	LH_Limbic_TempPole_1
157.3149606	2.648254655	LH_VisCent_ExStr_3
156.4566929	2.587356422	RH_Limbic_TempPole_3
155.4488189	2.5158429	RH_Limbic_TempPole_4
154.7086614	2.463325158	LH_Limbic_TempPole_3
151.3858268	2.227554016	LH_DorsAttnB_PostC_9
150.4409449	2.160510089	LH_VisCent_ExStr_5
149.9370079	2.124753328	LH_VisPeri_ExStrSup_4
149.4094488	2.087320469	LH_Limbic_TempPole_4
148.4409449	2.018600445	RH_SalVentAttnA_ParMed_2
147.3385827	1.94038253	RH_SomMotB_S2_9

146.4724409	1.878925598	RH_SomMotA_15
146.2440945	1.862723315	LH_VisCent_ExStr_1
146.2047244	1.859929818	RH_SomMotA_20
145.7874016	1.830318751	RH_ContC_Cingp_1
144.0708661	1.708522284	LH_DefaultB_Temp_1
143.0551181	1.636450063	LH_SomMotA_6
142.9370079	1.628069572	RH_SomMotA_14
142.8503937	1.621923879	RH_ContA_IPS_3
142.511811	1.597899805	RH_VisCent_ExStr_2
141.5984252	1.533090676	RH_SomMotA_8
141.5905512	1.532531977	LH_SomMotA_19
141.5826772	1.531973277	RH_SomMotA_16
141.2834646	1.510742701	RH_DefaultB_AntTemp_1
140.9133858	1.484483829	LH_ContC_Cingp_2
140.6535433	1.46604675	LH_DefaultC_Rsp_1
140.4488189	1.451520565	RH_DorsAttnB_FEF_3
139.4488189	1.380565743	RH_VisCent_ExStr_6
139.4094488	1.377772246	LH_DorsAttnB_FEF_3
139.3307087	1.372185252	LH_DorsAttnA_SPL_5
139.1181102	1.357100369	RH_DorsAttnA_SPL_4
138.8818898	1.340339387	RH_Limbic_TempPole_5
137.5984252	1.249271387	LH_TempPar_2
137.5669291	1.247036589	LH_DefaultC_Rsp_2
137.4251969	1.23698	LH_DefaultC_PHC_1
137.4094488	1.235862602	LH_DefaultB_PFCv_2
136.8031496	1.192842749	RH_SomMotA_6
136.6535433	1.18222746	RH_VisCent_ExStr_5
136.6456693	1.181668761	LH_SalVentAttnA_ParMed_2
136.5511811	1.174964368	LH_Limbic_OFC_1
136.3937008	1.16379038	LH_VisCent_ExStr_7
135.9527559	1.132503215	RH_SomMotA_2
135.7716535	1.119653129	RH_DorsAttnB_PostC_4
135.1811024	1.077750675	LH_DorsAttnA_SPL_6
134.8818898	1.056520098	LH_VisPeri_ExStrSup_5

Table A6: Distribution of nodes based on degree centrality at sparsity level 15% in High Stress group. The first column contains the DC values, 2nd column are the DC values standardized to Z values, and 3rd column the name of the ROI.

DC value (raw)	DC value (*z*)	ROI
187.2388889	2.932386233	LH_Limbic_TempPole_3
184.9194444	2.682677393	RH_SalVentAttnA_ParMed_8
181.9361111	2.361495004	LH_VisCent_ExStr_3
181.1555556	2.277461251	LH_Limbic_TempPole_2
179.6555556	2.1159729	LH_DorsAttnB_PostC_9
179.1805556	2.064834922	RH_Limbic_TempPole_1

178.4805556	1.989473691	LH_SomMotA_6
178.1833333	1.957475073	RH_Limbic_TempPole_3
178.1305556	1.951793075	LH_SomMotA_5
177.9916667	1.93684045	RH_Limbic_TempPole_4
177.1027778	1.841143649	LH_SomMotA_19
177.0722222	1.837854072	RH_SomMotA_17
176.6666667	1.794192406	LH_SomMotA_13
176.525	1.778940729	RH_Limbic_TempPole_2
176.3444444	1.759502316	LH_VisPeri_ExStrSup_4
175.9388889	1.715840651	LH_DorsAttnB_FEF_3
175.9333333	1.715242546	RH_VisCent_ExStr_2
175.875	1.708962443	RH_SomMotA_14
175.4777778	1.666197935	RH_SomMotA_8
175.2027778	1.636591737	RH_SalVentAttnA_ParMed_5
175.0694444	1.622237217	RH_DefaultC_Rsp_1
175.0416667	1.619246692	LH_SomMotA_7
174.7361111	1.586350917	RH_DefaultC_PHC_1
174.7111111	1.583659444	LH_SalVentAttnA_FrMed_3
174.5527778	1.566613452	LH_Limbic_TempPole_4
174.4166667	1.551959879	RH_SomMotA_15
174.3777778	1.547773144	LH_SomMotA_11
174.2583333	1.534913886	LH_DorsAttnB_PostC_2
174.2083333	1.529530941	LH_Limbic_TempPole_1
173.9916667	1.506204846	LH_VisCent_ExStr_4
173.8222222	1.487962643	RH_SomMotA_19
173.7055556	1.475402438	RH_VisPeri_ExStrSup_5
173.6888889	1.473608123	RH_SalVentAttnA_ParMed_2
173.3	1.431740773	RH_SomMotA_2
173.1027778	1.410508045	RH_DefaultB_AntTemp_1
172.7194444	1.3692388	LH_DefaultB_PFCd_4
172.0361111	1.295671884	LH_DorsAttnA_SPL_8
171.8166667	1.272046736	LH_DorsAttnA_SPL_6
171.7777778	1.267860001	LH_ContA_Cinga_1
171.6972222	1.259187479	RH_DorsAttnB_PostC_8
171.6527778	1.254402638	RH_SomMotA_13
171.65	1.254103586	RH_DorsAttnA_TempOcc_1
171.3305556	1.219712548	LH_SomMotA_1
171.1861111	1.204161818	RH_VisCent_ExStr_4
171.1777778	1.20326466	RH_SomMotA_12
171.0361111	1.188012983	LH_SomMotA_2
170.7805556	1.160500153	LH_DefaultA_PFCd_2
170.5027778	1.130594902	RH_SomMotA_16
170.4305556	1.122819537	RH_VisCent_ExStr_5
170.3805556	1.117436592	RH_SomMotA_20

Table A7: Distribution of nodes based on degree centrality at sparsity level 20% in Low Stress group. The first column contains the DC values, 2nd column are the DC values standardized to Z values, and 3rd column the name of the ROI.

DC value (raw)	DC value (*z*)	ROI
192.9606299	2.987571981	LH_VisCent_ExStr_4
189.1653543	2.643559679	RH_VisCent_ExStr_4
186.3307087	2.38662103	LH_Limbic_TempPole_2
185.5433071	2.315249183	LH_VisCent_ExStr_3
185.1259843	2.277422105	RH_SalVentAttnA_ParMed_2
185.0393701	2.269571201	LH_DorsAttnB_PostC_9
184.1259843	2.186779859	RH_Limbic_TempPole_4
183.6141732	2.140388159	RH_Limbic_TempPole_3
183.2047244	2.103274798	LH_Limbic_TempPole_3
182.2047244	2.012632553	RH_SomMotA_20
182.0708661	2.000499339	RH_SomMotA_8
181.9606299	1.99050728	RH_DorsAttnB_FEF_3
181.5984252	1.957676231	RH_SomMotA_15
181.5433071	1.952680201	LH_VisCent_ExStr_5
181.496063	1.948397891	RH_Limbic_TempPole_1
180.992126	1.902719909	RH_ContA_IPS_3
180.6614173	1.872743733	RH_Limbic_TempPole_2
180.2204724	1.832775499	RH_SomMotA_14
179.7637795	1.791379827	LH_VisPeri_ExStrSup_4
179.0314961	1.72500401	RH_SomMotB_S2_9
178.992126	1.721435418	LH_DorsAttnB_PostC_4
178.8346457	1.707161048	RH_SomMotA_16
178.1968504	1.649349852	LH_DorsAttnB_FEF_3
178.1417323	1.644353823	LH_SalVentAttnA_ParMed_2
177.9527559	1.62722458	LH_SomMotA_6
177.7716535	1.610809055	LH_SomMotA_18
177.5433071	1.590111219	RH_VisCent_ExStr_2
177.0944882	1.549429267	LH_DorsAttnB_PostC_6
177.0708661	1.547288111	LH_SalVentAttnA_ParMed_1
177.0551181	1.545860674	LH_Limbic_TempPole_4
176.8818898	1.530158868	LH_Limbic_TempPole_1
176.7952756	1.522307965	LH_DefaultB_Temp_1
176.0708661	1.456645866	RH_SomMotA_6
176.007874	1.450936118	LH_SomMotA_11
175.6692913	1.420246224	LH_DorsAttnA_SPL_5
175.6692913	1.420246224	LH_DorsAttnA_SPL_8
175.6614173	1.419532505	LH_VisCent_ExStr_1
175.6377953	1.41739135	RH_SomMotA_9
175.4488189	1.400262107	LH_DorsAttnA_SPL_6
175.4173228	1.397407233	LH_SomMotA_19
175.3149606	1.388128893	LH_TempPar_2
174.7874016	1.340309755	RH_DorsAttnB_PostC_7
174.5748031	1.321039357	RH_DefaultB_AntTemp_1
174.480315	1.312474735	RH_DorsAttnB_PostC_4

174.1338583	1.281071122	LH_DorsAttnB_FEF_1
173.7165354	1.243244044	LH_SomMotA_2
173.6692913	1.238961733	RH_SomMotA_2
173.4645669	1.220405053	LH_SomMotA_7
173.1259843	1.189715158	LH_ContC_Cingp_2
173.0551181	1.183291692	LH_DefaultC_Rsp_2

Table A8: Distribution of nodes based on degree centrality at sparsity level 20% in High Stress group. The first column contains the DC values, 2nd column are the DC values standardized to *Z* values, and 3rd column the name of the ROI.

DC value (raw)	DC value (*z*)	ROI
219.9944444	2.304922735	RH_SalVentAttnA_ParMed_8
217.4138889	2.007398262	RH_SomMotA_19
216.85	1.942384841	RH_SomMotA_17
216.8388889	1.941103788	RH_SomMotA_7
216.7194444	1.927332472	LH_SomMotA_9
216.6666667	1.921247472	LH_DefaultB_PFCl_1
216.5083333	1.902992472	LH_SomMotA_11
216.225	1.87032563	LH_DefaultB_PFCl_2
216.05	1.850149051	RH_SalVentAttnA_ParMed_7
215.1833333	1.750226946	RH_SomMotA_12
214.6277778	1.686174315	RH_DorsAttnA_SPL_8
214.6138889	1.684572999	LH_DorsAttnB_PostC_6
214.5944444	1.682331157	RH_DorsAttnB_PostC_7
214.5555556	1.677847473	RH_DorsAttnB_PostC_6
214.5555556	1.677847473	RH_ContA_PFCd_1
214.3833333	1.657991157	RH_SomMotA_13
214.1972222	1.636533525	RH_SomMotA_18
214.0527778	1.619879841	LH_SomMotA_1
214.0138889	1.615396157	LH_DefaultA_PFCd_2
213.775	1.587853525	LH_DorsAttnB_FEF_2
213.6527778	1.573761946	LH_DorsAttnB_FEF_1
213.5	1.556147473	LH_SomMotA_16
213.4166667	1.546539578	LH_SomMotA_7
213.3666667	1.540774841	LH_SalVentAttnA_FrMed_3
213.3277778	1.536291157	RH_SomMotA_14
213.1472222	1.515474052	RH_DefaultA_PFCd_2
213.0916667	1.509068789	RH_ContB_PFCld_4
213.0722222	1.506826947	LH_SomMotA_5
213	1.498500104	RH_SomMotA_11
212.9888889	1.497219052	RH_ContB_PFCld_3
212.8222222	1.478003262	RH_SomMotA_5
212.7861111	1.473839841	LH_Limbic_TempPole_3
212.6805556	1.461669841	LH_SomMotA_6
212.6638889	1.459748262	LH_DefaultB_PFCd_5

212.5944444	1.451741683	RH_SalVentAttnA_ParMed_1
212.5916667	1.45142142	LH_DorsAttnB_FEF_3
212.5861111	1.450780894	LH_DefaultB_PFCd_4
212.5777778	1.449820105	RH_SomMotA_8
212.3527778	1.423878789	RH_SalVentAttnA_PrC_1
211.9805556	1.380963526	LH_ContA_IPS_4
211.9555556	1.378081157	LH_DorsAttnB_PostC_2
211.8666667	1.367832736	LH_SomMotA_17
211.8444444	1.365270631	RH_SomMotA_2
211.7111111	1.349897999	LH_SalVentAttnA_FrMed_2
211.325	1.305381421	RH_DorsAttnB_FEF_2
211.2694444	1.298976157	LH_SomMotA_8
211.1638889	1.286806157	LH_SomMotA_14
211.0444444	1.273034842	LH_VisCent_ExStr_3
211.0388889	1.272394315	LH_SomMotA_2
210.8833333	1.254459578	LH_ContB_PFCmp_1

Table A9: Distribution of nodes based on degree centrality at sparsity level 25% in Low Stress group. The first column contains the DC values, 2nd column are the DC values standardized to Z values, and 3rd column the name of the ROI.

DC value (raw)	DC value (*z*)	ROI
222.0314961	2.315992449	RH_DorsAttnB_FEF_3
221.4645669	2.256350599	LH_DorsAttnB_PostC_4
221.3858268	2.248067009	LH_DorsAttnB_PostC_6
221.0629921	2.214104288	RH_DorsAttnB_PostC_7
220.5669291	2.161917669	LH_DorsAttnB_FEF_2
220.2598425	2.129611667	RH_ContB_PFCld_4
220.1968504	2.122984795	LH_SomMotA_18
220.0629921	2.108902691	RH_SomMotA_5
219.9291339	2.094820588	RH_SalVentAttnA_ParMed_2
219.6456693	2.064999663	LH_DorsAttnB_FEF_1
219.0393701	2.001216017	RH_SomMotA_8
218.7637795	1.972223451	LH_SalVentAttnA_ParMed_1
218.511811	1.945715962	LH_VisCent_ExStr_4
218.2125984	1.914238319	LH_DefaultA_PFCd_3
218.1023622	1.902641293	RH_ContA_PFCd_1
217.4724409	1.83637257	LH_SomMotA_11
216.5905512	1.743596358	LH_SalVentAttnA_ParMed_2
216.5748031	1.74193964	RH_SomMotA_13
216.1102362	1.693066458	LH_SomMotA_15
216.1023622	1.692238099	LH_DorsAttnB_PostC_9
215.984252	1.679812713	LH_DorsAttnB_PostC_8
215.7480315	1.654961942	RH_VisCent_ExStr_4

215.6141732	1.640879839	RH_SomMotA_20
215.2834646	1.606088759	RH_SomMotA_14
215.2283465	1.600290246	RH_SomMotA_9
215.1023622	1.587036502	RH_ContA_IPS_3
215.0314961	1.57958127	LH_DefaultB_PFCd_5
214.519685	1.525737933	LH_DorsAttnB_FEF_3
214.0866142	1.480178186	LH_SomMotA_1
214.007874	1.471894596	RH_DorsAttnB_PostC_3
213.9527559	1.466096083	RH_SomMotA_15
213.8897638	1.459469211	RH_SomMotA_19
213.6377953	1.432961722	LH_DorsAttnA_SPL_6
213.6377953	1.432961722	RH_SomMotA_16
213.5433071	1.423021413	RH_SomMotA_6
213.480315	1.416394541	LH_DorsAttnA_SPL_8
213.1732283	1.384088539	LH_SalVentAttnA_FrMed_1
213.1496063	1.381603462	LH_SalVentAttnA_FrMed_2
213.0708661	1.373319871	LH_SomMotA_7
212.8818898	1.353439255	LH_ContB_PFCmp_1
212.7480315	1.339357151	LH_SomMotA_2
212.5511811	1.318648175	LH_SomMotB_Aud_15
212.4724409	1.310364585	LH_VisCent_ExStr_3
212.3779528	1.300424277	LH_ContB_PFCd_1
212.2913386	1.291312327	RH_SomMotA_12
212.1732283	1.278886942	RH_DorsAttnB_FEF_2
212.1102362	1.272260069	RH_ContB_PFCmp_1
212.0708661	1.268118274	RH_DorsAttnA_SPL_7
212.0629921	1.267289915	LH_SomMotA_14
211.8188976	1.241610785	RH_Limbic_TempPole_4

Table A10: Distribution of nodes based on degree centrality at sparsity level 25% in High Stress group. The first column contains the DC values, 2nd column are the DC values standardized to Z values, and 3rd column the name of the ROI.

DC value (raw)	DC value (*z*)	ROI
268.25	2.477131614	LH_SomMotA_9
267.4361111	2.405763804	LH_DefaultB_PFCl_1
266.2833333	2.304679705	RH_ContB_PFCld_4
265.2527778	2.214312956	RH_ContA_PFCd_1
264.7388889	2.16925137	RH_SomMotA_7
263.1361111	2.028707936	LH_DefaultB_PFCl_2
262.1	1.937854035	LH_DefaultB_PFCd_1
261.9	1.920316553	RH_DefaultA_PFCd_2
261.8083333	1.91227854	RH_DorsAttnB_PostC_6
261.6138889	1.89522821	RH_SalVentAttnA_ParMed_7
260.2916667	1.779285966	LH_ContA_PFCd_1
260.0361111	1.756876961	RH_SalVentAttnA_ParMed_1

259.9388889	1.748351796	RH_SomMotA_5
259.5694444	1.715956169	LH_ContB_PFCmp_1
259.3111111	1.693303588	RH_SomMotA_19
258.7527778	1.644344783	RH_DorsAttnA_SPL_8
258.6305556	1.633627433	LH_DorsAttnB_FEF_2
258.6305556	1.633627433	LH_DefaultB_PFCd_5
258.5222222	1.624127963	RH_DorsAttnB_PostC_7
257.8944444	1.569079755	LH_DorsAttnB_PostC_6
257.7666667	1.557875253	RH_SomMotA_18
257.7444444	1.555926643	RH_DefaultB_PFCd_5
257.5944444	1.542773532	RH_DorsAttnB_FEF_2
257.3777778	1.523774593	LH_DorsAttnB_FEF_1
256.9805556	1.488943204	LH_SalVentAttnA_FrMed_2
256.7138889	1.465559895	RH_SomMotA_11
256.6805556	1.462636981	LH_SomMotA_11
256.6166667	1.45703473	LH_DefaultA_PFCd_2
256.5916667	1.454842544	RH_SomMotA_12
256.2527778	1.425126255	LH_SomMotA_4
255.8888889	1.39321778	LH_SomMotA_16
255.8083333	1.386154072	RH_ContB_PFCmp_1
255.5694444	1.365206524	LH_SomMotA_15
255.5611111	1.364475796	RH_SalVentAttnB_PFCmp_2
255.5416667	1.362770763	LH_SomMotA_12
255.4888889	1.358142816	LH_ContA_IPS_4
255.4555556	1.355219902	RH_SomMotA_13
255.2777778	1.339631029	RH_ContB_PFCld_2
255.2333333	1.335733811	RH_DorsAttnB_FEF_1
255.1916667	1.332080169	LH_SalVentAttnA_FrMed_1
255.1111111	1.32501646	RH_SalVentAttnA_PrC_1
255.0916667	1.323311427	RH_SomMotA_17
254.975	1.313081229	RH_ContB_PFCld_3
254.9222222	1.308453283	LH_SomMotA_1
254.7083333	1.28969792	RH_SalVentAttnB_PFCl_4
254.5333333	1.274352623	RH_DefaultA_PFCd_1
254.4277778	1.265096729	RH_SalVentAttnA_ParMed_8
254.3805556	1.260955935	LH_SomMotA_17
254.2861111	1.252674346	LH_SalVentAttnB_PFCl_2
254.1305556	1.239034082	LH_DefaultB_PFCd_6

Table A11: Distribution of nodes based on degree centrality at sparsity level 30% in Low Stress group. The first column contains the DC values, 2nd column are the DC values standardized to Z values, and 3rd column the name of the ROI.

DC value (raw)	**DC value (*z*)**	**ROI**
271.488189	2.850946064	RH_ContB_PFCld_4
268.3779528	2.569284872	LH_DorsAttnB_FEF_2

268.3543307	2.567145673	RH_ContA_PFCd_1
267.3228346	2.473733987	RH_SomMotA_5
265.5433071	2.312581001	RH_DorsAttnB_PostC_7
263.5354331	2.130749092	LH_DorsAttnB_FEF_1
262.9527559	2.077982185	LH_SomMotA_15
262.3858268	2.026641411	LH_DorsAttnB_PostC_4
262.2834646	2.017371549	LH_DorsAttnB_PostC_6
262.1417323	2.004536355	LH_DefaultA_PFCd_3
260.7480315	1.878323619	LH_ContB_PFCmp_1
260.3385827	1.84124417	RH_DefaultA_PFCm_1
260.2913386	1.836965773	LH_DefaultB_PFCd_5
260.1023622	1.819852181	LH_SomMotA_18
259.6929134	1.782772733	RH_DorsAttnB_FEF_3
258.7716535	1.699343975	LH_SalVentAttnA_FrMed_2
258.7559055	1.697917842	RH_ContB_PFCmp_1
258.3385827	1.660125328	RH_DorsAttnA_SPL_7
258.3149606	1.657986129	LH_DorsAttnB_PostC_8
258.2204724	1.649429333	RH_DorsAttnB_FEF_2
258.2047244	1.648003201	LH_SomMotA_11
257.9291339	1.62304588	LH_DefaultB_PFCl_2
257.7401575	1.605932288	RH_SomMotA_13
257.4645669	1.580974968	LH_SalVentAttnA_ParMed_1
257.3622047	1.571705106	RH_SomMotA_7
257.1732283	1.554591514	RH_DefaultA_PFCd_2
256.6614173	1.508242204	LH_DefaultB_PFCl_1
256.5748031	1.500398475	LH_DefaultB_PFCd_1
256.519685	1.49540701	RH_SomMotA_11
256.3464567	1.479719552	LH_SomMotA_1
256.2519685	1.471162756	RH_SomMotA_8
256.0944882	1.45690143	LH_SalVentAttnA_FrMed_1
255.976378	1.446205435	LH_SomMotB_Aud_15
255.9527559	1.444066236	RH_SomMotA_19
255.9212598	1.441213971	RH_DorsAttnB_PostC_3
255.7874016	1.429091844	RH_ContB_PFCld_2
255.4645669	1.399856125	RH_DorsAttnA_TempOcc_4
255.0708661	1.36420281	LH_SomMotA_14
254.9448819	1.352793749	LH_DefaultB_PFCd_6
254.7637795	1.336393223	RH_DorsAttnA_SPL_8
254.7244094	1.332827892	LH_ContA_PFCd_1
254.6299213	1.324271096	LH_SomMotA_9
254.4015748	1.303592173	RH_SomMotA_12
253.9606299	1.26366046	LH_SalVentAttnA_ParMed_2
253.8425197	1.252964465	RH_SomMotA_3
253.7637795	1.245833802	LH_ContB_PFCd_1
253.5748031	1.228720211	LH_SalVentAttnB_PFCl_2
253.5511811	1.226581012	RH_SalVentAttnA_PrC_1
253.2755906	1.201623691	RH_DorsAttnB_PostC_6
253.2440945	1.198771426	RH_SomMotA_9

Table A12: Distribution of nodes based on degree centrality at sparsity level 30% in High Stress group. The first column contains the DC values, 2nd column are the DC values standardized to Z values, and 3rd column the name of the ROI.

DC value (raw)	DC value (*z*)	ROI
314.4055556	2.29736072	RH_ContB_PFCld_4
314.1638889	2.281226859	LH_SomMotA_9
312.9722222	2.201670235	LH_DefaultB_PFCl_1
312.0055556	2.137134791	RH_ContA_PFCd_1
310.1472222	2.013070964	LH_DefaultB_PFCd_1
308.7027778	1.916638692	RH_SomMotA_7
307.9916667	1.869164343	LH_ContA_PFCd_1
306.9555556	1.799992733	RH_DefaultA_PFCd_2
306.7638889	1.787196912	LH_DefaultB_PFCl_2
305.7361111	1.718581642	RH_DorsAttnB_PostC_6
304.7833333	1.654973432	RH_SalVentAttnA_ParMed_7
304.7666667	1.653860752	LH_ContB_PFCmp_1
303.6194444	1.577271274	RH_SomMotA_5
303.4111111	1.563362773	RH_SalVentAttnA_ParMed_1
303.0916667	1.542036406	RH_SalVentAttnB_PFCl_4
302.2055556	1.482878916	RH_DefaultB_PFCd_5
302.1972222	1.482322576	LH_DefaultB_PFCd_5
301.9805556	1.467857735	LH_DorsAttnB_FEF_2
301.6277778	1.444306007	RH_SalVentAttnB_PFCmp_2
301.4722222	1.433920993	LH_SomMotA_4
300.9833333	1.401282378	RH_DorsAttnB_FEF_2
300.8138889	1.389970131	RH_ContB_PFCmp_1
300.7277778	1.384221284	RH_SomMotA_18
300.4277778	1.364193043	RH_SomMotA_19
300.2944444	1.355291602	RH_DorsAttnA_SPL_8
300.2944444	1.355291602	RH_DorsAttnB_PostC_7
300.1777778	1.347502842	RH_ContB_PFClv_4
300.0138889	1.336561488	LH_SomMotA_12
299.9722222	1.333779788	LH_SalVentAttnB_PFCl_2
299.9666667	1.333408894	RH_ContB_PFCld_2
299.9333333	1.331183534	RH_DorsAttnB_FEF_1
299.6222222	1.310413506	LH_SalVentAttnA_FrMed_2
299.2361111	1.284636418	LH_SomMotA_15
299.2222222	1.283709185	LH_DorsAttnB_PostC_6
298.9861111	1.267946217	LH_ContA_PFCl_4
298.9722222	1.267018984	RH_DefaultA_PFCd_1
298.8833333	1.26108469	LH_DorsAttnB_FEF_1
298.7	1.24884521	RH_DorsAttnA_SPL_7

298.475	1.233824029	RH_SomMotA_11
298.4333333	1.231042329	LH_DefaultB_PFCd_6
297.975	1.200443627	RH_SomMotA_12
297.9333333	1.197661927	RH_DefaultB_PFCd_4
297.8194444	1.190058613	LH_SomMotA_16
297.7027778	1.182269853	LH_ContA_IPS_4
297.5222222	1.170215819	LH_SalVentAttnA_FrMed_1
297.3805556	1.160758038	RH_DefaultA_PFCm_3
297.0666667	1.139802564	LH_DefaultA_PFCd_2
296.9388889	1.131272017	LH_DefaultB_PFCd_2
296.8027778	1.12218513	RH_ContB_PFCld_1
296.6916667	1.114767262	LH_SomMotA_11

Table A13: Distribution of nodes based on degree centrality at sparsity level 35% in Low Stress group. The first column contains the DC values, 2nd column are the DC values standardized to Z values, and 3rd column the name of the ROI.

DC value (raw)	**DC value (*z*)**	**ROI**
316.0866142	2.581644609	RH_ContB_PFCld_4
315.5275591	2.541644572	RH_ContA_PFCd_1
311.6062992	2.261080936	LH_DorsAttnB_FEF_2
310.9212598	2.212066807	RH_SomMotA_5
307.4724409	1.965306018	LH_SomMotA_15
306.8661417	1.921925697	LH_ContB_PFCmp_1
306.6929134	1.90953132	RH_DorsAttnB_PostC_7
306.3779528	1.886996088	LH_DefaultB_PFCd_1
305.8818898	1.851503098	RH_DefaultA_PFCm_1
305.1259843	1.797418541	LH_DefaultB_PFCl_1
305.0944882	1.795165018	LH_DorsAttnB_FEF_1
304.8976378	1.781080498	LH_SomMotA_9
304.488189	1.751784697	RH_DefaultA_PFCd_2
304.3622047	1.742770604	LH_DefaultB_PFCl_2
304.2992126	1.738263558	LH_DefaultA_PFCd_3
302.7086614	1.624460637	RH_SomMotA_7
302.3937008	1.601925405	LH_DefaultB_PFCd_5
302.3464567	1.59854512	RH_ContB_PFCmp_1
302.2204724	1.589531028	RH_DorsAttnA_SPL_7
301.2283465	1.518545047	RH_DorsAttnB_FEF_2
301.2204724	1.517981667	LH_DorsAttnB_PostC_6
300.8897638	1.494319673	LH_SalVentAttnA_FrMed_2
300.7874016	1.486995723	LH_ContA_PFCd_1
300.7795276	1.486432342	RH_ContB_PFCld_2
300.1889764	1.444178782	LH_SomMotA_18
299.8267717	1.418263266	LH_DorsAttnB_PostC_4
299.7952756	1.416009743	RH_DorsAttnB_PostC_6
299.2519685	1.377136468	RH_DorsAttnA_TempOcc_4

299.1811024	1.372066041	RH_SomMotA_11
298.8976378	1.351784332	LH_DorsAttnB_PostC_8
298.8740157	1.35009419	RH_SalVentAttnB_PFCmp_2
298.6850394	1.33657305	LH_DefaultB_PFCd_6
298.496063	1.323051911	RH_SalVentAttnA_ParMed_1
298.3700787	1.314037819	LH_SomMotA_14
298.3543307	1.312911057	RH_SalVentAttnB_PFCl_4
297.7165354	1.267277213	RH_DorsAttnA_SPL_8
297.4724409	1.249812408	LH_SomMotA_1
297.4488189	1.248122266	RH_SomMotA_13
297.3464567	1.240798315	RH_DorsAttnB_PostC_3
297.3228346	1.239108173	RH_DorsAttnB_FEF_3
297.2755906	1.235727888	LH_SomMotB_Aud_15
297.2283465	1.232347603	LH_ContA_PFCl_4
297.0393701	1.218826464	LH_SomMotA_11
297.0314961	1.218263083	RH_SalVentAttnA_ParMed_7
297.023622	1.217699703	LH_SalVentAttnB_PFCl_2
297.015748	1.217136322	LH_SalVentAttnA_FrMed_1
296.9212598	1.210375752	RH_SomMotA_19
296.8188976	1.203051802	RH_DefaultC_Rsp_2
296.5354331	1.182770093	RH_ContB_PFClv_4
296.4094488	1.173756	RH_DefaultB_PFCd_5

Table A14: Distribution of nodes based on degree centrality at sparsity level 35% in High Stress group. The first column contains the DC values, 2nd column are the DC values standardized to Z values, and 3rd column the name of the ROI.

Distribution of nodes based on betweenness centrality for all the sparsity levels (from 5% to 35%) in both groups

BC value (raw)	BC value (*z*)	ROI
6.374136022	7.376297433	RH_ContC_Cingp_1
5.162778829	5.791608337	LH_ContC_Cingp_1
4.5214281	4.952597752	LH_SomMotA_19
4.056436048	4.344298368	LH_DefaultC_Rsp_1
3.846999885	4.070315429	LH_DorsAttnB_PostC_9
3.706372358	3.886347472	LH_VisPeri_ExStrSup_4
3.429851424	3.524604699	RH_DorsAttnA_SPL_4
3.126673043	3.12798884	LH_ContC_Cingp_2
3.093006439	3.083946421	LH_SomMotA_13
3.078710931	3.065245136	RH_DefaultC_Rsp_1
2.909428025	2.843790411	LH_DefaultA_PCC_6
2.87331049	2.796541701	RH_ContA_Cinga_1
2.670939185	2.531800962	RH_SomMotA_15

2.585846894	2.420483815	RH_SomMotB_S2_5
2.406717134	2.186147503	LH_SomMotA_5
2.345809127	2.10646807	RH_SomMotB_S2_9
2.343536519	2.103495059	LH_SalVentAttnA_Ins_4
2.296620897	2.042120367	LH_SomMotA_6
2.206050314	1.923636558	LH_ContA_Cinga_1
2.19530667	1.909581797	RH_SalVentAttnA_ParMed_8
2.172373718	1.879581068	RH_VisPeri_ExStrSup_2
2.096919677	1.780872614	RH_SomMotA_8
2.036645103	1.702021833	RH_SomMotA_20
1.954288056	1.594282914	RH_SomMotA_14
1.95379675	1.593640191	RH_SomMotB_S2_12
1.930255057	1.562843111	RH_SomMotB_S2_13
1.887578461	1.507013884	RH_SalVentAttnA_ParMed_2
1.874473265	1.489869757	RH_SalVentAttnA_ParMed_5
1.869661462	1.483574989	RH_SomMotA_1
1.83808438	1.442266069	LH_DefaultB_PFCv_2
1.786153293	1.37433018	LH_ContB_IPL_3
1.681631507	1.237595504	LH_DefaultC_Rsp_2
1.676999553	1.231536014	LH_SomMotB_Aud_16
1.6250506	1.163576753	RH_SomMotA_6
1.615476247	1.15105165	RH_SomMotB_S2_7
1.579607223	1.104128042	RH_ContA_IPS_2
1.564316488	1.084124808	RH_ContC_pCun_1
1.549903696	1.065270093	RH_TempPar_10
1.520916983	1.027349876	LH_SalVentAttnB_PFCv_1
1.464971389	0.954162236	RH_ContA_IPS_3
1.456519408	0.943105414	LH_SalVentAttnB_PFCv_3
1.435528976	0.915645876	RH_DefaultA_PCC_5
1.428643104	0.906637826	RH_SomMotB_S2_4
1.428268428	0.906147677	RH_SomMotB_S2_11
1.428186483	0.906040478	LH_SalVentAttnA_FrMed_3
1.416622871	0.89091304	RH_ContC_Cingp_2
1.41089549	0.88342052	RH_SalVentAttnA_Ins_5
1.404872472	0.87554125	LH_DorsAttnB_PostC_2
1.403054354	0.8731628	LH_DorsAttnB_FEF_3
1.388387316	0.853975482	LH_SomMotA_7

Table A15: Distribution of nodes based on betweenness centrality at sparsity level 5% in Low Stress group. The first column contains the BC values, 2nd column are the BC values standardized to Z values, and 3rd column the name of the ROI.

BC value (raw)	**BC value (*z*)**	**ROI**
6.590557412	7.476650146	RH_ContC_Cingp_1
5.262942671	5.782030629	LH_ContC_Cingp_1
4.040491187	4.221645616	LH_DefaultC_Rsp_1

3.895330224	4.036356471	RH_DorsAttnA_SPL_4
3.767766802	3.873529517	LH_ContC_Cingp_2
3.648095905	3.720776892	LH_DorsAttnB_PostC_9
3.545549675	3.589882861	LH_VisPeri_ExStrSup_4
3.144079829	3.077431007	RH_DefaultC_Rsp_1
3.057129372	2.966444034	RH_SomMotB_S2_9
3.056579385	2.965742008	RH_SalVentAttnA_ParMed_2
3.0072831	2.902818298	RH_SomMotA_15
3.006235468	2.901481059	RH_SomMotB_S2_13
2.651231832	2.448340497	LH_SomMotA_13
2.593376949	2.374492255	LH_SomMotA_6
2.420978639	2.154436292	LH_ContA_Cinga_1
2.381817517	2.1044495	LH_SomMotA_19
2.376180169	2.097253768	RH_ContA_Cinga_1
2.344741683	2.057124452	RH_SomMotB_S2_5
2.23937521	1.922630554	LH_DefaultB_PFCv_2
2.217396699	1.89457632	RH_VisPeri_ExStrSup_2
2.203178292	1.876427387	LH_DefaultA_PCC_6
2.198521533	1.870483318	RH_SomMotA_20
2.179843624	1.846642102	RH_SomMotA_16
2.125912721	1.777802584	RH_SalVentAttnA_ParMed_8
2.059169577	1.692609016	RH_SomMotA_8
2.028729752	1.653754431	LH_SalVentAttnA_Ins_4
2.025737301	1.649934748	RH_SomMotB_S2_7
1.980145877	1.591740067	RH_SalVentAttnA_ParMed_5
1.949724815	1.552909431	LH_ContB_IPL_3
1.900926782	1.490621708	RH_ContA_IPS_3
1.897634256	1.486418999	RH_DorsAttnB_FEF_3
1.883169388	1.467955473	RH_SomMotB_S2_4
1.859343252	1.437542859	LH_DorsAttnA_SPL_5
1.813076688	1.378486403	RH_TempPar_10
1.79577798	1.356405654	RH_VisCent_ExStr_4
1.750981395	1.299225535	RH_SomMotA_1
1.744808967	1.291346806	RH_Limbic_OFC_6
1.712038144	1.249516843	LH_VisCent_ExStr_4
1.663681127	1.187792051	RH_SomMotA_14
1.651627737	1.17240663	RH_DorsAttnB_PostC_8
1.637143623	1.153918539	LH_DefaultB_PFCd_4
1.522169649	1.00716125	LH_DefaultC_Rsp_2
1.513441751	0.996020619	RH_SomMotA_6
1.503383906	0.983182391	RH_DefaultA_PFCm_6
1.494041415	0.97125727	LH_SomMotA_5
1.491760305	0.968345571	RH_SomMotB_S2_12
1.452073144	0.917687323	LH_TempPar_2
1.430208941	0.889778997	LH_DorsAttnB_FEF_3
1.422363363	0.879764593	LH_SomMotA_7
1.40383779	0.856117825	RH_VisCent_ExStr_6

Table A16: Distribution of nodes based on betweenness centrality at sparsity level 5% in High Stress group. The first column contains the BC values, 2nd column are the BC values standardized to Z values, and 3rd column the name of the ROI.

BC value (raw)	BC value (*z*)	ROI
5.311662473	6.425486191	RH_ContC_Cingp_1
4.352356278	5.025751278	LH_ContC_Cingp_1
3.868755838	4.320124209	LH_SomMotA_19
3.510197591	3.796947668	LH_DefaultC_Rsp_1
3.484858297	3.759974807	LH_DorsAttnB_PostC_9
3.323507383	3.524545797	LH_VisPeri_ExStrSup_4
3.191221192	3.331525465	RH_DorsAttnA_SPL_4
3.083463249	3.174294587	LH_ContC_Cingp_2
3.067678119	3.151262319	RH_DefaultC_Rsp_1
2.9574651	2.990449212	LH_SomMotA_13
2.938686858	2.963049659	RH_ContA_Cinga_1
2.757772468	2.699075352	LH_DefaultA_PCC_6
2.662917079	2.560670741	RH_SomMotB_S2_5
2.555921062	2.4045516	RH_SomMotA_15
2.530582583	2.367579928	RH_SomMotB_S2_9
2.523229331	2.356850712	RH_SalVentAttnA_ParMed_8
2.497812494	2.319764706	LH_SomMotA_5
2.481390157	2.295802683	LH_SomMotA_6
2.389970775	2.162411591	LH_SalVentAttnA_Ins_4
2.225716265	1.92274591	LH_ContA_Cinga_1
2.17847066	1.853809294	RH_SomMotA_20
2.160417068	1.827467086	RH_SomMotA_14
2.127584286	1.779560389	RH_VisPeri_ExStrSup_2
2.063214705	1.685637979	LH_DefaultB_PFCv_2
2.062468599	1.684549326	RH_SomMotB_S2_12
2.046154471	1.660745192	RH_SomMotA_8
2.040243288	1.652120115	RH_SalVentAttnA_ParMed_2
1.993446081	1.583837763	RH_SomMotA_1
1.986359122	1.573497098	RH_SalVentAttnA_ParMed_5
1.976373164	1.558926469	LH_ContB_IPL_3
1.968581126	1.547557016	RH_SomMotB_S2_13
1.859728702	1.388729167	LH_DefaultC_Rsp_2
1.836370911	1.354647541	RH_SomMotB_S2_7
1.749732787	1.228232838	RH_ContA_IPS_2
1.722620187	1.188672526	RH_ContC_pCun_1
1.712251213	1.173543035	LH_SomMotB_Aud_16
1.710611777	1.171150915	RH_SomMotA_6
1.689209862	1.13992313	RH_TempPar_10
1.68501021	1.133795367	RH_DefaultA_PCC_5

1.684324294	1.13279454	RH_SomMotB_S2_4
1.681128837	1.12813201	LH_SalVentAttnB_PFCv_3
1.677210253	1.122414359	LH_DorsAttnB_FEF_3
1.67411386	1.117896376	RH_SalVentAttnA_Ins_5
1.671975685	1.11477654	RH_ContC_Cingp_2
1.667078489	1.107630983	LH_SalVentAttnB_PFCv_1
1.661971006	1.100178595	RH_ContA_IPS_3
1.661961989	1.100165439	RH_DorsAttnB_FEF_3
1.625777358	1.047368019	LH_SomMotA_7
1.622031797	1.041902827	LH_SalVentAttnA_FrMed_3
1.6057464	1.018140613	LH_DorsAttnB_PostC_2

Table A17: Distribution of nodes based on betweenness centrality at sparsity level 10% in Low Stress group. The first column contains the BC values, 2nd column are the BC values standardized to Z values, and 3rd column the name of the ROI.

BC value (raw)	**BC value (*z*)**	**ROI**
5.883207848	6.965755438	RH_ContC_Cingp_1
4.450612064	4.959974905	LH_ContC_Cingp_1
3.709491718	3.922330666	LH_ContC_Cingp_2
3.540938208	3.686338523	LH_DefaultC_Rsp_1
3.527709379	3.66781681	LH_DorsAttnB_PostC_9
3.234636221	3.257484431	RH_DorsAttnA_SPL_4
3.132686107	3.114743852	RH_SalVentAttnA_ParMed_2
3.006510628	2.938085284	LH_VisPeri_ExStrSup_4
2.904592266	2.79538916	RH_SomMotA_15
2.890477081	2.775626457	RH_SomMotB_S2_9
2.83344814	2.69578011	RH_DefaultC_Rsp_1
2.803145928	2.653353917	RH_SomMotB_S2_13
2.700820288	2.510087562	LH_SomMotA_6
2.536559362	2.280105475	LH_SomMotA_19
2.530350882	2.271412967	LH_SomMotA_13
2.477397624	2.197272994	LH_ContA_Cinga_1
2.465991277	2.181302942	RH_ContA_Cinga_1
2.450414343	2.159493643	RH_SomMotB_S2_5
2.401314126	2.090748319	LH_DefaultA_PCC_6
2.321107977	1.978451513	RH_SomMotA_20
2.288369214	1.932613898	RH_SalVentAttnA_ParMed_8
2.270980044	1.908267283	RH_SomMotA_8
2.244008185	1.870503923	LH_DefaultB_PFCv_2
2.204965822	1.815840624	RH_SomMotA_16
2.204348338	1.814976084	RH_ContA_IPS_3
2.146003794	1.733287758	RH_VisPeri_ExStrSup_2
2.084857354	1.647676492	LH_DorsAttnA_SPL_5
2.074511287	1.633190941	LH_DorsAttnB_FEF_3

2.035561915	1.578657839	RH_DorsAttnB_FEF_3
2.025901644	1.565132472	RH_VisCent_ExStr_4
2.023450709	1.561700913	RH_SomMotB_S2_7
2.021432694	1.558875485	LH_SalVentAttnA_Ins_4
2.01228462	1.546067246	RH_TempPar_10
2.012055341	1.545746232	LH_ContB_IPL_3
2.006294093	1.537679896	RH_SalVentAttnA_ParMed_5
1.966638197	1.482157588	RH_SomMotB_S2_4
1.923865412	1.422271318	RH_SomMotA_1
1.920264955	1.417230309	LH_DefaultB_PFCd_4
1.912784904	1.406757473	RH_Limbic_OFC_6
1.873030711	1.35109754	LH_DefaultC_Rsp_2
1.824481077	1.28312309	RH_SomMotA_14
1.819325072	1.275904155	LH_VisCent_ExStr_4
1.813912614	1.268326162	RH_DorsAttnB_PostC_8
1.77301069	1.211059287	RH_SalVentAttnA_Ins_5
1.717451803	1.133271165	RH_DefaultA_PFCm_6
1.709553748	1.122213082	RH_SomMotA_6
1.708362778	1.120545601	RH_SomMotB_S2_11
1.698354741	1.106533326	RH_SomMotB_S2_12
1.69132672	1.096693379	LH_TempPar_2
1.672639972	1.070530021	RH_ContA_IPS_2

Table A18: Distribution of nodes based on betweenness centrality at sparsity level 10% in High Stress group. The first column contains the BC values, 2nd column are the BC values standardized to Z values, and 3rd column the name of the ROI.

BC value (raw)	**BC value (*z*)**	**ROI**
3.85934774	5.569526142	RH_ContC_Cingp_1
3.15530589	4.214562951	LH_ContC_Cingp_1
3.082759969	4.074944756	LH_SomMotA_19
2.801306941	3.533274552	LH_DorsAttnB_PostC_9
2.692775724	3.324400883	LH_DefaultC_Rsp_1
2.672063345	3.284538892	LH_VisPeri_ExStrSup_4
2.594530883	3.135323852	LH_ContC_Cingp_2
2.538693257	3.027861593	RH_DorsAttnA_SPL_4
2.476477599	2.908124497	LH_SomMotA_13
2.425065851	2.809180058	RH_DefaultC_Rsp_1
2.397923086	2.75694247	RH_ContA_Cinga_1
2.35428979	2.672968045	RH_SomMotB_S2_5
2.274193428	2.518818653	RH_SalVentAttnA_ParMed_8
2.208174661	2.391762288	LH_SomMotA_6
2.206776931	2.389072289	LH_DefaultA_PCC_6
2.177157977	2.332069154	LH_SomMotA_5
2.150847108	2.281432592	RH_SomMotB_S2_9
2.135520208	2.251935216	RH_SomMotA_15

2.075474767	2.136374811	LH_SalVentAttnA_Ins_4
2.040694417	2.069438316	LH_ContA_Cinga_1
1.953044484	1.900751707	RH_SomMotA_14
1.945028321	1.885324206	RH_SalVentAttnA_ParMed_2
1.894779768	1.788618393	LH_DefaultB_PFCv_2
1.890734714	1.780833488	RH_SomMotA_20
1.873914447	1.748462055	RH_SomMotB_S2_12
1.841529415	1.686135467	RH_SomMotA_1
1.837985258	1.679314563	RH_SomMotA_8
1.837090795	1.677593125	RH_SomMotB_S2_13
1.821964288	1.648481418	RH_SalVentAttnA_ParMed_5
1.7884454	1.583972667	LH_ContB_IPL_3
1.771934681	1.552196977	RH_VisPeri_ExStrSup_2
1.758921256	1.527151999	LH_DefaultC_Rsp_2
1.687241072	1.389199958	RH_DefaultA_PCC_5
1.665526659	1.347409501	LH_DorsAttnB_FEF_3
1.658548518	1.333979726	LH_SalVentAttnB_PFCv_3
1.653177697	1.323643317	RH_ContA_IPS_2
1.650391689	1.318281507	RH_SomMotB_S2_7
1.619310242	1.258463733	RH_SomMotB_S2_4
1.612836821	1.246005316	RH_ContC_Cingp_2
1.599703385	1.220729372	LH_DorsAttnB_PostC_2
1.597228623	1.215966569	RH_ContC_pCun_1
1.590551096	1.20311534	RH_ContA_IPS_3
1.58048556	1.183743722	LH_DefaultB_PFCd_4
1.574305538	1.171849965	LH_SomMotA_7
1.571169336	1.165814189	RH_SomMotA_6
1.566135421	1.156126172	LH_SalVentAttnB_PFCv_1
1.565151675	1.154232904	RH_SomMotA_16
1.558136992	1.140732803	LH_SalVentAttnA_FrMed_3
1.550727696	1.126473247	LH_SomMotB_Aud_16
1.543278362	1.112136638	RH_SalVentAttnA_Ins_5

Table A19: Distribution of nodes based on betweenness centrality at sparsity level 15% in Low Stress group. The first column contains the BC values, 2nd column are the BC values standardized to Z values, and 3rd column the name of the ROI.

BC value (raw)	**BC value (*z*)**	**ROI**
4.254057965	6.051259976	RH_ContC_Cingp_1
3.342817262	4.374122829	LH_ContC_Cingp_1
2.9068389	3.571705307	LH_ContC_Cingp_2
2.706847072	3.203620647	LH_DorsAttnB_PostC_9
2.654800238	3.107828526	LH_VisPeri_ExStrSup_4
2.644916467	3.089637462	RH_DorsAttnA_SPL_4
2.611506403	3.028146288	LH_DefaultC_Rsp_1
2.539387968	2.895412417	RH_SomMotB_S2_9
2.538838275	2.894400709	RH_SalVentAttnA_ParMed_2

2.334075647	2.517535398	LH_SomMotA_6
2.291778192	2.439686996	RH_SomMotA_15
2.290138198	2.436668588	RH_SomMotB_S2_13
2.239082479	2.342700615	LH_SomMotA_19
2.205377828	2.280667254	RH_DefaultC_Rsp_1
2.202681469	2.275704611	LH_DefaultA_PCC_6
2.197159011	2.265540535	LH_SomMotA_13
2.142696214	2.165301839	RH_ContA_IPS_3
2.105483349	2.096811616	RH_SomMotA_8
2.097677114	2.082444252	LH_ContA_Cinga_1
2.071910223	2.035020328	RH_SomMotB_S2_5
2.051431409	1.997329102	RH_SomMotA_20
2.044034955	1.983715938	RH_SalVentAttnA_ParMed_8
1.999043168	1.900908622	RH_ContA_Cinga_1
1.99402961	1.891681177	LH_DorsAttnB_FEF_3
1.970697512	1.848738485	RH_SomMotA_16
1.967887973	1.843567533	LH_DefaultB_PFCv_2
1.932088289	1.777678268	LH_DorsAttnA_SPL_5
1.915328736	1.746832336	RH_DorsAttnB_FEF_3
1.867988517	1.659702733	RH_SomMotB_S2_4
1.838199929	1.604876882	RH_VisPeri_ExStrSup_2
1.837031184	1.602725809	LH_ContB_IPL_3
1.836876925	1.602441896	RH_TempPar_10
1.805559356	1.544801957	RH_SalVentAttnA_ParMed_5
1.78935707	1.514981674	LH_SalVentAttnA_Ins_4
1.782491466	1.50234554	LH_DefaultB_PFCd_4
1.773441484	1.485689061	RH_VisCent_ExStr_4
1.745260669	1.433822314	LH_DefaultC_Rsp_2
1.743549829	1.430673515	RH_Limbic_OFC_6
1.740250045	1.424600269	RH_SomMotA_1
1.689532741	1.331255145	RH_SomMotA_6
1.68942013	1.331047885	RH_SomMotA_2
1.686425642	1.325536536	LH_DorsAttnA_SPL_8
1.661086902	1.278900622	RH_SomMotA_14
1.658929974	1.2749308	RH_SomMotB_S2_3
1.657531456	1.272356829	RH_SomMotB_S2_11
1.650180975	1.25882828	RH_SalVentAttnA_Ins_5
1.639242467	1.238695973	RH_DorsAttnB_PostC_8
1.637970074	1.236354134	LH_TempPar_2
1.629644023	1.22103005	RH_DefaultA_PFCm_6
1.625442043	1.213296312	RH_SomMotB_S2_7

Table A20: Distribution of nodes based on betweenness centrality at sparsity level 15% in High Stress group. The first column contains the BC values, 2nd column are the BC values standardized to Z values, and 3rd column the name of the ROI.

BC value (raw)	BC value (*z*)	ROI
2.694058481	4.738001803	RH_ContC_Cingp_1
2.322337576	3.707769169	LH_SomMotA_19
2.302497986	3.652783312	LH_ContC_Cingp_1
2.263842191	3.545647928	LH_DorsAttnB_PostC_9
2.08037818	3.037173401	LH_VisPeri_ExStrSup_4
2.024628904	2.882663061	LH_ContC_Cingp_2
1.990583884	2.788306542	LH_DefaultC_Rsp_1
1.984768255	2.772188401	LH_SomMotA_13
1.943432013	2.6576241	RH_SomMotB_S2_5
1.941536485	2.652370603	RH_ContA_Cinga_1
1.93358919	2.630344498	RH_SalVentAttnA_ParMed_8
1.930484513	2.62173982	RH_DorsAttnA_SPL_4
1.906038461	2.553987051	RH_DefaultC_Rsp_1
1.787345281	2.225026303	LH_SomMotA_6
1.77448241	2.189376573	RH_SomMotB_S2_9
1.764745826	2.162391416	LH_SomMotA_5
1.762222781	2.155398743	LH_DefaultA_PCC_6
1.721901827	2.043648333	RH_SomMotA_15
1.713658612	2.020802084	LH_SalVentAttnA_Ins_4
1.681950338	1.932921908	LH_ContA_Cinga_1
1.662622366	1.879354011	RH_SalVentAttnA_ParMed_2
1.640772643	1.818797024	RH_SomMotA_14
1.630306881	1.789790934	RH_SomMotB_S2_13
1.624911345	1.77483709	RH_SomMotA_8
1.620933067	1.763811204	RH_SomMotA_20
1.617051051	1.753052112	LH_DefaultB_PFCv_2
1.585160408	1.664666495	RH_SomMotB_S2_12
1.574852516	1.636097947	RH_SomMotA_1
1.573331392	1.631882118	RH_SalVentAttnA_ParMed_5
1.562635898	1.602239323	LH_ContB_IPL_3
1.560614143	1.596635985	LH_SalVentAttnB_PFCv_3
1.538951268	1.536596851	LH_DorsAttnB_FEF_3
1.530311199	1.51265071	RH_DefaultA_PCC_5
1.510123512	1.456700095	LH_DorsAttnB_PostC_2
1.497170451	1.420800403	LH_DefaultC_Rsp_2
1.493198365	1.409791679	LH_DefaultB_PFCd_4
1.492593346	1.408114855	RH_ContA_IPS_2
1.47688736	1.36458537	LH_SalVentAttnA_FrMed_3
1.474299077	1.357411887	RH_VisPeri_ExStrSup_2
1.46893238	1.34253797	LH_SomMotA_7
1.448661483	1.286356735	RH_SomMotB_S2_4
1.447474089	1.283065846	RH_SomMotA_17
1.441660729	1.266953992	RH_SomMotA_16
1.44005629	1.262507253	RH_ContC_Cingp_2
1.435852963	1.250857641	RH_SomMotB_S2_7
1.426070973	1.223746642	RH_SomMotA_6
1.423752742	1.217321613	RH_SomMotB_S2_3

1.418446724	1.202615868	RH_DorsAttnB_FEF_3
1.414510082	1.191705378	LH_SalVentAttnB_PFCv_1
1.409637012	1.178199557	RH_ContC_pCun_1

Table A21: Distribution of nodes based on betweenness centrality at sparsity level 20% in Low Stress group. The first column contains the BC values, 2nd column are the BC values standardized to Z values, and 3rd column the name of the ROI.

BC value (raw)	**BC value (*z*)**	**ROI**
2.899217454	5.016225457	RH_ContC_Cingp_1
2.350893331	3.578479219	LH_ContC_Cingp_1
2.137863226	3.019898591	LH_ContC_Cingp_2
2.126318876	2.989628454	LH_DorsAttnB_PostC_9
2.098965654	2.917906293	LH_VisPeri_ExStrSup_4
2.089155454	2.892183225	RH_DorsAttnA_SPL_4
2.080317392	2.869009175	RH_SalVentAttnA_ParMed_2
2.033111751	2.745232507	RH_SomMotB_S2_9
2.000602019	2.659989596	LH_DefaultC_Rsp_1
1.957129283	2.546000879	LH_SomMotA_6
1.929496206	2.473544918	RH_SomMotB_S2_13
1.873961439	2.327928666	LH_SomMotA_19
1.870933191	2.319988377	RH_SomMotA_15
1.826177644	2.202636037	RH_DefaultC_Rsp_1
1.826073278	2.20236238	LH_DorsAttnB_FEF_3
1.822946709	2.194164286	RH_ContA_IPS_3
1.800755636	2.13597766	RH_SomMotA_8
1.75231716	2.008968408	LH_DorsAttnA_SPL_5
1.743398255	1.98558238	RH_SomMotB_S2_5
1.739240578	1.974680645	RH_SalVentAttnA_ParMed_8
1.730693585	1.9522698	LH_SomMotA_13
1.725379506	1.938335894	LH_DefaultA_PCC_6
1.70879899	1.894860561	RH_DorsAttnB_FEF_3
1.708108374	1.893049714	RH_SomMotA_16
1.703461764	1.880865961	RH_SomMotA_20
1.687369351	1.838670467	LH_ContA_Cinga_1
1.667478783	1.786515934	LH_DefaultB_PFCv_2
1.663915121	1.777171748	RH_ContA_Cinga_1
1.642323478	1.720556871	RH_SomMotB_S2_4
1.619515952	1.660753859	RH_SomMotB_S2_11
1.615675328	1.650683458	LH_ContB_IPL_3
1.577183105	1.549754016	RH_DefaultA_PFCm_6
1.576878488	1.548955286	RH_SomMotA_6
1.567457811	1.524253579	LH_TempPar_2
1.558850949	1.501685751	LH_DefaultC_Rsp_2

1.555342635	1.492486694	LH_DorsAttnA_SPL_8
1.550614657	1.480089588	RH_TempPar_10
1.546988246	1.47058087	RH_SomMotA_2
1.538522462	1.448382962	LH_DorsAttnA_SPL_6
1.535969344	1.441688498	LH_SalVentAttnA_Ins_4
1.53136984	1.429628258	RH_Limbic_OFC_6
1.528594923	1.422352223	RH_SalVentAttnA_Ins_5
1.52014573	1.400197817	RH_SalVentAttnA_ParMed_5
1.511994746	1.378825335	RH_DorsAttnB_PostC_8
1.506959696	1.365623063	LH_DefaultB_PFCd_4
1.50100951	1.350021237	RH_SomMotA_1
1.471538423	1.272745877	RH_SomMotB_S2_3
1.464705527	1.254829519	RH_VisPeri_ExStrSup_2
1.452281688	1.2222533	RH_SomMotA_14
1.426406203	1.154405872	RH_VisCent_ExStr_4

Table A22: Distribution of nodes based on betweenness centrality at sparsity level 20% in High Stress group. The first column contains the BC values, 2nd column are the BC values standardized to Z values, and 3rd column the name of the ROI.

BC value (raw)	BC value (*z*)	ROI
1.83062622	3.646491866	RH_ContC_Cingp_1
1.760090782	3.340154328	LH_SomMotA_19
1.708544604	3.11628772	LH_DorsAttnB_PostC_9
1.59364725	2.617285041	RH_SalVentAttnA_ParMed_8
1.582990402	2.57100203	LH_ContC_Cingp_1
1.569839421	2.513886922	LH_SomMotA_13
1.557365652	2.459712968	RH_SomMotB_S2_5
1.554795589	2.448551107	LH_VisPeri_ExStrSup_4
1.548435243	2.420927932	LH_ContC_Cingp_2
1.538651811	2.37843819	RH_ContA_Cinga_1
1.523074039	2.310783458	LH_SomMotA_6
1.519163508	2.293799902	LH_SomMotA_5
1.513790604	2.270465218	RH_DefaultC_Rsp_1
1.47941713	2.121180182	LH_DefaultC_Rsp_1
1.455878837	2.018952664	RH_SomMotB_S2_9
1.454766218	2.014120525	RH_DorsAttnA_SPL_4
1.444430991	1.969234326	RH_SomMotA_14
1.426345696	1.890689344	RH_SomMotA_8
1.422728942	1.874981671	RH_SalVentAttnA_ParMed_2
1.42182803	1.871068982	LH_SalVentAttnA_Ins_4
1.41353816	1.835065828	RH_SomMotA_15
1.403626066	1.792017303	LH_ContA_Cinga_1
1.396835407	1.762525267	RH_SomMotB_S2_13
1.390183223	1.733634629	LH_DefaultB_PFCv_2

1.375001921	1.667701779	LH_ContB_IPL_3
1.369476861	1.643706276	LH_DefaultB_PFCd_4
1.368191094	1.63812215	LH_DefaultA_PCC_6
1.36254095	1.613583402	LH_DorsAttnB_FEF_3
1.362385672	1.612909025	LH_SalVentAttnB_PFCv_3
1.361866309	1.610653419	RH_SomMotA_17
1.350070913	1.559425656	RH_SomMotA_20
1.348940852	1.554517768	LH_SomMotA_7
1.347894549	1.549973642	RH_SalVentAttnA_ParMed_5
1.338473672	1.509058488	RH_SomMotA_1
1.33845384	1.50897236	LH_DorsAttnB_PostC_2
1.329455277	1.469891329	RH_SomMotB_S2_12
1.319871962	1.428270699	LH_SalVentAttnA_FrMed_3
1.31252356	1.396356369	RH_ContA_IPS_2
1.30575351	1.366953837	RH_SomMotB_S2_3
1.300497106	1.344125118	RH_SomMotA_16
1.28614681	1.281801348	RH_DorsAttnB_FEF_3
1.284474888	1.274540139	RH_DefaultA_PCC_5
1.280885625	1.258951863	RH_ContC_Cingp_2
1.280177601	1.255876891	LH_DefaultC_Rsp_2
1.269988768	1.211626482	RH_SomMotB_S2_7
1.268921399	1.206990866	LH_SomMotB_Aud_13
1.268831566	1.206600719	RH_SomMotA_6
1.267457648	1.200633752	RH_SomMotB_S2_4
1.25336773	1.139440813	LH_DorsAttnA_SPL_6
1.252651997	1.136332365	RH_SalVentAttnA_ParMed_6

Table A23: Distribution of nodes based on betweenness centrality at sparsity level 25% in Low Stress group. The first column contains the BC values, 2nd column are the BC values standardized to Z values, and 3rd column the name of the ROI.

BC value (raw)	**BC value (*z*)**	**ROI**
1.973665677	3.958525124	RH_ContC_Cingp_1
1.705172488	2.875525024	RH_SalVentAttnA_ParMed_2
1.671205166	2.738513677	LH_DorsAttnB_PostC_9
1.666088732	2.717875917	RH_DorsAttnA_SPL_4
1.660361967	2.694776307	LH_ContC_Cingp_2
1.62292356	2.543763919	LH_VisPeri_ExStrSup_4
1.614599234	2.510186731	RH_SomMotB_S2_9
1.604335441	2.468786467	LH_DorsAttnB_FEF_3
1.583261211	2.383780983	LH_ContC_Cingp_1
1.568521639	2.324327119	RH_SomMotB_S2_13
1.546731403	2.236433538	LH_SomMotA_6
1.544773448	2.228535886	RH_SomMotA_8
1.540644097	2.211879644	RH_ContA_IPS_3
1.532520966	2.179114003	RH_DorsAttnB_FEF_3

1.518877854	2.124082843	LH_DefaultC_Rsp_1
1.510487916	2.090241004	RH_SalVentAttnA_ParMed_8
1.492228454	2.016589231	LH_SomMotA_19
1.491111342	2.012083225	RH_SomMotA_15
1.466133063	1.911330282	LH_DorsAttnA_SPL_5
1.460077766	1.886905499	RH_SomMotB_S2_4
1.438924886	1.801582773	RH_SomMotA_20
1.438224145	1.798756248	LH_ContB_IPL_3
1.43709111	1.794186012	LH_TempPar_2
1.430268083	1.766664501	LH_ContA_Cinga_1
1.430122607	1.766077704	RH_SomMotA_16
1.420704261	1.728087654	LH_SomMotA_13
1.415442137	1.706862235	RH_SomMotB_S2_5
1.411463583	1.690814249	LH_DefaultB_PFCv_2
1.409498755	1.682888878	RH_SomMotA_2
1.399064918	1.640802719	LH_DorsAttnA_SPL_6
1.396782446	1.631596088	RH_SomMotB_S2_11
1.387034155	1.592275168	RH_DefaultA_PFCm_6
1.381917522	1.5716366	RH_ContA_Cinga_1
1.377059225	1.552040068	RH_DefaultC_Rsp_1
1.371708225	1.530456155	RH_SomMotA_6
1.342028036	1.410737482	RH_DorsAttnB_PostC_8
1.34091401	1.406243924	RH_SalVentAttnA_Ins_4
1.337954519	1.394306455	RH_TempPar_10
1.335330501	1.383722158	LH_DefaultA_PCC_6
1.314675246	1.300406659	RH_SalVentAttnA_ParMed_5
1.311842586	1.288980779	LH_DorsAttnA_SPL_8
1.310140396	1.282114787	RH_DorsAttnB_PostC_2
1.308812212	1.276757395	LH_DefaultC_Rsp_2
1.304417492	1.259030758	LH_DorsAttnB_PostC_4
1.299426329	1.238898292	LH_SomMotB_Aud_11
1.299342443	1.238559924	RH_SomMotA_14
1.29207181	1.20923294	LH_DorsAttnA_SPL_1
1.286753438	1.187780633	LH_SomMotA_7
1.284271837	1.177770793	LH_DefaultB_PFCd_4
1.279926716	1.160244217	RH_ContA_IPS_2

Table A24: Distribution of nodes based on betweenness centrality at sparsity level 25% in High Stress group. The first column contains the BC values, 2nd column are the BC values standardized to Z values, and 3rd column the name of the ROI.

BC value (raw)	**BC value (*z*)**	**ROI**
1.346452524	2.422248933	LH_SomMotA_19
1.343858943	2.404467506	LH_DorsAttnB_PostC_9
1.34173461	2.389903208	LH_SomMotA_13

1.328502984	2.299187993	RH_SalVentAttnA_ParMed_8
1.308751802	2.163775105	RH_ContC_Cingp_1
1.292040663	2.049204563	LH_SomMotA_6
1.290036251	2.035462436	RH_SomMotA_14
1.283744855	1.992329015	RH_SomMotB_S2_5
1.280379894	1.969259046	RH_SomMotA_8
1.265726872	1.868798834	LH_SomMotA_5
1.257208628	1.810398275	LH_DefaultB_PFCd_4
1.24789143	1.746520135	RH_ContA_Cinga_1
1.245468585	1.729909265	RH_SomMotA_17
1.236537072	1.668675355	LH_ContC_Cingp_2
1.225929296	1.595949095	LH_SomMotA_7
1.221920112	1.568462377	LH_VisPeri_ExStrSup_4
1.216717502	1.532793609	LH_DorsAttnB_FEF_3
1.214413856	1.516999951	RH_DefaultC_Rsp_1
1.20947318	1.48312698	RH_SalVentAttnA_ParMed_2
1.20795688	1.472731318	LH_DorsAttnB_PostC_2
1.203829429	1.444433772	LH_SomMotB_Aud_13
1.197842208	1.403385754	LH_SalVentAttnA_FrMed_3
1.197412061	1.400436692	RH_SomMotA_15
1.193650354	1.374646659	LH_DefaultA_PFCd_2
1.187242776	1.330716696	LH_SomMotA_16
1.186813794	1.327775625	RH_SomMotB_S2_9
1.186373176	1.324754775	RH_SomMotA_12
1.186250236	1.323911902	RH_SalVentAttnA_ParMed_5
1.184601724	1.312609807	RH_SomMotA_18
1.181435472	1.290902182	LH_ContB_IPL_3
1.174633253	1.244266581	LH_SomMotA_8
1.174370768	1.242467005	RH_DorsAttnA_SPL_4
1.169811452	1.211208613	LH_SomMotA_18
1.168738447	1.203852154	RH_SomMotA_1
1.167788355	1.197338381	RH_SomMotA_19
1.16718403	1.193195167	RH_SomMotA_10
1.167157658	1.193014364	LH_ContA_Cinga_1
1.166038652	1.185342528	RH_DorsAttnB_FEF_3
1.165443234	1.181260376	LH_SalVentAttnB_PFCv_3
1.164725028	1.176336405	RH_SomMotB_S2_12
1.164447318	1.17443244	RH_SomMotB_S2_13
1.164320272	1.17356142	LH_SalVentAttnA_Ins_4
1.162875523	1.163656307	RH_DorsAttnB_PostC_5
1.162289083	1.159635716	RH_DorsAttnB_PostC_3
1.160866511	1.149882648	RH_SomMotA_16
1.156530633	1.120156135	RH_SomMotA_13
1.15639315	1.119213557	RH_SomMotA_6
1.155190898	1.110970991	RH_SomMotB_S2_3
1.154065352	1.103254317	RH_SomMotA_20
1.153330468	1.098215997	RH_ContA_IPS_2

Table A25: Distribution of nodes based on betweenness centrality at sparsity level 30% in Low Stress group. The first column contains the BC values, 2nd column are the BC values standardized to Z values, and 3rd column the name of the ROI.

BC value (raw)	BC value (*z*)	ROI
1.392197718	2.4889632	RH_SomMotA_8
1.375829465	2.386633043	LH_DorsAttnB_FEF_3
1.37543186	2.384147318	RH_SalVentAttnA_ParMed_2
1.375051741	2.381770914	RH_DorsAttnB_FEF_3
1.347491093	2.20946875	RH_ContC_Cingp_1
1.347249101	2.20795588	LH_SomMotA_6
1.338156461	2.151111005	RH_ContA_IPS_3
1.316687268	2.016891075	LH_ContC_Cingp_2
1.306588897	1.953758628	LH_DorsAttnB_PostC_9
1.300462407	1.91545737	RH_DorsAttnA_SPL_4
1.280426536	1.790198198	LH_DorsAttnB_PostC_4
1.277405317	1.771310307	RH_SomMotB_S2_9
1.276229821	1.763961407	RH_SalVentAttnA_ParMed_8
1.27183783	1.736503791	LH_ContB_IPL_3
1.266641569	1.70401809	RH_SomMotA_16
1.260182821	1.663639641	LH_DorsAttnA_SPL_5
1.259946777	1.662163954	RH_SomMotB_S2_4
1.259733741	1.660832107	RH_SomMotB_S2_13
1.25215507	1.613452184	RH_DefaultA_PFCm_6
1.247192469	1.582427267	LH_TempPar_2
1.243803353	1.561239371	LH_SomMotA_19
1.240199309	1.538707808	LH_VisPeri_ExStrSup_4
1.238733973	1.5295469	RH_SomMotA_6
1.231706138	1.485610661	LH_DefaultA_PFCd_3
1.229683492	1.472965592	RH_DorsAttnB_PostC_8
1.22633709	1.452044741	LH_SomMotA_18
1.222654032	1.4290192	RH_SalVentAttnA_Ins_4
1.222230167	1.426369301	RH_SomMotA_15
1.22149981	1.421803296	RH_SomMotA_2
1.217613779	1.39750882	LH_DorsAttnA_SPL_6
1.215675143	1.385388958	RH_DorsAttnB_PostC_7
1.215018255	1.381282265	RH_DorsAttnB_PostC_3
1.21346212	1.371553701	LH_DorsAttnB_FEF_2
1.213295296	1.370510763	LH_ContA_Cinga_1
1.208793669	1.342367733	RH_SomMotA_20
1.202524399	1.303173852	RH_SomMotB_S2_11
1.202444787	1.302676138	LH_DorsAttnA_SPL_8
1.199231861	1.282589745	RH_SalVentAttnA_ParMed_5

1.199153421	1.282099357	RH_SomMotA_14
1.189211382	1.219944256	LH_SomMotA_11
1.188696816	1.21672732	LH_ContC_Cingp_1
1.185012011	1.193690855	LH_DorsAttnB_FEF_1
1.184221888	1.18875121	LH_SomMotA_7
1.183569377	1.184671879	RH_SomMotB_S2_5
1.182169424	1.175919727	RH_SomMotA_17
1.180867663	1.167781446	LH_SomMotA_13
1.18067805	1.166596036	RH_SomMotA_9
1.1804192	1.164977773	LH_DefaultB_PFCv_2
1.179624493	1.160009467	LH_DefaultC_Rsp_2
1.176707327	1.141772085	LH_SomMotA_15

Table A26: Distribution of nodes based on betweenness centrality at sparsity level 30% in High Stress group. The first column contains the BC values, 2nd column are the BC values standardized to Z values, and 3rd column the name of the ROI.

BC value (raw)	**BC value (*z*)**	**ROI**
1.224111718	1.708260768	RH_ContB_PFCld_4
1.199378099	1.695274617	RH_SomMotA_18
1.197815131	1.687817421	RH_SomMotA_7
1.196917609	1.682147126	LH_SomMotA_9
1.196235152	1.606919022	RH_DefaultA_PFCd_2
1.187180959	1.524939106	RH_SalVentAttnA_ParMed_7
1.177314142	1.508717353	RH_SomMotA_12
1.175361748	1.498253635	LH_ContA_PFCd_1
1.174102371	1.479603583	LH_DefaultB_PFCl_1
1.171857716	1.44389401	LH_SomMotA_16
1.167559836	1.428450217	RH_SomMotA_19
1.165701075	1.419765069	LH_DefaultA_PFCd_2
1.164655761	1.413904154	RH_ContA_PFCd_1
1.163950361	1.356809647	LH_DefaultB_PFCd_4
1.157078665	1.355900326	LH_DefaultB_PFCl_2
1.156969222	1.341486066	RH_SomMotA_17
1.155234372	1.310982407	LH_SomMotA_13
1.151563058	1.294487002	RH_DorsAttnB_PostC_7
1.149577729	1.290398681	RH_SomMotA_14
1.149085672	1.282667743	LH_DorsAttnB_FEF_2
1.148155204	1.277734316	LH_ContB_PFCd_1
1.147561434	1.263697187	RH_SomMotA_11
1.145871974	1.263599558	RH_DorsAttnB_PostC_6
1.145860223	1.258207885	LH_SomMotA_8
1.1452113	1.242723581	RH_SalVentAttnA_ParMed_8
1.143347663	1.239552503	LH_ContB_PFCmp_1
1.142966003	1.239311358	RH_SomMotA_13

1.14293698	1.219320096	LH_SomMotA_4
1.140530901	1.21890876	LH_SomMotA_15
1.140481394	1.185316041	LH_SomMotA_18
1.136438292	1.184364624	RH_DorsAttnA_SPL_8
1.136323782	1.167064533	RH_DorsAttnB_FEF_1
1.134241604	1.15388826	LH_DefaultB_PFCd_5
1.132655753	1.153640005	LH_SomMotA_14
1.132625874	1.1414515	LH_SomMotA_6
1.131158908	1.135912298	RH_ContB_PFCld_3
1.130492229	1.134776888	LH_SomMotA_12
1.130355575	1.133111129	LH_DorsAttnB_PostC_8
1.13015509	1.128730436	LH_SomMotB_Aud_13
1.129627845	1.126568518	LH_DorsAttnB_PostC_6
1.129367644	1.104019954	RH_DorsAttnB_PostC_3
1.126653777	1.095421487	RH_DefaultB_PFCd_5
1.125618896	1.090534709	RH_SomMotA_8
1.12503074	1.087019357	RH_SomMotA_5
1.124607645	1.057436873	LH_SomMotA_11
1.1210472	1.041791429	LH_DefaultB_PFCd_1
1.119164169	1.038280126	RH_ContB_PFCmp_1
1.118741561	1.029812072	LH_DefaultA_PFCd_3
1.117722375	1.013173271	LH_SomMotA_17
1.115719787	0.991743581	LH_DorsAttnB_FEF_1

Table A27: Distribution of nodes based on betweenness centrality at sparsity level 35% in Low Stress group. The first column contains the BC values, 2nd column are the BC values standardized to Z values, and 3rd column the name of the ROI.

BC value (raw)	**BC value (*z*)**	**ROI**
1.267407265	2.136499035	RH_ContB_PFCld_4
1.263564641	2.106393847	LH_DorsAttnB_FEF_2
1.257345431	2.057669194	RH_DorsAttnB_FEF_3
1.244252685	1.955093547	LH_DefaultA_PFCd_3
1.233713881	1.872526866	LH_ContB_PFCmp_1
1.230701246	1.848924257	LH_SomMotA_15
1.221873716	1.779764612	RH_DorsAttnB_PostC_7
1.21671362	1.739337635	RH_ContA_PFCd_1
1.214280625	1.720276239	RH_SomMotA_8
1.211189335	1.696057401	LH_DorsAttnB_FEF_3
1.20880751	1.677396898	LH_DorsAttnB_PostC_4
1.207692248	1.668659335	LH_DorsAttnB_FEF_1
1.199334071	1.603176859	LH_SomMotA_18
1.199306741	1.60296274	RH_SomMotA_5
1.18766402	1.51174737	RH_DorsAttnB_PostC_3
1.18746932	1.510221988	RH_DefaultA_PFCd_2
1.186942145	1.506091814	RH_ContB_PFCmp_1

1.180942703	1.459088945	LH_DorsAttnB_PostC_6
1.178411025	1.439254411	RH_SalVentAttnA_ParMed_7
1.174196885	1.406238559	RH_SomMotA_11
1.170329559	1.375939838	LH_ContA_PFCd_1
1.167692943	1.355283166	RH_DorsAttnB_PostC_8
1.16160945	1.307621793	LH_SomMotB_Aud_15
1.159008044	1.287240973	RH_SalVentAttnA_ParMed_2
1.158995386	1.287141809	LH_SomMotA_8
1.154798485	1.254261017	RH_SalVentAttnA_PrC_1
1.154730091	1.253725177	LH_SomMotA_16
1.15349917	1.244081478	RH_SomMotA_19
1.153237504	1.242031444	RH_ContA_IPS_3
1.151692122	1.229924088	LH_ContB_PFCd_1
1.150604956	1.22140664	RH_DefaultC_Rsp_2
1.148158814	1.202242243	LH_SomMotA_6
1.141743711	1.151982864	RH_SomMotA_6
1.141066099	1.146674084	RH_SomMotA_7
1.140350973	1.141071402	LH_DefaultB_PFCl_1
1.139907877	1.137599948	RH_DefaultA_PCC_1
1.139450761	1.134018652	RH_SomMotA_12
1.139196168	1.132024032	LH_DorsAttnB_PostC_8
1.13735101	1.11756807	LH_ContB_IPL_3
1.136739805	1.112779559	LH_SomMotA_14
1.135904854	1.106238103	LH_DorsAttnA_SPL_6
1.133354354	1.086256106	RH_DorsAttnA_SPL_7
1.133016356	1.083608049	LH_DefaultB_PFCd_5
1.132242175	1.077542699	LH_SomMotA_11
1.131210046	1.069456442	RH_SomMotA_17
1.130797212	1.066222077	RH_SomMotA_3
1.12995214	1.059601323	LH_SalVentAttnA_FrMed_2
1.129641286	1.05716593	RH_SomMotA_13
1.127997236	1.044285551	LH_SalVentAttnA_ParMed_1
1.127123377	1.037439271	RH_DefaultA_PFCm_6

Table A28: Distribution of nodes based on betweenness centrality at sparsity level 35% in High Stress group. The first column contains the BC values, 2nd column are the BC values standardized to Z values, and 3rd column the name of the ROI.

Tables A1-28: Nodes ranking based on degree centrality (1-14) and betweenness centrality (15-28) at each sparsity level for both groups (Low stress and High stress).

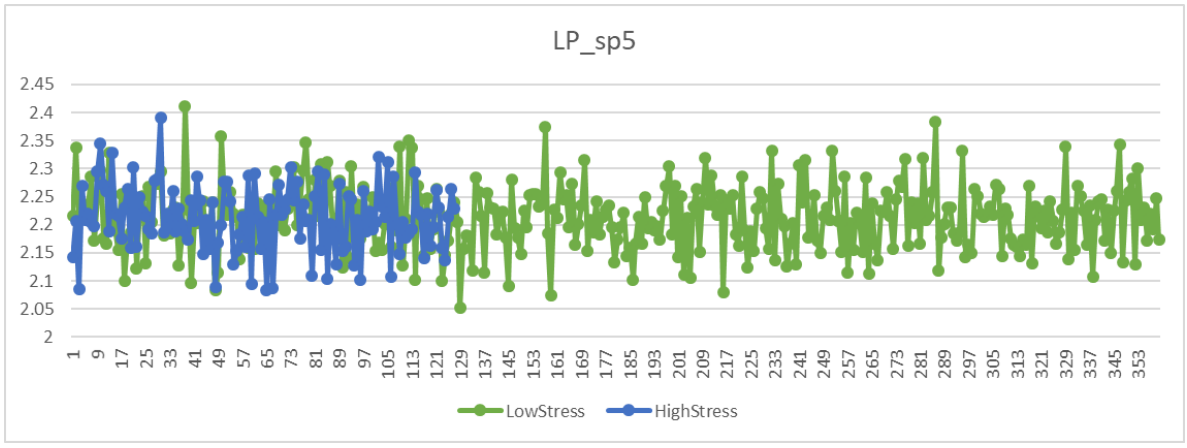
LP_sp5
2.45
2.4
2.35
2.3
2.25
2.2
2.15
2.1
2.05
2
1 9 17 25 33 41 49 57 65 73 81 89 97 105 113 121 129 137 145 153 161 169 177 185 193 201 209 217 225 233 241 249 257 265 273 281 289 297 305 313 321 329 337 345 353
LowStress
HighStress

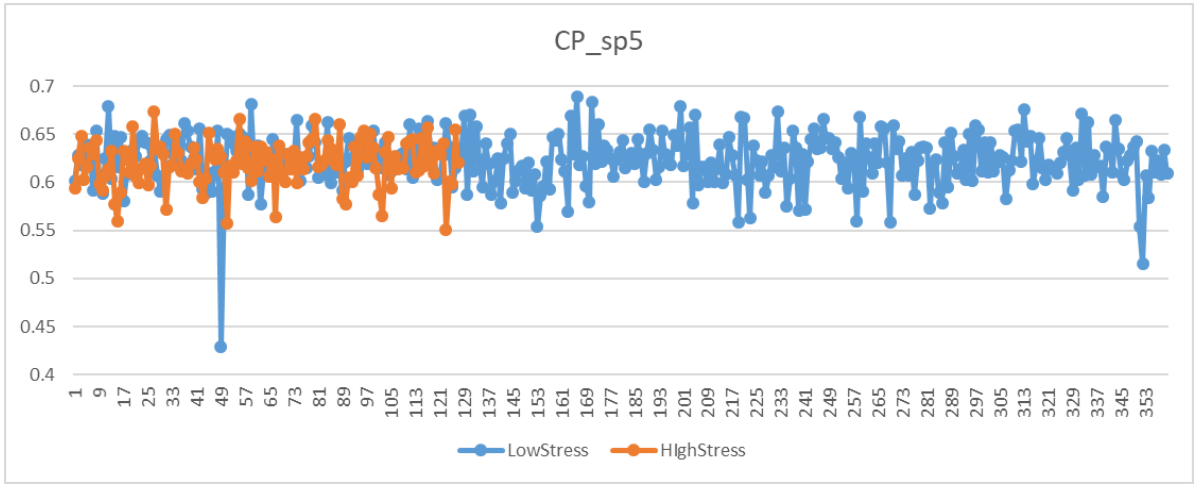
CP_sp5
0.7
0.65
0.6
0.55
0.5
0.45
0.4
1 9 17 25 33 41 49 57 65 73 81 89 97 105 113 121 129 137 145 153 161 169 177 185 193 201 209 217 225 233 241 249 257 265 273 281 289 297 305 313 321 329 337 345 353
LowStress
HIghStress

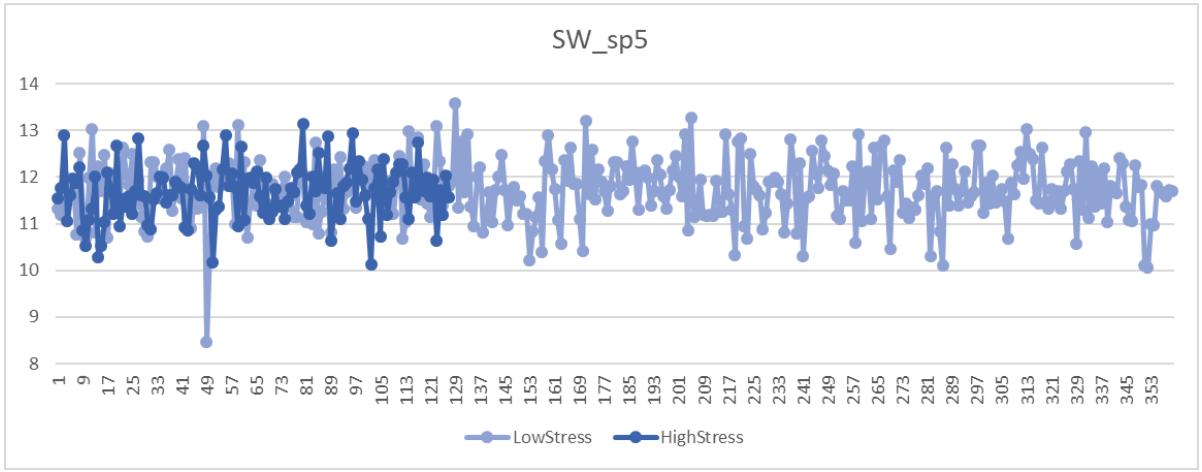
SW_sp5
14
13
12
11
10
9
8
1 9 17 25 33 41 49 57 65 73 81 89 97 105 113 121 129 137 145 153 161 169 177 185 193 201 209 217 225 233 241 249 257 265 273 281 289 297 305 313 321 329 337 345 353
LowStress
HighStress

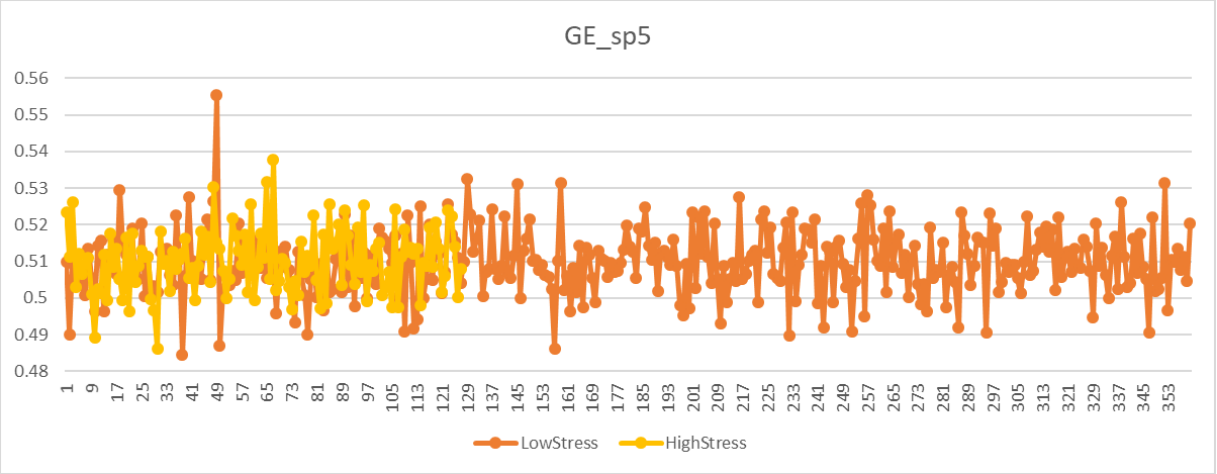

Figure A6: Graphical representation of global graph theory measures vary within and between-group (here only sparsity 5% is shown), even if they were not statistically different. The graph theory measures plotted are characteristic path length, cluster coefficient, small-worldness and global efficiency.

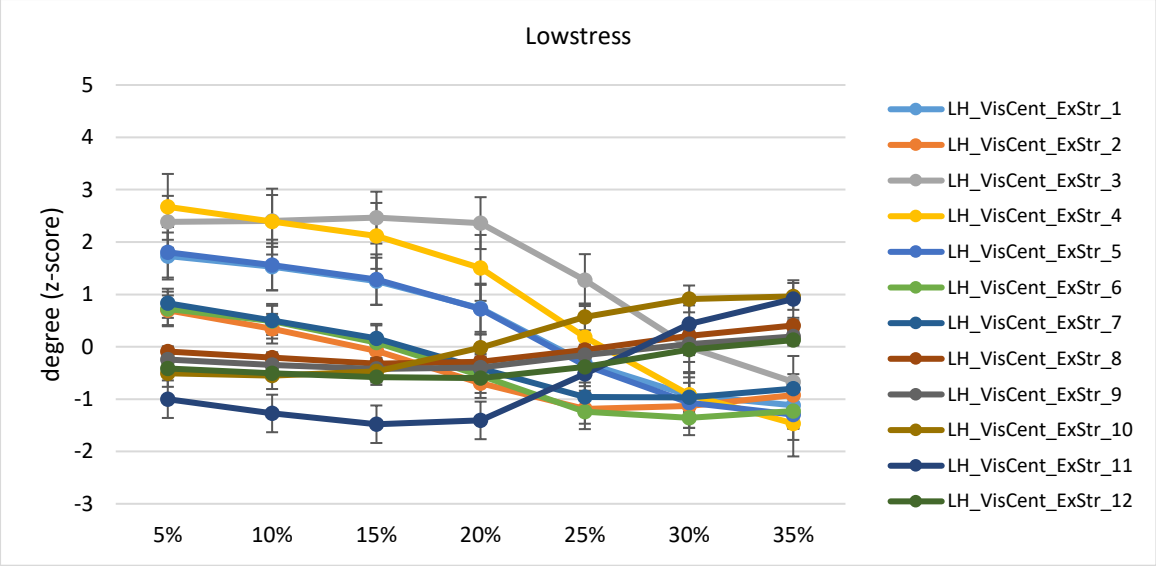
Lowstress
degree (z-score)
5
4
3
2
1
0
-1
-2
-3
5%
10%
15%
20%
25%
30%
35%
LH_VisCent_ExStr_1
LH_VisCent_ExStr_2
LH_VisCent_ExStr_3
LH_VisCent_ExStr_4
LH_VisCent_ExStr_5
LH_VisCent_ExStr_6
LH_VisCent_ExStr_7
LH_VisCent_ExStr_8
LH_VisCent_ExStr_9
LH_VisCent_ExStr_10
LH_VisCent_ExStr_11
LH_VisCent_ExStr_12

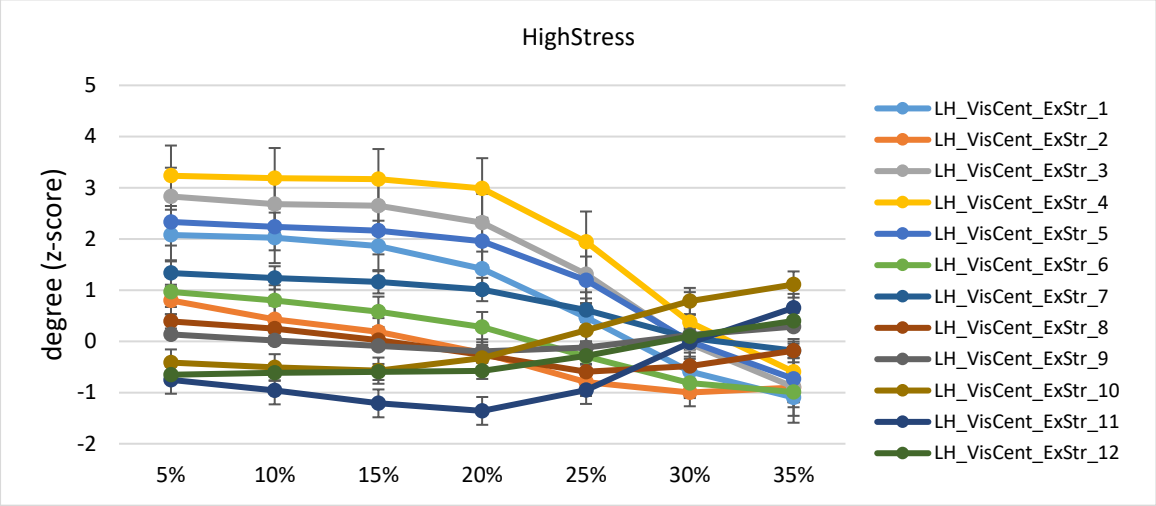
HighStress
degree (z-score)
5
4
3
2
1
0
-1
-2
5%
10%
15%
20%
25%
30%
35%
LH_VisCent_ExStr_1
LH_VisCent_ExStr_2
LH_VisCent_ExStr_3
LH_VisCent_ExStr_4
LH_VisCent_ExStr_5
LH_VisCent_ExStr_6
LH_VisCent_ExStr_7
LH_VisCent_ExStr_8
LH_VisCent_ExStr_9
LH_VisCent_ExStr_10
LH_VisCent_ExStr_11
LH_VisCent_ExStr_12

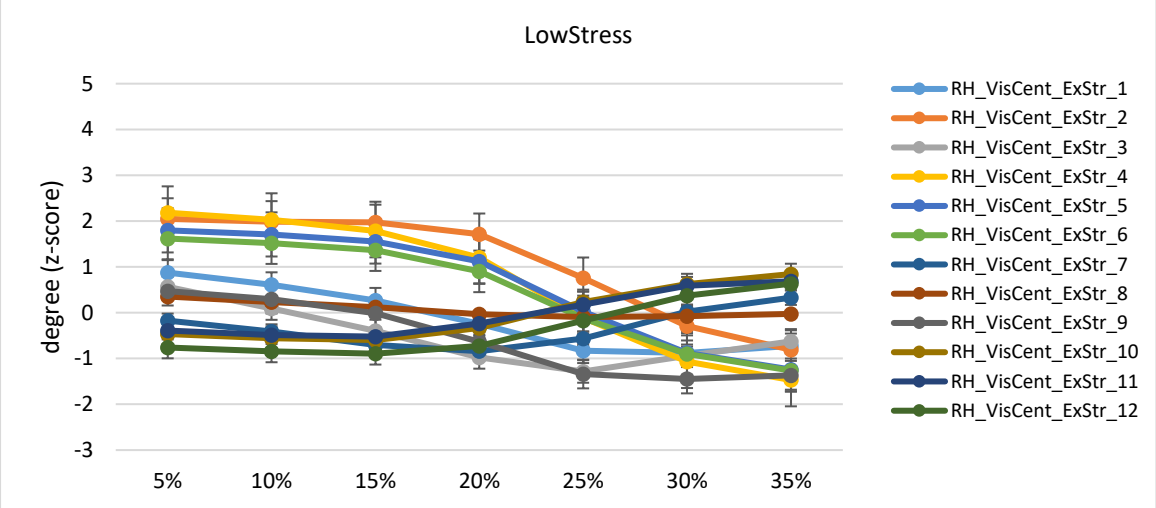
LowStress
degree (z-score)
5
4
3
2
1
0
-1
-2
-3
5%
10%
15%
20%
25%
30%
35%
RH_VisCent_ExStr_1
RH_VisCent_ExStr_2
RH_VisCent_ExStr_3
RH_VisCent_ExStr_4
RH_VisCent_ExStr_5
RH_VisCent_ExStr_6
RH_VisCent_ExStr_7
RH_VisCent_ExStr_8
RH_VisCent_ExStr_9
RH_VisCent_ExStr_10
RH_VisCent_ExStr_11
RH_VisCent_ExStr_12

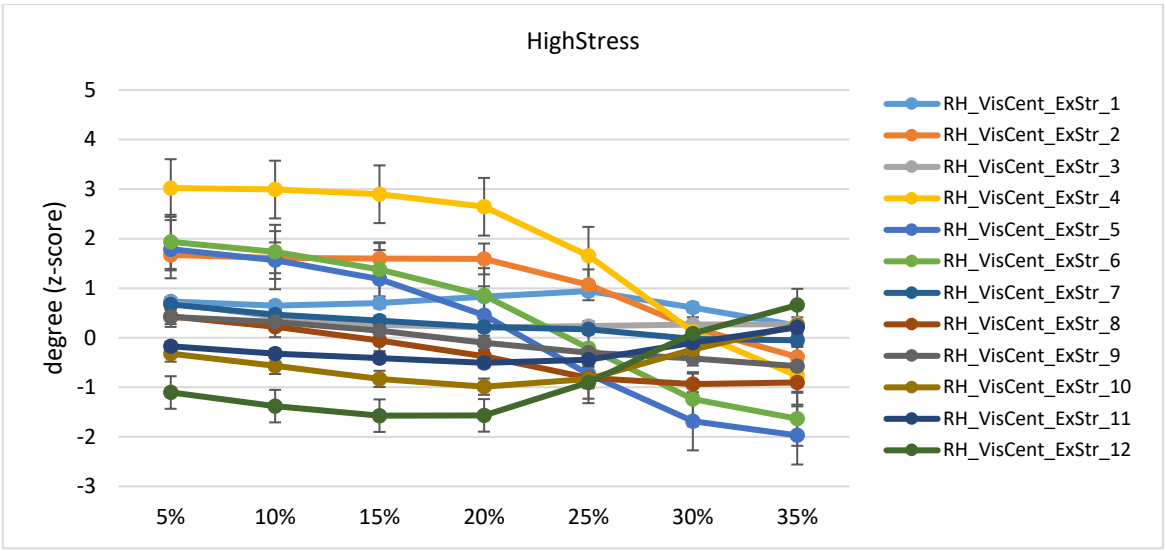
HighStress
degree (z-score)
5
4
3
2
1
0
-1
-2
-3
5%
10%
15%
20%
25%
30%
35%
RH_VisCent_ExStr_1
RH_VisCent_ExStr_2
RH_VisCent_ExStr_3
RH_VisCent_ExStr_4
RH_VisCent_ExStr_5
RH_VisCent_ExStr_6
RH_VisCent_ExStr_7
RH_VisCent_ExStr_8
RH_VisCent_ExStr_9
RH_VisCent_ExStr_10
RH_VisCent_ExStr_11
RH_VisCent_ExStr_12

a)

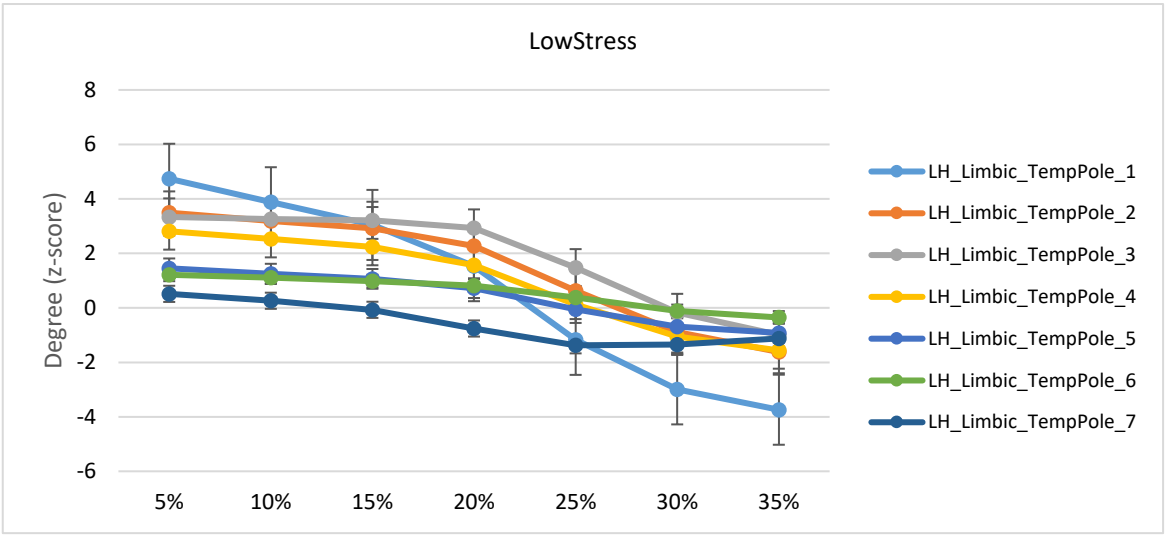
LowStress
Degree (z-score)
8
6
4
2
0
-2
-4
-6
5%
10%
15%
20%
25%
30%
35%
LH_Limbic_TempPole_1
LH_Limbic_TempPole_2
LH_Limbic_TempPole_3
LH_Limbic_TempPole_4
LH_Limbic_TempPole_5
LH_Limbic_TempPole_6
LH_Limbic_TempPole_7

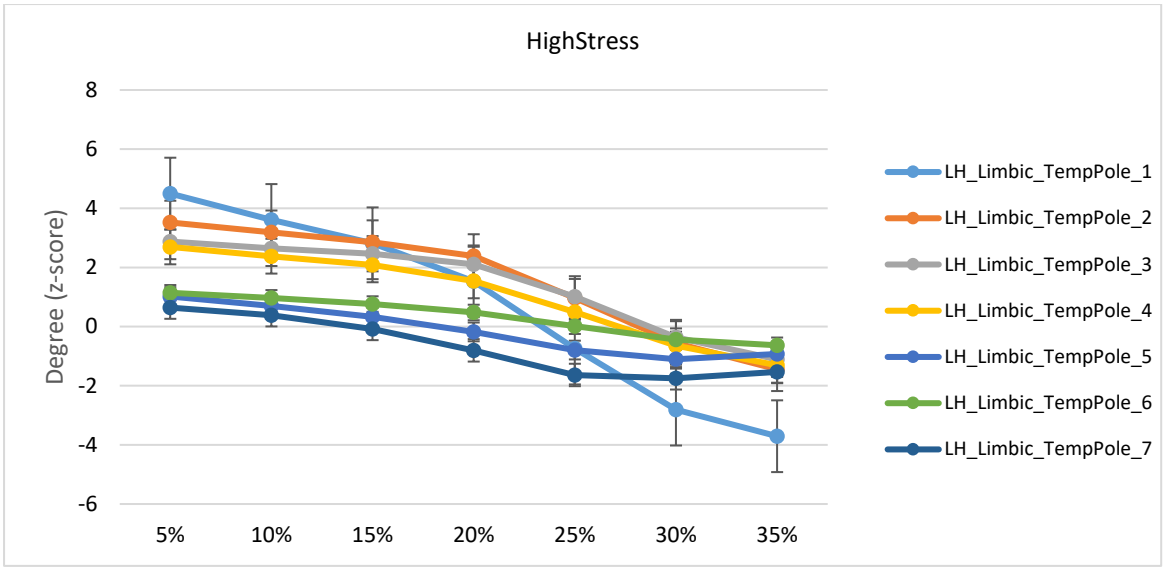
HighStress
Degree (z-score)
8
6
4
2
0
-2
-4
-6
5%
10%
15%
20%
25%
30%
35%
LH_Limbic_TempPole_1
LH_Limbic_TempPole_2
LH_Limbic_TempPole_3
LH_Limbic_TempPole_4
LH_Limbic_TempPole_5
LH_Limbic_TempPole_6
LH_Limbic_TempPole_7

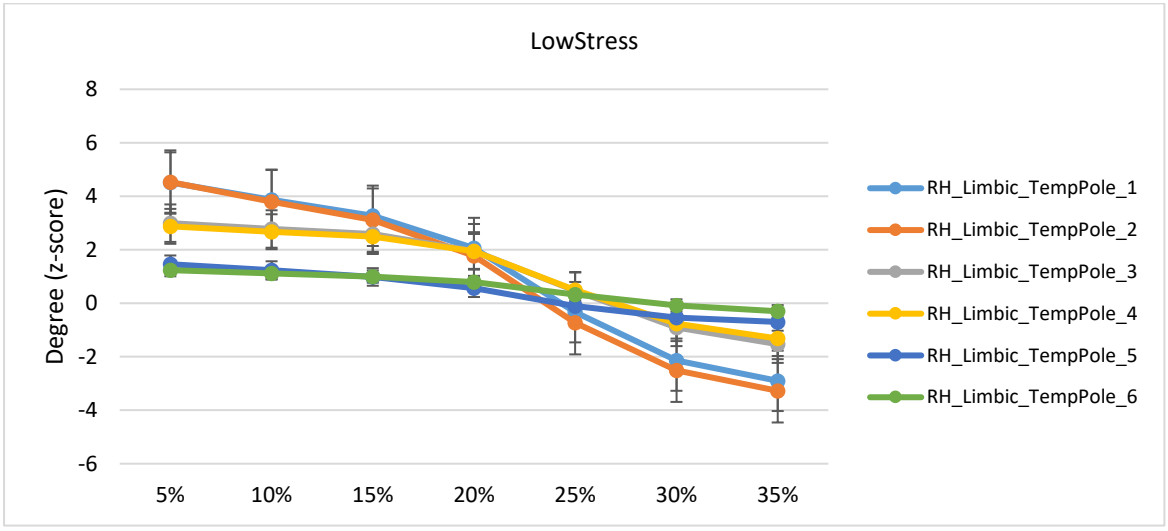
LowStress
Degree (z-score)
8
6
4
2
0
-2
-4
-6
5%
10%
15%
20%
25%
30%
35%
RH_Limbic_TempPole_1
RH_Limbic_TempPole_2
RH_Limbic_TempPole_3
RH_Limbic_TempPole_4
RH_Limbic_TempPole_5
RH_Limbic_TempPole_6

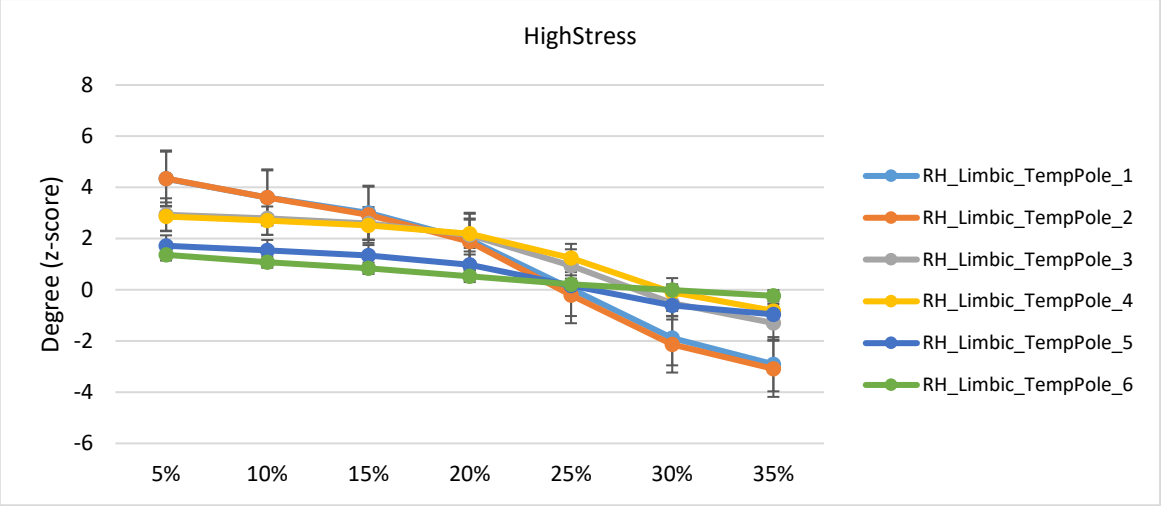
HighStress
Degree (z-score)
8
6
4
2
0
-2
-4
-6
5%
10%
15%
20%
25%
30%
35%
RH_Limbic_TempPole_1
RH_Limbic_TempPole_2
RH_Limbic_TempPole_3
RH_Limbic_TempPole_4
RH_Limbic_TempPole_5
RH_Limbic_TempPole_6

b)

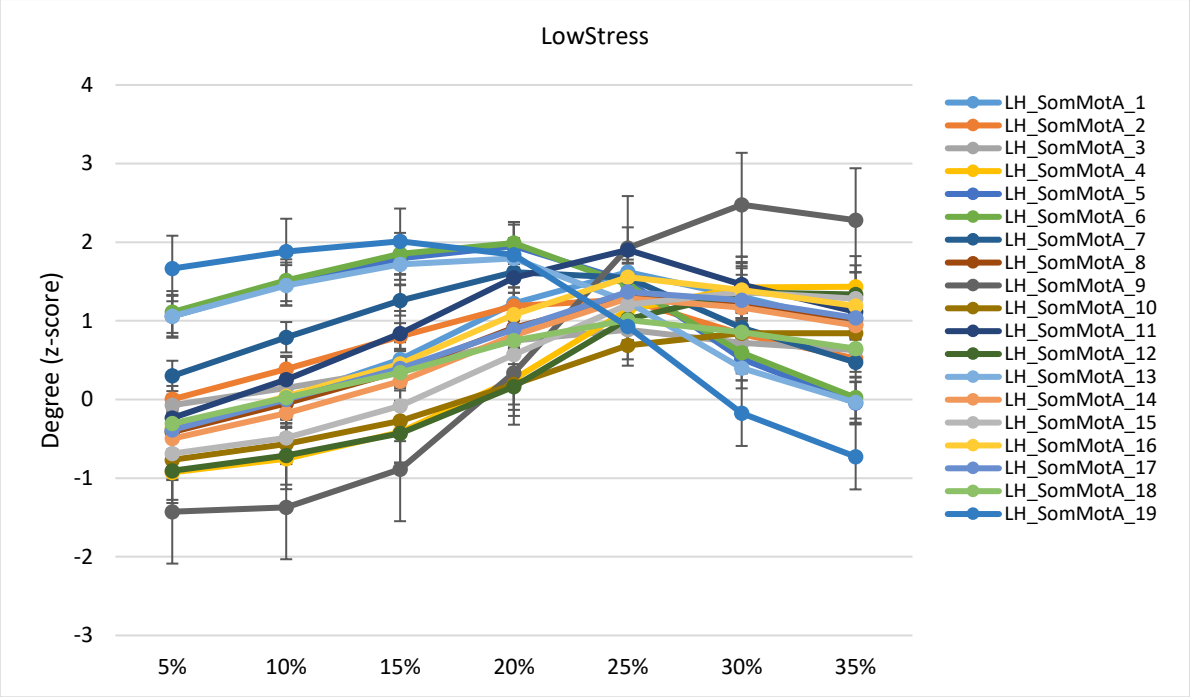
LowStress
Degree (z-score)
4
3
2
1
0
-1
-2
-3
5%
10%
15%
20%
25%
30%
35%
LH_SomMotA_1
LH_SomMotA_2
LH_SomMotA_3
LH_SomMotA_4
LH_SomMotA_5
LH_SomMotA_6
LH_SomMotA_7
LH_SomMotA_8
LH_SomMotA_9
LH_SomMotA_10
LH_SomMotA_11
LH_SomMotA_12
LH_SomMotA_13
LH_SomMotA_14
LH_SomMotA_15
LH_SomMotA_16
LH_SomMotA_17
LH_SomMotA_18
LH_SomMotA_19

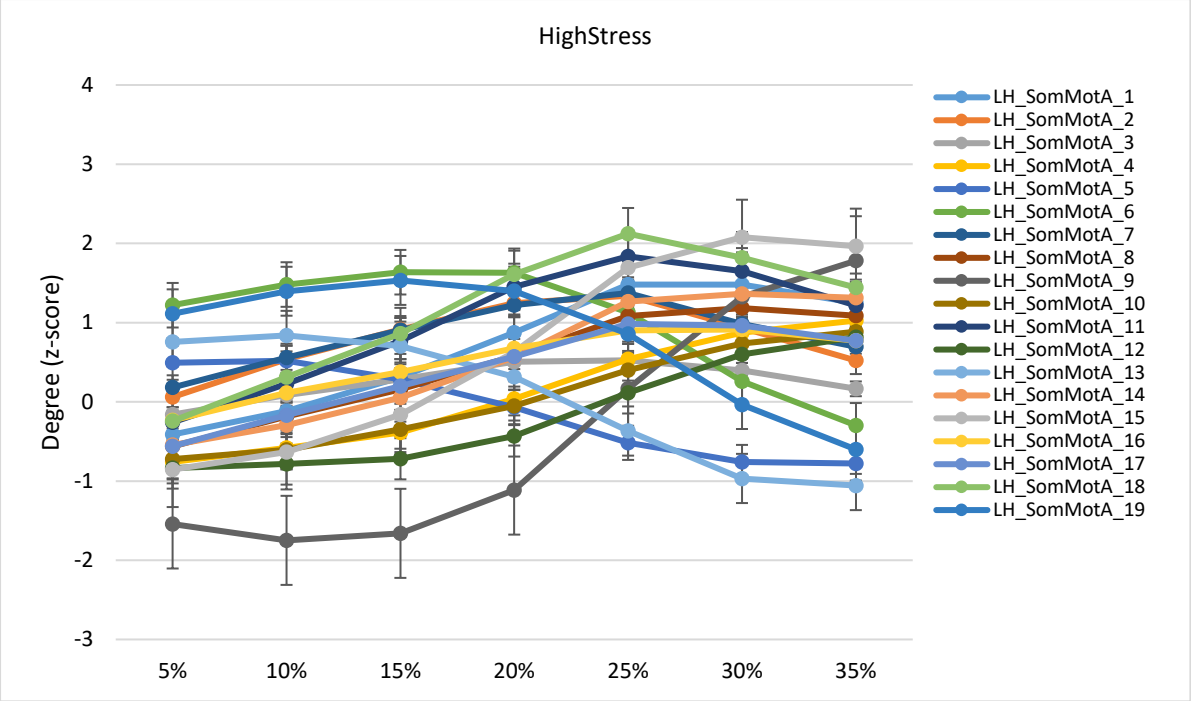
HighStress
Degree (z-score)
4
3
2
1
0
-1
-2
-3
5%
10%
15%
20%
25%
30%
35%
LH_SomMotA_1
LH_SomMotA_2
LH_SomMotA_3
LH_SomMotA_4
LH_SomMotA_5
LH_SomMotA_6
LH_SomMotA_7
LH_SomMotA_8
LH_SomMotA_9
LH_SomMotA_10
LH_SomMotA_11
LH_SomMotA_12
LH_SomMotA_13
LH_SomMotA_14
LH_SomMotA_15
LH_SomMotA_16
LH_SomMotA_17
LH_SomMotA_18
LH_SomMotA_19

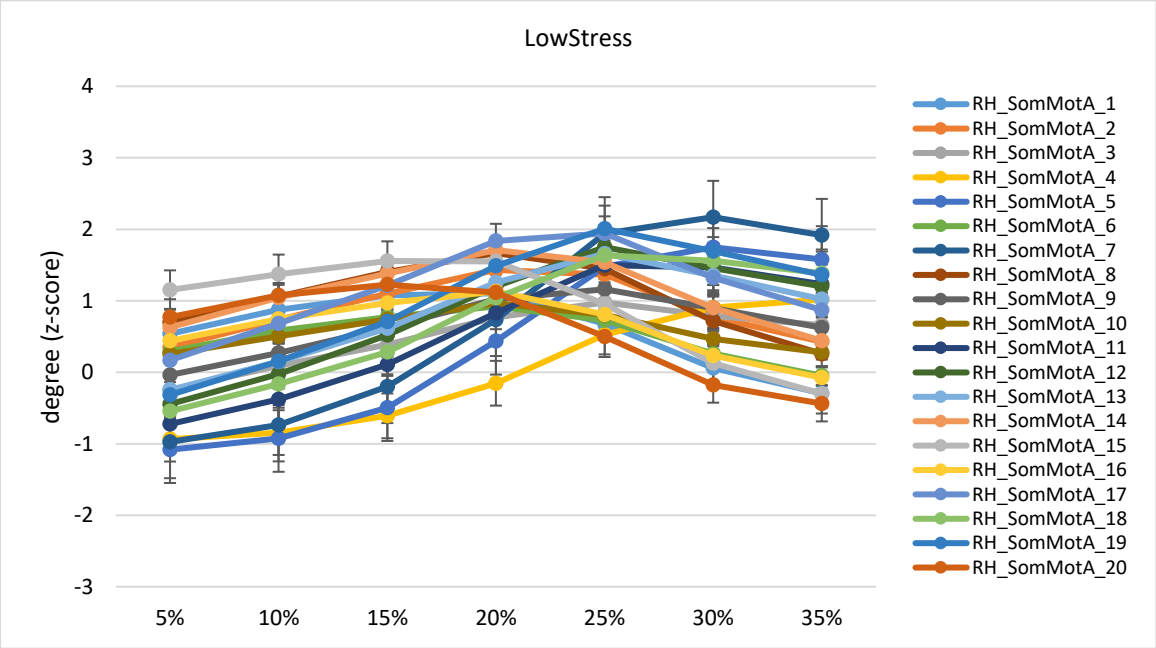
LowStress
degree (z-score)
4
3
2
1
0
-1
-2
-3
5%
10%
15%
20%
25%
30%
35%
RH_SomMotA_1
RH_SomMotA_2
RH_SomMotA_3
RH_SomMotA_4
RH_SomMotA_5
RH_SomMotA_6
RH_SomMotA_7
RH_SomMotA_8
RH_SomMotA_9
RH_SomMotA_10
RH_SomMotA_11
RH_SomMotA_12
RH_SomMotA_13
RH_SomMotA_14
RH_SomMotA_15
RH_SomMotA_16
RH_SomMotA_17
RH_SomMotA_18
RH_SomMotA_19
RH_SomMotA_20

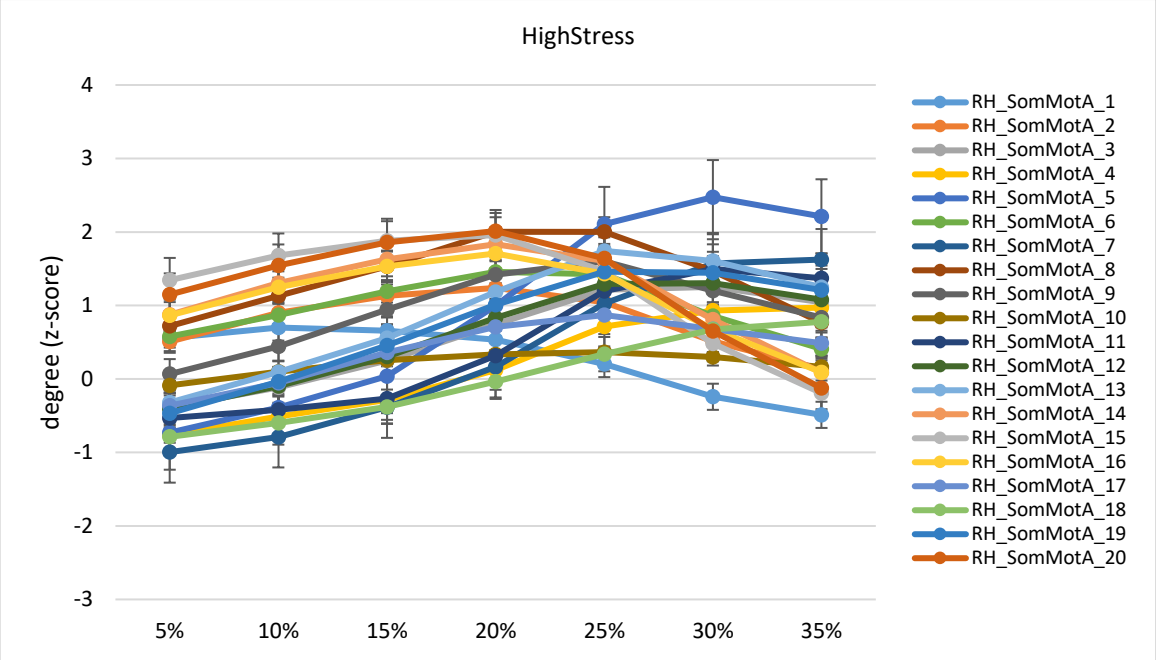
HighStress
degree (z-score)
4
3
2
1
0
-1
-2
-3
5%
10%
15%
20%
25%
30%
35%
RH_SomMotA_1
RH_SomMotA_2
RH_SomMotA_3
RH_SomMotA_4
RH_SomMotA_5
RH_SomMotA_6
RH_SomMotA_7
RH_SomMotA_8
RH_SomMotA_9
RH_SomMotA_10
RH_SomMotA_11
RH_SomMotA_12
RH_SomMotA_13
RH_SomMotA_14
RH_SomMotA_15
RH_SomMotA_16
RH_SomMotA_17
RH_SomMotA_18
RH_SomMotA_19
RH_SomMotA_20

c)

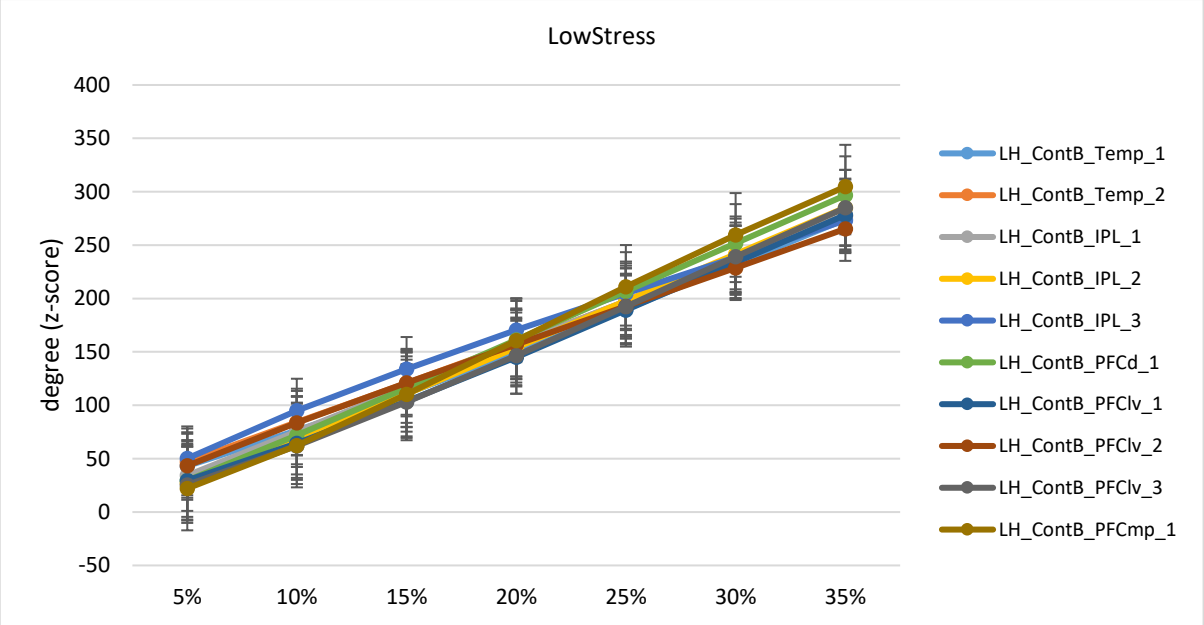
LowStress
degree (z-score)
400
350
300
250
200
150
100
50
0
-50
5%
10%
15%
20%
25%
30%
35%
LH_ContB_Temp_1
LH_ContB_Temp_2
LH_ContB_IPL_1
LH_ContB_IPL_2
LH_ContB_IPL_3
LH_ContB_PFCd_1
LH_ContB_PFClv_1
LH_ContB_PFClv_2
LH_ContB_PFClv_3
LH_ContB_PFCmp_1

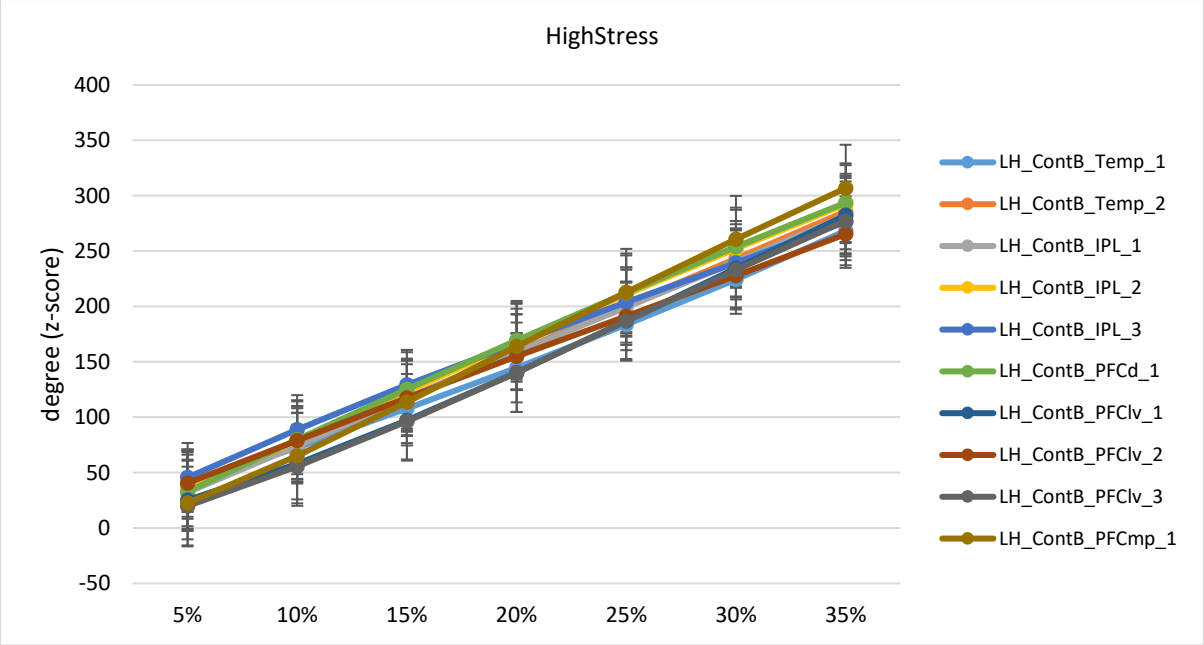
HighStress
400
350
300
250
200
150
100
50
0
-50
degree (z-score)
5%
10%
15%
20%
25%
30%
35%
LH_ContB_Temp_1
LH_ContB_Temp_2
LH_ContB_IPL_1
LH_ContB_IPL_2
LH_ContB_IPL_3
LH_ContB_PFCd_1
LH_ContB_PFClv_1
LH_ContB_PFClv_2
LH_ContB_PFClv_3
LH_ContB_PFCmp_1

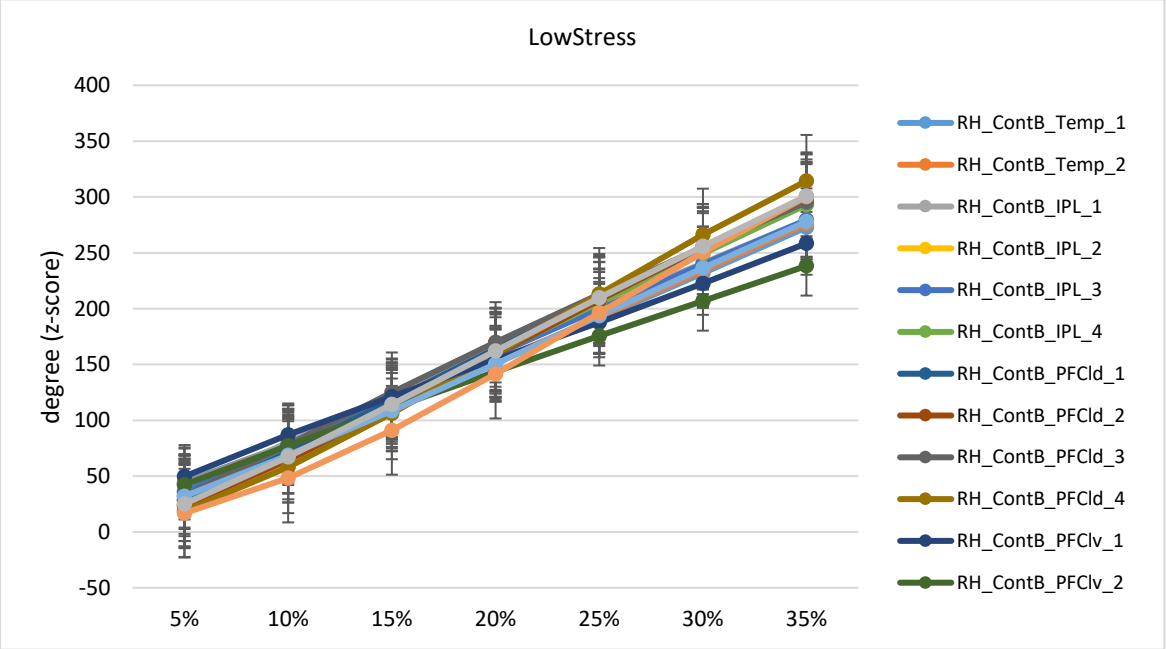
LowStress
400
350
300
250
200
150
100
50
0
-50
degree (z-score)
5%
10%
15%
20%
25%
30%
35%
RH_ContB_Temp_1
RH_ContB_Temp_2
RH_ContB_IPL_1
RH_ContB_IPL_2
RH_ContB_IPL_3
RH_ContB_IPL_4
RH_ContB_PFCld_1
RH_ContB_PFCld_2
RH_ContB_PFCld_3
RH_ContB_PFCld_4
RH_ContB_PFClv_1
RH_ContB_PFClv_2

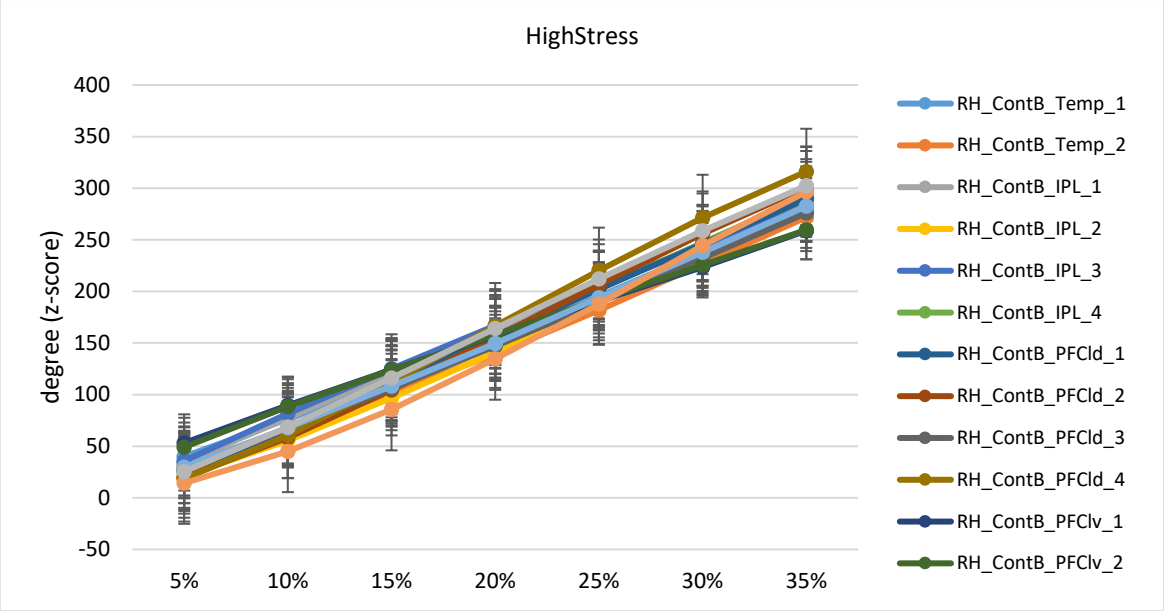

d)

Figure A7: Graphs of nodal degree at all the sparsity levels considered in this study based on four different networks: a) visual central, b) limbic – temporal pole, c) somatomotor and d) executive control networks. All the networks are displayed for both hemispheres. Error bars represents standard error.

Appendix B

Subfield	Location	Information
CA1	It is located between CA2/3 and subiculum.	Connected with the CA3 and subiculum. It is a key component of the trisynaptic circuit.
CA2/3	The two subfields are combined in Freesurfer. Located between CA4 and CA1	Part of the trisynaptic circuit and site of synapses of mossy fiber pathway. Involved in encoding short-term memory
CA4	It is located within the hilum of the dentate.	Functionally considered part of the dentate gyrus.
Dentate	Contains the granule cell and molecular layer	Input region of trisynaptic hippocampal circuit. Site of neurogenesis. Origin of mossy fiber pathway
Subiculum	Lies between the CA1 and presubiculum. The molecular layer separates it from the fissure.	Key output substructure of hippocampal circuitry.
Presubiculum	It lies between subiculum and the parasubiculum along the fissure.	Important for scene recognition and visospatial processing.
Parasubiculum	Lies between entorhinal cortex and presubiculum, along the base of the fissure.	Involved in the same function of presubiculum
Hippocampal tail	The posterior end of the hippocampus	Defined by the first coronal slice showing contact with the fornix and all regions posterior to this.
Molecular layer	Upper layer of the CA1-3 and subiculum	Relatively neuronal cell body free. Contains inflammatory cells, connective tissue and axons of connecting neurons.
HATA	Essentially lies between the hippocampus and amygdala	Involved in the amygdalo-hippocampal network.
Fimbria	It functions as bridge between the fornix and the hippocampus.	
Fissure	CSF space between the molecular layer of the hippocampal gyrus and the dentate gyrus.	

Table B1: Hippocampal subfields segmented in FreeSurfer6.0. Abbreviations: HATA = Hippocampal Amygdalar Transition Area; CA = Cornu Ammonis

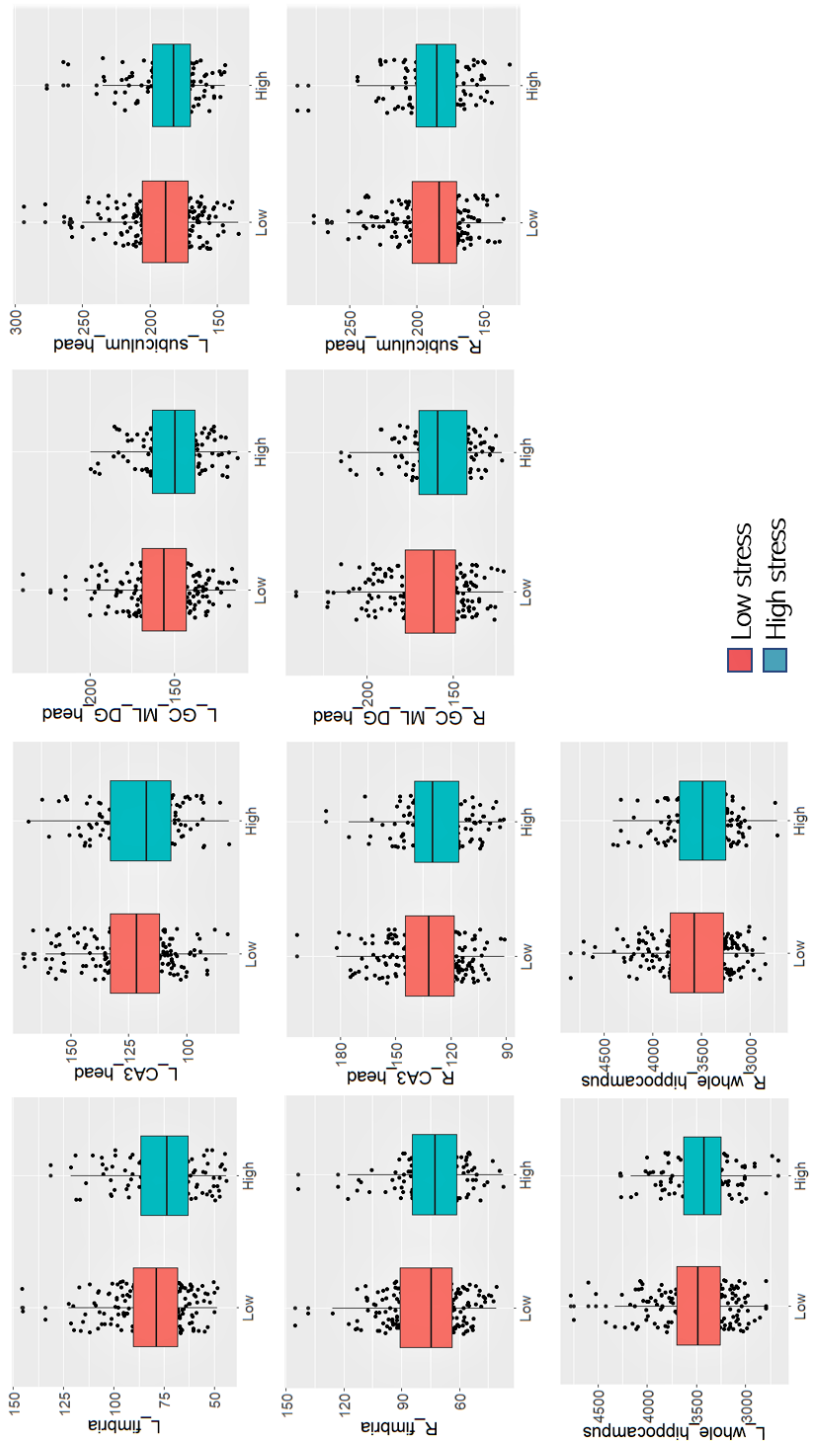

Figure B1: Beeswarm boxplots showing no between-group differences in some of the hippocampal subfields

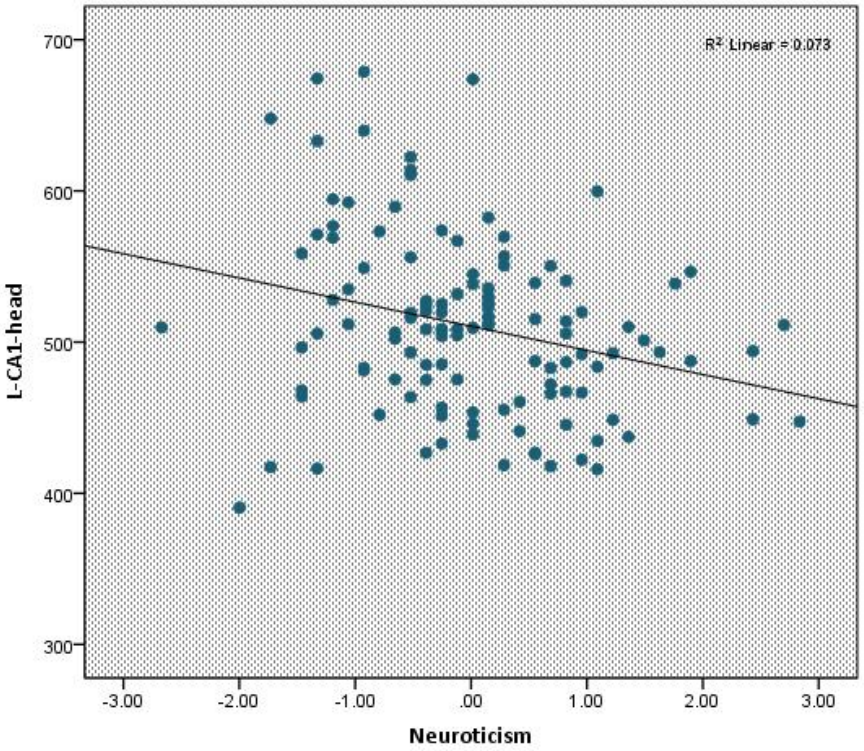
R² Linear = 0.073
L-CA1-head
Neuroticism
700
600
500
400
300
-3.00
-2.00
-1.00
.00
1.00
2.00
3.00

a)

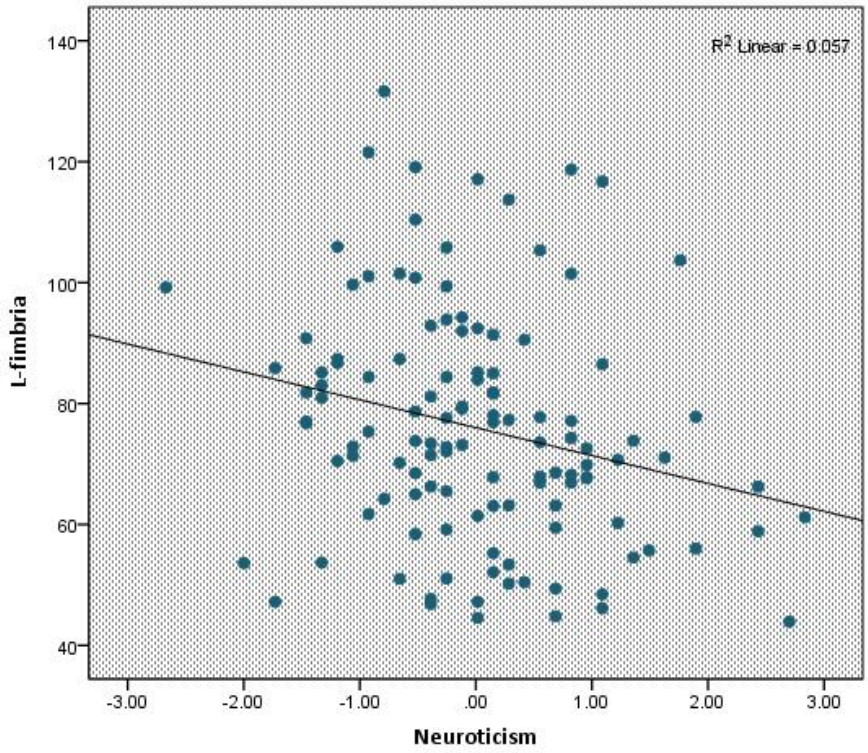
R² Linear = 0.057
L-fimbria
Neuroticism
140
120
100
80
60
40
-3.00
-2.00
-1.00
.00
1.00
2.00
3.00

b)

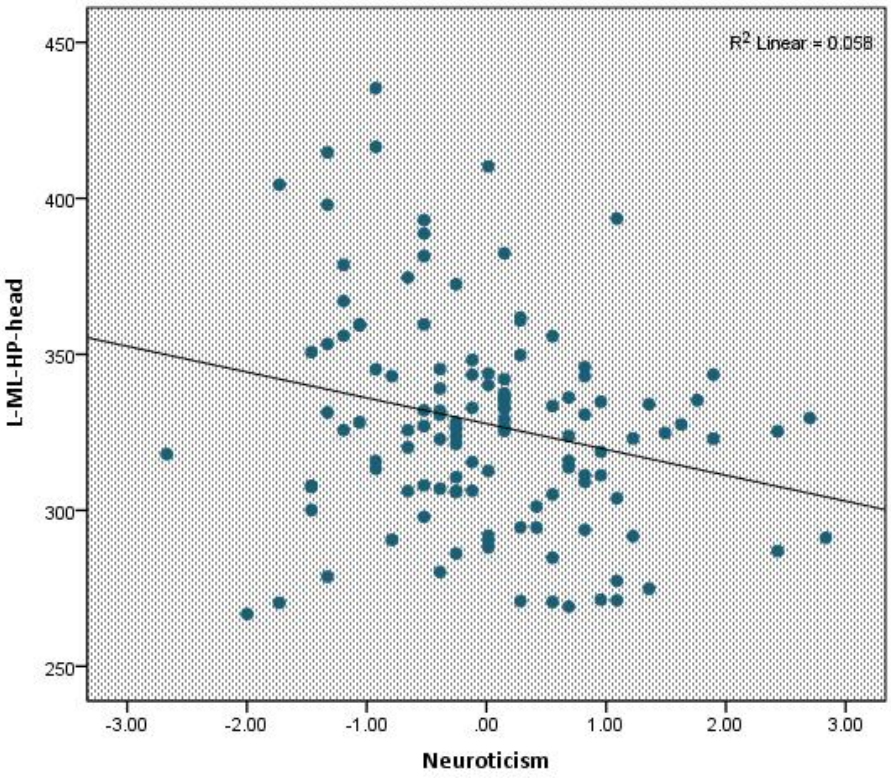

c)

Figure B2: Negative linear correlations in the High stress group between the level of Neuroticism and a) left CA1-head, b) left fimbria, c) left molecular layer of the hippocampal head

	Low stress	High stress
l_Hippocampal_tail	0.833	0.064
l_subiculum_body	0.337	0.04578*
l_CA1_body	0.789	0.151
l_subiculum_head	0.864	0.75
l_CA1_head	0.21	0.792
l_molecular_layer_HP_head	0.33	0.795
l_molecular_layer_HP_body	0.774	0.93
l_GC_ML_DG_head	0.158	0.654
l_CA3_body	0.396	0.109
l_GC_ML_DG_body	0.299	0.02*
l_CA4_head	0.323	0.676
l_CA4_body	0.141	0.0423*
l_CA3_head	0.0597	0.518
l_Whole_hippocampal_body	0.421	0.7878
l_Whole_hippocampus	0.516	0.90371
r_Hippocampal_tail	0.0371*	0.4676
r_subiculum_body	0.578	0.11
r_CA1_body	0.919	0.15
r_subiculum_head	0.0412*	0.563
r_CA1_head	0.332	0.855
r_molecular_layer_HP_head	0.3684	0.79
r_molecular_layer_HP_body	0.537	0.633
r_GC_ML_DG_head	0.968	0.4916
r_CA3_body	0.9122	0.878
r_GC_ML_DG_body	0.537	0.36
r_CA4_head	0.8467	0.5273
r_CA4_body	0.577	0.184
r_CA3_head	0.8467	0.665
r_Whole_hippocampal_body	0.584	0.6
r_Whole_hippocampus	0.72	0.4546

Table B2: Uncorrected p-values of the linear mixed model for each of the subfields considered in both groups. None of the significant results survived FDR correction.

Appendix C

1.1. Along-tract analysis. Analyses along the tract length showed a significant increase of MD (p=0.012) and RD (p=0.0098) in the right subgenual branch in the older group.

1.2. Tract averaged-measures analysis. Before correction for multiple comparisons, in the subgenual branch, significant decreases were found in the left FA (p=0.001), AD (p=0.004) and the volume tract (p=0.001), as well as an increase in the left RD (p=0.00000001). In the right hemisphere there was an increase in MD (p= 0.005). The retrosplenial tract showed a statistically significant increase in the left tract volume (p=0.0005), but in none of the DTI measures. Likewise, in the parahippocampal branch, there was a significant increase only in the left tract volume (p=0.00005). Overall, these results confirmed the along-tract analysis outcomes.

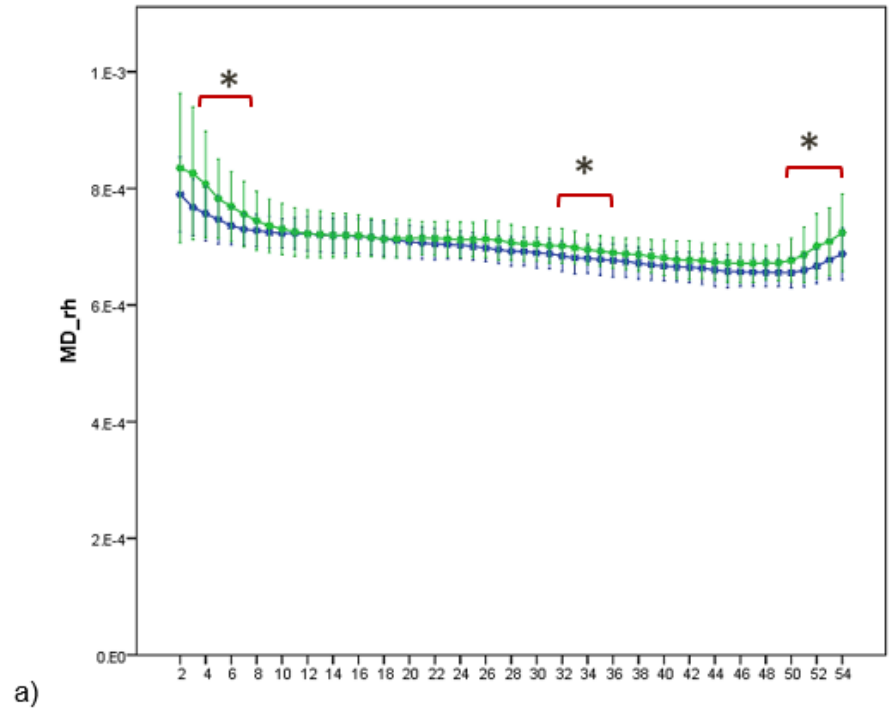

a)

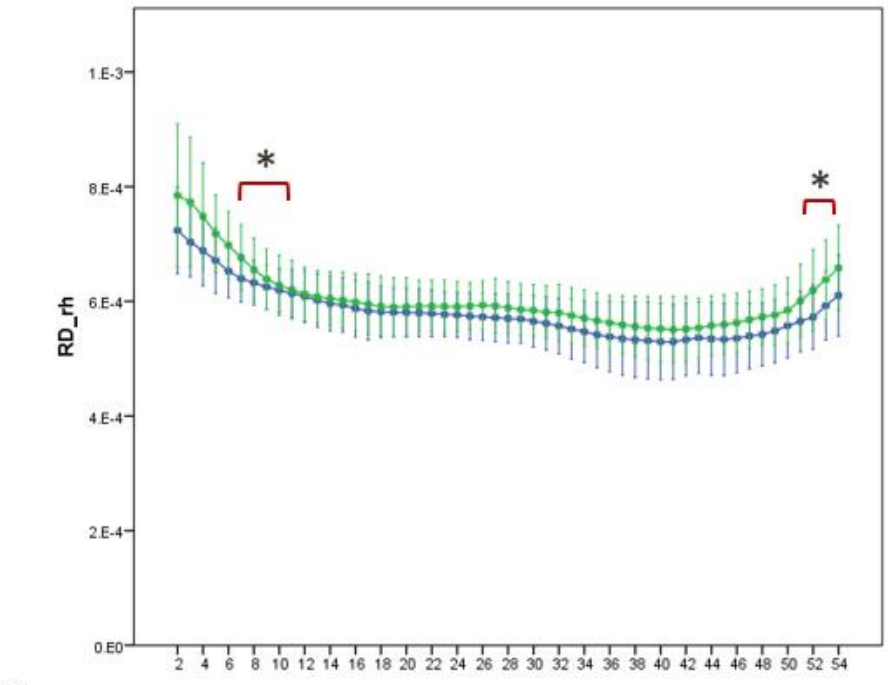

b)

Figure C1: Along-tract analysis of the right hemisphere subgenual tract between young (blue line) and older (green line) healthy people. a) mean diffusivity, b) radial diffusivity. The data represent the mean of DTI-measures for each point along the tract +/- 1 standard deviation. Stars indicate the location of between-group significant differences.

Appendix D

Instructions to Perform Brain Connectivity and Graph Theory Measures Analyses

Overview

To run the brain connectivity and graph theory analysis, the first step is to extract the grey matter segmentations using SPM. The version used in this study is SPM8 in Matlab 2012a.

After the segmentation, the pipeline developed by Tijms et al., 2012 is applied. The github page to get the scripts is: https://github.com/bettytijms/Single_Subject_Grey_Matter_Networks. The version used in this study is "Extract_individual_GM_networks_v20150902". Following the instructions of github, correlation matrices at an individual level are extracted, together with other files describing how th matrices were calculated and obtained. All the details can be found in the script called "batch_extract_networks_v20150902". This will create a directory called 'results', containing one sub-folder for each subject. Each sub-folder contains two sub-directories. In the sub-directory "/data", the file named 'rotcorr.mat' is the matrix which is used for the calculation of graph theory measures. Another file used as input for the analysis is the actual GM

segmentation image, called ‘iso2mm_s(subj_nr)’, which is the resliced image with 2x2x2mm^3 voxels (details for each file created can found in Tijms’ paper and github page).

Once the analysis has run for all the participants, an atlas is applied to each of the GM segmentations. The atlas used in this study is the Schaefer template with 400 ROIs and 17 networks. Each GM segmentation was registered to the atlas space with a non-linear transformation performed in DARTEL in SPM8.

Since correlation matrices are extracted in native space, (meaning they have different sizes across subjects), a further step is necessary to reduce the matrix size to 400x400, which are the number of ROIs in the Schaefer template.

The scripts conceived by F.S and A.L.W.B. and developed by C.J.M. calculate to the so-called “matrix reshaping”: individual correlation matrices (of different size *n*x*n*) are “reshaped” to a size of 400x400. Starting from this step, Matlab2016a was used.

The scripts to run this step are:

- Create_Schafer_template.m

- simplify_bind.m

- ber_reshape.m (script that ‘reshapes’ the matrix to 400x400).

- Fisher_r2z.m (converting r coefficients in the correspondent z-values using Fisher’s r-to-z transformation)

To compute graph theory measures, an additional folder with all the functions downloaded from Brain Connectivity toolbox (BCT) is needed. The web page where to find the list of graph theory measures used in the analysis is: https://sites.google.com/site/bctnet/measures/list.

Instructions:

1) create a directory to store all the subjects run with Tijms' pipeline

2) In each subject directory, create a directory (we called it 'reshape') where to save all the new files generated by the reshaping step

3) run 'Create_Schafer_template.m' and 'simplify_bind.m' (we saved these output files in the 'reshape' folder)

4) run the script 'ber_reshape.m' to obtain the reshaped correlation matrix.

5) run the script 'Fisher_r2z.m' to convert each correlation matrix value in its correspondent z-value

To run the graph theory measures analysis:

- BCT_calculation_Fisher.m: this script calculates graph theory measures for each subject at each sparsity level. The files are saved in the subject directory and correspondent sparsity sub-folder. Note: the sub-folder 'essential functions' is needed to compute each graph theory.

- Avg_measures_stressGroups.m: this script loads the graph theory measures from each subject folder and it puts them all together in a single

.mat file for each measure, after averaging the values both across subjects and across nodes. The files generated can be then imported in statistical packages (for example, SPSS or R) to run between-group statistical comparison.

To run the whole-brain analysis with NBS, two scripts are needed:

- Create_design_matrix.m

- Create_ConnectivityMatrix_NBS_ber.m

The files generated are used as input in NBS gui to run whole-brain connectivity analysis.

LIST OF SCRIPTS

(In order of how their appearance)

- Avg_measures_stressGroups.m
- BCT_calculation_Fisher.m
- ber_reshape.m
- Create_ConnectityMatrix_NBS_ber.m
- Create_design_matrix.m
- Create_Schaefer_template.m
- Fisher_r2z.m
- simplify_bind.m

```
function [] = Avg_measures_stressGroups()
% This function calculates and concatenates measures form BCT to use
them in statistical analyses


% Load the file that contains the subject's index of each stress group
     cd('/path-to-txtfiles');
     load('HighStress_subgroup.txt');
     load('LowStress_subgroup.txt');

     betw_allspars_wholeGroup=zeros(400,8);

     for k=5:5:35
     tic


 %creates the folder that will contain all the other folders
         BCT_name_dir=strcat('BCT_487_',num2str(k));
         mkdir('/path-where-to-save-data/',BCT_name_dir);

% Creates the matrices that will contain the data of each group
         bet_allnodes_LS=[];
         bet_allnodes_HS=[];

         clust_allnodes_LS=[];
         clust_allnodes_HS=[];

         connections_LS=[];
         connections_HS=[];

         lp_LS=[];
         lp_HS=[];

         gl_efficiency_LS=[];
         gl_efficiency_HS=[];

         degree_allsubj_LS=[];
         degree_allsubj_HS=[];

         degree_allnodes_LS=[];
         degree_allnodes_HS=[];

% go through all the subject folders that belong to the low stress
group
         for i=1:length(LowStress_subgroup)

       % get the IDs of the subjects that belong to the low stress
       group
              ID_low=LowStress_subgroup(i);

              % Get the name of the folder according to the IDs
              cd('/path-to-subj-dir');
              fold_name =strcat ('*', num2str(ID_low));
              all_sub_fold = dir(fold_name);
              name_sub_fold = {all_sub_fold.name};
              subj_fold = strjoin(name_sub_fold);
```

```
        % go into their folder according to their IDs
         spar_fold=strcat('/path-to-subj-
dir/',subj_fold,'/conn_matrix_sym/spar',num2str(k));
        cd(spar_fold);

        %load the betweenness
        bet_file=('betw*.mat');
        bet_file = dir(bet_file);
        bet_file_name = { bet_file.name };
        load(bet_file_name{1});

         % concatenate horizontally the betweenness of all the
400 nodes for all the subjects
        % of this group
        bet_allnodes_LS=cat(2,bet_allnodes_LS,betw_S);

betw_allspars_wholeGroup(:,k/5)=betw_allspars_wholeGroup(:,k/5)+
betw_S;



        %load the clustering values
        clust_file=('clust*.mat');
        clust_file = dir(clust_file);
        clust_file_name = { clust_file.name };
        load(clust_file_name{1});

         % concatenate horizontally the clustering of all the 400
nodes for all the subjects
        % of this group
        clust_allnodes_LS=cat(2,clust_allnodes_LS,clustS);

        %load the tot nr connection values
        connect_file=('connections*.mat');
        connect_file = dir(connect_file);
        connect_file_name = { connect_file.name };
        load(connect_file_name{1});

         % concatenate vertically the number connections of all
networks that belong to the subjects
        % of this group
        connections_LS=cat(1,connections_LS,connections);

        %load the global efficiency
        gl_eff_file=('gl_efficiency*.mat');
        gl_eff_file = dir(gl_eff_file);
        gl_eff_file_name = { gl_eff_file.name };
        load(gl_eff_file_name{1});

         % concatenate vertically the global efficiency of the
subjects
        % of this group for each sparsity (that's why k/5)
        gl_efficiency_LS=cat(1,gl_efficiency_LS,efficiency);

        % concatenate the degree for all the subjects
        degree_file=('degree*.mat');
        degree_file = dir(degree_file);
        degree_file_name = {degree_file.name };
        load(degree_file_name{1});
```

```
        degree_allnodes_LS=cat(2,degree_allnodes_LS,degree);

        degree_allsubj_LS=cat(1,degree_allsubj_LS,mean(degree));

  %specify the folder and path where Lp is stored, because it is
 different from all the other measures
         lp_fold=strcat('/path-to-subj-
       dir/',subj_fold,'/conn_matrix_sym');
        cd(lp_fold);

        %load the lp
        Lp_file=('Lp*.mat');
        Lp_file = dir(Lp_file);
        Lp_file_name = { Lp_file.name };
        load(Lp_file_name{1});

   % concatenate vertically the characteristic path length of the
 subjects of this group for each sparsity (that's why k/5)
         lp_LS=cat(1,lp_LS,Lp(k/5)); % since th efile of LP has
 the values for each sparsity, we divide k/5 so that for each
 iteration it gets only one Lp value according to each sparsity
 level

    end

     % Average the betweenness for each node of all the subjects
 of this group
    avgBet_allnodes_LS=mean(bet_allnodes_LS,2);


    % Average the clustering for each node of all the subjects of
this group
    avgClust_allnodes_LS=mean(clust_allnodes_LS,2);

    % average the degree for each node of all the subjects of
this group
    avgDegree_allnodes_LS=mean(degree_allnodes_LS,2);


    % go through all the subject folders that belong to the high
stress group
    for i=1:length(HighStress_subgroup)

        % get the IDs of the subjects that belong to the low
stress group
        ID_high=HighStress_subgroup(i);

        % Get the name of the folder according to the IDs
        cd('/path-to-subj-dir/');
        fold_name =strcat ('*', num2str(ID_high));
        all_sub_fold = dir(fold_name);
        name_sub_fold = {all_sub_fold.name};
        subj_fold = strjoin(name_sub_fold);

        % go into their folder according to their IDs
        spar_fold=strcat('/path-to-subj-
dir/',subj_fold,'/conn_matrix_sym/spar',num2str(k));
```

```
        cd(spar_fold);

        %load the betweenness
        bet_file=('betw*.mat');
        bet_file = dir(bet_file);
        bet_file_name = { bet_file.name };
        load(bet_file_name{1});

        % concatenate horizontally the betweenness of all the 400
nodes for all the subjects of this group
        bet_allnodes_HS=cat(2,bet_allnodes_HS,betw_S);

betw_allspars_wholeGroup(:,k/5)=betw_allspars_wholeGroup(:,k/5)+b
etw_S;

        %load the clustering values
        clust_file=('clust*.mat');
        clust_file = dir(clust_file);
        clust_file_name = { clust_file.name };
        load(clust_file_name{1});

        % concatenate horizontally the clustering of all the 400
nodes for all the subjects of this group
        clust_allnodes_HS=cat(2,clust_allnodes_HS,clustS);

        %load the clustering values
        connect_file=('connections*.mat');
        connect_file = dir(connect_file);
        connect_file_name = { connect_file.name };
        load(connect_file_name{1});

        % concatenate vertically the number connections of all
networks that belong to the subjects of this group
        connections_HS=cat(1,connections_HS,connections);

        %load the clustering values
        gl_eff_file=('gl_efficiency*.mat');
        gl_eff_file = dir(gl_eff_file);
        gl_eff_file_name = { gl_eff_file.name };
        load(gl_eff_file_name{1});

        % concatenate vertically the global efficiency of the
subjects of this group for each sparsity (that's why k/5)
        gl_efficiency_HS=cat(1,gl_efficiency_HS,efficiency);

        % concatenate the degree for all the subjects
        degree_file=('degree*.mat');
        degree_file = dir(degree_file);
        degree_file_name = {degree_file.name };
        load(degree_file_name{1});

        degree_allnodes_HS=cat(2,degree_allnodes_HS,degree);

        degree_allsubj_HS=cat(1,degree_allsubj_HS,mean(degree));

        lp_fold=strcat('/path-to-subj-
dir/',subj_fold,'/conn_matrix_sym');
        cd(lp_fold);
```

```
        %load the lp
        Lp_file=('Lp*.mat');
        Lp_file = dir(Lp_file);
        Lp_file_name = { Lp_file.name };
        load(Lp_file_name{1});

        % concatenate vertically the characteristic path length
of the subjects of this group for each sparsity (that's why k/5)
        lp_HS=cat(1,lp_HS,Lp(k/5));

    end

    % Average the betweenness for each node of all the subject of
this group
    avgBet_allnodes_HS=mean(bet_allnodes_HS,2);

    % Average the clustering for each node of all the subject of
this group
    avgClust_allnodes_HS=mean(clust_allnodes_HS,2);

    % average the degree for each node of all the subjects of
this group
    avgDegree_allnodes_HS=mean(degree_allnodes_HS,2);

    % Calculate the mean of each column and take the transposed
matrix
    bet_allsubj_LS=mean(bet_allnodes_LS,1)';
    bet_allsubj_HS=mean(bet_allnodes_HS,1)';

    clust_allsubj_LS=mean(clust_allnodes_LS,1)';
    clust_allsubj_HS=mean(clust_allnodes_HS,1)';

    save_dir=strcat('/path-where-to-save-
data/BCT_487_',num2str(k));
    cd(save_dir);

    % save all the file with the sparsity level inside of their
names
    save (['avgBet_allnodes' num2str(k) '_LS.mat'],
'avgBet_allnodes_LS');
    save (['avgBet_allnodes' num2str(k) '_HS.mat'],
'avgBet_allnodes_HS');

    save (['bet_allnodes' num2str(k) '_LS.mat'],
'bet_allnodes_LS');
    save (['bet_allnodes' num2str(k) '_HS.mat'],
'bet_allnodes_HS');

    save (['avgClust_allnodes' num2str(k) '_LS.mat'],
'avgClust_allnodes_LS');
    save (['avgClust_allnodes' num2str(k) '_HS.mat'],
'avgClust_allnodes_HS');

    save (['clust_allnodes' num2str(k) '_LS.mat'],
'clust_allnodes_LS');
    save (['clust_allnodes' num2str(k) '_HS.mat'],
'clust_allnodes_HS');
```

```
    save (['connections' num2str(k) '_LS.mat'],
'connections_LS');
    save (['connections' num2str(k) '_HS.mat'],
'connections_HS');


    save (['lp' num2str(k) '_LS.mat'], 'lp_LS');
    save (['lp' num2str(k) '_HS.mat'], 'lp_HS');

    save (['gl_efficiency' num2str(k) '_LS.mat'],
'gl_efficiency_LS');
    save (['gl_efficiency' num2str(k) '_HS.mat'],
'gl_efficiency_HS');

    save (['degree_allnodes' num2str(k) '_LS.mat'],
'degree_allnodes_LS');
    save (['degree_allnodes' num2str(k) '_HS.mat'],
'degree_allnodes_HS');

    save (['degree_allsubj' num2str(k) '_LS.mat'],
'degree_allsubj_LS');
    save (['degree_allsubj' num2str(k) '_HS.mat'],
'degree_allsubj_HS');

    save (['avgDegree_allnodes' num2str(k) '_LS.mat'],
'avgDegree_allnodes_LS');
    save (['avgDegree_allnodes' num2str(k) '_HS.mat'],
'avgDegree_allnodes_HS');

    % save the metrics averaged for each subject
    save (['bet_allsubj' num2str(k) '_LS.mat'],
'bet_allsubj_LS');
    save (['bet_allsubj' num2str(k) '_HS.mat'],
'bet_allsubj_HS');

    save (['clust_allsubj' num2str(k) '_LS.mat'],
'clust_allsubj_LS');
    save (['clust_allsubj' num2str(k) '_HS.mat'],
'clust_allsubj_HS');

toc

end

betw_allspars_wholeGroup =
betw_allspars_wholeGroup/(length(LowStress_subgroup)+length(HighS
tress_subgroup));

cd('/path-where-to-save-data');
save betw_allspars_wholeGroup.mat betw_allspars_wholeGroup

end
```

```
% This script calculates all the measures from the correlation
matrix with Fisher transformed matrices
%
% INPUTS:
%   - The z-transformed correlation matrix according to the
schaefer template
%   - The excel file that contain all the name of the ROIs
%
% % % NEED TO CHANGE:
% % % Line 49: The path to the excel file (ROI names)
% % % Line 50: The name of the excel file
% % % Line 61: The path to run the functions
% % % Line 65: Define the number of the subjects in the study
% % % Line 66: Define the number of nodes of the atlas chosen
% % % Line 68: The path where the list of IDs for both groups is
saved
% % % Line 73&74: path where the correlation matrices are stored
% % % Line 82&83: path where to save graph theory calculated
% % % Line 81: The path to go inside the subject folder and to
create the folder that will contain the measures

% OUTPUTS:
%      For each sparcity level:
%       -treshold.mat
%       -connections.mat
%       -tresh_matrix.mat
%       -clust.mat
%       -BET_S.mat
%       -betw_S.mat
%       -M_S.mat
%       -Q_S.mat
%       -LV_S.mat
%       -ord_S.mat
%       -number.mat
%       -plot.fig

%      For each subject
%       -cp_allspars.mat
%       -Lp_allspars.mat
%       -LV_allspars.mat
%       -ord_allspars.mat
%       -bet_allspars.mat
%       -M_allspars.mat
%       -gamma_allspars.mat
%       -lambda_allspars.mat
%       -lp_rand_allspars.mat'
%       -cp_rand_allspars.mat
%-----------------------------------------------------------------
--------

random=1000;    %number of random permutation for lambda and
gamma parameter

%Read the excel file to get the name of all the ROI
cd('/path-to-the-rois-list-directory'); %go to where the file
with the roi list is stored
[A1,txt]=xlsread('Schaefer_rois.xlsx',1);
```

```
%Initialize the values for the sparcity level
x=400;
y=400;
sparcity=(0.05:0.05:0.35); %values of sparcity that you want to
test
max=y*y;  %values of maximum values possible in the matrix
k=max.*sparcity;

% Initialize the path to run the functions needed to compute
graph theory measures (here the folder name is essential_folder)
function_dir='/path-to-the-BCT-functions-
directory/essential_functions';

num_sub=487;   % number of participants
nb_nodes = 400; % nr of nodes/Schafer_400

txtFileFolder = '/path-where-the-text-files-of-the-two-groups-
are-stored'; %indicate directory where the text files for both
groups are stored
txt_file_HS= 'HighStress_IDs.txt'; %load the txt files
txt_file_LS= 'LowStress_IDs.txt';

%load the folders containing z-transformed matrices for both
groups
matrix_fold_HS= '/path/Ztransf_mat_HS';
matrix_fold_LS= '/path/Ztransf_mat_LS';

% load the txt files for both groups
cd(txtFileFolder);
load(txt_file_HS);
load(txt_file_LS);


mkdir('/path-where-store-the-measures-
folder/graphTheoryFolder_name'); %create new folder to store
graph theory measures will be computed -indicate path and name of
the folder
subj_dir=('/path-where-store-the-measures-
folder/graphTheoryFolder_name'); %define the new folder as
'subj_dir'
cd(subj_dir); %go to that directory


for t = 1:length(HighStress_IDs)  %for loop for the HS

    ID_High = HighStress_IDs(t);
    matrix_filename = ['ber_zTransf_',num2str(ID_High),'.mat'];

    cd(matrix_fold_HS); % go tp the matrix folder
    load(matrix_filename);   % load the matrix

    mkdir( subj_dir, 'graph_theory_z_HS');  % Create the
directory that will contains the folder of each subject of HS
    connectivity_dir =
strcat(subj_dir,'/graph_theory_z_HS/GT_',num2str(ID_High));%
Initialize the path to this new folder and create folder for each
subject
```

```
    %initialization of the different parameters
    cp=zeros(size(k));
    Lp=zeros(size(k));
    Lambda=zeros(size(k));
    Gamma=zeros(size(k));
    lp_rand=zeros(size(k));
    cp_rand=zeros(size(k));
    M_allspars = [];
    bet_allspars = [];
    LV_allspars = [];
    ord_allspars = [];

    for n = 1:length(k)

        % Go to the directory to run the functions
        cd(function_dir');

        % Calculate all the different threshold and binary
connection matrix
        % compared to the different values of the sparcity
        [ bin_matrix,err,treshold,connections] =
binary_bis(ber_zTransf_HS,k(n));

        %apply the threshold to the correlation matrix
        tresh_matrix = zeros(x,y);

        for i=1:x
           for j=1:y
               if abs(ber_zTransf_HS(i,j) ) >= abs(treshold) % to
calculate the thresholded matrix, the absolute values are
considered, which removes any issue regarding the negative
correlations!
                   tresh_matrix(i,j) = ber_zTransf_HS(i,j);
               end
           end
        end


        % Calculate the clustering coefficient of each node and
mean cp
        clustS = clustering_coef_bu(bin_matrix);
        cp(n) = mean(clustS);

        % Calculate the length path
        Lp(n) = lp_prog( bin_matrix );

        % Calculate the lambda and gamma parameter with 1000
random permutation

[Lambda(n),Gamma(n),lp_rand(n),cp_rand(n)]=Copy_of_lambda(
Lp(n),cp(n),bin_matrix,random,connections);

        % Calculate the betweenness of each node
        BET_S=betweenness_bin(bin_matrix);

        BET_S=BET_S';  %transposed matrix is used just for the
visibility of the matrix
```

```
        % Normalize the betweenness
        b=BET_S;
        BET_S(BET_S==0)=[];
        betw_S=b/mean(BET_S);

        %store in a matrix the normalized betweenness for all the
sparcity
        bet_allspars=cat(2,bet_allspars,betw_S);

        % louvain parameter
        [M_S, Q_S] = community_louvain(bin_matrix,0);

        %store in a matrix the M_S for all the sparcity
        M_allspars = cat ( 2, M_allspars, M_S);

        % Put all the area that have the same louvain parameter
values in the same lines
        [LV_S,ord_S,number]=Copy_of_order(M_S,txt);

        LV_allspars = cat( 1, LV_allspars, LV_S);
        ord_allspars = cat( 1, ord_allspars , ord_S);

        % Plot matrix
        plot=figure(n);
        set(gcf,'Visible', 'off');
            plot_order( number,tresh_matrix );
            title(strcat('spar=',num2str(sparcity(n)*100)));
            colorbar;

        % Create a folder for each sparcity level and go into it
        spar_dir_name=strcat('spar',int2str(n*5));
        mkdir(connectivity_dir,spar_dir_name);
        cd(strcat(connectivity_dir,'/',spar_dir_name));

        %saving all the measures calculate for each sparcity
        save(['bin_matrix' num2str(n*5) '.mat'],'bin_matrix');
        save(['treshold' num2str(n*5) '.mat'],'treshold');
        save(['connections' num2str(n*5) '.mat'],'connections');
        save(['tresh_matrix' num2str(n*5) '.mat'],
'tresh_matrix');
        save(['clust' num2str(n*5) '.mat'], 'clustS') ;
        save(['BET_S' num2str(n*5) '.mat'], 'BET_S');
        save(['betw_S' num2str(n*5) '.mat'], 'betw_S');
        save(['M_S' num2str(n*5) '.mat'], 'M_S');
        save(['Q_S' num2str(n*5) '.mat'], 'Q_S');
        save(['LV_S' num2str(n*5) '.mat'], 'LV_S');
        save(['ord_S' num2str(n*5) '.mat'], 'ord_S');
        save(['number' num2str(n*5) '.mat'], 'number');
        savefig( plot, [ 'plot_spar' num2str(n*5) ] );

        Sparcity_level_done=num2str(n*5) %to know where the
scripts is
    end

    %saving all the averaged measures calculate for each subject
    cd(connectivity_dir);
    save('cp_allspars.mat', 'cp');
    save('Lp_allspars.mat', 'Lp');
```

```
    save('LV_allspars.mat', 'LV_allspars');
    save('ord_allspars.mat', 'ord_allspars');
    save('bet_allspars.mat', 'bet_allspars');
    save('M_allspars.mat', 'M_allspars');
    save('gamma_allspars.mat','Gamma' );
    save('lambda_allspars.mat','Lambda' );
    save('lp_rand_allspars.mat','lp_rand' );
    save('cp_rand_allspars.mat','cp_rand' );

    Subject_done=num2str(t) %to know where the scripts is

end

%do it for Low stress

for t = 1:length(LowStress_IDs)  %for loop for the LS

    ID_Low = LowStress_IDs(t);
    matrix_filename = ['ber_zTransf_',num2str(ID_Low),'.mat'];

    cd(matrix_fold_LS);          % go to the matrix folder
    load(matrix_filename);   % load the matrix

    mkdir( subj_dir, 'graph_theory_z_LS');  % Create the
directory that will contains the folder of each subject of LS
    connectivity_dir =
strcat(subj_dir,'/graph_theory_z_LS/GT_',num2str(ID_Low)); %
Initialize the path to this new folder and create folder for each
subject


    %initialization of the different parameters
    cp=zeros(size(k));
    Lp=zeros(size(k));
    Lambda=zeros(size(k));
    Gamma=zeros(size(k));
    lp_rand=zeros(size(k));
    cp_rand=zeros(size(k));
    M_allspars = [];
    bet_allspars = [];
    LV_allspars = [];
    ord_allspars = [];

    for n = 1:length(k)

        % Go to the directory to run the functions
        cd(function_dir');

        % Calculate all the different thresholds and binary
connection matrix at different sparsity levels
        [ bin_matrix,err,treshold,connections] =
binary_bis(ber_zTransf_LS,k(n));

        %define the thresholded correlation matrix
        tresh_matrix = zeros(x,y);

        for i=1:x                   %apply the threshold to the
correlation matrix
```

```
            for j=1:y
                if abs(ber_zTransf_LS(i,j) ) >= abs(treshold)
                    tresh_matrix(i,j) = ber_zTransf_LS(i,j);
                end
            end
        end


        % Calculate the clustering coefficient
        clustS = clustering_coef_bu(bin_matrix);
        cp(n) = mean(clustS);

        % Calculate the length path
        Lp(n) = lp_prog( bin_matrix );

        % Calculate the lambda and gamma parameter with 1000
random permutation

[Lambda(n),Gamma(n),lp_rand(n),cp_rand(n)]=Copy_of_lambda(
Lp(n),cp(n),bin_matrix,random,connections);

        % Calculate the betweenness of each node
        BET_S=betweenness_bin(bin_matrix);

        BET_S=BET_S';  %transposed matrix is used just for the
visibility of the matrix

        % Normalize the betweenness
        b=BET_S;
        BET_S(BET_S==0)=[];
        betw_S=b/mean(BET_S);

        %store in a matrix the normalized betweenness for all the
sparcity
        bet_allspars=cat(2,bet_allspars,betw_S);

        % louvain parameter
        [M_S, Q_S] = community_louvain(bin_matrix,0);

        %store in a matrix the M_S for all the sparcity
        M_allspars = cat ( 2, M_allspars, M_S);

        % Put all the area that have the same louvain parameter
values in the same lines
        [LV_S,ord_S,number]=Copy_of_order(M_S,txt);

        LV_allspars = cat( 1, LV_allspars, LV_S);
        ord_allspars = cat( 1, ord_allspars , ord_S);

        % Plot all matrices
        plot=figure(n);
        set(gcf,'Visible', 'off');
            plot_order( number,tresh_matrix );
            title(strcat('spar=',num2str(sparcity(n)*100)));
            colorbar;

        % Create a folder for each sparcity level and go into it
        spar_dir_name=strcat('spar',int2str(n*5));
```

```
        mkdir(connectivity_dir,spar_dir_name);
        cd(strcat(connectivity_dir,'/',spar_dir_name));

        %saving all the measures calculate for each sparcity
        save(['bin_matrix' num2str(n*5) '.mat'],'bin_matrix');
        save(['treshold' num2str(n*5) '.mat'],'treshold');
        save(['connections' num2str(n*5) '.mat'],'connections');
        save(['tresh_matrix' num2str(n*5) '.mat'],
'tresh_matrix');
        save(['clust' num2str(n*5) '.mat'], 'clustS') ;
        save(['BET_S' num2str(n*5) '.mat'], 'BET_S');
        save(['betw_S' num2str(n*5) '.mat'], 'betw_S');
        save(['M_S' num2str(n*5) '.mat'], 'M_S');
        save(['Q_S' num2str(n*5) '.mat'], 'Q_S');
        save(['LV_S' num2str(n*5) '.mat'], 'LV_S');
        save(['ord_S' num2str(n*5) '.mat'], 'ord_S');
        save(['number' num2str(n*5) '.mat'], 'number');
        savefig( plot, [ 'plot_spar' num2str(n*5) ] );

        Sparcity_level_done=num2str(n*5)  %to know where the
scripts is
    end

    %saving all the averaged measures calculated for each subject
    cd(connectivity_dir);
    save('cp_allspars.mat', 'cp');
    save('Lp_allspars.mat', 'Lp');
    save('LV_allspars.mat', 'LV_allspars');
    save('ord_allspars.mat', 'ord_allspars');
    save('bet_allspars.mat', 'bet_allspars');
    save('M_allspars.mat', 'M_allspars');
    save('gamma_allspars.mat','Gamma' );
    save('lambda_allspars.mat','Lambda' );
    save('lp_rand_allspars.mat','lp_rand' );
    save('cp_rand_allspars.mat','cp_rand' );

    Subject_done=num2str(t) %to know where the scripts is

end
```

```
function ber_reshape
%This function creates the reshaped matrix from betty scripts to
400*400 matrices (schaefer)

% Determine the number of subjects to analyse
files = dir('/subj-dir');
directory_subject_names = {files([files.isdir]).name};
directory_subject_names =
directory_subject_names(~ismember(directory_subject_names,{'.','.
.'}));
num_sub = length( directory_subject_names);

% go through all the subjects
for i = 1 : num_sub
 tic
    sub_fold=strjoin(directory_subject_names(i));

    % load the correlation matrix in the 'data' directory
    rotcorr_dir= strcat('/path-to-subj-
dir/',sub_fold,'/data/rotation');
    cd(rotcorr_dir);
    load('rotcorr.mat');

    %load the sheafer template
    schaefer_dir = strcat('/path-to-subj-
dir/',sub_fold,'/reshape');
    cd(schaefer_dir);
    load('schaefer_template.mat');

    % initialize the reshaped matrix
    reshape_ber=zeros(400,400,'double');

    % go through all the columns of the schaefer template (--> to
all the ROIs) to know wich cube belong to the xth ROI
    for x=1:400

        ind_voxels_x=schaefer_template(:,x); % read the xth
column to get all the indices of the cubes that belong to th xth
ROI

        ind_voxels_x(~any(ind_voxels_x,2), :) = []; % suppress
zeros at the end of the columns if any

        for y=x+1:400 %go through all the upper triangle of the
matrices (without taking into account the diagonal because y
represent the column and always begin at x+1)

            sum_values=[]; % reinitialize the vector that sums up
all the correlation coefficients, representing the new
correlation coefficient

            % read the yth columns to get all the indices of the
cubes that belong to the yth ROI and supress the zeros at the end
of the columns if there are
            ind_voxels_y=schaefer_template(:,y);
            ind_voxels_y(~any(ind_voxels_y,2), :) = [];
```

```
            for i=1:length(ind_voxels_x) % go through all the
cubes indices of the xth ROI
                for j=1:length(ind_voxels_y)% go through all the
cubes indices of the yth ROI
                    % put all the correlation coefficient that
belong to the two ROIs (when the cube indices of the xth ROI
cross the cube indices of the yth ROI in rotcorr)
                    sum_values = cat(1,sum_values ,
rotcorr(ind_voxels_x(i),ind_voxels_y(j))); % all the values are
concatenated in an horizontal vector
                end
            end
            % Do the mean of the vector that contains all the
correlation coefficients and store it in position xth-yth (ROI)
in the reshaped matrix
            reshape_ber(x,y)=mean(sum_values);
            reshape_ber(isnan(reshape_ber))=0;
        end
    end

    % take the transposed matrix (lower triangle) and add it to
the upper to create symmetric matrix
    reshape_ber = reshape_ber + reshape_ber';

    % save the new correlation matrix
    save_dir=strcat('/path-to-subj-dir/',sub_fold,'/reshape');
    cd(save_dir);
    save reshape_ber.mat reshape_ber
 toc
end
end
```

```
function [] = Create_ConnectityMatrix_NBS_ber()
% This function gathers in one 3d matrices all the connectivity
matrices in the right order according to
% the order of the stress level (low first and then high level)

%%%%%%%%%%%%%%%%%%%%%%%%%%%%%%%%%%%%%%%%%%%%%%%%%%%%%%%%%%%%%%%%%%%%%%%%
%%%%%%%%%%
%%%% Change those values to get the design matrix that you want
%%%%
%%%%%%%%%%%%%%%%%%%%%%%%%%%%%%%%%%%%%%%%%%%%%%%%%%%%%%%%%%%%%%%%%%%%%%%%
%%%%%%%%%%

 %number of subjects
nb_sub=487;
nb_nodes = 400; % number of nodes in a matrix (here 400 x 400)
%%%%%%%%%%%%%%%%%%%%%%%%%%%%%%%%%%%%%%%%%%%%%%%%%%%%%%%%%%%%%%%%%%%%%%%%
%%%%%%%%%%


% Create the 3d matrix that will contain all the matrix
all_corr_z=zeros(nb_nodes,nb_nodes,nb_sub);

% Load the file that contains the subject's index of each stress
group
cd('/path-where-txtfiles-are-stored');
load('LowStress_ID.txt');
load('HighStress_ID.txt');

% Initialize the index that count the slice of the 3d matrix
l=1;

% Add to the 3d matrix all the low stress matrices in first
for i=1:length(LowStress_IDs)

    ID_low=LowStress_IDs(i);

    cd('/path-to-correl-matrices');
    corr_z_file=['correl_coeff_LS',num2str(ID_low),'.mat'];
    file = dir(corr_z_file);
    file_name = { file.name };
    load(file_name{1});

    all_corr_z(:,:,l)= corr_coeff;
    l=l+1;
end

% Add to the 3d matrix all the high stress matrices in second
for i=1:length(HighStress_IDs)

    ID_high=HighStress_IDs(i);

    cd('/path-to-correl-matrices');
    corr_z_file=['corr_coeff_HS_',num2str(ID_high),'.mat'];
    file = dir(corr_z_file);
    file_name = { file.name };
```

```
    load(file_name{1});

    all_corr_z(:,:,l)=correl_coeff;
    l=l+1;

end

cd('/path-where-to-save-matrix');
all_corr_z =real(all_corr_z);
save all_corr_z.mat all_corr_z;

end
```

```
function [] = Create_design_matrix
% CREATE_DESIGN_MATRIX This function creates the design matrix to
analyse the connectivity matrices with NBS.
% BE CAREFUL!!!!: this design matrix needs to be used with the
connectivity matrices organized in a special order --> the
connectivity matrices of all the subjects of one sparcity level
first, then all the connectivity matrices of all the subjects of
another sparcity level (the sparcity level should be organized in
the numerical order)
% MOREOVER!!!! the connectivity matrices have to be organized
with the low level stress before the high level stress if the
stress level is take into account

%%%%%%%%%%%%%%%%%%%%%%%%%%%%%%%%%%%%%%%%%%%%%%%%%%%%%%%%%%%%%%%%
%%%%%% Change those values to get the design matrix that you want
%%%%%%%%%%%%%%%%%%%%%%%%%%%%%%%%%%%%%%%%%%%%%%%%%%%%%%%%%%%%%%%%
%%%%%%%%%
nb_sub=487;    %number of subjects
nb_spar=1;      %number of sparsity level
stress_division=1; % if =1 the group will be divided in 2
according to the stress level, if =0, don't take into account the
stress level for the analyse
%%%%%%%%%%%%%%%%%%%%%%%%%%%%%%%%%%%%%%%%%%%%%%%%%%%%%%%%%%%%%%%%
%%%%%%%%%%

l=1;%%% used if the sparsity level if above 1 (see script from
line 37)

% if you want to have the influence of the stress of not
if stress_division==1

    % Go to the directory where the file with the ID of subject
for each stress level is
    cd('/path-to-subj-dir');
    load('LowStr_IDs.txt'); %%% comment this out if you don't
want to divide to create 2 group according to the stress level
and change the 'for loop' and the 'if' conditions

    % Create the design matrix according to the parameters
    design_matrix=zeros(nb_sub*nb_spar,2);

    if nb_spar==1
        for i=1:size(design_matrix,1) %this goes from the first
to the last row
            if i<=length(LowStr_IDs)
                design_matrix(i,1)=1;  % put a 1 in the 1st
column if in the low stress group
            else
                design_matrix(i,2)=1;  % put a 1 in the 2nd
column if in the high stress group
            end
        end

        save designMatrix_stress.mat design_matrix
    else
        % Do the same thing as above but repeated for each
sparsity level
```

```
        for k=1:nb_spar
            j=1;
            for i=l:l+nb_sub-1 %this goes from the first to the
last row
                if j<=length(LowStr_IDs)
                    design_matrix(i,1)=1;
                    j=j+1;
                else
                    design_matrix(i,2)=1;
                    j=j+1;
                end
            end
            l=l+nb_sub;
        end
        save (['designMatrix_stress_' num2str(nb_spar) '.mat'],
'design_matrix')
    end

% If the stress level is not taken into account
elseif stress_division==0

    cd('/path-to-subj-dir');

    design_matrix=zeros(nb_sub*nb_spar,nb_spar);

    % with 1 sparsity level, put ones everywhere
    if nb_spar==1
        for i=1:size(design_matrix,1)
            design_matrix(i,1)=1;
        end

    % if several sparcity level, put 'nb_sub'ones in each column
after each other
    else
        for k=1:nb_spar
            for i=l:l+nb_sub-1
                design_matrix(i,k)=1;
            end
            l=l+nb_sub;
        end
    end

    save (['designMatrix_average' num2str(nb_spar) '.mat'],
'design_matrix')
end

end
```

```
function [schaefer_template] =
Create_Schaefer_template(schaefer_image ,new_bind, nb_par, dimx,
dimy ,dimz)
%CREATE_SCHEAFER_TEMPLATE is a function that creates a matrix
containingin each column (that represents each ROI) the index of
the cubes thatbelong to this ROI

% Create the matrix that will contains the cube value for each
ROI
schaefer_template = zeros(1000,nb_par);

% Initialize the voxel counter
vox_count = 1;

% Initialize the cube counter
cube_count = 1;

% Initialize the counting that allows us to know how many values
are store at each moment in a column
ROI_count = ones(1,nb_par);

% For each voxel, look up if the index of the cube is in the bind
and store
% the index of the cube (that correspond to the index in the
% correlation matrix)  in the schaefer_template in the ROI
column) corresponding
for z = 1 : dimz
    for y = 1 : dimy
        for x = 1 : dimx
            roi_ind = schaefer_image(x,y,z);
             if roi_ind == 0
                 vox_count = vox_count +1;
             else
                if (find( new_bind == vox_count)) ~= 0
                    schaefer_template( ROI_count(roi_ind) ,
roi_ind)= cube_count;
                    cube_count = cube_count + 1;
                    ROI_count( roi_ind ) = ROI_count( roi_ind )
+1;
                end
                vox_count = vox_count +1;
             end
        end
    end
end

% Delete all the rows full of zeros at the bottom
schaefer_template( ~any( schaefer_template , 2 ), : ) = [];

end
```

```
function [] = Fisher_r2z()
% This function transforms each connectivity matrix with Fishers
% transformation. I have two groups (LowStress & HighStress), and
in the
% two txt files at the beginning, I "select" the connectivity
matrices that
% I want to use in this analysis. In the text files there are IDs
of
% participants whose I want to use the conn matrix.

 ber_zTransf_LS=zeros(400,400); %Initiate the output matrices for
each groups
 ber_zTransf_HS=zeros(400,400);


% Load the file that contains the subject IDs of each stress
group
cd('/path-to-two-groups-txtfiles');
load('HighStress_IDs.txt'); %here there are 417 IDs, which
correspond to the matrices it's going to consider
load('LowStress_IDs.txt');
%here there are 559

save_dir=
mkdir('/media/SeagateBU/FRAN/ConnectivityAnalysis/BCT_976/Ben_scr
ipt_try/Ztransf_mat_LS');

for i=1:length(LowStress_IDs)
    tic
     ID_low=LowStress_IDs(i);

    % Get the name of the folder according to the IDs
     cd('/subj-dir'); %in this directory I have a list of tot
subjects and each subject folder has 4 subfolders; in one of this
subfolder there is the connectivity matrix
     fold_name =strcat ('*', num2str(ID_low));
     all_sub_fold = dir(fold_name);
     name_sub_fold = {all_sub_fold.name};
     subj_fold = strjoin(name_sub_fold);

    %go to reshape_ber (that's the name of the connectivity
matrix) directory
    reshape_ber_dir= strcat('/subj-dir/',subj_fold,'/reshape');
%reshape is the directory name where the reshape_ber connect
matrix is saved
    cd(reshape_ber_dir);
    load('reshape_ber.mat');


    ber_fTransf_LS=atanh(reshape_ber);
    ber_zTransf_LS= real(ber_fTransf_LS);

    cd('/path/Ztransf_mat_LS');
    save (['ber_zTransf_',num2str(ID_low),'.mat'],
'ber_zTransf_LS');
    toc
end
```

```
%do the same for the HighStress group (here I didn't comment
because I want to do exactly the same thing as above)

save_dir= mkdir('/path/Ztransf_mat_HS');

for i=1:length(HighStress_IDs)

     ID_high=HighStress_IDs(i);

    % Get the name of the folder according to the IDs
     cd('/subj-dir');
     fold_name =strcat ('*', num2str(ID_high));
     all_sub_fold = dir(fold_name);
     name_sub_fold = {all_sub_fold.name};
     subj_fold = strjoin(name_sub_fold);

    reshape_ber_dir= strcat('/subj-dir/',subj_fold,'/reshape');
    cd(reshape_ber_dir);
    load('reshape_ber.mat');


     ber_fTransf_HS=atanh(reshape_ber);
     ber_zTransf_HS= real(ber_fTransf_HS);

    cd('/path/Ztransf_mat_HS');
    save (['ber_zTransf_',num2str(ID_high),'.mat'],
'ber_zTransf_HS');
end

end
```

```
function [ new_bind ] = simplify_bind ( bind )
%SIMPLIFY_BIND is a function that create the new_bind vector that
just contains the index of the 14th voxels of each cube (i.e. the
center of the cube)

% Create the vector new_bind that will store the voxels index
new_bind = [];

% Store values of all the 14th voxels of each cube in new_bind
i = 14 : 27 : (length(bind)-13);
new_bind = bind(i);

% Save the new_bind into the right directory
save new_bind.mat new_bind;

end
```

List of scripts needed to run ‘BCT_calculation_Fisher.m’, found in the ‘essential_scripts’ folder:

- betweenness_bin.m
- binary_bis.m
- charpath.m
- clustering_coef_bu.m
- community_louvain.m
- Copy_of_lambda.m
- Copy_of_lp_prog.m
- Copy_of_order.m
- degrees_und.m
- distance_bin.m
- modularity_und.m
- nbrone.m
- plot_order.m

```
function BC=betweenness_bin(G)
%BETWEENNESS_BIN    Node betweenness centrality

%   BC = betweenness_bin(A);

%   Node betweenness centrality is the fraction of all shortest
paths in the network that contain a given node. Nodes with high
values of betweenness centrality participate in a large number of
shortest paths.

%   Input:  A,binary (directed/undirected) connection matrix.
%   Output: BC, node betweenness centrality vector.
%
%   Note: Betweenness centrality may be normalised to the range
[0,1] as  BC/[(N-1)(N-2)], where N is the number of nodes in the
network.
%
%Reference: Kintali (2008) arXiv:0809.1906v2 [cs.DS]
(generalization to directed and disconnected graphs)

%   Mika Rubinov, UNSW/U Cambridge, 2007-2012


n=length(G);                %number of nodes
I=eye(n)~=0;                %logical identity matrix
d=1;                        %path length
NPd=G;                      %number of paths of length |d|
NSPd=NPd;                 %number of shortest paths of length |d|
NSP=NSPd; NSP(I)=1;       %number of shortest paths of any length
L=NSPd; L(I)=1;             %length of shortest paths

%calculate NSP and L
while find(NSPd,1)
    d=d+1;
    NPd=NPd*G;
    NSPd=NPd.*(L==0);
    NSP=NSP+NSPd;
    L=L+d.*(NSPd~=0);
end
L(~L)=inf; L(I)=0;          %L for disconnected vertices is inf
NSP(~NSP)=1;                %NSP for disconnected vertices is 1

Gt=G.';
DP=zeros(n);                %vertex on vertex dependency
diam=d-1;                   %graph diameter

%calculate DP
for d=diam:-1:2
    DPd1=(((L==d).*(1+DP)./NSP)*Gt).*((L==(d-1)).*NSP);
    DP=DP + DPd1; %DPd1:dependencies on vertices |d-1| from
source
end

BC=sum(DP,1);               %compute betweenness



function [ Abin,err,tresh,bin ] = binary_bis( Acorr,K)
%UNTITLED5 Summary of this function goes here
```

```
%   Detailed explanation goes here
%     input:  matrix of the networks
%                 stats: threshold to have an edge compared to
correlation values
%     output: Abin binary connection matrix with K values not
equal to zeros
%     tresh: is the values that it stay K one on the binary
connection matrix Abin

%   this programs convert the correlation matrix to a binary
connection matrix

% THIS IS THE ORIGINAL BINARY_BIS WRITTEN BY COLINE, I HAVEN'T
EDITED

a=1;
corr=2;

[n,m]=size(Acorr);
% stats=mean(mean(Acorr));    % random threshold to begin
stats=0.8;
Abin=zeros(n,m);
error=0;
% resol_stats=0.01;    %resolution to calculate threshold
 resol_stats=0.1;
% max_corr=max(max(Acorr));
% min_corr=min(min(Acorr));
% max_error1=max(1/resol_stats,floor(abs((max_corr-
1)/resol_stats)));
% max_error=max(max_error1,floor(abs((min_corr-1)/resol_stats)));
%max range for find threshold
max_error1=11;
err=0;
b=0;
range=1;

while a==1
    error=error+1;

    for i=1:n
        for j=1:m
             if abs(Acorr(i,j))>= stats   %convert all lower than
stats in zero( no connectivity) and upper in 1 (connect)
            Abin(i,j)=1;
            else
            Abin(i,j)=0;

            end
        end
    Abin(i,i)=0;
    end
    bin=nbrone(Abin,corr);    %calculate the number of connection

    if bin>=(K-range)  %if they keep 70% to 80% of maximum
connection is good
        if bin<=(K+range)
            a=0;
        end
    end
```

```
    if bin<(K-range)
        stats=stats-resol_stats;        %if threshold is to high,
decrease of threshold
    end

    if bin>(K+range)
        stats=stats+resol_stats;        %if threshold is to low,
increase of threshold
    end

    if error>=max_error1                % case of to high
resolution for threshold
        b=b+1;
        if b<4
        resol_stats=resol_stats/10;
%         max_error1=max(1/resol_stats,abs((max_corr-
1)/resol_stats));
%         max_error=max(max_error1,abs((min_corr-
1)/resol_stats));
        error=0;
        else
            range=20;
            error=0;
        end

        if b==3
           range=2;
        end

        if b==7
           a=0;
           err=1;
           disp('problem of threshold, perhaps correlation number
are too close, change perhaps resolution stats');
        end
    end
    if b==4 && error==1
        resol_stats=resol_stats/10;
    end
end

 tresh=stats;

end
```

```
function  [lambda,efficiency,ecc,radius,diameter] =
charpath(D,diagonal_dist,infinite_dist)
%CHARPATH       Characteristic path length, global efficiency and
related statistics
%
%   lambda = charpath(D);
%   lambda = charpath(D);
%   [lambda,efficiency] = charpath(D);
%   [lambda,efficiency,ecc,radius,diameter] =
charpath(D,diagonal_dist,infinite_dist);
%
%   The network characteristic path length is the average
shortest path length between all pairs of nodes in the network.
The global efficiency is the average inverse shortest path length
in the network. The nodal eccentricity is the maximal path length
between a node and any other node in the network. The radius is
the minimal eccentricity, and the diameter is the maximal
eccentricity.
%
%   Input: D,  distance matrix
%          diagonal_dist   optional argument
                           include distances on the main diagonal
%                          (default: diagonal_dist=0)
%          infinite_dist   optional argument
                           include infinite distances in
calculation
%                           (default: infinite_dist=1)
%
%   Outputs: lambda, network characteristic path length
%            efficiency, network global efficiency
%            ecc, nodal eccentricity
%            radius, network radius
%            diameter, network diameter
%
%   Notes:  The input distance matrix may be obtained with any of
the distance functions, e.g. distance_bin, distance_wei.
%       Characteristic path length is defined here as the mean
shortest  path length between all pairs of nodes, for consistency
with common usage. Note that characteristic path length is also
defined as the median of the mean shortest path length from each
node to all other nodes.
%       Infinitely long paths (i.e. paths between disconnected
nodes) are included in computations by default. This behavior may
be modified with via the infinite_dist argument.
%
%
%   Olaf Sporns, Indiana University, 2002/2007/2008
%   Mika Rubinov, U Cambridge, 2010/2015

%   Modification history
%   2002: original (OS)
%   2010: incorporation of global efficiency (MR)
%   2015: exclusion of diagonal weights by default (MR)
%   2016: inclusion of infinite distances by default (MR)

n = size(D,1);
if any(any(isnan(D)))
    error('The distance matrix must not contain NaN values');
end
if ~exist('diagonal_dist','var') || ~diagonal_dist ||
isempty(diagonal_dist)
```

```
    D(1:n+1:end) = NaN;            % set diagonal distance to NaN
end
if  exist('infinite_dist','var') && ~infinite_dist
    D(isinf(D))  = NaN;            % ignore infinite path lengths
end

Dv = D(~isnan(D));                 % get non-NaN indices of D

% Mean of entries of D(G)
lambda     = mean(Dv);

% Efficiency: mean of inverse entries of D(G)
efficiency = mean(1./Dv);

% Eccentricity for each vertex
ecc        = nanmax(D,[],2);

% Radius of graph
radius     = min(ecc);

% Diameter of graph
diameter   = max(ecc);
```

```
function C=clustering_coef_bu(G)
%CLUSTERING_COEF_BU     Clustering coefficient
%
%   C = clustering_coef_bu(A);
%
%   The clustering coefficient is the fraction of triangles
around a node(equiv. the fraction of node's neighbours that are
neighbours of each other).
%
%   Input:      A,      binary undirected connection matrix
%
%   Output:     C,      clustering coefficient vector
%
%   Reference: Watts and Strogatz (1998) Nature 393:440-442.
%
%
%   Mika Rubinov, UNSW, 2007-2010

n=length(G);
C=zeros(n,1);

for u=1:n
    V=find(G(u,:));
    k=length(V);
    if k>=2                 %degree must be at least 2
        S=G(V,V);
        C(u)=sum(S(:))/(k^2-k);
    end
end
```

```
function [M,Q]=community_louvain(W,gamma,M0,B)
%COMMUNITY_LOUVAIN     Optimal community structure
%
%   M     = community_louvain(W);
%   [M,Q] = community_louvain(W,gamma);
%   [M,Q] = community_louvain(W,gamma,M0);
%   [M,Q] = community_louvain(W,gamma,M0,'potts');
%   [M,Q] = community_louvain(W,gamma,M0,'negative_asym');
%   [M,Q] = community_louvain(W,[],[],B);
%
%   The optimal community structure is a subdivision of the network
into nonoverlapping groups of nodes which maximizes the number of
within-group edges, and minimizes the number of between-group
edges. This function is a fast and accurate multi-iterative
generalization of the Louvain community detection algorithm. This
function subsumes and improves upon, modularity_louvain_und.m,
modularity_finetune_und.m,              modularity_louvain_dir.m,
modularity_finetune_dir.m,   modularity_louvain_und_sign.m,   and
additionally allows to optimize other objective functions (includes
built-in Potts-model Hamiltonian, allows for custom objective-
function matrices).
%
%    Inputs:   W, directed/undirected weighted/binary connection
matrix with positive and possibly negative weights.
%       gamma,  resolution parameter (optional)
%               gamma>1,        detects smaller modules
%               0<=gamma<1,     detects larger modules
%               gamma=1,        classic modularity (default)
%       M0,     initial community affiliation vector (optional)
%       B,  objective-function  type  or  custom  objective  matrix
(optional)
%           'modularity',       modularity (default)
%           'potts', Potts-model Hamiltonian (for binary networks)
%         'negative_sym', symmetric treatment of negative weights
%          'negative_asym',asymmetric treatment of negative weights
%           B,   custom objective-function matrix
%
%         Note: see Rubinov and Sporns (2011) for a discussion of
%          symmetric vs. asymmetric treatment of negative weights.
%
%   Outputs:
%       M,  community affiliation vector
%       Q,  optimized community-structure statistic (modularity by
default)
%
%   Example:
%       % Iterative community finetuning.
%       % W is the input connection matrix.
%       n  = size(W,1);             % number of nodes
%      M  = 1:n;                  % initial community affiliations
%       Q0 = -1; Q1 = 0;            % initialize modularity values
%       while Q1-Q0>1e-5;           % while modularity increases
%           Q0 = Q1;                % perform community detection
%           [M, Q1] = community_louvain(W, [], M);
%       end
%
%   References:
%       Blondel et al. (2008)  J. Stat. Mech. P10008.
%       Reichardt and Bornholdt (2006) Phys. Rev. E 74, 016110.
%       Ronhovde and Nussinov (2008) Phys. Rev. E 80, 016109
%       Sun et al. (2008) Europhysics Lett 86, 28004.
```

```
%       Rubinov and Sporns (2011) Neuroimage 56:2068-79.
%
%   Mika Rubinov, U Cambridge 2015-2016

%   Modification history
%   2015: Original
%   2016: Included generalization for negative weights.
%        Enforced binary network input for Potts-model Hamiltonian.
%         Streamlined code and expanded documentation.

W=double(W);                                % convert to double format
n=length(W);                                   % get number of nodes
s=sum(sum(W));                                 % get sum of edges

if ~exist('B','var') || isempty(B)
    type_B = 'modularity';
elseif ischar(B)
    type_B = B;
else
    type_B = 0;
    if exist('gamma','var') && ~isempty(gamma)
        warning('Value of gamma is ignored in generalized mode.')
    end
end
if ~exist('gamma','var') || isempty(gamma)
    gamma = 1;
end

if strcmp(type_B,'negative_sym') || strcmp(type_B,'negative_asym')
    W0 = W.*(W>0);                            %positive weights matrix
    s0 = sum(sum(W0));                       %weight of positive links
    B0 = W0-gamma*(sum(W0,2)*sum(W0,1))/s0; %positive modularity

    W1 =-W.*(W<0);                            %negative weights matrix
    s1 = sum(sum(W1));                       %weight of negative links
    if s1                                       %negative modularity
        B1 = W1-gamma*(sum(W1,2)*sum(W1,1))/s1;
    else
        B1 = 0;
    end
elseif min(min(W))<-1e-10
    err_string = [
        'The   input   connection   matrix   contains   negative
weights.\nSpecify ' ...
        '''negative_sym'' or ''negative_asym'' objective-function
types.'];
    error(sprintf(err_string))                  %#ok<SPERR>
end
if strcmp(type_B,'potts') && any(any(W ~= logical(W)))
    error('Potts-model Hamiltonian requires a binary W.')
end

if type_B
    switch type_B
        case    'modularity';                          B    =    (W-
gamma*(sum(W,2)*sum(W,1))/s)/s;
        case 'potts';           B =  W-gamma*(~W);
        case 'negative_sym';    B = B0/(s0+s1) - B1/(s0+s1);
        case 'negative_asym';   B = B0/s0      - B1/(s0+s1);
        otherwise;           error('Unknown objective function.');
```

```
    end
else                    % custom objective function matrix as input
    B = double(B);
    if ~isequal(size(W),size(B))
        error('W and B must have the same size.')
    end
end
if ~exist('M0','var') || isempty(M0)
    M0=1:n;
elseif numel(M0)~=n
    error('M0 must contain n elements.')
end

[~,~,Mb] = unique(M0);
M = Mb;

B = (B+B.')/2;                          % symmetrize modularity matrix
Hnm=zeros(n,n);                             % node-to-module degree
for m=1:max(Mb)                             % loop over modules
    Hnm(:,m)=sum(B(:,Mb==m),2);
end

Q0 = -inf;
Q = sum(B(bsxfun(@eq,M0,M0.')));    % compute modularity
first_iteration = true;
while Q-Q0>1e-10
    flag = true;                % flag for within-hierarchy search
    while flag
        flag = false;
        for u=randperm(n)     % loop over all nodes in random order
            ma = Mb(u);                     % current module of u
            dQ = Hnm(u,:) - Hnm(u,ma) + B(u,u);
            dQ(ma) = 0;          % (line above) algorithm condition

            [max_dQ,mb] = max(dQ);              % maximal increase
in modularity and corresponding module
            if max_dQ>1e-10       % if maximal increase is positive
                flag = true;
                Mb(u) = mb;                 % reassign module

                Hnm(:,mb) = Hnm(:,mb)+B(:,u);       % change node-
to-module strengths
                Hnm(:,ma) = Hnm(:,ma)-B(:,u);
            end
        end
    end
    [~,~,Mb] = unique(Mb);      % new module assignments

    M0 = M;
    if first_iteration
        M=Mb;
        first_iteration=false;
    else
        for u=1:n         % loop through initial module assignments
            M(M0==u)=Mb(u);                 % assign new modules
        end
    end

    n=max(Mb);                              % new number of modules
    B1=zeros(n);                                % new weighted matrix
```

```
    for u=1:n
        for v=u:n
            bm=sum(sum(B(Mb==u,Mb==v))); % pool weights of nodes in
same module
            B1(u,v)=bm;
            B1(v,u)=bm;
        end
    end
    B=B1;

    Mb=1:n;                              % initial module assignments
    Hnm=B;                                  % node-to-module strength

    Q0=Q;
    Q=trace(B);                                % compute modularity
end
```

```
function [ lamb,gamm,lamrand,gamrand ] = Copy_of_lambda(
lp,cp,Abin,krandom,bin )
%UNTITLED Summary of this function goes here
%   Detailed explanation goes here

% [x,y]=size(Abin);

% L=zeros(x*y,1);
%
% for i=1:x*y
%     L(i)=i;
% end

lp_RAND=zeros(krandom,1);
cp_RAND=zeros(krandom,1);

% L1=L;
for m=1:krandom
    Abin_bis=zeros(size(Abin));
    Abin_bis(randperm(numel(Abin_bis), floor(bin))) = 1;
%     L1=L;
%     for i=1:bin
%         len=length(L1);
%         k=randi([1,len]);
%         Abin_bis(L1(k))=1;
%         L1(k)=[];
%     end

    lp_RAND(m)=lp_prog(Abin_bis);
    cp_RAND(m)=mean(clustering_coef_bu(Abin_bis));
end

lamrand=mean(lp_RAND);
gamrand=mean(cp_RAND);
lamb=lp/lamrand;
gamm=cp/gamrand;

end
```

```
function [ Lp , efficiency] = Copy_of_lp_prog( A )
%UNTITLED3 Summary of this function goes here
%   Detailed explanation goes here

% input:  A :binarry connection matrix
% output: Lp= charactheristic path length of the matrix A

D=distance_bin(A);       % D is the distance matrix

%%remove all the infynite values
Lia = ismember(D,Inf);
[x,y]=size(D);

a=0;
err=0;
lim=0.8*x;
while a==0
    err=err+1;
for i=1:x
    if (sum(Lia(x-i+1,:))>=lim) == 1
        D(x-i+1,:)=[];
    end
    if (sum(Lia(:,x-i+1))>=lim) == 1
       D(:,x-i+1)=[];
    end
end
Lia = ismember(D,Inf);
if sum(sum(Lia))==0
    a=1;
end

if err==10
    disp('probelms, infiny is always in the matrix')
end


[Lp,efficiency]=charpath(D);    % calculate parameters of the
distance matrix



end
end
```

```
function [ A,ordre,number ] = Copy_of_order( M,txt)
%UNTITLED Summary of this function goes here
%   Detailed explanation goes here
% aim: put all the region in list compared to theire values of M
%
% input : M list of values ,
%         txt the name of all the area correspond to the M list
%
% output : A name of the area, each lines is for one values of
the M list,
%         order, is a list that contains the values of the lines
of the A matrix
%         number is the number of the column, area of each region
of the A matrix


x=length(M);
M_bis=unique(M);
x_bis=length(M_bis);
A=zeros(x_bis,x);
A=num2cell(A);
number=zeros(x,x);
ordre=zeros(x_bis,1);

for i=1:x_bis

    f=find(M==M_bis(i));
    for j=1:length(f)
        A(i,j)=txt(f(j));
        number(i,j)=f(j);
        ordre(i,1)=M_bis(i);

    end
end

end
```

```
function [deg] = degrees_und(CIJ)
%DEGREES_UND        Degree
%
%   deg = degrees_und(CIJ);
%
%   Node degree is the number of links connected to the node.
%
%   Input:   CIJ,  undirected (binary/weighted) connection matrix
%
%   Output:  deg,    node degree
%
%   Note: Weight information is discarded.
%
%
%   Olaf Sporns, Indiana University, 2002/2006/2008


% ensure CIJ is binary...

CIJ = double(CIJ~=0);

deg = sum(CIJ);
```

```
function D=distance_bin(A)
%DISTANCE_BIN       Distance matrix
%
%   D = distance_bin(A);
%
%   The distance matrix contains lengths of shortest paths
between all pairs of nodes. An entry (u,v) represents the length
of shortest path from node u to node v. The average shortest
path length is the characteristic path length of the network.
%
%   Input:      A,  binary directed/undirected connection matrix
%
%   Output:     D,  distance matrix
%
%   Notes:
%       Lengths between disconnected nodes are set to Inf.
%       Lengths on the main diagonal are set to 0.
%
%   Algorithm: Algebraic shortest paths.
%
%
%   Mika Rubinov, U Cambridge
%   Jonathan Clayden, UCL
%   2007-2013

% Modification history:
% 2007: Original (MR)
% 2013: Bug fix, enforce zero distance for self-connections (JC)

A=double(A~=0);           %binarize and convert to double format

l=1;                            %path length
Lpath=A;                        %matrix of paths l
D=A;                            %distance matrix

Idx=true;
while any(Idx(:))
    l=l+1;
    Lpath=Lpath*A;
    Idx=(Lpath~=0)&(D==0);
    D(Idx)=l;
end

D(~D)=inf;                    %assign inf to disconnected nodes
D(1:length(A)+1:end)=0;         %clear diagonal
```

```
function [Ci,Q]=modularity_und(A,gamma)
%MODULARITY_UND     Optimal community structure and modularity
%
%   Ci = modularity_und(W);
%   [Ci Q] = modularity_und(W,gamma);
%
%   The optimal community structure is a subdivision of the network
into nonoverlapping groups of nodes in a way that maximizes the
number of  within-group edges, and minimizes the number of between-
group edges.
%    The modularity is a statistic that quantifies the degree to
which the network may be subdivided into such clearly delineated
groups.
%
%   Inputs:
%       W,        undirected weighted/binary connection matrix
%       gamma,    resolution parameter (optional)
%                 gamma>1,        detects smaller modules
%                 0<=gamma<1,     detects larger modules
%                 gamma=1,        classic modularity (default)
%
%   Outputs:    Ci,     optimal community structure
%               Q,      maximized modularity
%
%    Note:  This algorithm is essentially deterministic. The only
potential  source  of  stochasticity  occurs  at  the  iterative
finetuning step, in the presence of non-unique optimal swaps.
However,  the  present  implementation  always  makes  the  first
available optimal swap and is therefore deterministic.
%
%   References:
%       Newman (2006) -- Phys Rev E 74:036104, PNAS 23:8577-8582.
%       Reichardt and Bornholdt (2006) Phys Rev E 74:016110.
%
%   2008-2016
%   Mika Rubinov, UNSW
%   Jonathan Power, WUSTL
%   Dani Bassett, UCSB
%   Xindi Wang, Beijing Normal University
%   Roan LaPlante, Martinos Center for Biomedical Imaging

%   Modification History:
%   Jul 2008: Original (Mika Rubinov)
%    Oct 2008: Positive eigenvalues made insufficient for division
(Jonathan Power)
%   Dec 2008: Fine-tuning made consistent with Newman's description
(Jonathan Power)
%   Dec 2008: Fine-tuning vectorized (Mika Rubinov)
%   Sep 2010: Node identities permuted (Dani Bassett)
%   Dec 2013: Gamma resolution parameter included (Mika Rubinov)
%  Dec 2013: Detection of maximum real part of eigenvalues enforced
(Mika Rubinov)
%   Thanks to Mason Porter and Jack Setford, University of Oxford
%   Dec 2015: Single moves during fine-tuning enforced (Xindi Wang)
%    Jan 2017: Removed node permutation and updated documentation
(Roan LaPlante)

if ~exist('gamma','var')
    gamma = 1;
end
```

```
N=length(A);                                %number of vertices
% n_perm = randperm(N);        %DB: randomly permute order of nodes
% A = A(n_perm,n_perm);%DB: use permuted matrix for subsequent
analysis
K=sum(A);                                %degree
m=sum(K);  %number of edges (each undirected edge is counted twice)
B=A-gamma*(K.'*K)/m;                        %modularity matrix
Ci=ones(N,1);                               %community indices
cn=1;                                       %number of communities
U=[1 0];                          %array of unexamined communites
ind=1:N;
Bg=B;
Ng=N;

while U(1)                                  %examine community U(1)
    [V,D]=eig(Bg);
    [~,i1]=max(real(diag(D)));   %maximal positive (real part of)
eigenvalue of Bg
    v1=V(:,i1);                %corresponding eigenvector

    S=ones(Ng,1);
    S(v1<0)=-1;
    q=S.'*Bg*S;                %contribution to modularity

    if q>1e-10            %contribution positive: U(1) is divisible
        qmax=q;             %maximal contribution to modularity
        Bg(logical(eye(Ng)))=0; %Bg is modified, to enable fine-
tuning
        indg=ones(Ng,1);                %array of unmoved indices
        Sit=S;
        while any(indg)                 %iterative fine-tuning
            Qit=qmax-4*Sit.*(Bg*Sit); %this line is equivalent to:
            [qmax,imax]=max(Qit.*indg); %for i=1:Ng
            Sit(imax)=-Sit(imax);       %   Sit(i)=-Sit(i);
            indg(imax)=nan;             %   Qit(i)=Sit.'*Bg*Sit;
            if qmax>q                   %   Sit(i)=-Sit(i);
                q=qmax;                 %end
                S=Sit;
            end
        end

        if abs(sum(S))==Ng          %unsuccessful splitting of U(1)
            U(1)=[];
        else
            cn=cn+1;
            Ci(ind(S==1))=U(1);   %split old U(1) into new U(1) and
into cn
            Ci(ind(S==-1))=cn;
            U=[cn U];                   %#ok<AGROW>
        end
    else             %contribution nonpositive: U(1) is indivisible
        U(1)=[];
    end

    ind=find(Ci==U(1));       %indices of unexamined community U(1)
    bg=B(ind,ind);
    Bg=bg-diag(sum(bg));                %modularity matrix for U(1)
    Ng=length(ind);                     %number of vertices in U(1)
end
```

```
s=Ci(:,ones(1,N));                          %compute modularity
Q=~(s-s.').*B/m;
Q=sum(Q(:));
% Ci_corrected = zeros(N,1);                    % DB: initialize
Ci_corrected
% Ci_corrected(n_perm) = Ci;                 % DB: return order of
nodes to the order used at the input stage.
% Ci = Ci_corrected;                          % DB: output corrected
community assignments
```

```
function [ bin ] = nbrone( Abin,c)
%UNTITLED Summary of this function goes here
%   Detailed explanation goes here
bin=0;
[n,m]=size(Abin);


for i=1:n
    for j=1:m
        if Abin(i,j)==1
            bin=bin+1;
        end
    end
end
bin=bin/c;


end
```

```
function plot_order( number,Atresh )
%UNTITLED Summary of this function goes here
%   Detailed explanation goes here

% input : list of area number that have the same louvain parameter
values,
%     A tresh, matrix that have the values of the linear correlation
of the area after applied treshold
%
% output: make a graph with linear correlation matrix reorder by
low to high louvain parameter values


[x1,y1]=size(number);
[x,y]=size(Atresh);
A_treshbis=zeros();
L=zeros(1,x);
a=1;
for i=1:x1 %make a list of area low to high louvain parameter
values, L
    for j=1:y1
        if number(i,j)>=1
            L(1,a)=number(i,j);
            a=a+1;
        end
    end
end

for i=1:x %make A_treshbis the matrix of linear correlation values
with area list is order low to high louvain parameter values
    for j=1:x
        z=L(1,i);
        e=L(1,j);

        A_treshbis(i,j)=Atresh(z,e);
    end
end


[x_tresh,y_tresh]=size(A_treshbis);
X_axis=zeros(x_tresh,y_tresh);     % matrix of position X,Y,Z
Y_axis=zeros(x_tresh,y_tresh);
Z_axis=ones(x_tresh,y_tresh);

 for i=1:x_tresh  %create the matrix of position for each points
for use surf
     for j=1:y_tresh
         X_axis(i,j)=j;
            if j<=x_tresh
                Y_axis(i,j)=x_tresh-i-1;


            end
         if j>=floor(x_tresh/2)+1
             Y_axis(i,j)=Y_axis(i,j-floor(x_tresh/2));

        end
```

```
        end


    end
        surf(X_axis,Y_axis,Z_axis,A_treshbis);

end
```